Transport and Dielectric Properties of Thin Fullerene (C_{60}) Films

by

Boris Pevzner

Submitted to the Department of Electrical Engineering and Computer Science
in partial fulfillment of the requirements for the degrees of

Bachelor of Science in Electrical Engineering

and

Master of Science in Electrical Engineering

at the

MASSACHUSETTS INSTITUTE OF TECHNOLOGY

December 1995

© Boris Pevzner, MCMXCV. All rights reserved.

The author hereby grants to MIT permission to reproduce and distribute publicly paper and electronic copies of this thesis document in whole or in part, and to grant others the right to do so.

Author .....
Department of Electrical Engineering and Computer Science
December 12, 1995

Certified by .....
Mildred S. Dresselhaus
Institute Professor of Physics and
Electrical Engineering and Computer Science
Thesis Supervisor

Certified by .....
Arthur F. Hebard
Member of Technical Staff, AT&T Bell Laboratories
Thesis Supervisor

Accepted by .....
Frederic R. Morgenthaler
Chairman, Departmental Committee on Graduate Students

MASSACHUSETTS INSTITUTE OF TECHNOLOGY
JUL 16 1996
Eng.
LIBRARIES

Transport and Dielectric Properties of Thin Fullerene (C_{60}) Films

by

Boris Pevzner

Submitted to the Department of Electrical Engineering and Computer Science
on December 12, 1995, in partial fulfillment of the
requirements for the degrees of
Bachelor of Science in Electrical Engineering
and
Master of Science in Electrical Engineering

Abstract

Dielectric behavior of pristine and modified fullerene (C_{60}) films was investigated over the frequency range of 0.5 mHz to 100 kHz. The presence of mobile ions in the large interstitial spaces of the C_{60} lattice compromises the breakdown voltage and makes pure C_{60} unsuitable for applications requiring high-quality dielectric films (such as microelectronic applications). However, various immobile ions or neutral species (e.g., oxygen) can be made to fill the interstitial volume, changing the characteristics of the C_{60} films and, in some cases, improving their dielectric properties. Based on the low-frequency behavior of the dielectric constant, a model is developed for the mechanism for diffusion of oxygen and other impurities into the interstitial spaces of fullerene materials. It is concluded that dielectric and, especially, microdielectric spectroscopy can be used to assess the content of oxygen or other impurities in the interstitial spaces of solid C_{60}. Using this technique, both tracer and chemical diffusion coefficients can be determined, and the effect of various intercalants on the dielectric properties of C_{60} films can be ascertained.

Thesis Supervisor: Mildred S. Dresselhaus
Title: Institute Professor of Physics and
Electrical Engineering and Computer Science

Thesis Supervisor: Arthur F. Hebard
Title: Member of Technical Staff, AT&T Bell Laboratories

Acknowledgements

I would like to thank Professor M. S. Dresselhaus for her invaluable professional help and guidance in conducting my research on fullerenes, as well as for her almost infinite patience while waiting for this project to be completed.

I am equally grateful to Dr. Arthur Hebard of AT&T Bell Labs who provided support and inspiration throughout each stage of my work both at Bell and at M.I.T. The expertise that I have acquired at Bell Labs under Art's supervision will undoubtedly serve me for years to come.

In the course of this work, I had the benefit of getting advice from a number of M.I.T. faculty. First and foremost, I would like to thank Professor Stephen Senturia for sharing his insights and ideas with me, as well as for lending me his microdielectrometer and lots of other measurement equipment. Professor Markus Zahn has also been of very considerable help by providing valuable advice, and by putting me in touch with his current and former students working on projects whose technical aspects are similar to mine. Professor Gerbrand Ceder assisted in supplying me with access to molecular visualization and computer simulation hardware and software. Thanks goes also to Dr. Gene Dresselhaus for helpful discussions.

I am also thankful to Dr. Huan Lee, David Sheppard, and other good folks at Micromet Instruments (Newton, MA) who let me use their equipment, and generously donated hours of their time to help me with my experiments.

I would also like to acknowledge the other members of Professor Dresselhaus's group whose company I have enjoyed in the past two years: Siegfried (our past-midnight coffee breaks were a lot of fun), Lyndon, Ibo, James, Sun, Nathan and Joe, as well as Dr. Ching-Hwa Kiang, our current postdoc. Dr. Gillian Reynolds has been a pleasure to work with as well, and I wish her luck at her new job at DuPont. Dr. Xiang-Xin (Sean) Bi and his enthusiastic attitude toward life opportunities contributed considerably to my quality of life during the year when Sean was my officemate. My particularly heartfelt thanks goes to Dr. Alex Fung who generously let me make use of his apartment during my frequent visits to New Jersey. Alex, your

friendship and advice are greatly appreciated. Thanks also to Ona Wu of MIT AI Lab for her companionship, support, and technical help.

On the Bell Labs side, I would like to thank Dr. Robert Haddon for helping with obtaining the material for the samples, and to R. H. Eick for technical assistance. Janet Konopka, Mike Milner, Marty and Frances Kaplan, Jeannie Moskowitz, and Mike Yang — all of AT&T — have, each in his or her own way, made my New Jersey experience livelier than it otherwise would have been.

I am grateful to AT&T Bell Laboratories for their financial support that made this project possible. A lot has changed at Bell since I first went there four years ago. Witnessing (from inside) this "national treasure" transforming itself into two separate streamlined industrial laboratories has been a very educational experience indeed.

Most importantly, I would like to thank my parents for their unmitigated support.

Contents

1 Introduction to Fullerenes **18**

1.1 Overview 18

1.2 Synthesis 25

1.3 Structure of Fullerenes 28

1.3.1 Molecular Structure of C_{60} 28

1.3.2 Crystalline Structure 30

1.4 Electronic Structure 40

1.5 Doping 43

1.6 Vibrational Properties 49

1.7 Applications 51

1.7.1 Overview 54

1.7.2 C_{60} Transistors 55

1.7.3 C_{60}-Based Heterojunction Diodes 57

1.7.4 C_{60}–Polymer Composite Heterojunction Rectifying Diode . . . 58

1.7.5 C_{60}–Polymer Composite Heterojunction Photovoltaic Devices 61

1.7.6 Microelectronic Fabrication and Photoresists 62

1.7.7 Silicon Wafer Bonding 65

1.7.8 Fullerenes Used for Uniform Electric Potential Surfaces 66

1.7.9 Sensors 66

1.7.10 Nanotechnology 67

1.7.11 Commercialization and Patents 71

2 Theory of Dielectric Relaxation in Solids **75**

2.1 Introduction and Motivation: Technological importance of dielectrics in modern industry 75

2.2 Dielectrics in Static Fields 79

2.2.1 Electric susceptibility and permittivity 79

2.2.2 Mechanisms of electric polarization 79

2.2.3 Static polarization 82

2.3 Dielectrics in Time-Dependent Fields: Dielectric Relaxation 91

2.3.1 Maxwell's Equations 91

2.3.2 Complex Permittivity 93

2.3.3 Microscopic Models of Dielectric Relaxation 100

2.3.4 Effect of Residual DC Conductivity 116

3 Low frequency dielectric measurements **118**

3.1 Introduction 118

3.2 Parallel-plate measurements 119

3.2.1 Overview 119

3.2.2 Special considerations 121

3.2.3 Measurement equipment 124

3.3 Microdielectrometry 127

3.4 Transport Measurements 134

4 Dielectric Properties of Pristine and Modified C_{60} Films **142**

4.1 Introduction 142

4.2 Optical dielectric function of C_{60} 143

4.3 Experimental difficulties in obtaining intrinsic electrical characteristics of C_{60} solids 147

4.4 Film modification: Motivation and justification 149

4.4.1 NMR and ESR evidence for oxygen diffusion 151

4.4.2 Transport Evidence of Oxygen Diffusion 156

4.5 Sample preparation and characterization 161

4.6 Measurement of the intrinsic dielectric constant of C_{60} 170
4.7 Dielectric properties as a function of oxygen diffusion 172
4.7.1 Low-frequency nonlinearities in the dielectric data 172
4.7.2 Development of the dielectric loss peaks as a result of oxygen diffusion 173
4.7.3 Calculation of added polarization 176
4.7.4 Dynamics of the dielectric loss peaks as a function of oxygen diffusion 179
4.7.5 Obtaining the chemical and tracer diffusion constants from the dielectric loss data 184
4.7.6 Alternative dipole-forming mechanisms 191
4.8 Temperature dependence of the dielectric function in oxygenated C_{60} 196
4.8.1 Dielectric behavior at $T > T_{01}$ 196
4.8.2 Dielectric behavior at $T < T_{01}$ 201
4.9 Effect of humidity 206
4.10 Effect of other film treatments 210

5 Conclusions and Future Work **216**
5.1 Conclusions 216
5.2 Possible Applications 217
5.3 Future Work 218

A LabView Software Listings **220**
A.1 HP 4274A Impedance Bridge 220
A.2 SI 1254 Frequency Response Analyzer 220
A.3 Microdielectrometer 220

List of Figures

1-1 Icosahedral symmetry of C_{60}. 19

1-2 Relationship between the crystal structure of the three forms of carbon (graphite, diamond, and C_{60}) and their relative binding energies per carbon atom. 20

1-3 Time of flight mass spectrum of carbon clusters produced in a supersonic beam by laser vaporization of graphite. 22

1-4 Higher fullerenes. 23

1-5 Formation of carbon nanotubules from graphene sheets. 24

1-6 Schematic view of a simple contact-arc apparatus for the production of fullerene-rich soot. 26

1-7 Golden ratio, golden rectangle, and icosahedral symmetry. 31

1-8 Unit cell of C_{60} crystalline solid and the structural phase transition. . 34

1-9 Correlated orientations of a pair of C_{60} molecules. 35

1-10 Specific heat of solid C_{60} as a function of temperature. 36

1-11 Temperature variation of the cubic lattice constant a_0 for solid C_{60}. . 36

1-12 Phototransformation of C_{60} films under laser irradiation. 38

1-13 Mechanism of photopolymerization in solid C_{60}. 39

1-14 High resolution transmission electron microscopy (HRTEM) photograph of a C_{60} crystallite before and after photopolymerization in a 488 nm Argon-ion laser. 41

1-15 Electronic structure calculations of an isolated C_{60} molecule and of fcc solid C_{60}. 42

1-16 Endohedral and radial-exohedral doping of fullerenes. 45

1-17 Structures for solid C_{60}, M_3C_{60}, and M_6C_{60} (M=K,Rb). 46
1-18 Dependence of the resistivity of a K_xC_{60} film on exposure to K vapor, and superconducting transition at T_c=18 K and temperature dependence of the resistivity ρ of single crystal K_3C_{60}. 47
1-19 Dependence of T_c on the lattice constant a for various M_3C_{60} compounds (M=Li,Na,K,Rb,Cs). 48
1-20 Overview of vibrations in the M_3C_{60} compounds. 50
1-21 Infrared and Raman spectra for C_{60} before and after photopolymerization. 53
1-22 Conventional MOSFET. 55
1-23 C_{60} field effect transistor (FET). 56
1-24 Schematic cross section of a Nb/C_{60}/p-Si structure. 58
1-25 Room temperature current–voltage characteristics of a C_{60}/p-Si and C_{60}/n-Si junctions. 59
1-26 (a) ITO/polymer/C_{60}/metal heterojunctions. 60
1-27 Electrical and optical characteristics of an ITO/MEH-PPV/C_{60}/Au photovoltaic device. 61
1-28 Sequence of steps used in fullerene photolithography. 64
1-29 The principle of moving C_{60} molecules by a rotating external electric field. 68
1-30 Schematic presentation of several proposed electronic device applications for carbon nanotubes. 70

2-1 Mechanisms of polarization. 80
2-2 Electric dipole. 81
2-3 "Dipole chains" forming under the influence of an applied electric field. 82
2-4 Dielectric in the electric field of a capacitor. 83
2-5 Model for calculation of Clausius-Mossotti internal field. 85
2-6 The Clausius-Mossotti and the Onsager cavities. 89

2-7 Mathcad worksheet illustrating the difference between Debye and Onsager results for the dipole moment μ. 90
2-8 Mathcad worksheet showing the response of the polarization of a dielectric to the step-up and step-down excitations. 95
2-9 An illustration of the manner in which the static dielectric permittivity $\varepsilon(0)$ is made up of contributions of all loss processes. 98
2-10 Dispersion of polarization in dielectric measurements. 99
2-11 Idealized view of the polarization due to dipole orientation in the presence of an applied electric filed. 101
2-12 Mathcad worksheet showing the frequency dependence of the Debye single relaxation time model for dipole orientation. 103
2-13 A schematic representation of the significance of the existence of a distribution of relaxation times in the application to the interpretation of a "non-Debye" loss peak in a dielectric material. 104
2-14 Mathcad worksheet showing a Cole-Cole plot of the Debye single relaxation time model for dipole orientation. 105
2-15 Mathcad worksheet calculating and displaying the Williams-Watts relaxation time distribution function for different values of the β_{ww} parameter. 108
2-16 Mathcad worksheet calculating and displaying Cole-Cole plots of the Debye single relaxation time model (ε_{DEBYE}), Cole-Cole model (ε_{CC}), Davidson-Cole model (ε_{CD}), and Williams-Watts model (ε_{WW}). . . . 109
2-17 Mathcad worksheet calculating and displaying relaxation time distribution functions for Cole-Cole $G_{CC}(\tau/\tau_{CC})$, Davidson-Cole $G_{CD}(\tau/\tau_{CD})$, and Williams-Watts $G_{WW}(\tau/\tau_{WW})$ models. 110
2-18 The potential energy diagram of a many-body two-level system representing the energy of a large number of interacting systems. 113
2-19 The effect of temperature on the shape of the loss peak of a dipolar material. 115

2-20 Mathcad worksheet illustrating the effective dielectric loss of a Debye dielectric having DC conductivity σ_0, for different values of σ_0. 117

3-1 Parallel plate electrodes. 120
3-2 Equivalent circuits for the material under test with and without taking the interfacial capacitance into account. 122
3-3 Idealized view of the polarization due to ions. 122
3-4 Schematic diagram of a measurement system illustrating the effect of cable capacitance and shielding. 124
3-5 A schematic of the working principle of the SI 1254 Frequency Response Analyzer. 125
3-6 Schematic view of active portion of microdielectrometer sensor chip. . 128
3-7 Cross section of microdielectrometer sensor. 129
3-8 Calibration of the microdielectric sensor. 130
3-9 Schematic of "ribbon cable" packaging of the integrated microdielectrometer sensor. 131
3-10 The Micron Sensor geometry. 132
3-11 Functional block diagram of sampled data system used in microdielectrometry measurements. 133
3-12 Current measurement circuits. 137
3-13 A block diagram of the SR570 Low Noise Current Amplifier. 138

4-1 Summary of real $\varepsilon'(\omega)$ and imaginary $\varepsilon''(\omega)$ parts of the dielectric function for C_{60} vacuum-sublimed solid films over all optical frequencies. . 144
4-2 C_{60} molecules arranged in a face-centered cubic lattice, with oxygen molecules occupying octahedral interstitial sites of the C_{60} solid. . . . 152
4-3 NMR evidence for pressure-assisted oxygen diffusion into C_{60} films. . 153
4-4 Resonant alpha particle backscattering evidence for UV-assisted oxygen diffusion into C_{60} films. 154
4-5 ESR evidence for UV-assisted oxygen diffusion into a C_{60} film. 156
4-6 Transport measurements of a C_{60} film. 159

4-7 Thermal conductivity of a number of electrically insulating solids as a function of temperature. 162
4-8 A schematic of the vacuum deposition system used to grow the C_{60} films.164
4-9 A Dektak 8000 profilometer measurement of a 1000 Å C_{60} film. . . . 165
4-10 Optical characterization of C_{60} films: infrared transmission and wavelength-dependent absorbance. 166
4-11 X-ray characterization of polycrystalline C_{60} films. 167
4-12 Photopolymerization of C_{60} films studied with Raman spectroscopy. . 168
4-13 A typical trilayer ("sandwich") structure composed of five identical Al-C_{60}-Al junctions. 169
4-14 Plot of the reciprocal areal capacitance of Al-C_{60}-Al and Al-C_{70}-Al trilayer structures as a function of fullerene film thickness, measured at 100 kHz. 171
4-15 Evidence of nonlinear behavior of a C_{60} film at low frequencies due to the presence of weakly bound dipoles. 174
4-16 Dielectric response of a C_{60} film after 16 hours of exposure to the ambient environment at room temperature. 175
4-17 A schematic drawing showing oxygen molecules located in the interstitials of the C_{60} solid. 178
4-18 A schematic plot of dielectric loss vs frequency for a C_{60} film, prepared initially without exposure to oxygen, showing peaks moving after various durations of oxygen exposure. 180
4-19 Evolution of the dielectric peaks in an oxygenated C_{60} film with exposure to the ambient atmosphere. 182
4-20 Enhanced polarization and anomalous dispersion effects observed in a Al-C_{60}-Ag trilayer structure. 183
4-21 Illustration of the tracer and chemical diffusion processes in two dimensions. 184
4-22 Illustration of the approximations made in deriving the equations of diffusion. 186

4-23 Mathcad worksheet calculating Fick's law solutions for the concentration $C(x,t)$ as a function of time t and coordinate x. 188
4-24 Plot of $\varepsilon'(\omega)$ and $\varepsilon''(\omega)$ used to determine the molecular oxygen diffusion into a C_{60} film. 189
4-25 Frequency dependence of the real and imaginary parts of the dielectric function of a C_{60} film plotted on the log-log scale for temperatures 215–290 K. 197
4-26 Arrhenius plot of the position of the dielectric loss peak frequency. . . 199
4-27 Summary of the results of measurements of the second-order phase transition in C_{60} by various methods at different frequencies. 203
4-28 Capacitance and dielectric loss tangent vs temperature, for a C_{60} film measured at 100 kHz. 204
4-29 Real and imaginary parts of the dielectric function of a C_{60}/C_{70} mixture pellet plotted as a function of temperature at different frequencies. . . 205
4-30 Frequency dependence of the real and imaginary parts of the dielectric function of a C_{60} polycrystalline film plotted for different values of ambient humidity. 209
4-31 Capacitance C and dielectric loss tangent D vs frequency on a log scale showing the effect of 10-minute exposure of a C_{60} film to chlorine. . . 211
4-32 Plot of capacitance and dielectric loss tangent vs frequency for C_{60} films grown in the absence and in the presence of UV light during deposition.213
4-33 Real and imaginary parts of the dielectric function of a C_{60} film before and after photopolymerization. 214
4-34 Plot of the reciprocal areal capacitance vs thickness for pristine and UV-polymerized C_{60} films. 215

A-1 HP 4274A VI's front panel. 221
A-2 HP 4274A VI's wiring diagram. 222
A-3 HP 4274A VI's position in hierarchy. 223
A-4 SI 1254 VI's front panel. 224

A-5 SI 1254 VI's wiring diagram. 225
A-6 The Microdielectrometer VI's front panel. 226
A-7 The Microdielectrometer VI's wiring diagram. 227
A-8 The Microdielectrometer VI's position in hierarchy. 228

List of Tables

1.1 Physical constants for C_{60} molecules 32

1.2 Physical constants for C_{60} solid materials 33

1.3 Intramolecular vibrational frequencies of C_{60} 52

1.4 Some uses of fullerenes suggested by patents and patent applications. 73

2.1 The average relaxation times $\langle\tau\rangle$ and the average relaxation frequencies $\langle\omega\rangle$ for various dielectric relaxation models. 111

2.2 A summary of various dielectric relaxation functions and their power-law exponents. 115

3.1 Microdielectric sensor specifications. 132

4.1 Intrinsic conductivity and activation energy reported for crystalline, polycrystalline, and amorphous C_{60} solids. 157

Preface

Since its discovery in 1985 [1], carbon-60 (C_{60}), a newly found all-carbon molecule, has captured the attention of scientists all over the world. It has been designated the 1991 "Molecule of the Year" on the cover of *Science* magazine [2], while investigation of its physical and chemical properties, as well as the properties of its compounds, became one of the most popular topics of today's research in solid state physics, material science, and chemistry.

The principal contribution of the present work has been the development of a comprehensive model for the dielectric properties of solid C_{60}, particularly explaining how the dielectric properties are affected by various dopants, impurities, and processing. The need for better dielectrics with improved properties suitable for modern integrated manufacturing needs was one of the main motivations for studying ways to enhance the dielectric properties of C_{60} thin films. And since in today's silicon technology, the enhancement of SiO_2 by nitrogen incorporation has been shown to result in an increased dielectric constant and resistance to impurity diffusion, as well as much higher resistance to interface state generation under avalanche, high-field and hot-carrier stress, and irradiation, a similar path has been chosen for attempting to improve the dielectric properties of C_{60} thin films.

It is known that solid C_{60} has a substantial amount of interstitial volume. The presence of mobile ions in these spaces compromises the breakdown voltage and makes pure C_{60} unsuitable for applications requiring high-quality dielectric films. However, various immobile ions or neutral species (e.g. oxygen) can be made to fill the interstitial volume, changing the characteristics of the C_{60} films and, in some cases, improving the dielectric properties. In this study, dielectric measurements of pris-

tine and modified C_{60} films were performed for frequencies ranging from 0.5 mHz to 100 kHz. Based on the low-frequency behavior of the dielectric constant, a model is proposed for the mechanism of oxygen diffusion into the interstitial spaces of the C_{60} solid.

The thesis is organized into five major chapters. We start by reviewing the state of the art in the science of C_{60} and its sister materials (*fullerites*) in Chapter 1. While the theoretical and experimental knowledge in this area is still being accumulated and interpreted, a rather clear overall picture of the structure and properties of fullerites has already emerged. We briefly review synthesis of C_{60}; explain its molecular, crystalline, and electronic structure; discuss its vibrational properties and doping compounds (including superconductors), and then discuss in some detail the possible applications of this new material, paying particular attention to emerging electronic applications.

While Chapter 1 is laying the groundwork for the thesis by introducing the essential structure and properties of C_{60} necessary for understanding the material's dielectric and transport properties, Chapter 2 is similarly important as it introduces the theoretical background and mathematical machinery necessary for describing dielectric properties of materials. Chapter 3 complements Chapter 2 by explaining the techniques of low frequency dielectric measurements, including the recently developed microdielectrometry technique [3], that have been used in this study. Chapter 4 builds on the preceding chapters, and presents the data on dielectric properties of C_{60} as a function of oxygen diffusion, temperature, and other material treatments. A model for the dielectric relaxation in C_{60} that takes the role of impurities into account is also developed in Chapter 4. We conclude with a summary of main results of the work in Chapter 5.

The rationalized (MKS) system of units is used throughout this work. The typesetting convention used calls for real scalar variables to be set in regular font, complex variables — in bold font, and vector variables — with a vector sign on top.

Chapter 1

Introduction to Fullerenes

1.1 Overview

Carbon-60, a hollow, all-carbon molecule [see Figure 1-1(c)], consists of sixty carbon atoms arranged at the vertices of a truncated icosahedron and joined with a mixture of single and double bonds. Its 12 pentagonal and 20 hexagonal faces form a symmetrical soccer-ball-like structure. Named for the American architect, inventor, and evangelist, R. Buckminster Fuller, who designed a geodesic dome with the same fundamental symmetry [4, 5], C_{60} molecules are called *buckminsterfullerenes* (or more affectionately, *buckyballs*).

Due to its all-carbon structure and extraordinarily high chemical and structural stability, C_{60} has often been referred to as the third major form of pure carbon, after diamond and graphite. Figure 1-2 shows the relationship between the crystal structure of these solids and the relative binding energies per carbon atom. All sixty carbon atoms comprising the C_{60} cage are equivalent, each sharing a double bond and two single bonds with its nearest neighbors. Since all bonds for each carbon atom are satisfied, pure C_{60} is expected to be either an insulator or a semiconductor.

Curiously, the original stimulus for the work that led to the discovery of C_{60} molecule [1] was an interest in certain unexplained features in the absorption and

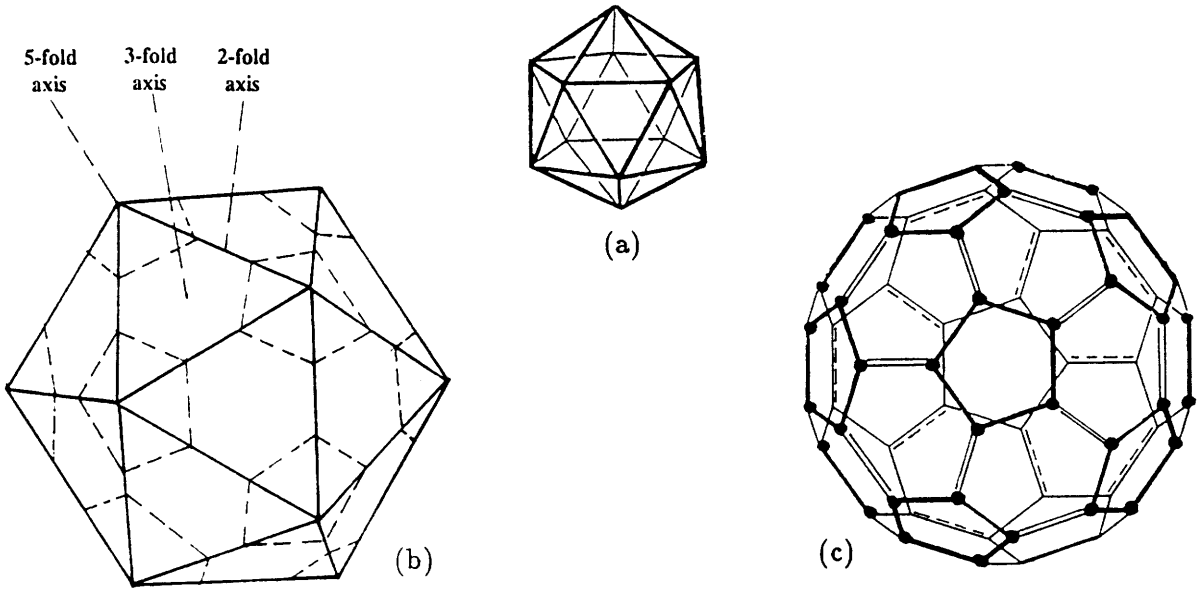


Figure 1-1: Icosahedral symmetry of C_{60}. (a) Icosahedron, one of the five Platonic solids. (b) Formation of a truncated icosahedron by cutting off the vertices of the icosahedron. Three types of symmetry axes of truncated icosahedron are indicated. (c) C_{60} molecule. All carbon atoms in C_{60} are equivalent, each sharing a double bond and two single bonds with its nearest neighbors. All bonds are satisfied, so that the chemical and structural stability of the molecule is very high.

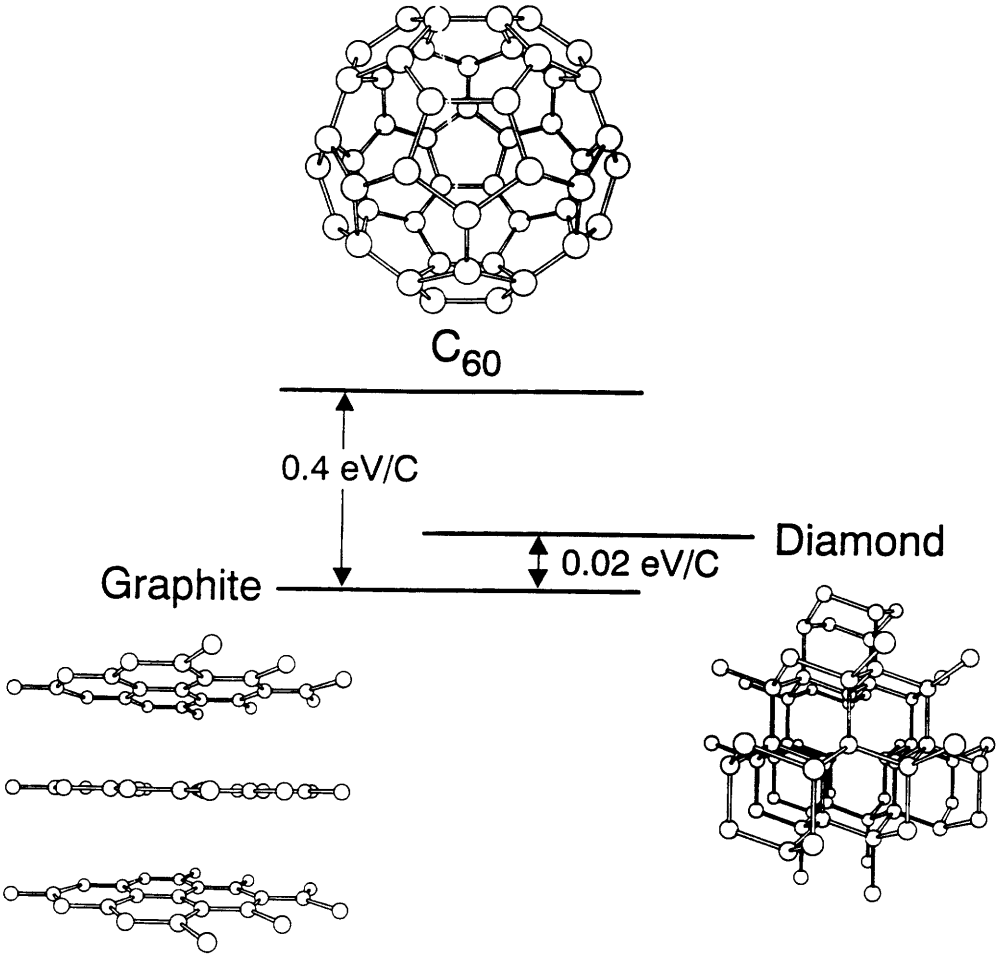


Figure 1-2: Schematic showing the relationship between the crystal structure of the three forms of carbon (graphite, diamond, and C_{60}) and their relative binding energies per carbon atom. Under normal conditions there are barriers present that prevent spontaneous conversion of C_{60} to diamond or graphite. (Adapted from Ref. [6].)

emission spectra of interstellar matter [7]. It has been proposed that C_{60} is indeed ubiquitous in the cosmos, and the special properties of C_{60} explain the observed spectral anomalies. Writes Harold Kroto, a co-discoverer of C_{60}:

> It is interesting to note that the motives for the experiments which serendipitously revealed the spontaneous creation and remarkable stability of C_{60} were astrophysical. Behind this goal lay a quest for an understanding of the curiously pivotal role that carbon plays in the origin of stars, planets, and biospheres. ...It is fascinating to now ponder over whether buckminsterfullerene is distributed throughout space, and we have not recognized it, and that it may have been under our noses on earth, or at least played an important role in some very common environmental processes, since time immemorial." [8]

It has also been suggested [9] that C_{60} may be responsible for the high abundance of certain elements in the Universe (notably, ^{22}Ne), and for the recently discovered [10] diamond-like domains in meteorites.

However, the first sighting of buckyballs in the wild happened here on Earth, and in the most unlikely place: Shunga, a Russian town in the lake region of Karelia, about 200 miles northeast of St. Petersburg. Peter Buseck *et al.* [11] discovered that a rock sample from Shunga they had been studying contained trace amounts of both C_{60} and C_{70}. Says Richard Smalley of Rice University, a co-discoverer of C_{60}: Next thing you know, they "might find a mine for buckyballs." [12]

In addition to C_{60}, many other closed-shell all-carbon molecules with different masses, *fullerenes*, have been observed. It has been shown [1, 13] that hollow three-dimensional carbon clusters with even numbers of carbon atoms (C_{2n} with $n > 15$) created, for instance, by laser vaporization of graphite, are fullerenes of various shape and stability (Fig. 1-3). Under most conditions, C_{60} is produced in noticeably greater yield that other C_{2n} clusters. The second most plentiful member of the fullerene family is C_{70}, a prolate-shaped molecule, which contains 10 additional carbon atoms

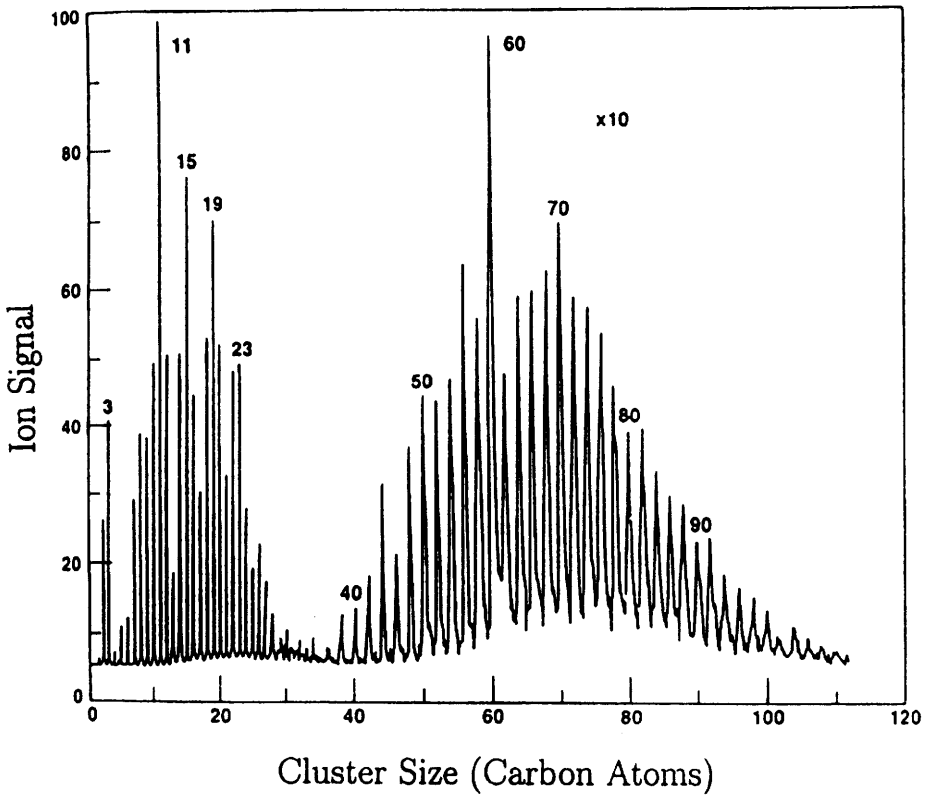


Figure 1-3: Time of flight mass spectrum of carbon clusters produced in a supersonic beam by laser vaporization of graphite [14].

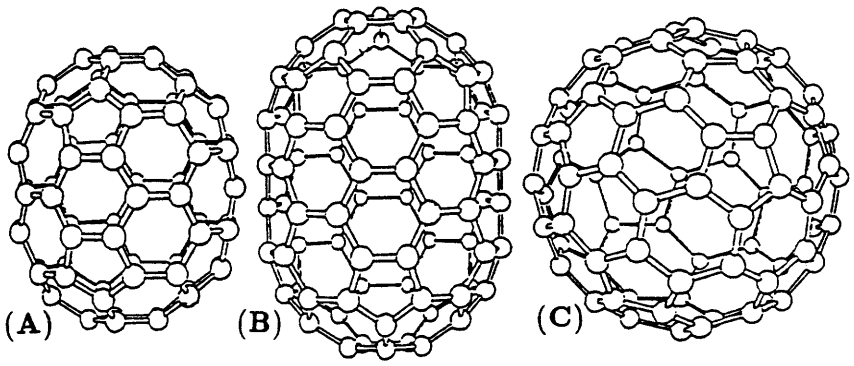


Figure 1-4: (**A**) C_{70} molecule as a rugby ball. (**B**) C_{80} molecule as an extended rugby ball. (**C**) C_{80} molecule as an icosahedron.

at the "equator" of the buckyball [Fig. 1-4(a).] Approximately 3–4% of a typical buckminsterfullerene output contains fullerenes larger than C_{60} and C_{70}. Some higher fullerenes [such as C_{80} on the Fig. 1-4(b,c)] can come in different shapes, forming isomers. Fullerenes consisting of as many as over a thousand carbon atoms have been observed. (See, for example, Curl and Smalley [15] for an overview of higher fullerenes and a variety of other fullerene structures.)

In addition to fullerenes, microtubules comprising coaxial tubes of graphite sheets terminated with fullerene end caps have been discovered [16] and dubbed *buckytubes* or *bucky fibers* (Fig. 1-5). Diameters on the order of tens of angstroms and lengths on the order of microns are typical, but recently, buckytubes with the diameter of a single C_{60} molecule have been synthesized [17, 18].

In this chapter, we shall briefly review the state of the art in the science of fullerenes. We shall start with an overview of synthesis (Sec 1.2) and an outline of molecular (Sec. 1.3.1) and crystalline (Sec. 1.3.2) structure of the fullerenes, concentrating on C_{60}, the most plentiful fullerene. The electronic structure of C_{60} molecules and solids will be briefly reviewed in Sec. 1.4. Various ways to introduce dopants into a C_{60} solid and the effects associated with doping (e.g., superconductivity) will be discussed in Sec. 1.5. In Sec. 1.6, a brief overview of the vibrational properties of

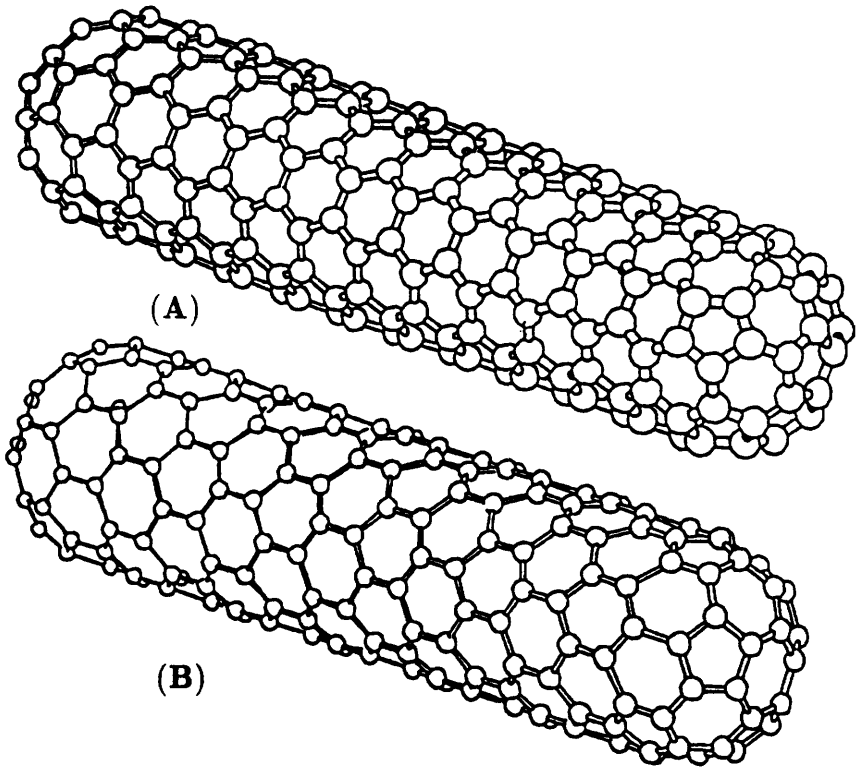


Figure 1-5: By rolling up a graphene sheet (a single layer from a 3-dimensional crystal of graphite) as a cylinder and capping each end of the cylinder with half of a C_{60} molecule, a "C_{60} tubule" one layer in thickness is formed. Shown here is a schematic model arising from: (**A**) an armchair cap with 5-fold axis, and (**B**) a zigzag cap with 3-fold axis. (Adapted from Ref. [19].)

C_{60} and C_{60}-based solids will be presented. We shall conclude with a brief outline of potential applications of the fullerenes (Sec. 1.7).

In the last few years, a number of thorough reviews on the subject of fullerenes have appeared [6, 15, 19–22], and a definitive book on fullerenes is about to be published [23]. It is not the aim of this overview to recount every conceivable property of the fullerenes that has ever been discovered. Instead, we shall mainly concentrate on those discoveries that are essential for understanding the structure and properties of the fullerenes and important to practical, in particular electronic, applications.

1.2 Synthesis

Although the fullerenes were discovered in 1985 [1, 14], and their unique structure received a good deal of attention in the scientific community at that time, experimental progress was hindered by the minuscule amounts produced in the gaseous residues of laser desorption experiments (see Fig. 1-3). This situation rapidly turned around in 1990 with the discovery by Krätschmer and Huffman of a simple and efficient technique to synthesize and concentrate macroscopic amounts of C_{60} and C_{70} [7]. A simplified schematic of their apparatus is presented on Fig. 1-6. The method is based on an AC arc discharge between graphite electrodes in approximately 200 Torr of He; the current can be supplied by a low-cost AC arc welder. The heat generated at the contact point between the electrodes evaporates carbon to form soot and fullerenes, which condense on the water-cooled walls of the reactor. Such an apparatus is capable of producing several grams of C_{60}/C_{70} per day. The discharge produces a carbon soot which can contain up to ~15% of the fullerenes C_{60} (~13%) and C_{70} (~2%). Smaller fullerenes ($n \leq 84$ in C_n) are separated from the soot using Soxhlet extraction with a toluene solvent. The separation of C_{60} from C_{70} and the higher molecular weight fullerenes is typically accomplished using liquid chromatography.

For experiments where rigid exclusion of solvent impurities is necessary, it is pos-

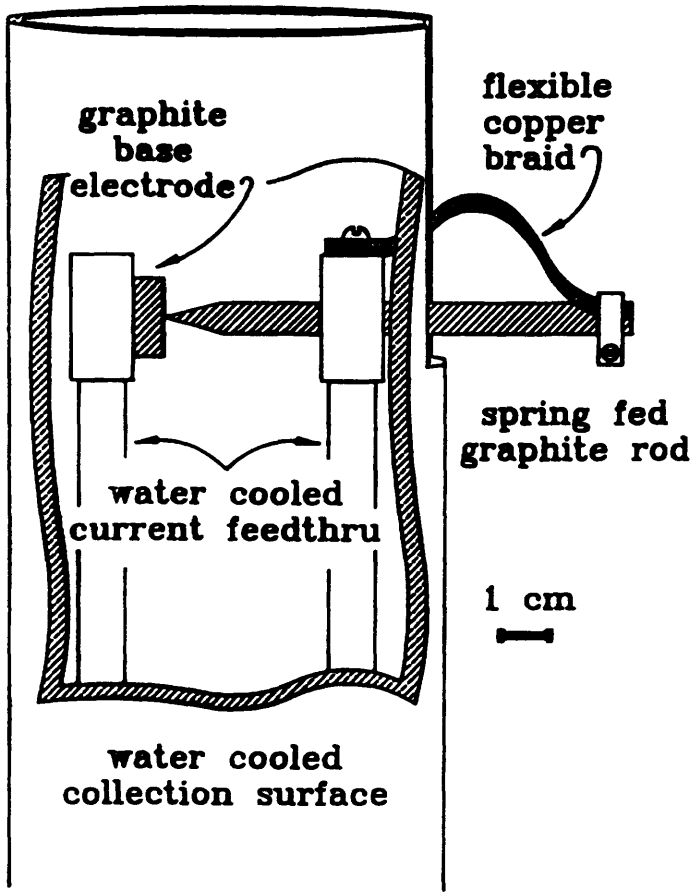


Figure 1-6: Schematic view of a simple contact-arc apparatus for the production of fullerene-rich soot.

sible to separate C_{60} and C_{70} from the arc-derived soot without the use of solvents by heating the soot in vacuum and in a temperature gradient. The C_{60} and C_{70} both are sublimed from the soot that is placed in the hottest part of the furnace and the fullerene molecules drift toward the cold end of a quartz tube connected to a vacuum line. The C_{60} and C_{70} molecules condense in separate bands on the tube wall, and the positions of these bands are related to different sublimation temperatures for C_{60} and C_{70}. For C_{60} or C_{70} powders obtained from liquid chromatography (LC), heat treatment in a dynamic vacuum of flowing inert gas (300°C for 1/2 to 1 day) is used to reduce the solvent impurity. Furthermore, solid C_{60} has been shown to intercalate or accept oxygen quite easily at 1 atm., particularly in the presence of visible or UV light. Thus, degassed powders should be stored in vacuum or in an inert gas (preferably in the dark).

Actual property measurements of fullerenes are made either on powder samples, films or single crystals. C_{60} powder is obtained from the solution which has passed through the LC column by vacuum evaporation of the solvent from the solution. Pristine C_{60} films can be deposited onto a substrate such as a clean silicon (100) or quartz surface by sublimation of the C_{60} powder in a vacuum of $\sim 10^{-6}$ Torr [7, 24]. Ellipsometry can be used to measure the thickness of the C_{60} films as they are deposited [25]. By variation of the substrate material and crystalline orientation, and by variation of the film growth temperature, the crystallite size and microstructure of the film can be varied. Single crystals can be grown either from solution using solvents such as CS_2, hexane and toluene or by vacuum sublimation [26]. The solution growth method tends to yield larger single crystals, but such crystals tend to contain trapped solvent. The smaller crystals ($\sim$0.5 mm in size) grown by sublimation (in vacuum or in an inert gas such as argon) tend to be more pure chemically and more perfect structurally.

1.3 Structure of Fullerenes

Prior to the discovery of the fullerenes [1], the only known forms of pure carbon were graphite and diamond (Sec. 1.1), both of which are *crystalline* materials. By contrast, the materials formed from fullerenes (called *fullerites*) are *molecular* solids, and their structure and properties are therefore strongly dependent on the structure and properties of the constituent fullerene molecules. The structure of the molecules is addressed below in Sec. 1.3.1, while the structure of fullerene molecular solids is reviewed in Sec. 1.3.2. This review is mainly limited to C_{60}, the most plentiful fullerene. While some information about the next most abundant fullerene, C_{70}, has been published, very little is known about higher fullerenes (C_{76}, C_{78}, C_{84}, etc.), and their practical importance is, therefore, very limited.

1.3.1 Molecular Structure of C_{60}

The sixty carbon atoms in C_{60} are located at the vertices of a regular truncated icosahedron where every site is equivalent to every other site [see Fig. 1-1(c)]. Since (1) the average nearest neighbor carbon-carbon (C–C) distance in C_{60} (1.44 Å) is almost identical to that in graphite (1.42 Å), (2) each carbon atom in graphite and in C_{60} is trigonally bonded to other carbon atoms and (3) most of the faces on the regular truncated icosahedron are hexagons, we can to a first approximation think of the C_{60} molecule as a "rolled-up" graphene sheet (a single layer of crystalline graphite) [19].

Like all polyhedra, the regular truncated icosahedron is subject to Euler's theorem:

$$f + v - e = 2 \tag{1.1}$$

where f, v, and e are, respectively, the number of faces, vertices, and edges of the polyhedron. Generally, for polyhedra formed by h hexagonal faces and p pentagonal

faces, the total number of faces is

$$f = p + h \tag{1.2}$$

and, since each edge is shared by two faces, the total number of edges is

$$e = \frac{5p}{2} + \frac{6h}{2}. \tag{1.3}$$

By requiring that the polyhedron consist of only pentagons and hexagons, an additional constraint that each vertex is shared by three faces is introduced (note that the sum of the angles of faces adjacent to each vertex can not exceed 360°):

$$v = \frac{5p}{3} + \frac{6h}{3}. \tag{1.4}$$

From equations (1.2), (1.3), and (1.4), we easily derive that

$$f + v - e = \frac{p}{6},$$

which, by Euler's equation (1.2), yields

$$p = 12. \tag{1.5}$$

From this we conclude that all fullerenes with only hexagonal and pentagonal faces must have 12 pentagonal faces, and the number of hexagonal faces is arbitrary. In particular, the regular truncated icosahedron (C_{60}) has 20 hexagonal faces, in addition to its 12 pentagonal faces. Since the addition of a single hexagon adds two carbon atoms, all fullerenes must have an even number of carbon atoms, in agreement with the observed mass spectra for fullerenes as illustrated in Fig. 1-3.

The symmetry operations of the icosahedron consists of the identity operation, 12 five-fold axes through the centers of the pentagonal faces, 20 three-fold axes through

the centers of the hexagonal faces, 15 two-fold axes through centers of the edges joining two hexagons [see Fig. 1-1(b)]. Each of the 60 rotational symmetry operations can be compounded with the inversion operation, resulting in 120 symmetry operations in the icosahedral point group I_h:

$$I_h = \{E, 12C_5, 12C_5^2, 20C_3, 15C_2\} \otimes i.$$

Molecules with I_h symmetry, of which C_{60} is the most prominent member, have the highest degree of symmetry of any known molecule.

The high aesthetic appeal of the buckyball has been linked to the famous golden ratio $\phi = \frac{1+\sqrt{5}}{2} \approx 1.61803$ prevalent in construction of the molecule (Fig. 1-7). Recently, the mathematics of the buckyball received great exposure in the works of Chung and Sternberg [28–30] and Bertram Kostant [31–33].

Although each carbon atom in C_{60} is equivalent to every other carbon atom, the three bonds emanating from each atom are not equivalent, two being electron-poor single bonds, and one being an electron-rich double bond (Fig. 1-1). This affects the length of the bonds making the single bonds around each pentagon longer than the double bonds at the edge of each pair of adjacent hexagons (see Table 1.1), which, however, preserves the icosahedral I_h symmetry of the molecule.

Table 1.1 summarizes some important physical constants for C_{60} molecules.

1.3.2 Crystalline Structure

Since each carbon atom has its valence requirements fully satisfied, the C_{60} molecules are expected to form a van der Waals bonded molecular solid which is either an insulator or a semiconductor (the band gap has been optically determined to be 1.7 eV [45]). The C_{60} molecules crystallize into a cubic structure with a lattice constant of 14.17 Å (see Table 1.2).

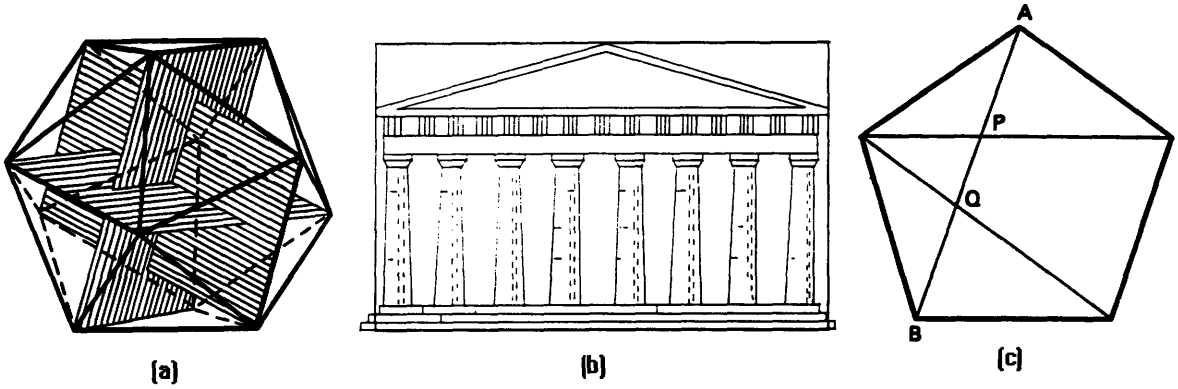


Figure 1-7: (a) *Regular icosahedron* is one of the five Platonic solids (polyhedra whose surface is bound by congruent regular polygons). Its twelve vertices can be divided into three coplanar groups of four. These lie at the corners of three golden rectangles which are mutually perpendicular and situated symmetrically with respect to each other, their common point being the centroid of the icosahedron. (b) A *golden rectangle* (a rectangle with sides of ratio ϕ) has been noted to have a particular aesthetic appeal. For example, the dimensions of The Parthenon at Athens (built in the fifth century B.C.), one of the world's most famous structures, can be fitted almost exactly into a golden rectangle. (c) Truncation of each vertex of an icosahedron [see Fig. 1-1(b)] results in 12 additional pentagonal faces being created. In each pentagon, the point of intersection (P or Q) of any two diagonals divides each in the golden ratio ϕ. The resulting solid, *truncated icosahedron*, maintains the high I_h symmetry of the regular icosahedron. (An excellent book by Huntley (Ref. [27]), from which figure (b) was taken, is full of fascinating facts about the golden ratio ϕ, with examples drawn from physics, mathematics, biology, architecture, and many other fields.)

Table 1.1: Physical constants for C_{60} molecules (after Ref. [23]).

Quantity	Value	Reference
Average C–C distance	1.44 Å	[34]
C–C bond length on a pentagon	1.46 Å	[35]
C–C bond length between adjacent hexagons	1.40 Å	[35]
C_{60} mean ball diameter[a]	7.10 Å	[36]
C_{60} ball outer diameter[b]	10.34 Å	–
Moment of inertia I	1.0×10^{-43}kg m^2	[37]
Volume per C_{60}	1.87×10^{-22}/cm^3	–
Number of distinct C sites	1	–
Number of distinct C–C bonds	2	–
Binding energy per atom	7.40 eV	[38]
Heat of formation (per g C atom)	10.16 kcal	[39]
Electron affinity	2.65±0.05 eV	[40]
Cohesive energy per C atom	1.4 eV/atom	[41]
Spin–orbit splitting of C($2p$)	0.00022 eV	[42]
First ionization potential	7.58 eV	[43]
Second ionization potential	11.5 eV	[44]
HOMO–LUMO gap	1.65 eV	[38]

[a] This value was obtained from NMR measurements. The calculated geometric value for the diameter is 7.09 Å (treating carbon atoms as mathematical points).

[b] This value for the outer diameter is found by assuming the thickness of the C_{60} shell to be 3.35 Å (taking account of the size of the π-electron cloud associated with the carbon atoms). In the solid, the C_{60}–C_{60} nearest-neighbor distance is 10.02 Å (see Table 1.2).

Table 1.2: Physical constants for crystalline C_{60} in the solid state (after Ref. [23]).

Quantity	Value	Reference
fcc Lattice constant	14.17 Å	[46]
C_{60}–C_{60} distance	10.02Å	[47]
C_{60}–C_{60} cohesive energy	1.6 eV	[48]
Tetrahedral interstitial site radius	1.12 Å	[47]
Octahedral interstitial site radius	2.07 Å	[47]
Mass density	1.72 g/cm^3	[47]
Molecular density	1.44 $\times 10^{21}$/cm^3	[47]
Compressibility $(-d\ln V/dP)$	6.9×10^{-12}cm^2/dyn	[49]
Bulk modulus[a]	14–18 GPa	[49–51]
Young's modulus[b]	15.9 GPa	[52]
Structural phase transition (T_{01})	261 K	[53]
dT_{01}/dp	11 K/kbar	[54, 55]
Vol. coeff. of thermal expansion	6.1×10^{-5}/K	[56]
Band gap (HOMO-LUMO)	1.7 eV	[45]
Velocity of sound v_t	2.1×10^5 cm/sec.	[52]
Velocity of sound v_l	3.6×10^5 cm/sec.	[52]
Debye temperature	185 K	[57, 58]
Thermal conductivity (300 K)	0.4 W/mK	[59]
Electrical conductivity (300 K)	1.7×10^{-7} S/cm	[60]
Phonon mean free path	50 Å	[59]
Static dielectric constant	4.0 – 4.5	[24, 25, 61]
Melting temperature	1180°C	[62]
Sublimation temperature	~350°C	[63]
Heat of sublimation	40.1 kcal/mol	[64]
Latent heat	1.65 eV	[65]

[a]Recently, the bulk modulus at room temperature of 6.8 GPa in the fcc phase and 8.8 GPa in the sc phase below T_{01} has been reported [66]. The conversion of units for pressure measurements is 1 GPa $= 10^9$ N/m^2 $= 0.99$ kbar $= 7.52 \times 10^6$ torr $= 10^{10}$ dyn/cm^2. Also, 1 atm $= 760$ torr $= 1.01 \times 10^5$ Pa.
[b]For solvated C_{60} crystals measured by vibrating reed method [52]. Measurements on film samples suggest a higher Young's modulus [67].

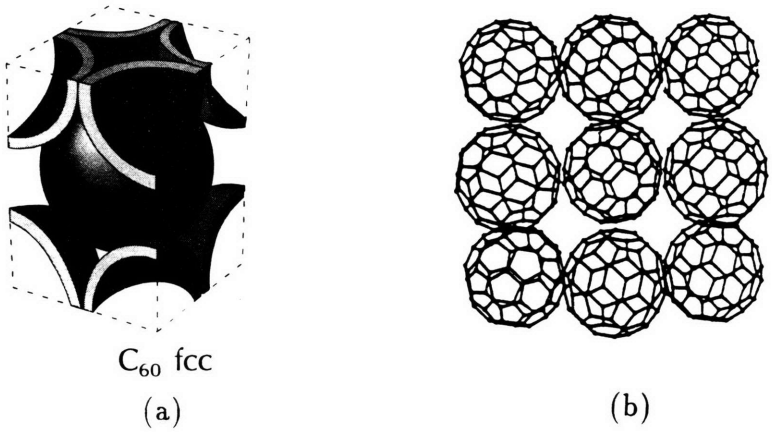


Figure 1-8: (a) A bct unit cell illustrating the fcc structure of C_{60} crystalline solid at $T > 255$ K. The buckyballs are rotating rapidly with three degrees of rotational freedom, rendering all balls equivalent on average (on the time scale greater than one over the frequency of rotation). (b) C_{60} solid at low temperatures: the buckyballs are frozen in inequivalent positions in a simple cubic lattice [68].

Structural phase transition

At room temperature, the balls are rotating rapidly with three degrees of rotational freedom, and the ball centers are arranged on a face centered cubic (fcc) lattice (space group O_h^5 or $Fm\bar{3}m$) with one C_{60} ball per primitive fcc unit cell, or 4 balls per simple cubic unit cell [see Fig. 1-8(a)].

Below the structural phase transition $T_{01} \approx 260$ K, the C_{60} balls completely lose two of their 3 degrees of rotational freedom, and the residual *hindered* rotational motion occurs only along the four $\langle 111 \rangle$ axes. The structure of solid C_{60} below $\sim$260 K thus becomes simple cubic (space group T_h^6 or $Pa\bar{3}$) with a lattice constant $a_0 =$ 14.17 Å and four C_{60} molecules per unit cell, as the four balls within the fcc structure become inequivalent [Fig. 1-8(b)]. The reason for this transition lies in the fact that, at temperatures below 260 K, adjacent C_{60} molecules develop correlated orientations. The lowest energy is achieved when an electron-rich double bond of one C_{60} molecule is aligned with the electron-poor pentagonal face of an adjacent C_{60} ball [Fig. 1-

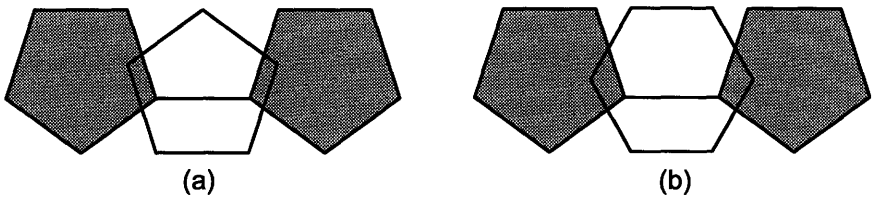


Figure 1-9: Electron-rich double bond on one C_{60} molecule (shaded) opposite an electron-poor (a) pentagonal face and (b) hexagonal face of the adjacent molecule (not shaded).

9(a)]. Another structure with only slightly higher energy places the electron-rich double bond of one C_{60} molecule opposite an electron-poor hexagonal face [see Fig. 1-9(b)]. (Predictably, as the temperature T is lowered below 260 K, the probability of occupying the lower energy configuration increases [69].) A mixture of these alignment configurations in the fullerene solid is achieved by the ratcheting motion of the C_{60} molecules around the $\langle 111 \rangle$ axes as they execute a hindered rotational motion. The ratcheting motion begins below the 250 K phase transition and continues down to low temperatures, but the residual structural disorder has been shown to persist to temperatures as low as 5 K [69].

The 260 K phase transition affects almost all properties of the C_{60} solid, and it has been observed in differential scanning calorimetry [70], specific heat [58] (Fig. 1-10), resistivity [71], NMR [36, 70, 72, 73], ultrasonic attenuation [52], Raman spectroscopy [74], thermal conductivity [59], and the thermal coefficient of the lattice expansion [56] (Fig. 1-11). The effects of this phase transition on the measured transport and dielectric properties of C_{60} films are discussed in Sections 4.4.2 and 4.8, respectively.

Second-order phase transition

Evidence for a second phase transition at $T_{02} \sim 165$ K is provided by ultrasonic attenuation studies [52], specific heat measurements [58, 75] (Fig. 1-10), dielectric relaxation

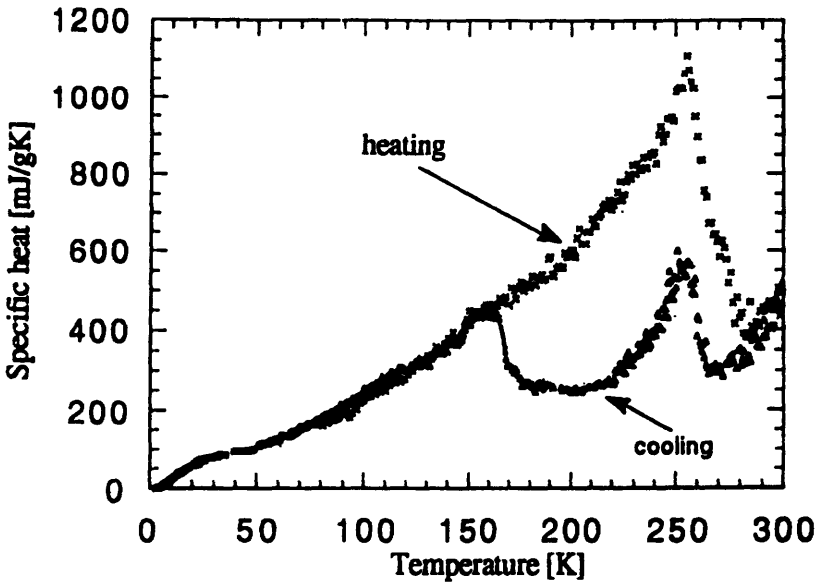


Figure 1-10: Comparison between the temperature dependence of the specific heat for C_{60} on cooling (Δ) and heating ($\times$) [58].

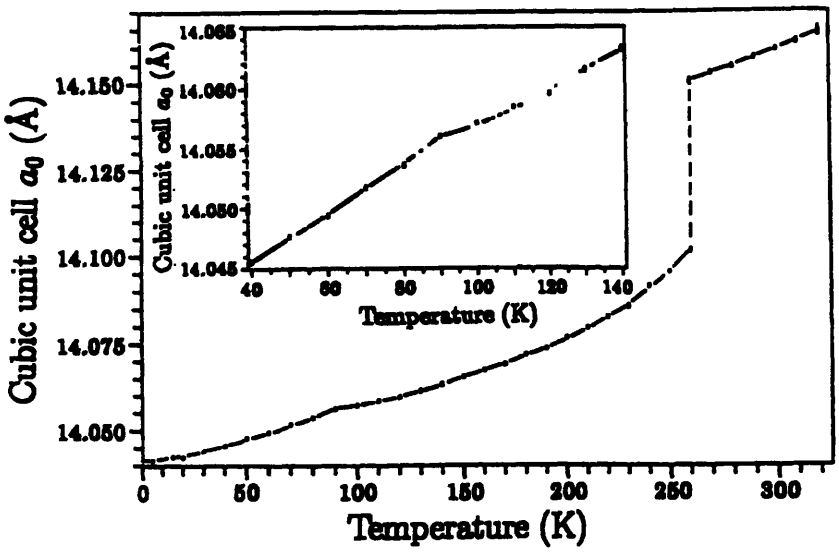


Figure 1-11: Temperature variation of the cubic lattice constant a_0 for solid C_{60}. The inset shows the low temperature data for a_0 on an expanded scale. [56]

studies [76], electron microscopy observations [77], neutron scattering measurements [69] and Raman scattering studies [74].

In contrast to the $T_{01} = 260$ K structural phase transition, which is sensitively studied by static diffraction techniques, the phase transition occurring near 165 K is most sensitive to dynamic processes, such as the frequency dependence of the dielectric response function [76], ultrasonic attenuation [52], and dynamic NMR processes [36]. Characteristic of the behavior of a *glassy* phase transition, the transition temperature T_{02} is not fixed, but is a function of the temperature scanning rate of the probe [69, 76], its value varying by as much as 20 K.

The ratcheting motion described above allows a greater fraction of the C_{60} molecules to align so that the electron-rich double bonds are opposite the electron-poor pentagons as the temperature is decreased. By $T = 90$ K, $\sim$83% of the inter-molecular alignments are reported to be in the lower energy state, leaving $\sim$17% in the higher energy state where the double bond of one molecule is opposite a hexagonal face on the adjacent molecule [69]. Below 90 K, the ratcheting motion continues down to about 50 K, but in this regime, the same fraction ($\sim$83% and $\sim$17%) of the relative intermolecular orientations is maintained and the ratcheting motion is from one orientation to an equivalent orientation. The random occurrence of the higher energy alignment state gives rise to a disordered two-state tunneling system which has been studied by both specific heat [75] and thermal conductivity [59] measurements.

Photopolymerization

It has recently been shown [45] that, under laser or UV irradiation, the C_{60} molecules cross-link to form multi-ball polymers (mostly dimers). The figure 1-12 shows the laser desorption mass spectra for the pristine (a) and phototransformed (b) C_{60} films [45, 78]. The peaks in (a) are identified with clusters of cross-linked fullerene molecules. Clearly, the phototransformation process creates mostly dimers (C_{120}), a substantial amount of trimers (C_{180}), as well as other oligomers $(C_{60})_n$.

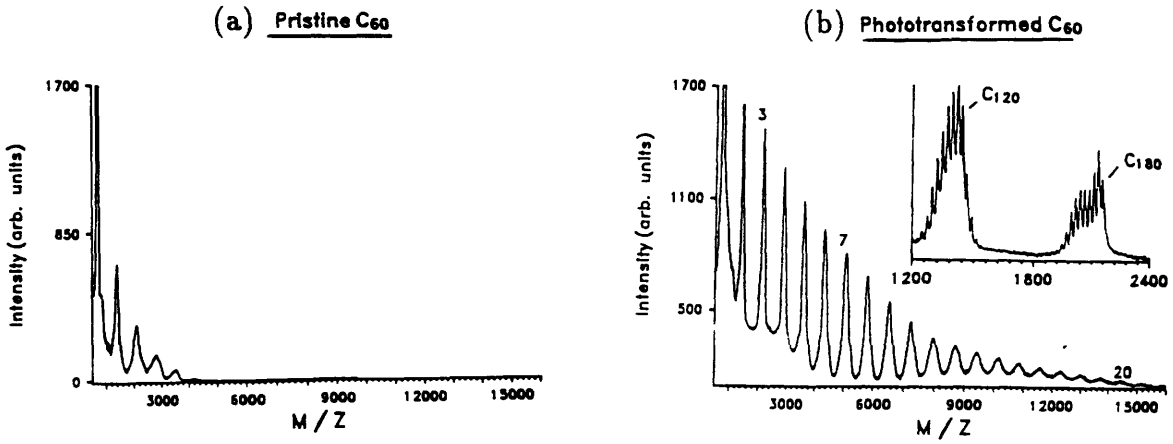


Figure 1-12: (a) Laser desorption mass spectrum (LDMS) for pristine C_{60} films (laser desorption fluence is 30 mJ·cm^{-2}). The spectrum indicates the presence of $(C_{60})_n$ clusters, $n < 4$. These peaks are identified with cross-linked C_{60} molecules produced by the desorption laser itself. (b) LDMS spectrum of a phototransformed C_{60} film. A succession of 20 clear peaks identified with large clusters of fullerene molecules $(C_{60})_n$ $(0 \leq n \leq 20)$ is observed in the spectrum. Inset demonstrates, on an expanded scale, the fine structure of the $n = 2$ and $n = 3$ peaks associated with C_2 loss and gain from the clusters in the desorption process [45, 78].

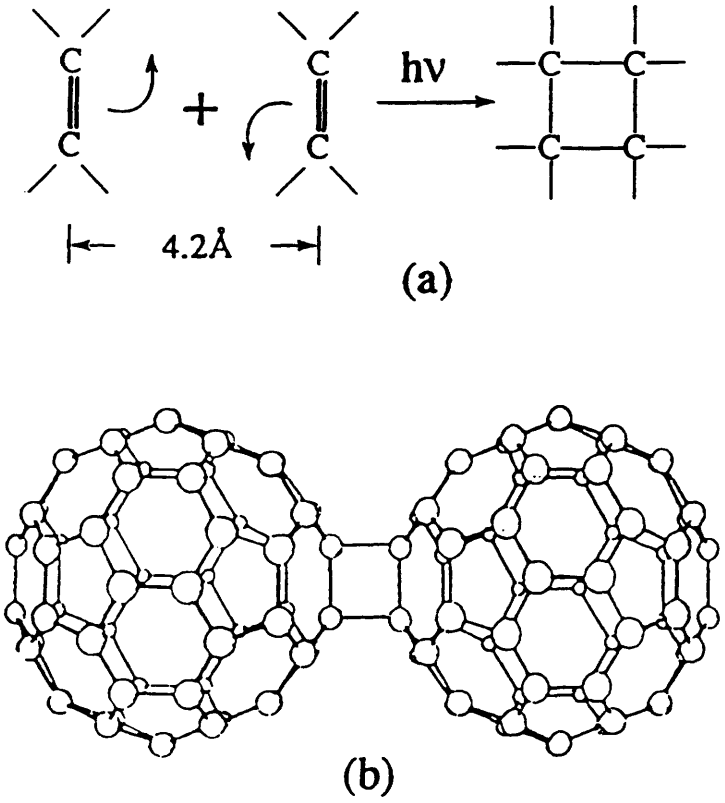


Figure 1-13: (a) A schematic of the photon-assisted 2+2 cycloaddition reaction between parallel carbon double bonds of adjacent C_{60} molecules. (b) A C_{60} dimer (C_{120}) produced by the photochemical reaction (a).

The evidence to date (AFM, SEM, HRTEM, X-rays, Raman, solubility and other physical property changes) suggests that the dimers are formed by light-induced 2+2 cycloaddition reaction between two buckyballs, which creates two covalent bonds between the fullerene shells (see Fig. 1-13). This structure has also been shown to be the one of lowest energy among all available dimer structures by, e.g., generalized tight-binding [79] and first principles [80] molecular dynamics calculations.

In addition to significantly affecting physical properties (optical and vibrational properties, solubility, high resistance to thermal sublimation) of the C_{60} crystalline solids, the photopolymerization reaction also causes marked structural changes. The cross-linking reduces the inter-ball separation in the solid, which results in a $\sim$5%

reduction of the lattice constant. This "shrinkage" has been confirmed by X-ray diffraction [81], by high resolution transmission electron microscopy (HRTEM, see Fig. 1-14), and by observing cracks in the surface layer of C_{60} films [45] and crystals [82] subjected to high intensity vis-UV illumination.

In order for the 2+2 cycloaddition mechanism to work, the adjacent C_{60} molecules must be able to align such that their double bonds are located in close proximity (Fig. 1-13). At $T > T_{01}$, when all molecules are spinning freely about their equilibrium fcc lattice locations, such alignment is very likely, as the molecules can adopt 30(30)=900 favorable orientations promoting the 2+2 cycloaddition. However, below the structural transition temperature ($T < T_{01}$), the molecules' orientations "freeze out," and alignment and cycloaddition are no longer observed [83]. A recent review [84] discusses photochemical transformations of the fullerenes in much detail.

1.4 Electronic Structure

On the basis of the spectroscopic studies (Sec. 1.6), it has been concluded that the fullerenes form molecular solids. Thus, their electronic structures are expected to be closely related to the electronic levels of the isolated molecules. Each carbon atom in C_{60} has two single bonds along adjacent sides of a pentagon and one double bond between two adjoining hexagons. If these bonds were coplanar, they would be very similar to the sp^2 trigonal bonding in graphite. The curvature of the C_{60} surface causes the planar-derived trigonal orbitals to hybridize, thereby admixing some sp^3 character to the sp^2 bonding. The shortening of the double bonds and lengthening of the single bonds also strongly influence the electronic structure.

Figure 1-15(a) displays the results of a Hückel energy calculation for an isolated C_{60} molecule. Because of the molecular nature of solid C_{60}, the electronic structure for the solid phase would be expected to be closely related to that of the free molecule. Indeed, the relatively small ($\sim$0.4 eV) dispersion of the bands derived from the h_u

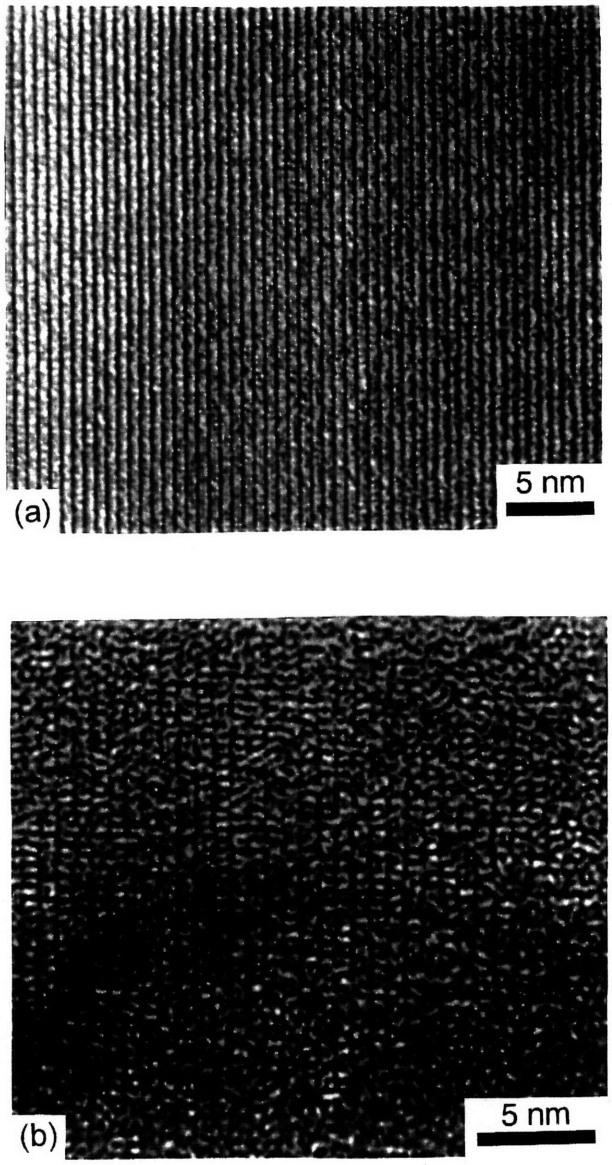


Figure 1-14: High resolution transmission electron microscopy (HRTEM) photograph of a C_{60} crystallite before (a) and after (b) photopolymerization in a 488 nm Argon-ion laser. The C_{60} film has been deposited on a carbon film TEM substrate as described in Sec. 4.5. A ~5% reduction in the lattice constant after polymerization has been demonstrated by Fourier transform image analysis. Note also that the microstructure of the film is considerably more disordered after photopolymerization, with long range ordering largely destroyed by exposure to light.

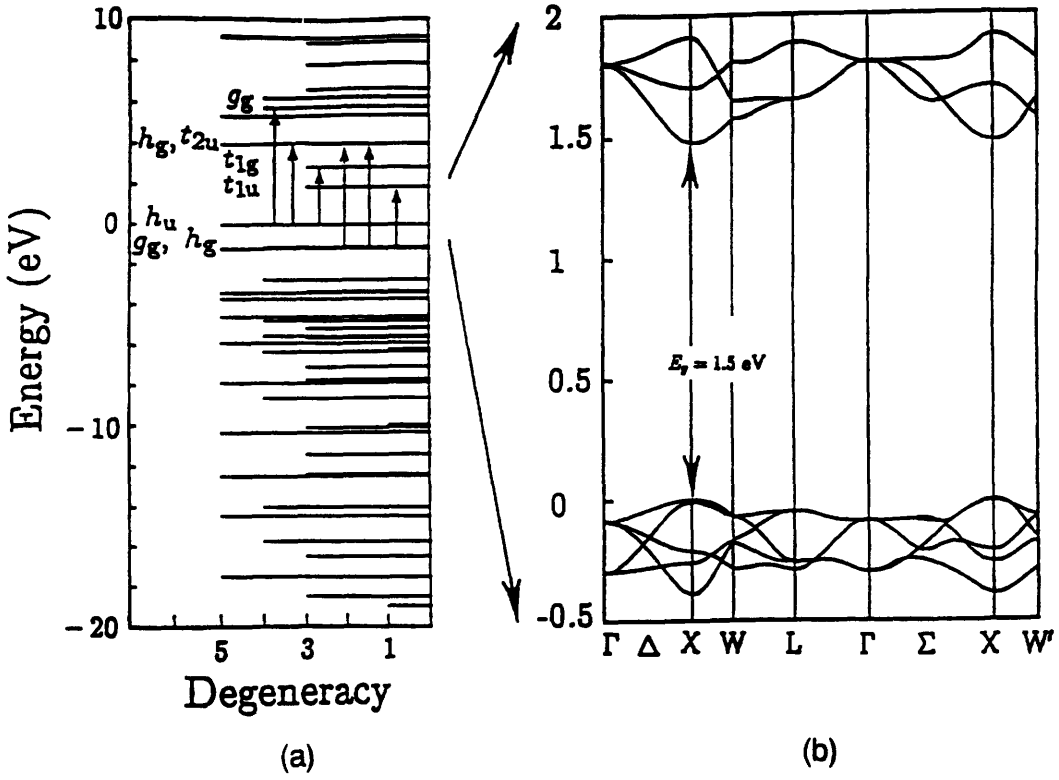


Figure 1-15: (a) Calculated electronic structure of an isolated C_{60} molecule. The allowed dipole transitions are indicated by arrows. (b) Local density approximation calculations for fcc solid C_{60} show energy dispersion of the five h_u-derived valence bands and the three t_{1u}-derived conduction bands. The direct gap at the X point is calculated to be 1.5 eV. The bands are relatively narrow (~0.4 eV), and the electronic structure of the solid strongly reflects the molecular character of the isolated molecule [85].

(HOMO) and t_{1u} (LUMO) levels, as calculated by the local density approximation, [see Fig. 1-15(b)] supports this conclusion.

1.5 Doping

As was pointed out above, all bonding requirement of the constituent carbon atoms of a C_{60} molecule are satisfied, and pristine C_{60} forms an insulator with a HOMO-LUMO band gap[1] of 1.7 eV [45]. However, by introducing various dopants into the large intersticial spaces of fullerenes, their properties can be modified dramatically in scientifically interesting and practically important ways. In particular, depending on the doping and processing, fullerene solids can be insulators, semiconductors, conductors, or superconductors, spanning the entire spectrum of electrical properties.

The four distinct ways to introduce foreign atoms into a C_{60}-based solid are reviewed below [86].

Endohedral Doping

One doping method is the addition of a rare earth, an alkaline earth or an alkali metal ion into the interior of the C_{60} ball to form an endohedrally doped molecular unit [Fig. 1-16(a)]. This configuration has, for example, been denoted by La@C_{60} for one endohedral lanthanum in C_{60}, or Y_2@C_{82} for two Y atoms inside a C_{82} fullerene [87]. The endohedral dopants of C_{60} confirmed to date include Ca, Co, Cs, Fe, He, K, La, La_2, Mu, Ne, Rb, U, U_2, and Y_2 [23].

Thus far, only very small quantities of endohedrally doped fullerenes have been prepared and their study has been limited to investigations of isolated endohedrally doped fullerenes. No studies of crystalline material composed of endohedrally doped constituents have yet been reported.

[1]Strictly speaking, this value refers to the optical absorption edge rather than to the HOMO-LUMO band gap. The value of 1.7 eV does not take into account the exciton binding energy.

Since the dopant atom (or atoms) is usually positioned asymmetrically inside the carbon cage of a fullerene, creating a permanent electric dipole, endohedral fullerene solids are expected to have very interesting dielectric properties. The heavier endohedral dopants may give rise to fullerene materials exhibiting high dielectric constants extending down to the practically important low frequency regimes. (For a review of the dielectric properties of fullerenes, see Chapter 4.)

Substitutional Doping

A second doping method is the substitution of an impurity atom with a different valence state for a carbon atom on the surface of a C_{60} ball. Since a carbon atom is so small, and since the average nearest-neighbor C–C distance on the C_{60} surface is only 1.44 Å, the only species that can be expected to substitute for a carbon atom on the C_{60} ball surface are boron and nitrogen. Boron induces an acceptor state making the charged ball *p*-type, whereas nitrogen induces a donor state, yielding an *n*-type material [88]. Smalley and coworkers have demonstrated that it is possible to replace more than one carbon atom by boron on a given ball [86]. A few groups have also reported detection of nitrogen-substituted fullerenes [89–91].

Radial Exohedral Doping

Dopants to fullerenes have also been added via radial bonds to the outside of C_{60} balls. Two examples of such radial exohedral doping have been observed for fluorine and hydrogen doping. In the case of radial exohedral fluorine doping, the attachment of an F atom converts a double bond in C_{60} into a single bond [92]. A report has been given of adding up to 60 fluorine atoms per ball, to form $C_{60}F_{60}$ [Fig. 1-16(b)] where all double bonds on the C_{60} molecule have been converted to single bonds [93]. However most authors report lower fluorine doping levels. Similar bonding arrangements of C_{60} to hydrogen have also been reported up to a maximum hydrogen concentration, $C_{60}H_{60}$ [94]. However, it is not known whether in the case of $C_{60}H_{60}$ all the H-bonds

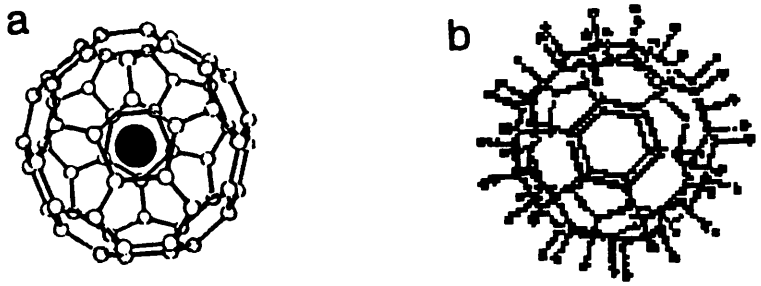


Figure 1-16: (a) Endohedrally doped La@C_{60} fullerene. (b) Proposed structure for fully fluorinated buckyball, $C_{60}F_{60}$ [93].

are directed radially outward, or whether some may perhaps be directed radially inward and be endohedrally bonded [87]. A variety of bromine [95], and chlorine [96] doped fullerenes have also been prepared, though the doping arrangement in the case of bromine and chlorine may well be different from that for fluorine and hydrogen.

Exohedral Donor Doping

The most common method of doping fullerene solids is exohedral donor doping (also called intercalation). In this case, the dopant (e.g., an alkali metal M) is introduced into the interstitial positions between adjacent balls (exohedral locations) [97]. Charge transfer can take place between the M atoms and the balls, so that the M atoms become positively charged ions and the balls become negatively charged with predominately delocalized electrons.

Among the alkali metals, Li, Na, K, Rb, and Cs have all been used as exohedral dopants for C_{60}, as well as intermetallic mixtures of these alkali metals such as Na_2K and Rb_xCs_y. Figure 1-17 illustrates the evolution of structure of the fullerene solid as the fcc C_{60} crystal is intercalated with alkali metal atoms.

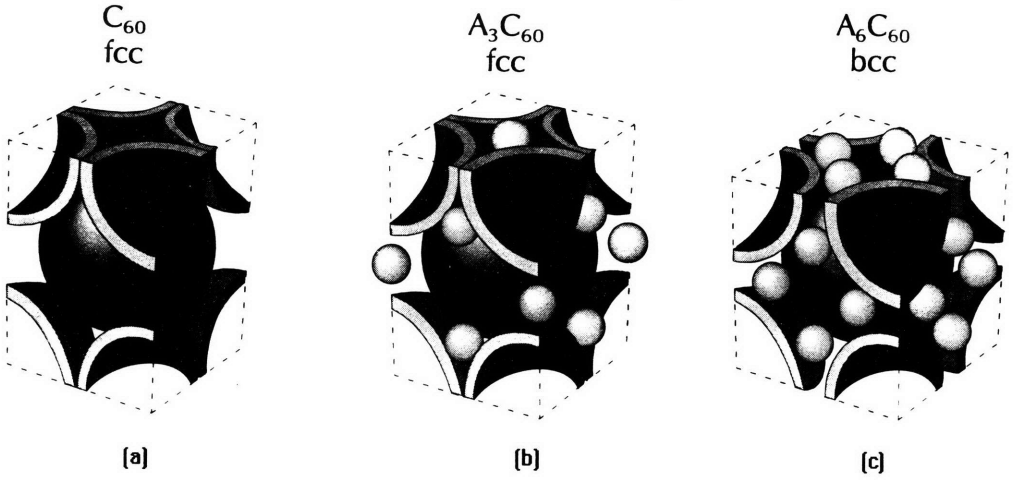


Figure 1-17: Structures for solid (a) C_{60}, (b) M_3C_{60}, (c) M_6C_{60} (M=K,Rb). The large balls denote C_{60} molecules, and the small balls are alkali metal ions. For fcc M_3C_{60} (b), which has four C_{60} balls per cubic unit cell, the M atoms can either be on octahedral or tetrahedral sites. Undoped solid C_{60} also exhibits this crystal structure, but in this case all tetrahedral and octahedral sites are unoccupied. For bcc M_6C_{60} (c) all the M atoms are on distorted tetrahedral sites. (Adapted from Ref. [98].)

While the electrical resistivity ρ of pristine C_{60} is relatively high (see Table 1.2), it can be decreased by several orders of magnitude by doping with alkali metals, which create carriers at the Fermi level. As x in M_xC_{60} increases, the resistivity ρ approaches a minimum at $x = 3.0 \pm 0.05$ [97], corresponding to a half-filled conduction band. Then, upon further increase in x from 3 to 6, ρ again increases, as is shown in Fig. 1-18(a) [99].

Perhaps the most striking property of the C_{60}-related materials is the observation of high temperature superconductivity [see Fig. 1-18(b)]. The early observation of superconductivity at 18 K in K_3C_{60} [100] was soon followed by observations of superconductivity at even higher temperatures: in Rb_3C_{60} (T_c = 30 K) [101, 102], $Rb_xCs_yC_{60}$ (T_c = 33 K) [103], and, most recently, Cs_3C_{60} (T_c = 40 K, under pressure) [104]. This large increase in T_c was achieved in going to compounds with larger intercalate atoms resulting in unit cells of larger size and with larger lattice constants (see Fig. 1-19). As the lattice constant increases, the ball-ball coupling decreases,

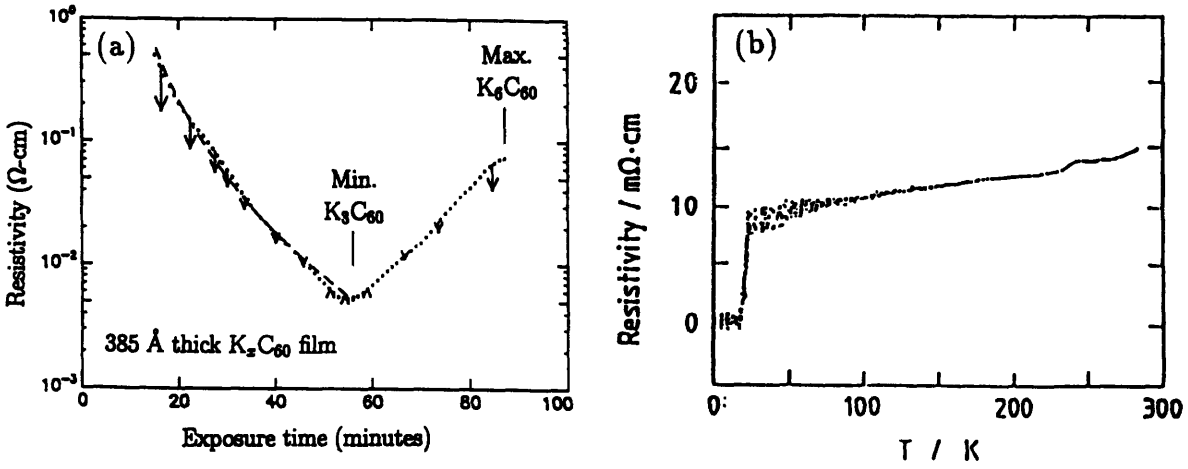


Figure 1-18: (a) Dependence of the resistivity (logarithmic scale) of a K_xC_{60} film on exposure to K vapor at ambient temperature near 70°C. The dashed curve is a fit to theory that treats the conductivity as an activated process with an activation energy derived from charging energies of individual K_3C_{60} grains (adapted from Ref. [99]). (b) Superconducting transition at T_c=18 K and temperature dependence of the resistivity ρ of single crystal K_3C_{60} showing a nearly linear increase in ρ above T_c. Note the anomaly in $\rho(T)$ at $T = T_{01} \approx 260$ K due to the structural transition.

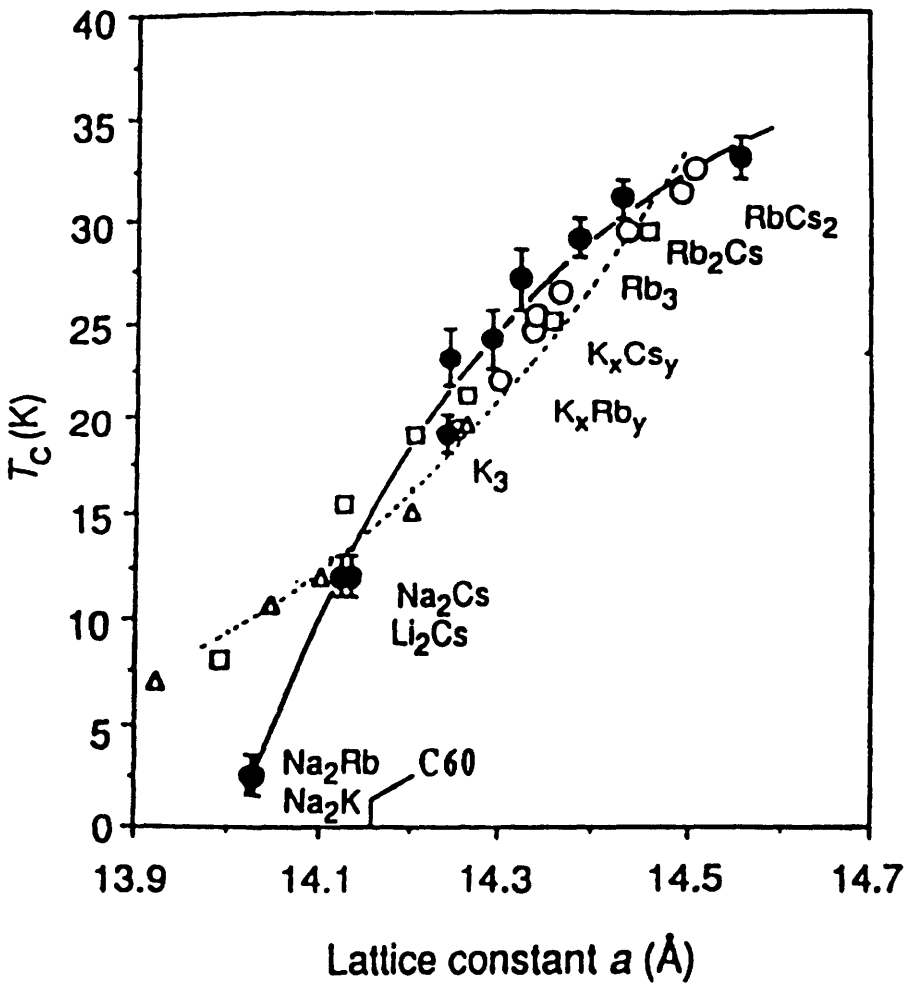


Figure 1-19: Dependence of T_c on the lattice constant a for various M_3C_{60} compounds (M=Li,Na,K,Rb,Cs) [98]. Note the almost linear relation between T_c and a for compounds with a greater than that for undoped C_{60} (M=K,Rb,Cs). [Note that this holds true for both ambient pressure (solid points) and high pressure (open points) results.] On the other hand, for the compounds intercalated with Li and Na, a falls below that for C_{60} itself, and the correlation between T_c and a breaks down because of the attractive electrostatic interaction introduced by the presence of the alkali metal ions in the lattice, and because of different rotational disorder.

narrowing the bandwidth of the LUMO-derived level, and thereby increasing the corresponding density of states at the Fermi level $N(E_F)$. Thus, the increase in T_c is consistent with the BCS expression relating the transition temperature to the density of states $N(E_F)$:

$$T_c \sim \omega_{ph} \exp\left(-\frac{1}{VN(E_F)}\right), \tag{1.6}$$

where V is the electron-phonon coupling energy.

While the crystalline phases formed by intercalation of alkali metals have been the ones most widely studied (because of their superconducting properties), some structural reports have been given for fullerene-derived crystals with alkaline earth [46] and iodine [105] intercalants.

A completely different type of exohedral intercalant of crystalline C_{60} is molecular oxygen (O_2), as well as some other gases (notably, NO). These intercalants also alter the properties of fullerites dramatically (in particular, transport, photoelectric, and dielectric properties), and their effect is discussed in Section 4.4.1.

1.6 Vibrational Properties

The normal modes for solid C_{60} can be clearly subdivided into two main categories: "intramolecular" and "intermolecular" modes, because of the apparent weak coupling between molecules. The former are often simply called "molecular" modes, since their frequencies and eigenvectors closely resemble those of an isolated molecule. The latter are also called lattice modes, and can be further subdivided into librational, acoustic and optic modes. All of these modes, except the acoustic lattice modes, appear schematically in Fig. 1-20 [106].

Because of the high symmetry of the C_{60} molecule (point group I_h), there are only 46 distinct molecular mode frequencies corresponding to the $180 - 6 = 174$ degrees of freedom for the isolated C_{60} molecule, and of these only 4 are infrared-active (all with T_{1u} symmetry) and 10 are Raman-active (2 with A_g symmetry and 8

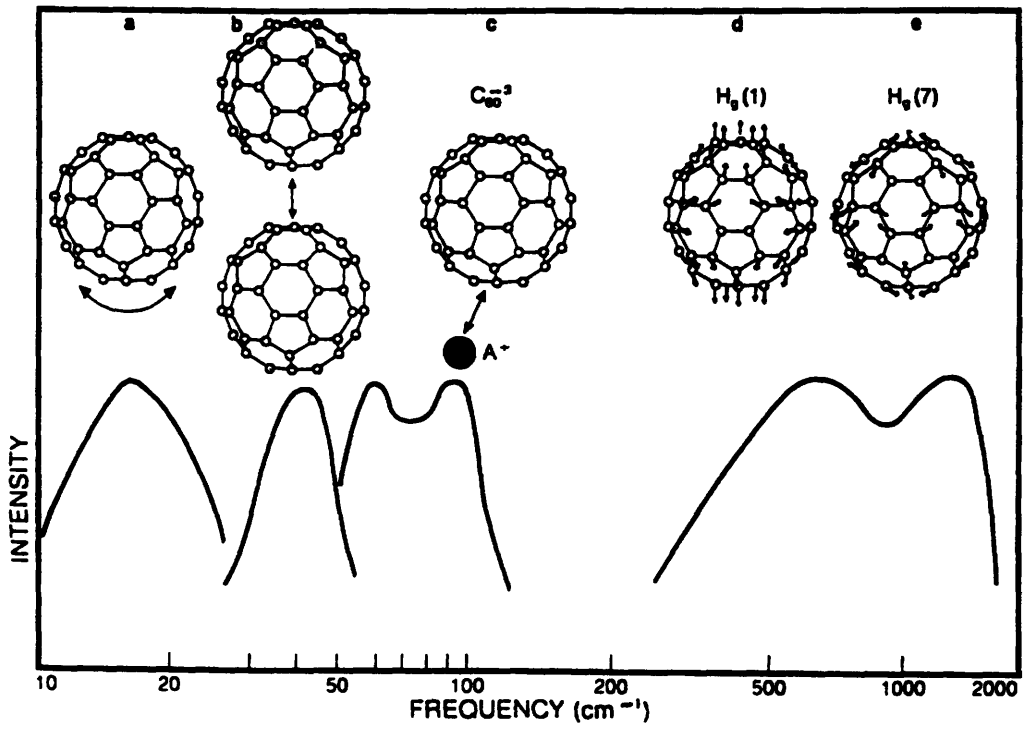


Figure 1-20: Various vibrations in the M_3C_{60} compounds. At lower energies the compounds exhibit librational modes of individual C_{60} molecules (a), inter-ball optic modes (b), and ball–alkali metal (see Sec. 1.5) optic modes (c). The schematic density of states shown for these modes represents a true continuum, which is found throughout the entire Brillouin zone. At higher energies the intramolecular modes dominate; these "on-ball" modes have a radial character (d) at lesser energies [for example the $H_g(1)$ mode] and a tangential character (e) at higher energies [for example, the $H_g(7)$ mode]. The arrows indicate the C-atom displacements in each mode. The schematic density of states for the intra-molecular vibrations exhibits two broad peaks, with the lower and upper peaks associated, respectively, with the modes having predominantly radial and tangential molecular displacements [106].

with H_g symmetry). The remaining 32 eigenfrequencies correspond to silent modes (Table 1.3).

Raman and infrared spectroscopy provide sensitive methods for distinguishing C_{60} from higher molecular weight fullerenes and modified [photopolymerized (Sec. 1.3.2) or doped (Sec. 1.5)] fullerene solids. Since most of the higher molecular weight fullerenes have lower symmetry as well as more degrees of freedom, they have many more infrared- and Raman-active modes. Figure 1-21 illustrates this by comparing the Raman and IR spectra of fullerene films before and after polymerization.

The vibrational properties of C_{60} and other fullerenes have been modeled with a variety of force-constant [110, 111] and first principles calculations [79, 80]. We have also conducted a classical molecular dynamics study of the vibration properties of C_{60} and photopolymerized C_{60}, but the discussion of results of this study is well beyond the scope of this thesis (see Sec. 5.3).

1.7 Applications†

Although research on solid C_{60} and related materials is still at an early stage, these materials are already beginning to show many exceptional properties, some of which may lead to practical applications. Small-scale applications will come first; then targeted applications utilizing the special properties of fullerenes are expected to follow.

In this section, we shall concentrate on those applications pertaining to novel fullerene-based electronic devices. An all-inclusive discusion of various applications of the fullerenes can be found in the Chapter 20 of Ref. [23].

†This section closely follows Chapter 20 of the Ref. [23].

Table 1.3: Experimental values for the intramolecular vibrational frequencies of the C_{60} molecule and their symmetries. The frequencies are derived from a fit to first-order and higher-order Raman [107] and IR spectra [108]. The Raman-active modes have A_g and H_g symmetry and the IR-active modes have F_{1u} symmetries. The remaining 32 modes are refereed to as silent modes.

Even-parity		Odd-parity	
$\omega_i(\mathcal{R})$	Frequency (cm^{-1})	$\omega_i(\mathcal{R})$	Frequency (cm^{-1})
$\omega_1(A_g)$	497.5	$\omega_1(A_u)$	1143.0
$\omega_2(A_g)$	1470.0		
		$\omega_1(F_{1u})$	526.5
$\omega_1(F_{1g})$	502.0	$\omega_2(F_{1u})$	575.8
$\omega_2(F_{1g})$	975.5	$\omega_3(F_{1u})$	1182.9
$\omega_3(F_{1g})$	1357.5	$\omega_4(F_{1u})$	1429.2
$\omega_1(F_{2g})$	566.5	$\omega_1(F_{2u})$	355.5
$\omega_2(F_{2g})$	865.0	$\omega_2(F_{2u})$	680.0
$\omega_3(F_{2g})$	914.0	$\omega_3(F_{2u})$	1026.0
$\omega_4(F_{2g})$	1360.0	$\omega_4(F_{2u})$	1201.0
		$\omega_5(F_{2u})$	1576.5
$\omega_1(G_g)$	486.0		
$\omega_2(G_g)$	621.0	$\omega_1(G_u)$	399.5
$\omega_3(G_g)$	806.0	$\omega_2(G_u)$	760.0
$\omega_4(G_g)$	1075.5	$\omega_3(G_u)$	924.0
$\omega_5(G_g)$	1356.0	$\omega_4(G_u)$	970.0
$\omega_6(G_g)$	1524.5†	$\omega_5(G_u)$	1310.0
		$\omega_6(G_u)$	1446.0
$\omega_1(H_g)$	273.0		
$\omega_2(H_g)$	432.5	$\omega_1(H_u)$	342.5
$\omega_3(H_g)$	711.0	$\omega_2(H_u)$	563.0
$\omega_4(H_g)$	775.0	$\omega_3(H_u)$	696.0
$\omega_5(H_g)$	1101.0	$\omega_4(H_u)$	801.0
$\omega_6(H_g)$	1251.0	$\omega_5(H_u)$	1117.0
$\omega_7(H_g)$	1426.5	$\omega_6(H_u)$	1385.0
$\omega_8(H_g)$	1577.5	$\omega_7(H_u)$	1559.0

† Interpretation of an isotopically-induced line in the Raman spectra implies that this $\omega_6(G_g)$ mode should be at 1490 cm^{-1} [109].

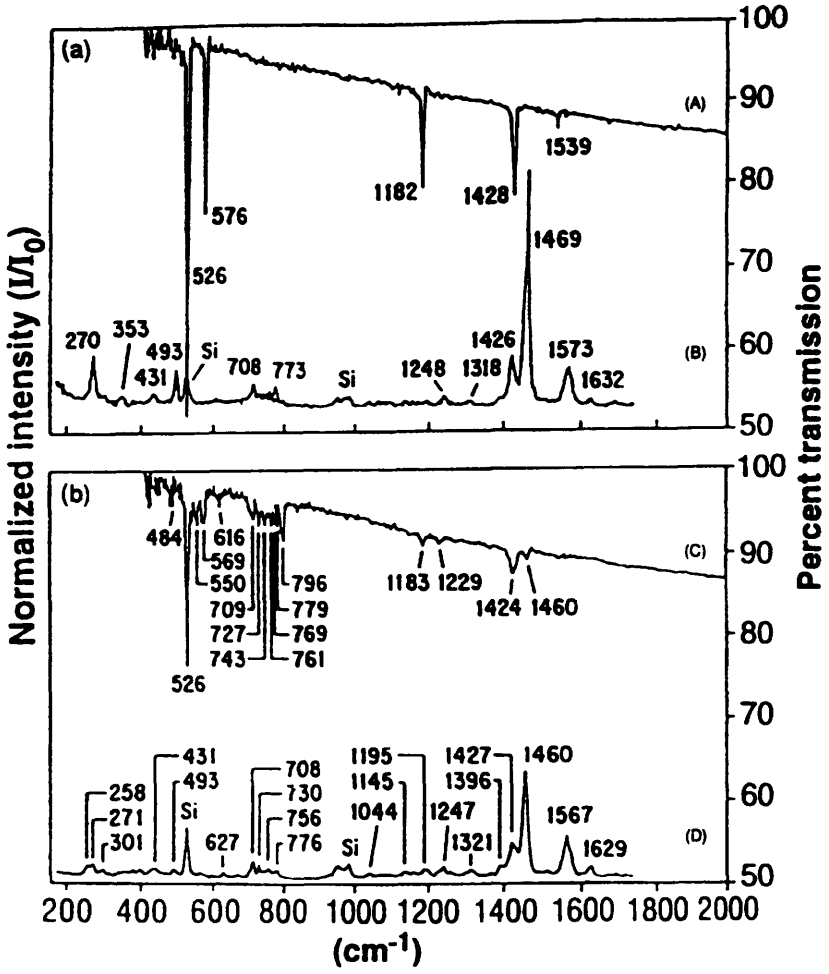


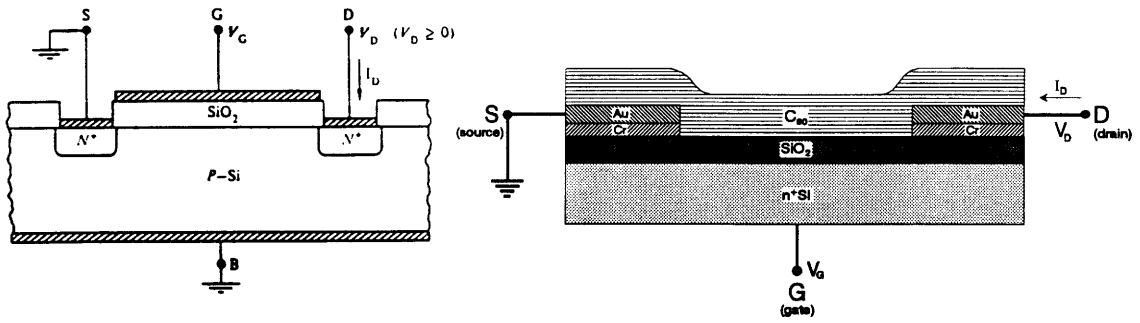
Figure 1-21: (a) Infrared (A) and Raman (B) spectra for C_{60} taken with low incident optical power levels (<50 mW/mm^2) to avoid photopolymerization. (b) Infrared (C) and Raman (D) spectra for C_{60} film subjected to intense optical power levels for several hours. Optical irradiation causes covalent bonding between the adjacent C_{60} molecules (see Sec. 1.3.2), thereby lowering the symmetry of the system, and giving rise to many more infrared and Raman lines in the spectra, as compared to pristine (unpolymerized) C_{60} films (a). [45].

1.7.1 Overview

To date, a variety of $M/C_{60}/M$ (M = metal) rectifying diodes, field effect transistors (FETs), as well as photovoltaic and photorefractive devices have been proposed, and measurements have been carried out on a number of actual electronic devices. A few research groups have concentrated on applications based on the strong bonding at the C_{60}–Si interface [112, 113] and the incorporation of C_{60} into existing microfabrication processes. It has been demonstrated that C_{60} films can be patterned on silicon using conventional photoresist and liftoff techniques [114] achieving linewidths between 3 and 5 μm. Moreover, the C_{60} film itself can serve as a negative photoresist (decreasing solubility upon exposure to light) [115], yielding line resolution of better than 1 μm as shown below.

While a number of devices based on pristine C_{60} films have been investigated, the most promising electronic applications proposed to date utilize C_{60} in conjunction with selected conducting polymer composites. In this section, the structure and properties of C_{60}-based transistors (Sec. 1.7.2) and rectifying diodes (Sec. 1.7.3) are discussed, and C_{60}–semiconducting polymer heterojunctions are described for both rectifying diodes (Sec 1.7.4) and photovoltaic (Sec. 1.7.5) applications. This is followed by a variety of other electronics applications based on fullerenes.

It should be noted that most C_{60} devices are unstable in air due to the diffusion and photodiffusion of dioxygen [116, 117] into the large interstitial sites of the fullerene solid. Therefore, if C_{60}–polymer devices are to be commercialized, they need to be packaged in oxygen-resistant coatings. While such packaging is done routinely in the semiconductor industry, fullerenes are unique in that they themselves can be used to make oxygen-resistant seals [118].



(a) (b)

Figure 1-22: Cross-sectional view of field effect transistor (FET) structures: (a) the terminal designations and biasing conditions for conventional Si-based MOSFETs [119]. G, D, B, and S, respectively, denote the gate, drain, base, and source. (b) The corresponding structure for the fullerene (C_{60}) FET device [120].

1.7.2 C_{60} Transistors

In this subsection, field effect transistors based on C_{60} are described and are compared to their conventional silicon-based counterparts. The conventional silicon-based metal–oxide–semiconductor field effect transistor [MOSFET; see Fig. 1-22(a)] consists of two p–n junctions placed immediately adjacent to the region of the semiconductor controlled by the MOS gate. The carriers enter the structure through the source (S), leave through the drain (D), and are subject to the control by the bias voltage on the gate (G). The voltage applied to the gate relative to ground is V_G, while the drain voltage relative to ground is V_D. In this particular device geometry the source (S) and base (B) are grounded. As the gate voltage V_G is increased $V_G > V_T$, where V_T is the depletion-inversion transition-point voltage, an inversion layer containing mobile carriers is formed adjacent to the Si surface, creating a source-to-drain channel. Now, by keeping V_G fixed and varying V_D, the current–voltage characteristic I_D *vs.* V_D of the transistor can be determined for various gate voltages.

Fullerene-based n-channel FETs have been constructed [120–123] and an example of such a device is shown in Fig. 1-22(b). The corresponding current–voltage characteristics for this fullerene FET are shown in Fig. 1-23. In the fullerene FET

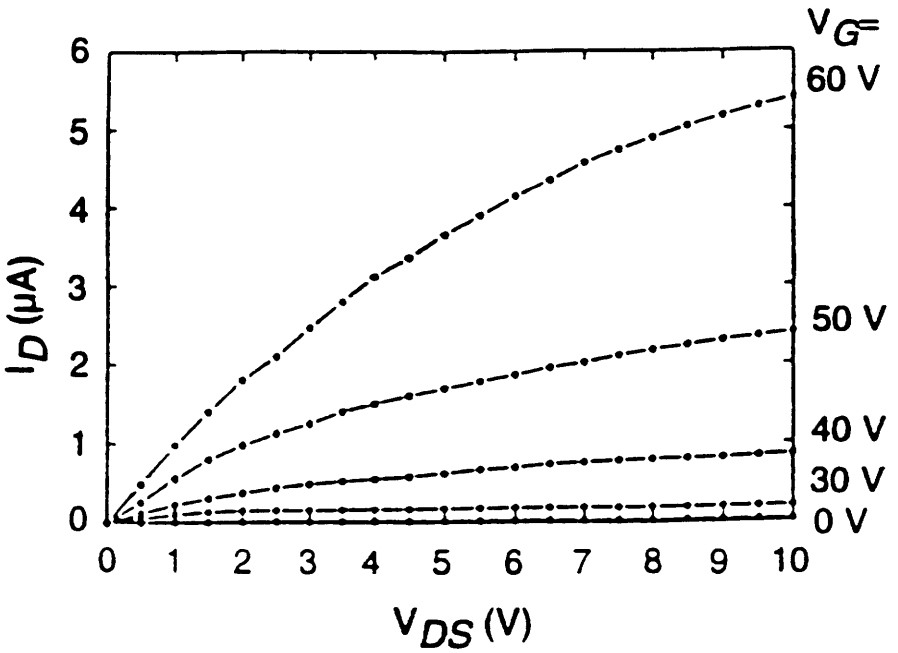


Figure 1-23: Room temperature drain current (I_D) *vs.* drain–source voltage (V_{DS}) characteristics at various gate voltages V_G (0, 30, 40, 50, 60 V) for a fullerene-derived field effect transistor with conduction in an *n*-type C_{60}/C_{70} channel induced at the SiO_2–C_{60} interface [120]. A schematic diagram for the device is shown in Fig. 1-22(b).

shown in Fig. 1-22(b), a highly doped *n*-type silicon wafer takes the place of the gate metal, a ~30–300 nm thick layer of SiO_2 serves as the oxide, and the fullerene film is the semiconductor. When an appropriate positive gate voltage V_G is applied (see Fig. 1-23), the drain current I_D increases, which indicates that a conduction channel is formed near the fullerene–insulator interface. The sign of the response indicates that the fullerene transistors are *n*-channel devices, consistent with C_{60} anion formation. Field effect mobilities of up to 0.08 $cm^2/V{\cdot}s$ were obtained from the I_D–V_D characteristics, which compares well with organic FETs, but is considerably lower than the carrier mobilities (0.5–1.0 $cm^2/V{\cdot}s$) observed in C_{60} films by the Dember effect [124] and by the time-of-flight mobility measurements on C_{60} single crystals [125, 126]. This suggests that localized states at the SiO_2–C_{60} interface may play an important role in the electronic conduction.

Because C_{60}-based FETs operate as *n*-channel devices, they are subject to prob-

lems that are not experienced by the majority of organic materials investigated to date, which tend to be *p*-type. The field effect mobilities of 0.08 $cm^2/V \cdot s$ and the on–off ratios of $\sim 10^6$ are rapidly degraded by exposure to oxygen, presumably because charge transport in the C_{60} FETs depends on electron transport rather than on hole transport as is common in most organic materials-based FETs [123]. The fact that the device performance is not degraded by exposure to nitrogen gas [123] suggests that the oxygen molecules act as electron traps in the lattice of the C_{60} molecular solid (see also Sec. 4.4.2).

It was also found [123] that the treatment of the SiO_2 surface with TDAE (tetrakis-dimethylamino-ethylene) prior to deposition of the C_{60} film reduces the threshold voltage of the device, increases the mobility of the carriers in the C_{60} conduction channel, narrows the barrier width, and increases the band bending at the C_{60}–metal interface.

Overall, the electronic properties of C_{60} as a FET channel material show strong resemblance to amorphous semiconductors. The mobility of fullerene FETs may perhaps be improved by epitaxial growth of C_{60} on the surface or the use of Langmuir–Blodgett techniques, which could reduce the concentration of defect-induced traps.

1.7.3 C_{60}-Based Heterojunction Diodes

Of importance to many potential applications of fullerenes is the nature of the interface between fullerenes and various semiconductors and metallic substrates. Rectifying diodes have been demonstrated both for C_{60}–metal interfaces and for C_{60}–polymer heterostructures. Direct rectification between solid C_{60} and *p*-type crystalline Si has been demonstrated in Nb/C_{60}/*p*-Si and Ti/C_{60}/*p*-Si heterojunctions (as shown in Fig. 1-24) [127, 128].

Since the potential barriers at the Nb–C_{60} and Ti–C_{60} interfaces are close to zero [127], it has been concluded that it is the C_{60}/*p*-Si interface that is responsible for the strong rectifying properties of this heterostructure [127, 128]. Since the rec-

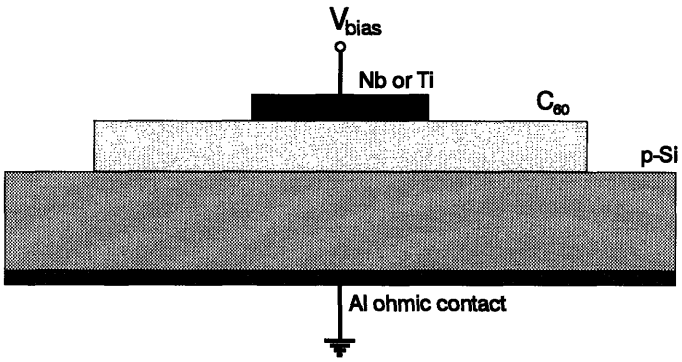


Figure 1-24: Schematic cross section of an Nb/C_{60}/p-Si structure used as a heterojunction diode. Rectification occurs at the C_{60}–Si interface [127].

tification occurs between the C_{60} and Si interfaces, and not between the C_{60}–metal interfaces, it is technically not proper to refer to these devices as Schottky diodes. Nevertheless, these heterojunctions were found to be strongly rectifying (by a factor of $\sim 10^4$ between +2 V and −2 V), and, as shown in Fig. 1-25, the sign of rectification is inverted when n-Si is used in place of p-Si. While rectifying behavior was observed in Al/AlO_x/C_{60}/Au devices [129], a different mechanism is responsible for rectification in this case, namely the tunneling of electrons through the AlO_x oxide layer, which is characteristic of the rectification behavior in metal–insulator–semiconductor (MIS) tunnel diodes. MIS devices with fullerenes as the active semiconductor contact were also studied by Pichler *et al.* [130].

1.7.4 C_{60}–Polymer Composite Heterojunction Rectifying Diode

Rectification behavior has also been demonstrated in C_{60}–polymer heterostructures, such as shown in Fig. 1-26(a) [131, 132]. Because of other optical experiments to be performed on these structures, a thin film transparent electrode, such as indium–tin oxide (ITO), is vacuum-deposited onto a glass substrate to form the lower transparent electrode. Next a thin film of polymer, such as a 1000 Å layer of methyl-ethyl-hydroxyl-polypropylvinyl (MEH-PPV) is spin-coated over the ITO, followed by a

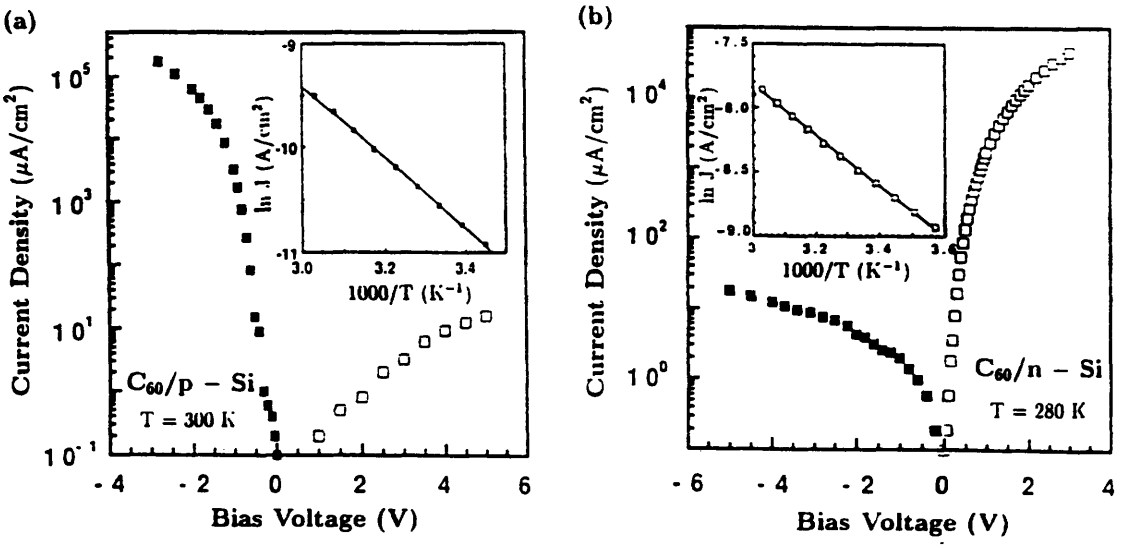


Figure 1-25: Room temperature current–voltage characteristics of C_{60}/p-Si and C_{60}/n-Si junctions with the filled squares for negative bias voltage and open squares for positive V. The complementary behavior between the junctions with n-Si and p-Si further supports the interpretation that it is the C_{60}–Si interfaces which yield efficient rectification and diode behavior in (Nb or Ti)/C_{60}/Si heterostructures. The insets, showing Arrhenius plots for each junction, yield activation energies (interpreted as barrier heights) of 0.30 eV for C_{60}/n-Si and 0.48 eV for C_{60}/p-Si [128].

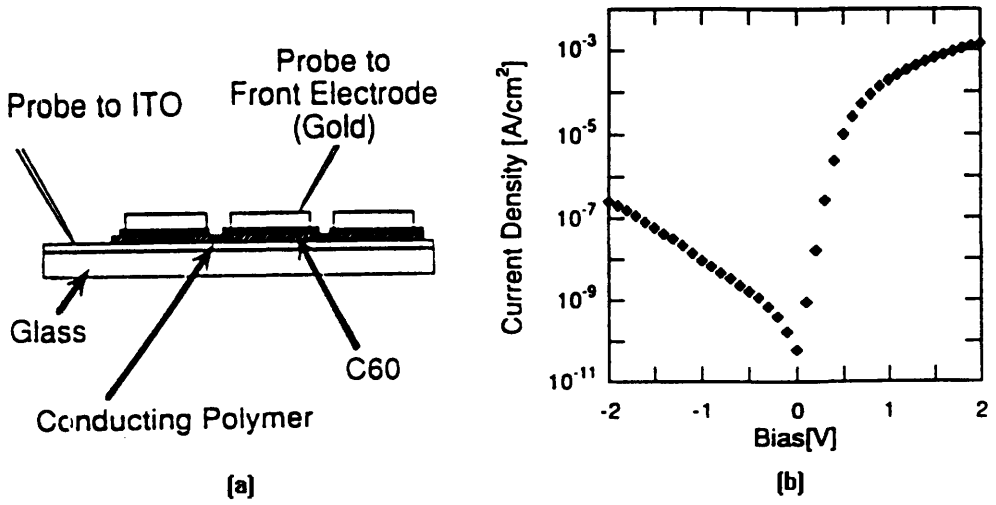


Figure 1-26: (a) ITO/polymer/C_{60}/Au heterojunction fabricated as a layered structure [132]. ITO denotes the optically transparent and electrically conducting indium–tin oxide. An example of a conducting polymer used in heterojunction applications is MEH–PPV. Light enters through the glass substrate and enters the device at the ITO electrode. (b) Dark current density *vs.* bias voltage showing rectification behavior in an ITO/MEH-PPV/C_{60}/Au device at room temperature [131].

vacuum-deposited C_{60} film of similar thickness. The active areas ($\sim$0.1 cm^2) of the device are defined by the Au or Al pads that are vacuum-deposited onto the upper C_{60} surface.

The I–V characteristics for such a C_{60}–polymer heterostructure diode are shown in Fig. 1-26(b) for a C_{60}/MEH-PPV heterojunction measured in the absence of light. Note that the current density is displayed on a log scale and that at $\pm$2 V bias voltage the rectification ratio is about four orders of magnitude, similar to the rectification behavior for the Nb/C_{60}/Si rectifying diodes discussed above that do not employ a C_{60}–polymer heterojunction. A positive voltage V implies that the ITO electrode is more positive than the metal electrode, so that the MEH-PPV polymer is positively biased with respect to the C_{60}. The forward current in Fig. 1-26(b) can be seen to exhibit a nearly exponential rise with applied bias voltage. Similar I–V measurements were made on Au/C_{60}/Au, Au/C_{60}/ITO, Au/MEH-PPV/Au, and Au/MEH-PPV/ITO layered structures, and all of these structures were found to

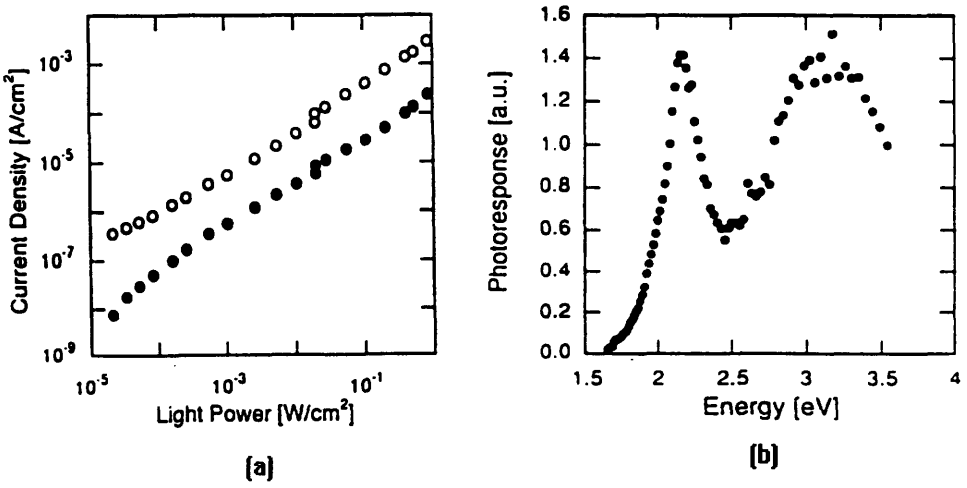


Figure 1-27: (a) Short-circuit current (closed circles) and photocurrent at −1 V bias (open circles) as a function of light intensity for the ITO/MEH-PPV/C_{60}/Au photovoltaic device. (b) Spectral response of the photocurrent in an ITO/MEH-PPV/C_{60}/Au photodiode at (reverse) −1 V bias [131].

exhibit ohmic (linear) I–V characteristics. It must therefore be concluded that the rectification occurs at the MEH-PPV/C_{60} interface [131].

1.7.5 C_{60}–Polymer Composite Heterojunction Photovoltaic Devices

C_{60}–polymer composite heterojunctions, such as the ITO/MEH-PPV/C_{60}/Al heterojunction shown in Fig. 1-26(a), have also been used to demonstrate photovoltaic behavior. In this context we show in Fig. 1-27(a) the short-circuit current density (closed circles with no applied bias voltage), and the photocurrent density (open circles with −1 V bias) as a function of the incident light flux on a log–log plot [131]. The open circuit (zero-current) voltage of the device under illumination was found to be ∼0.5 V. Furthermore, this voltage was identified with the MEH-PPV/C_{60} junction, since such bias voltages applied to other junctions (e.g., C_{60}/Au and C_{60}/Al) did not affect the photoresponse. Both the short-circuit photocurrent and the biased-device

photocurrent are reasonably linear over five decades of light intensity in the plot in Fig. 1-27(a), up to power densities approximately an order of magnitude greater than the terrestrial solar intensity level. The spectral dependence of the photocurrent (taken at -1 V bias) for an ITO/MEH-PPV/C_{60}/Au photovoltaic device is plotted in Fig. 1-27(b). The onset of the photocurrent near 1.7 eV matches the absorption edge for the MEH-PPV polymer, and the photoconductivity minimum near 2.5 eV matches the absorption maximum in the polymer. Since the light was incident from the polymer side of the polymer–C_{60} heterojunction [see Fig. 1-26(a)], it was concluded that the electron injection into the C_{60} must be from the polymer chains located very close to the heterojunction. Consistent with this experimental result, and using a charge carrier mobility of 10^{-4} cm^2/V-s for this device, an applied E-field of 10^5 V/cm, and a photocarrier lifetime of $\sim$1 ns [133], the distance a carrier could drift before recombination was estimated to be only a few angstroms.

Use of C_{60}–polymer heterojunctions for photovoltaic energy conversion device applications [131, 134] requires that the polymer be optimized for optical absorption at the peak of the solar spectrum, and the device must present a large effective area to the sunlight. C_{60}–polymer heterostructures appear promising for photovoltaic applications by further improving the materials and device design.

1.7.6 Microelectronic Fabrication and Photoresists

A number of advances have been made toward integrating fullerenes into the microfabrication processes for microelectronics. For instance, the use of fullerene films for patterning, as surfaces of uniform electric potential for electronics applications [135], for the pacification of surfaces [136], and as adhesives for direct bonding of the silicon wafers [113] have been suggested and are further discussed in this subsection.

The basis for patterning in microfabrication processes is the photochemical transformation that is induced by visible and ultraviolet (UV) light. In the absence of diatomic oxygen, solid C_{60} undergoes a photochemical transformation (see Sec. 1.3.2)

when exposed to visible or ultraviolet light with photon energies greater than the optical absorption edge (~1.7 eV) [45, 84]. Phototransformation renders the C_{60} films insoluble in fullerene monomer solvents such as toluene, a property which may be exploitable in photoresist applications. Because the optical penetration depth in crystalline C_{60} in this spectral region is on the order of ~0.1–1 μm, small particle size powders or thin films can undergo a significant fractional volume decrease upon phototransformation. The photochemical process is fairly efficient; a loss of 63% of the signature of monomeric units (i.e., van der Waals–bonded C_{60} molecules) is observed by Raman spectroscopy after the C_{60} film is exposed for ~20 min to a modest light flux (20 mW/mm^2). Heating the transformed films to ~100°C has been reported to return the system to the pristine monomeric state [137].

The patterning of micrometer-sized features on electronically compatible substrates has already been demonstrated using C_{60} on Si(100) [114]. The conventional photoresist and liftoff technique yielded lines of C_{60} with widths between 3 and 5 μm and heights of 0.4–0.8 μm [114]. This finding provides the opportunity to form many different structures using C_{60} films for a wide variety of applications, such as microelectronic devices, superconducting interconnects, and optical switching devices.

The C_{60} film itself can also serve as a negative photoresist (less soluble) [115] upon irradiation with ultraviolet light in vacuum. Such irradiation increases the cohesive energy in the fullerene solid substantially due to the presence of both molecular and reacted oxygen located at interstitial sites of the fcc C_{60} solid (see Sec. 4.4). The decreased solubility and lower vapor pressure of the phototransformed material enable wet (organic solvent) or dry (thermal or photoinduced sublimation) development of photodefined negative images, as shown on Fig. 1-28, where the sequence of steps in the photolithography process are shown schematically. The negative developing step shows that the C_{60} is retained on the Si substrate where it has been exposed to UV light. This photolithography process yields line resolution of better than 1 μm with good edge definition in the original Si substrate [138]. The efficiency of the

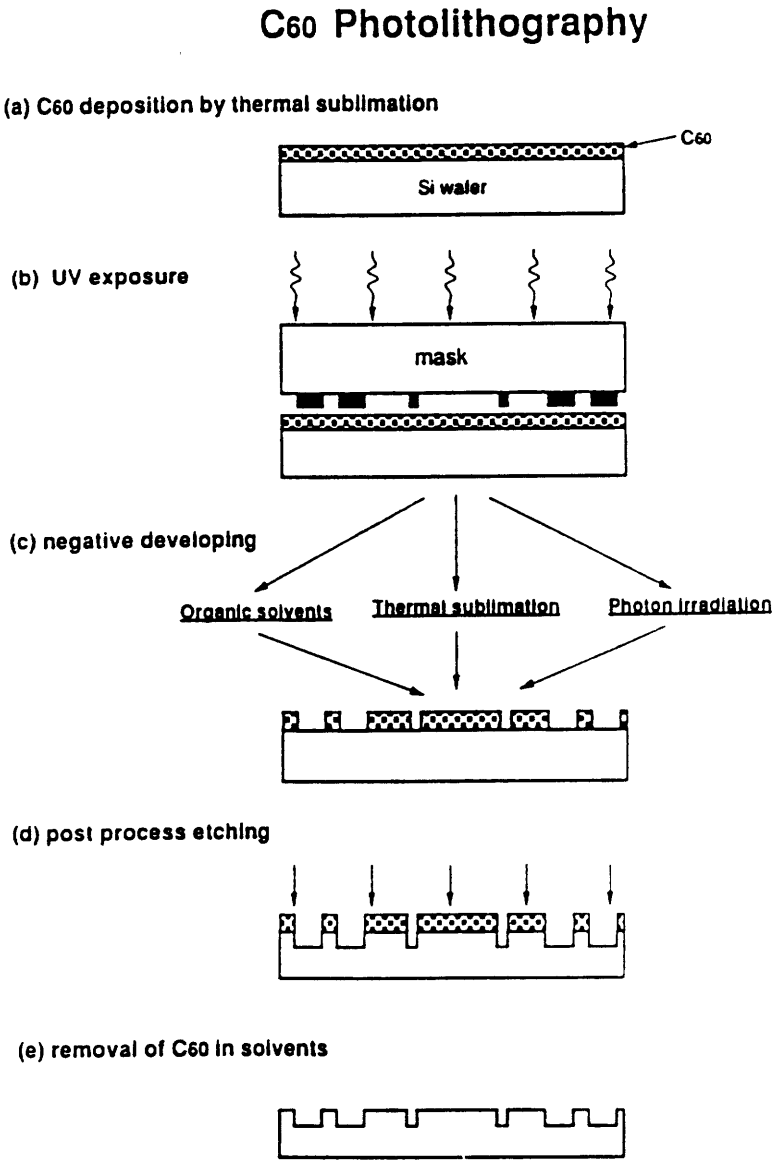


Figure 1-28: Sequence of steps (deposition, exposure, development, and pattern transfer) used in fullerene photolithography in which the C_{60} acts as a negative photoresist [138].

photolithography process can be greatly increased by exposing the C_{60} film to UV light in the presence of NO gas at ambient pressures [139], as discussed below.

Two methods, Raman scattering and chromatography, are typically used to monitor the photosensitivity of C_{60} as a photoresist, which is related to the degree of cross-linking of the C_{60} film. Raman scattering characterization shows a factor of 10^3 increase in photodimerization through introduction of NO gas at ambient pressures [139]. The enhanced photosensitivity of C_{60} in the presence of NO gas was confirmed by high-resolution chromatography characterization. The finding that amorphous carbon coatings can provide some protection for C_{60} films against the diffusion of oxygen and other species [118] could also be useful for photolithography applications.

In addition to photon beams, electron beams can be used to write patterns on C_{60} surfaces, either very fine lines on a nanometer scale using an STM tip operating at ~3 eV, or thicker lines using an electron gun operating at ~1500 eV [136]. This technology also appears promising for specific device applications.

1.7.7 Silicon Wafer Bonding

Utilizing the strong bonding between C_{60} and silicon at the C_{60}–Si interface, a thin layer (~600 Å) of C_{60} has been used as an adhesive to bond a 3 inch silicon wafer to another Si wafer at room temperature [113]. The thin C_{60} film between the two Si wafers was polycrystalline with grain sizes of ~60 Å, while the Si wafer surface had a (100) orientation and was prepared as a hydrophilic surface. Some pressure was needed to bond the pair of wafers together. Interface energies of ~40 erg/cm^2 and ~20 erg/cm^2 were reported for the C_{60}–SiO_2 and C_{60}–Si interfaces and were measured by the crack length generated by inserting a razor blade at the bonding interface [113]. Examination of the debonded surfaces did not show adhering C_{60} layers, indicating a lower cohesive energy at the interface than between C_{60} molecules. It was also found that two C_{60}-covered Si wafers can easily be bonded to each other [113]. It was further

speculated that a thin fullerene film could be used to bond selected smooth surfaces to one another or to bond a Si wafer to certain other smooth surfaces [140]. Since the strongest bonding is at the C_{60}–Si interface, a continuous single C_{60} monolayer would be expected to show bonding action to Si.

1.7.8 Fullerenes Used for Uniform Electric Potential Surfaces

For some electronics applications, surfaces with a uniform electrical potential are required. In the past, graphite and gold surfaces have been used to provide equipotential surfaces. It has been found that by applying a thin ($\sim$10 Å) deposit of germanium to a substrate (such as amorphous carbon, γ-irradiated NaCl or polished phosphorus bronze) and subsequently depositing an overlayer of $\sim$100 Å of fullerenes, a good equipotential surface is obtained [135]. The dangling bonds of the thin Ge interface layer would be expected to facilitate bonding to both the substrate and the fullerenes. Amorphous fullerene growth and uniform surface coverage of C_{60} on the Ge interface layer would be expected at room temperature, because of the low mobility and high sticking coefficient of the fullerenes to the Ge dangling bonds. The demonstration of this fullerene application was made with 85% C_{60} and 15% C_{70}. Fullerenes are useful for providing equipotential surfaces on metals because fullerenes are chemically stable and easy to deposit in vacuum [135].

1.7.9 Sensors

The possible use of C_{60} films as sensors for volatile polar gases such as NH_3 and tetrachloroethylene has been considered, exploiting the decrease in film resistance with gas adsorption and the resulting charge transfer. A linear dependence of the film resistance on gas concentration has been demonstrated as well as reversible and reproducible behavior on time scales of hours [141]. Sensitivity levels of a few ppm NH_3 in air have already been achieved, though many challenges remain before giving

serious consideration to this potential application, including selectivity to the detection of specific gas species, response time (now on the order of seconds), sensitivity of the film calibration to humidity levels, stability of the sensor over longer times (days), and cost/performance comparison with alternative sensors for the same gas.

1.7.10 Nanotechnology

Nanotechnology is a new, potent field on the crossroads of physics, engineering, and material science, which searches for ways to directly manipulate atoms and molecules to build new materials and molecular devices. One might describe nanotechnology as the physicists' answer to genetic engineering. While a biologist might manipulate single genes to modify a cell in a desired way, the physicist might manipulate a single molecule to build a device with desired characteristics. The ultimate feat of nanotechnology would be to fashion intelligent (logic) devices from plain matter that, by itself, possesses no intelligence of its own.

At the American Physical Society's 1959 annual meeting at the California Institute of Technology, Richard Feynman, the legendary physicist, delivered his landmark address entitled "There's Plenty of Room at the Bottom" [142] that started out the nanotechnology revolution. In his talk, Feynman suggested the possibility of creating new materials by mechanically assembling molecules, *an atom at a time.* Following Feynman's lead, other scientists delved into the field. Working independently, von Hippel predicted [143] dramatic material science possibilities if new advances in "molecular designing" and "molecular engineering" of materials could be achieved. After the basic concept of nanotechnology was proposed in 1974 by Toniguchi in Japan, the nanoscale fabrication principles were further advanced by Drexler [144–146] and many others.

Fullerenes, particularly C_{60}, are perhaps perfect for materials manipulations on the molecular scale, including the forming and tailoring of molecular size structures. The C_{60} molecules are quite inert, nearly spherical, and nonpolar due to symmetry,

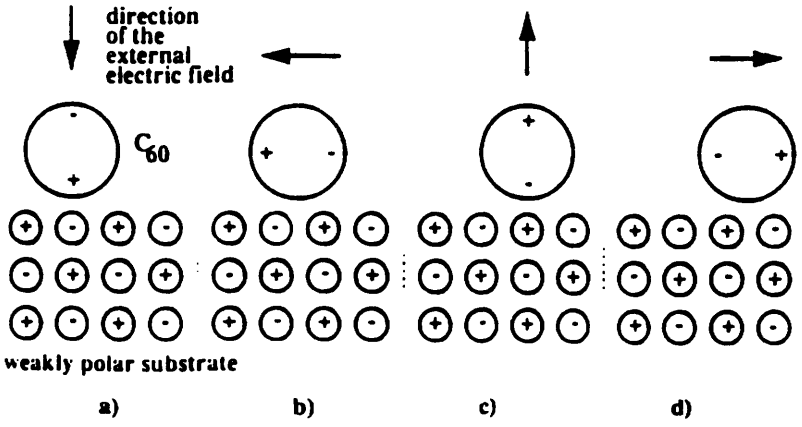


Figure 1-29: The principle of moving C_{60} molecules by a rotating external electric field. An isolated molecule is assumed to be adsorbed on an ideally flat, weakly polar substrate. A rotating external electric field induces a dipole moment that exceeds the effect of the substrate dipoles on the molecule; the successive directions of the field are shown in (a) through (d). The large diameter of the molecule should allow coupling to successive poles, thereby generating lateral movement [148].

their size is very large, the van der Waals bonds between the individual molecules are weak, and thin fullerene films can be grown easily. A C_{60} molecule can be compared to a huge atom, and it is, therefore, possible to manipulate such molecules using the same techniques that have been developed for the manipulation of noble gas atoms using STM probe tips [147]. Moreover, some other manipulation methods may be possible for C_{60} that are not possible for any other species. For instance, it has been proposed [148] that a C_{60} molecule can be "rolled" (diffused) along the surface of a suitable ionic substrate by a rotating external electric field, utilizing the large size and polarizability of C_{60} as illustrated in Fig. 1-29. A recent tribological study [149] suggested that nanocrystalline C_{60} islands grown on certain types of substrates [e.g., NaCl(011)] could be used as transport devices for fabrication processes of nanometer-sized machines. These 0.5–3 ML C_{60} islands might play the role of a tiny "nanosled" transporting larger molecules (e.g., biomolecules) to a desired location [149].

Since fullerenes are all-carbon molecules and have been shown to be of interest for biotechnology applications (from drug delivery to the treatment of AIDS [150,

151]), fullerene-based nanodevices may be capable of biological interfacing. Nanoscale fabrication of logic information devices capable of such interfacing should enable construction of valuable nanoscale robots, sensors, and machines.

To interconnect these nanoscale devices, it may someday be possible to utilize carbon nanotubes for nanowire applications. By varying the chirality and diameter of carbon nanotubes, it should be possible to alter their properties from metallic to semiconducting to insulating. Such nanotubes could, in their own right, lead to nanoscopic electronic devices based on concentric semiconducting and metallic carbon tubules as shown in Fig. 1-30. The significance of carbon nanotubes as electronic materials is the demonstration of quasi-1D cylindrical wires with a large aspect (length-to-diameter) ratio, thereby opening a new field of 1D physics for the study of 1D cylindrical wires or hollow tubes. There is also the possibility of the application of such filled nanotubes with regard to low-dimensional transport, magnetism, and superconductivity. The heterostructures shown in Fig. 1-30 could function as an insulation-clad metallic wire, a tunnel junction, a capacitor in memory devices, or a transistor in switching circuitry [152, 153]. Because the tubes do not require any doping by impurities, as conventional semiconductors do, but acquire their electronic properties from their geometry, the resulting devices should be highly thermally stable and have high intrinsic mobility. Schematics for several devices have been suggested (see Fig. 1-30). To facilitate such applications, the mechanical and electronic properties of a free-standing carbon nanowire have been measured [154]. By employing the low-energy electron projection microscope for *in situ* visual control, it was possible to attach or detach a fine manipulating tip to or from a carbon fiber network. In this way it was possible to apply an electrical potential to a single nanometer-sized fiber while observing the electron projection images at TV sampling rates. The maximum current passed through individual free-standing wires of diameter $\sim$10 nm and lengths $\sim 1\,\mu$m exceeded a current density of 10^6 A cm^{-2} at room temperature [154].

An alternative method of constructing an ultrathin wire involves filling the hollow

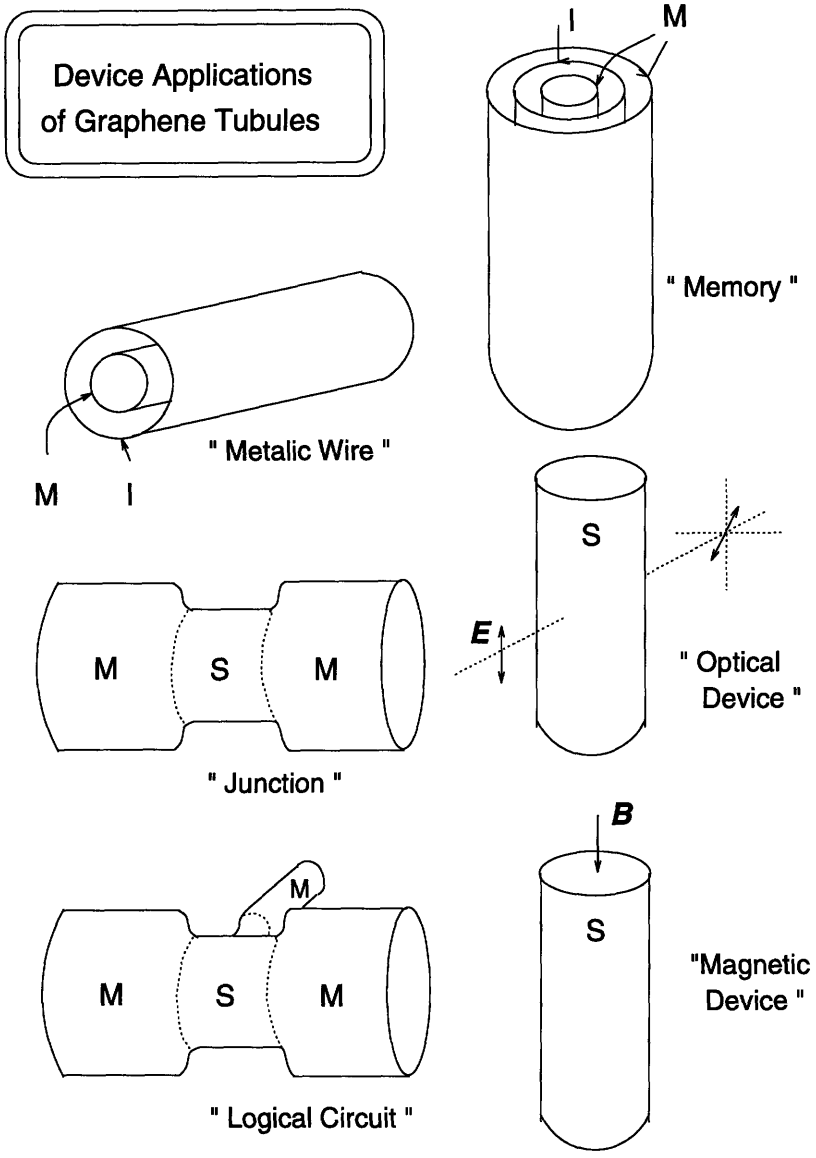


Figure 1-30: Schematic presentation of several proposed electronic device applications for carbon nanotubes [23].

cavity of the nanotubes (which are large enough in diameter to contain atoms of any element in the periodic table) with metallic atoms arranged much like "peas in a pod" [155,156]. Although the lengths of the filled nanowires thus far produced are impractically short [156], the use of carbon nanotubes as 1D quantum wires merits further attention.

While the field of nanotechnology is still about halfway between science and science fiction, it is a very active fast-growing field whose promise of nanoscale molecular devices and orders of magnitude increase in the integration density of electronic components is too appealing to be ignored. The discovery of fullerenes has given a significant boost to the field of nanotechnology by providing an abundance of stable, identical, highly symmetric, nonreactive, and relatively large molecules that can, in principle, be manipulated one at a time. Fullerenes at semiconductor interfaces can be utilized to modify electronic device behavior on nanometer length scales. In such applications, C_{60} anions alone represent an almost ideal spherical capacitor that can store charge. Together with other carbon structures, such as tubules (serving as nanowires), a new carbon-based nanotechnology can be envisioned.

1.7.11 Commercialization and Patents

It was not until after 1990, when fullerenes were first synthesized in macroscopic quantities [7], that the unique physical, chemical, and biological properties of fullerenes were fully appreciated, and fullerenes were used to build some prototype devices. Fullerenes, therefore, now appear ripe for commercial exploitation. Indeed, suggested fullerene uses have become a hot topic at the U.S. Patent Office [157].

Table 1.4 summarizes a wide range of possible practical fullerene applications for which a patent has been granted or a patent application has been disclosed. As suggested by the great number of polymer-related patents, it seems likely that the use of C_{60} and other fullerenes as building blocks for new chemicals will be a very important future application. Rechargeable batteries may turn out to be another

promising application, due to the fact that reversible attachment of hydrogen to C_{60} could provide a charge storage per unit mass that is better than current metal hydride battery technology [158]. Somewhat similar considerations apply to hydrogen storage, perhaps for vehicle propulsion. Use of fullerenes for conversion to other solid products, such as diamond or SiC, may be of value in the future. As a component of solid fuel rocket propellant, fullerenes or fullerene soot may have practical advantages. Fullerenes as optical limiters and as a component in chromatography columns appear to be small-scale applications already under consideration [158].

One of the largest impediments to the large-scale commercialization of fullerenes is their relatively high cost. Although the price has come down from about \$1000–\$2500 per gram for mixed fullerenes in 1990 to less than \$100 per gram for 99% pure C_{60} today, this is still prohibitively expensive for most commercial applications (e.g., batteries). This cost is bound to decrease further, however, since new methods of synthesis, production, purification, separation, processing, and deposition of various fullerenes and their numerous compounds are constantly being discovered. Recently, a joint venture company, Fullerene Technologies Inc., was formed by Mitsubishi and MER (Tucson, Arizona) to explore the commercialization of fullerene-based batteries and hydrogen-storage devices. This joint venture announced plans for a plant having a fullerene production capacity of a few tons per day [159]. Other companies actively working on fullerene commercialization include such giants as Exxon (fullerene precursors), duPont (fullerene-based compounds), Xerox (fullerene inks, toners, developers, and photoreceptors), SRI (fullerene catalysts, electronics, and fibers), NEC (fullerene-based polymers), and AT&T (fullerene photoconductors, superconductors, and photolithography) [160, 161].

Table 1.4: Some uses of fullerenes suggested by patents and patent applications.

Use	Patent[a]
Electronic applications	
Carbon films	JP 06184738
Electrophoretic display	JP 06148693 A2
Bilayer resist-coated substrate	JP 06061138 A2
Tunnel diode	JP 06029556 A2
Photolithography, photopolymer	US 08-037056 A, US 08-073533 A
Double layer capacitor and storage device	US 5319518
Atomic scale electronic switch	US 5323376
Conductive compounds	US 5391323, US 5380595
Superconductors	US 5294600, US 5325002, US 5332723, US 5380703, US 5356872, US 5348936
Optical applications	
Electrophotographic imaging	WO 9308509 A1, US 5215841, JP 06222575 A2, JP 05289381 A2, JP 05088387 A2, US 5215841, US 5178980, JP 6-298532 A, JP 7-1546 A
Sensitizer of a photorefractive polymer	US 5361148
Solar cells from fullerenes	JP 06244440 A2
Electroluminescent cell	JP 05331458 A2
Magneto-optical recording	JP 06002106 A2
Optical limiters (flash goggles)	US 5172278, US 5325227
Nonlinear optical thin films	JP 5-142597
Photoelectronic devices	WO 9405045, US 5171373, US 5331183
Materials applications	
Oriented diamond film	WO 9426953 A1
Nucleating diamond growth	WO 9305207 A1
Diamond-like carbon coating	US 5393572
Conversion of fullerenes to diamond	US 5209916, US 5273788, JP 05305227 A2, US 5308661, US 5328676, US 5360477, US 5370855
Sensors	
NO_x detector	JP 06186195 A2
Sensor for analyses in fluid media	DE 4241438 A1, US 5334351
Gas, temperature, particle sensor	JP 06118042, JP 5-099759, DE 4142959
Detection of organic vapors	US 5395589
Biological and medical applications	
Fullerene-coated surfaces and cell culture	WO 9400552 A1
Diagnostic and/or therapeutic agents	WO 9315768 A1
Biologically active material	JP 3-94692
Magnetic resonance imaging	WO 9303771 A1

Table 1.4: CONTINUED: Some uses of fullerenes suggested by patents and patent applications.

Use	Patent[a]
Chemicals	
Selective functionalization of fullerenes on molecular sieves	US 5364993
Synthesis of derivatized fullerenes	EP 546718 A2
Lubricants	JP 05179269 A2, US 5374463
Lubricants and adhesives	US 5382718, US 5382719, US 5354926
Charge transfer complexes	WO 9302012 A1
Polysubstituted fullerenes	US 5166248
Liquid ink compositions	US 5114477, US 5322756
Surface coating	US 5120669, US 5368890
Cosmetics	JP 5-17327, JP 5-17328
Catalyst	US 5336828, US 5347024
H_2O_2 production	US 5376353
Polymer chemistry and technology	
Fullerene–diamine adducts	DE 4229979 A1
Fullerene-grafted additives to lube oil	US 5292444
Grafted polymers	US 5292813
Anionically polymerized C_{60}–polymers	US 5270394
Modified viscoelastic polymer properties	EP 544513 A1
Electrochemical applications	
Secondary battery	JP 05101850 A2
Li secondary batteries	JP 07006764 A2, JP 05275078 A2, US 5302474, JP 05082132 A2, JP 05275083 A2
Nonaqueous batteries	JP 05325974 A2, JP 0531477 A2
Fuel cell electrodes	WO 9422176 A1, US 5277996, JP 05229966 A2, JP 527801 A2
Other applications	
Storage of nuclear materials	US 5350569
Solid-state rocket fuel	US 5341639
Ballistic missile shield	US 4922827
Metallurgy (additives to steel alloys)	US 5288342
Identification tracer in fuels	US 5234475
Electromagnetic shielding resin	JP 5124894

[a] US = United States patent; JP = Japanese; FR = French; DE = German; WO = International patent application; EP = European patent application.

Chapter 2

Theory of Dielectric Relaxation in Solids

2.1 Introduction and Motivation: Technological importance of dielectrics in modern industry

Electrical insulators, the materials preventing the flow of current where it is not desired, have been used in the context of electrical engineering since the earliest days of the science and technology of electrical phenomena about a century and a half ago. The best modern insulating materials, which are often working under the most extreme external stresses, combine the ability to withstand elevated temperatures with other essential properties such as high breakdown strength, chemical inertness, long life, and low cost.

Although the first capacitor (or *condensor*) was constructed by Cunaeus and Musschenbroek as far back as 1745 [162] (it became very popular for a variety of experimental purposes under the name of Leyden jar), relatively little attention had been paid to the properties of insulating materials until 1837, when Faraday [163] published the first numerical measurements on these materials, which he called *dielectrics.* [164]

Faraday found that the capacity of a condensor was dependent on the nature of the material separating the conducting surfaces. This discovery encouraged further empirical studies of insulating materials aiming, among other things, at maximizing the amount of charge that can be stored by a capacitor.

Throughout most of the 19th century, scientists searching for insulating materials for specific applications have become increasingly concerned with the detailed physical mechanisms governing the behavior of these materials. By contrast with the insulation aspect, dielectric phenomena are both more general and more fundamental, as they are concerned more intimately with the microscopic mechanisms of dielectric polarization and include, especially, the transient behavior under time-varying electric fields.

The works by Mossotti [165, 166] and Clausius [167] marked the beginning of the systematic investigation of the dielectric properties, as they attempted to correlate the *specific inductive capacity,* a macroscopic characteristic of insulators introduced by Faraday [163] and now generally known as the *dielectric constant*, with the microscopic structure of the materials. Following Faraday in considering the dielectric to be composed of conducting spheres in a non-conducting medium, Clausius and Mossotti succeeded in deriving a relation between the dielectric constant ε and the volume fraction occupied by the conducting particles in the dielectric (see Section 2.2.3).

In the beginning of this century, Debye [168] realized that some molecules had permanent electric dipole moments associated with them, and that it is this molecular dipole moment that gives rise to the macroscopic dielectric properties of the materials.[1] Debye succeeded in extending the Clausius-Mossotti theory to take into account the permanent moments of the molecules, which allowed him and others to calculate molecular dipole moments from measurements of the dielectric constant. His theory, later extended by Onsager [170] and Kirkwood [171, 172] (see Section 2.2.3),

[1]The concept of molecules with a permanent dipole moment goes as far back as 1819, when Berzelius [169] described molecules to be composed of oppositely charged regions. In the nineteenth century this concept was also discussed by Clausius, von Helmholtz, and others (see Ref. [164] p. 3).

is in excellent agreement with experimental results for most polar liquids.

Debye's other major contribution to the theory of dielectrics was his application of the concept of molecular permanent dipole moments to explain the anomalous dispersion of the dielectric constant observed by Drude [173] and others. His theory (described in more detail in Section 2.3.3) linked this dispersion to the characteristic time (which he called *relaxation time*) needed for the permanent molecular dipoles to reorient (*relax*) following the changes in the externally applied electric field. For an alternating field, Debye deduced that the time lag between the average orientation of the moments and the field becomes noticeable when the frequency of the field is within the same order of magnitude as the reciprocal relaxation time. This way, the molecular relaxation process leads to the macroscopic phenomena of *dielectric relaxation*, *i.e.* the anomalous dispersion of the dielectric constant and the accompanying absorption of electromagnetic energy.

While in polar liquids, where the dipoles are relatively far away from each other, Debye's approach of treating a dielectric material as a collection of independent dipoles floating in a viscous non-polar liquid gives excellent agreement with experiment, the dielectric behavior of solids deviates considerably from what is predicted by Debye's theory. To correct this, several modifications and extensions of Debye's theory of dielectric relaxation have been proposed, each generally falling into one of the two following groups.

The first approach, pioneered by Cole [174], Davidson [175], and Williams [176], interprets the non-Debye relaxation behavior of the materials in terms of a superposition of exponentially relaxing processes, which then leads to a distribution of relaxation times. The second one proposes that the relaxation behavior at the molecular level is intrinsically non-Debye-like due to the cooperative molecular motions (the Jonscher's "many-body interactions" approach [177]).

After more than seventy years of development, the theory of dielectric relaxation is still very much an active area of research (see Section 2.3 for an overview of basic

current theories). Understanding the behavior of dielectrics in varying electric fields is of particular importance for modern-day electronics, with its demand for dielectric materials with narrowly defined properties tailored for a particular application. For instance, the scaling of metal-oxide-semiconductor (MOS) devices for ultralarge scale integration (ULSI) applications has been placing an ever increasing burden upon the performance of gate dielectrics. Durability has become an issue as the dielectric thickness is decreased, leading to a search for dielectrics with better properties than, *e.g.*, thermal silicon oxide (SiO_2) commonly used in silicon-based electronic applications. And a gallium arsenide (GaAs) metal-insulator-semiconductor field effect transistor (MISFET, the basic building block for today's digital electronics technology) is still largely unavailable due to the lack of a suitable dielectric material for the insulation layer.[2]

The need for better dielectrics with improved properties suitable for modern integrated manufacturing needs was one of the main motivations for studying ways to enhance the dielectric properties of C_{60} thin films. And since in silicon technology, the enhancement of SiO_2 by nitrogen incorporation has been shown to result in an increased dielectric constant and resistance to impurity diffusion, as well as much higher resistance to interface state generation under avalanche, high-field, and hot-carrier stress, and irradiation (see, *e.g.*, Yount *et al.* [179] and references therein), a similar path has been chosen for attempting to improve the dielectric properties of fullerene solid films.[3] Chapter 4 is devoted to the discussion of experimental details and possible technological implications of various ways to introduce intercalants into the interstitial spaces of solid C_{60}.

[2]For recent advances in the attempts to create a molecularly designed insulator for this purpose, see, *e.g.*, Jenkins *et al.* [178]

[3]The use of fullerene composite thin films as gate dielectrics is the most immediate application that we had in mind in embarking on this project. It should be noted, however, that low-dielectric-constant materials, such as most fullerites, may also find applications in electronic packaging [180], as well as elsewhere in microelectronics [181].

2.2 Dielectrics in Static Fields

2.2.1 Electric susceptibility and permittivity

It was Michael Faraday [163] who first noticed that when a capacitor of value C_0 under vacuum is filled with a dielectric material, its charge storage capacity (*capacitance*) increases to a value C. The ratio χ' of the increase of capacitance $\Delta C = C - C_0$ to its initial capacitance C_0

$$\chi' = \frac{C - C_0}{C_0} = \frac{\Delta C}{C_0} \tag{2.1}$$

is called the *electric susceptibility* of the dielectric. Often, instead of the susceptibility, use is made of the *electric permittivity* (or *dielectric constant*), which is defined as the ratio of the capacitance C of a capacitor filled with the dielectric to the value C_0 of the same capacitor under vacuum:[4]

$$\varepsilon' = \frac{C}{C_0} \tag{2.2}$$

It follows from Eqns. (2.1) and (2.2) that the relation between the electric susceptibility and electric permittivity of a dielectric is

$$\chi' = \varepsilon' - 1 \tag{2.3}$$

Thus defined, the electric susceptibility and permittivity are non-dimensional real quantities.

2.2.2 Mechanisms of electric polarization

At the atomic level, all matter consists ultimately of positively and negatively charged particles whose charges balance each other macroscopically in the absence of an ex-

[4]Strictly speaking, the SI system defines the dielectric constant ε of a material as a product of its *relative dielectric constant* ε_r and the permittivity of free space ε_0: $\varepsilon = \varepsilon_r \varepsilon_0$. Our electric permittivity (dielectric constant) ε' is what SI calls the *relative* dielectric constant ε_r.

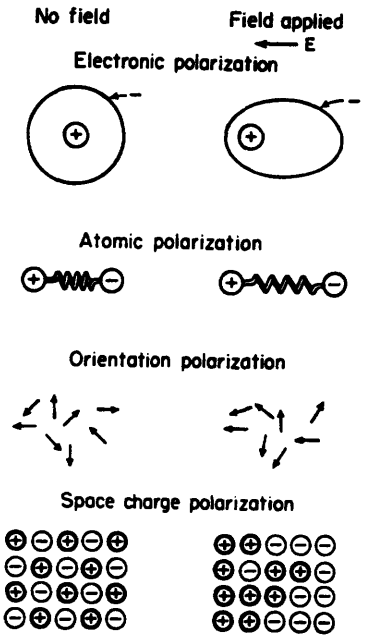


Figure 2-1: Mechanisms of polarization (after von Hippel [183]).

ternal electric field, giving rise to the overall charge neutrality of the material.[5] Once the electric field is applied, the balance of charges is perturbed by the following four basic polarization mechanisms (see Fig. 2-1).

Electronic polarization arises from the displacement of the electrons with respect to the atomic nuclei in the applied electric field. Electronic polarization is thus an *induced* polarization effect.

Atomic polarization is observed when different atoms that comprise a molecule share their electrons asymmetrically and cause the electron cloud to be shifted toward the stronger binding atoms. As a result, the atoms acquire charges of opposite polarity, and an external field acting on these net charges will tend to change the equilibrium positions of the atoms themselves creating this second

[5] In some materials, called *ferroelectrics* or *electrets*, the finite polarization is present even in the absence of the external electric field. [182] However, this effect of *permanent polarization* is beyond the scope of this work.

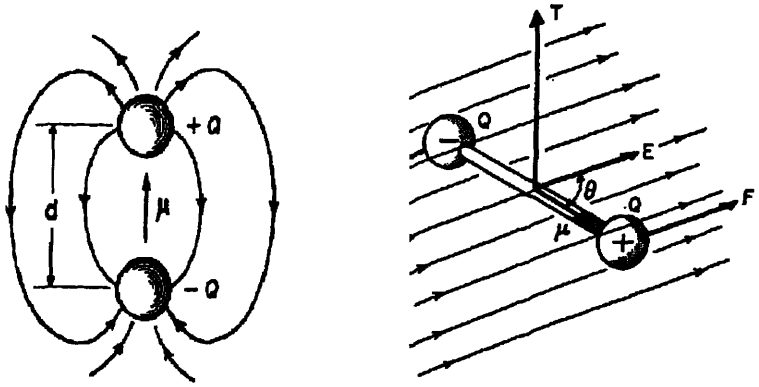


Figure 2-2: (a) Electric dipole of the moment $\vec{\mu} = Q\vec{d}$. (b) Torque $\vec{T} = \vec{\mu} \times \vec{E}$ acting on an electric dipole. (After von Hippel [183].)

type of *induced* polarization.

Orientational polarization, like the atomic polarization, is caused by the asymmetric charge distribution between the unlike components of a molecule. However, unlike the induced types of polarization, orientational (or *dipole*) polarization is created by *permanent* dipole moments, and exists also in the absence of an external field. Such moments experience a torque in an applied field (Fig. 2-2) that tends to orient them in the field direction.

Space-charge polarization is important in dielectric materials which contain charge carriers that can migrate for some distance through the bulk of the material (via, *e.g.*, diffusion, fast ionic conduction, or intercalation), thus creating a macroscopic field distortion. Such a distortion appears to an outside observer as an increase in the capacitance of the sample and may be indistinguishable from a real rise of the dielectric permittivity. Space-charge (or *interfacial*) polarization is the only type of electrical polarization that is accompanied by a macroscopic charge transport (and in the case when the migrating charge carriers are ions, a macroscopic mass transport as well).

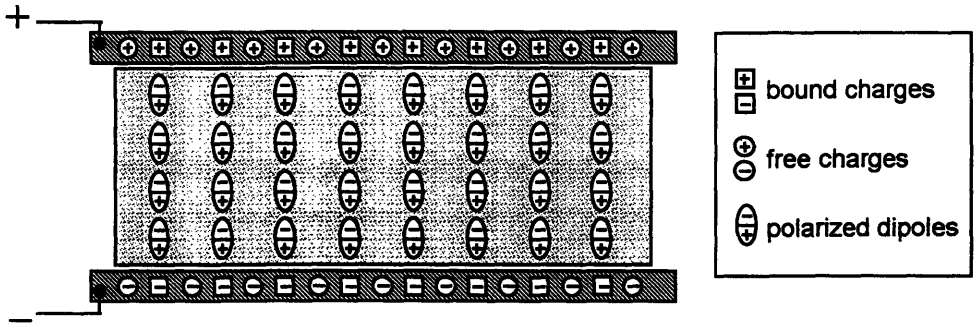


Figure 2-3: "Dipole chains" forming under the influence of an applied electric field bind countercharges with their free ends to the metal plates of the capacitor.

The total polarizability α of a dielectric material is a sum of these four contributions (see section 2.2.3 below). How these effects actually shape up the response characteristics of dielectrics will be discussed in section 2.3.

2.2.3 Static polarization

Suppose now that a dielectric material is inserted into an electric field E formed by the parallel plates of a capacitor. The charge storage capacity will be increased by neutralizing charges at the electrode surfaces which otherwise would contribute to the external field. This phenomenon of *dielectric polarization* can be visualized as the action of dipole chains which form under the influence of the applied field and bind countercharges with their free ends to the metal plates of the capacitor (see Fig. 2-3).

Generally, the polarization $\vec{P}$ of a dielectric material in a static electric field $\vec{E}$ depends on the electric field strength:

$$\vec{P} = \chi' \varepsilon_0 \vec{E} + o(\vec{E}^2), \tag{2.4}$$

where the dielectric susceptibility χ' is the proportionality factor, and $\varepsilon_0 = 8.854 \times 10^{-12}$ F/m is the electric permittivity of the vacuum. Retaining only the linear term

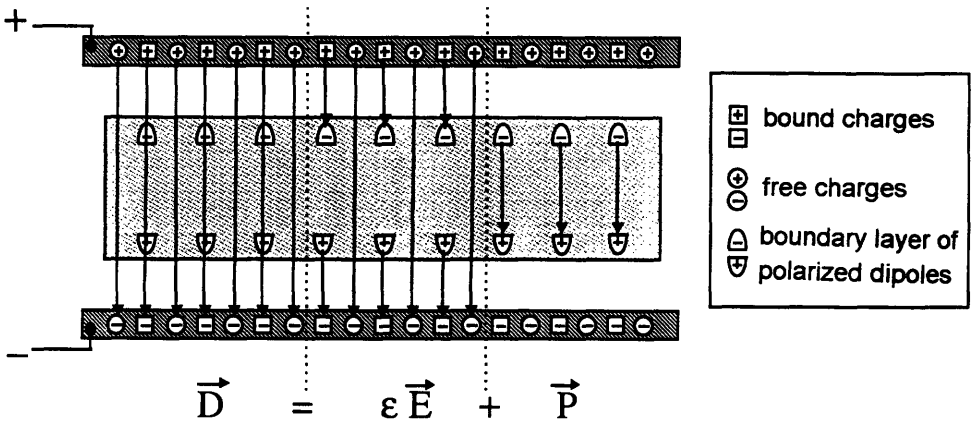


Figure 2-4: Dielectric in the electric field of a capacitor, showing field lines associated with $\vec{D}$ (free charge), $\varepsilon_0\vec{E}$ (all charges), and $\vec{P}$ (polarization charge).

in Eqn. (2.4) is sufficient for most isotropic dielectrics[6] provided that the strength of the applied field $\vec{E}$ is not very high. Keeping this in mind, the physical meaning of the electric susceptibility emerges:

$$\chi' = \frac{\vec{P}}{\varepsilon_0\vec{E}} = \frac{\text{bound charge density}}{\text{free charge density}}. \tag{2.5}$$

While the polarization vector $\vec{P}$ describes the polarization charge of the dielectric material, the electric displacement vector $\vec{D}$ (sometimes also called the *electric flux density*) is associated with the free charges collected on the plates of the capacitor. Using equations (2.3) and (2.4), we can therefore write for a linear dielectric medium

$$\vec{D} = \varepsilon_0\vec{E} + \vec{P} = (1+\chi')\varepsilon_0\vec{E} = \varepsilon'\varepsilon_0\vec{E}. \tag{2.6}$$

This relationship among the three vectors is illustrated by the Fig. 2-4.

A dielectric is described by a vector of dielectric polarization, and for that reason the electric susceptibility χ rather than the more usual electric permittivity ε is

[6]For non-isotopic dielectrics, the scalar susceptibility must be replaced by a tensor. Also, for ferroelectrics, Eqn. (2.4) is not true in general.

appropriate for describing the dielectric properties of a substance.[7] [177, 184] On the other hand, for an engineer who is interested in the phenomena taking place in a capacitor and its behavior in an electric field, the dielectric constant ε will have more relevance.

Static Polarizability

While the electric susceptibility and permittivity are the macroscopic characteristics of electric polarization, polarizability is its microscopic measure. As was mentioned in section 2.2.2 above, the total polarizability α of a dielectric material is a sum of the contributions from four polarization mechanisms:

$$\alpha = \alpha_e + \alpha_a + \alpha_o + \alpha_s \tag{2.7}$$

where α_e, α_a, α_o, and α_s are electronic, atomic (ionic), orientational (dipole), and space-charge (interfacial) polarizabilities, respectively. In the static and low-frequency fields that we shall be considering, the electronic polarizability α_e cannot be separated from the atomic polarizability α_a.[8] We shall therefore only be interested in the induced polarizability $\alpha_{ind} = \alpha_e + \alpha_a$ as a high-frequency "background" of the low-frequency dielectric behavior.

Non-Polar Dielectrics: Clausius-Mossotti and Lorentz-Lorenz equations

Let us first attempt to relate electric susceptibility and electric polarization for the case of non-polar dielectrics, in which the induced polarizability α_{ind} is the only type of polarizability present. To find the *internal* (or *local*) field $\vec{E}_A$ acting upon each

[7] For example, it will be shown later (Sec. 2.3.2) that the important parameter from the physical point of view is the phase shift between the polarization vector $\vec{P}$ and the electric field vector $\vec{E}$, and not between the electric displacement vector $\vec{D}$ and the electric vector $\vec{E}$.

[8] Purely electronic polarizability can be determined only in monatomic molecules where atomic polarization does not occur. Atomic polarization always occurs together with electronic polarization and, consequently, it can only be measured indirectly, usually by taking advantage of dispersion effects.[184, p. 20]

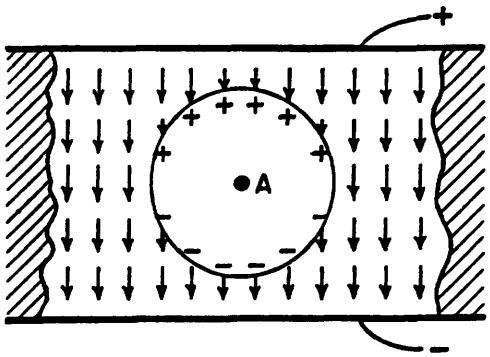


Figure 2-5: Model for calculation of Clausius-Mossotti internal field. (After von Hippel [183].)

molecule A of such a dielectric, we follow Mossotti [166] in constructing the following model (see Fig. 2-5).

Let the reference molecule A be surrounded by an imaginary sphere large enough to allow us to treat the dielectric outside it as a continuum. The total field $\vec{E}_A$ acting upon the molecule A can then be decomposed into the following three components:

$\vec{E}_1 = \vec{E}$ - the field due to the free charges at the capacitor plates, which, by definition, is equal to the applied electric field $\vec{E}$;

$\vec{E}_2 = \chi'\vec{E}/3$ - the field from the free ends of the dipole chains that line the cavity walls; and

$\vec{E}_3$ - the *near field* arising from the individual contributions of the molecules inside the sphere.

In the Clausius-Mossotti approximation, the near field $\vec{E}_3$ is set to zero, *i.e.* the additional individual field effects of the surrounding molecules on the particle A are presumed to cancel out. This roughly corresponds to the case of non-polar disordered weakly interacting matter, such as gases at moderate pressures. [164, p.172]

Macroscopically, the polarization $\vec{P}$ of a dielectric material was defined in Eqn. (2.4) as a function of the applied electric field:

$$\vec{P} = \chi' \varepsilon_0 \vec{E}. \tag{2.8}$$

On the molecular level, on the other hand, polarization will depend on the locally acting electric field $\vec{E}_A$:

$$\vec{P} = N_m \alpha_{ind} \vec{E}_A \tag{2.9}$$

where N_m is the number of polarizable molecules per unit volume, and

$$\vec{E}_A = \vec{E}_1 + \vec{E}_2 + \vec{E}_3. \tag{2.10}$$

From the equations (2.3), (2.8), and (2.9) we get:

$$\frac{\chi'}{\chi' + 3} = \frac{\varepsilon' - 1}{\varepsilon' + 2} = \frac{N_m}{3\varepsilon_0} \alpha_{ind}. \tag{2.11}$$

This relation is generally called the *Clausius-Mossotti equation.* It interprets the static (low frequency) dielectric constant ε' of a medium (a macroscopic quantity), in terms of the polarizability α_{ind} of the contributing molecules (a microscopic parameter).

By using the *Maxwell relation* for a lossless (non-absorbing), non-magnetic medium

$$n^2 = \varepsilon', \tag{2.12}$$

where n is the *index of refraction* of the material, the equation (2.11) can be rewritten as

$$\frac{n^2 - 1}{n^2 + 2} = \frac{N_m}{3\varepsilon_0} \alpha_{ind}. \tag{2.13}$$

In this form, it is known as *Lorentz-Lorenz equation* [185, 186]. While it can be used to approximate the static dielectric constant ε' of non-polar non-magnetic materials from their optical properties (such as the index of refraction n), one should always keep in

mind that such estimates will only be valid when the optical frequencies at which n is measured are low enough to incorporate the effects of the induced (electronic and atomic) polarization.

Polar Dielectrics: The Debye equation and the Mossotti catastrophe

In addition to the induced polarizability α_{ind} present in all dielectric materials, polar dielectrics possess orientational (dipole) polarizability α_o that exists even in the absence of an applied electric field. Because α_o has to do with reorientation of molecules, which are much heavier objects that either atoms or electrons responsible for the α_{ind}, α_o contributes to the total molecular polarizability α at much lower frequencies than α_{ind} does. For this reason, in the dielectric relaxation literature (which is mainly concerned with orientational polarizability), it is customary to designate the dielectric constant due to α_{ind} (or the *unrelaxed* dielectric constant) as ε_∞. In this notation, the Lorentz-Lorenz equation (2.13) becomes

$$\frac{\varepsilon_\infty - 1}{\varepsilon_\infty + 2} = \frac{N_m}{3\varepsilon_0}\alpha_{ind}. \tag{2.14}$$

To account for the orientational contribution to the dielectric constant, Debye [168] used classical Boltzmann statistics and the Langevin function $L(y) = \coth y - \frac{1}{y}$ from paramagnetism theory to estimate the temperature dependence of permanent-dipole orientation. Assuming that these dipoles do not interact with each other, Debye [168] derived the following formula for the orientational polarizability:

$$\alpha_o = \frac{\mu^2}{3kT}. \tag{2.15}$$

Using Clausius-Mossotti's "internal field" argument discussed above, this additional polarization contributes to the static dielectric constant according to the following

formula (*cf.* Eqn. (2.11))

$$\frac{\varepsilon' - 1}{\varepsilon' + 2} = \frac{N_m}{3\varepsilon_0}\alpha_{ind} + \frac{N_d}{3\varepsilon_0}\alpha_o \tag{2.16}$$

where N_d is the number of dipolar molecules per unit volume (which may, of course, be the same as N_m).

Using Eqn. (2.13), we can now rewrite the Eqn. (2.16) in the following form, with the contribution of the orientational polarization of the permanent dipole set out separately:

$$\frac{\varepsilon' - 1}{\varepsilon' + 2} - \frac{\varepsilon_\infty - 1}{\varepsilon_\infty + 2} = \frac{N_d\mu^2}{9\varepsilon_0 kT}. \tag{2.17}$$

This result, due to Debye [187], has been used to successfully predict static dielectric constants of many polar gases and some polar liquids. However, when applied to the condensed state of matter, Debye's theory breaks down predicting infinite dielectric susceptibility (*Mossotti catastrophe*). The reason for this breakdown lies in the assumption that we made in the expression for the Clausius-Mossotti local field (2.10), setting the near field E_3 to zero. In condensed phases, permanent dipoles tend to lose their individual freedom of orientation through association and steric hindrance. Their interaction with their surroundings has to be taken into account, and the near field E_3 of Eqn. (2.10) cannot be neglected.

Polar Dielectrics: Onsager equation

To avoid the Mossotti catastrophe, Onsager [170] modified Debye's theory by introducing a different kind of cavity (see Fig. 2-6) with the following distinct properties:

- While the Clausius-Mossotti cavity is a mathematical fiction, the Onsager cavity is real, thus causing the electric field lines to be bent.

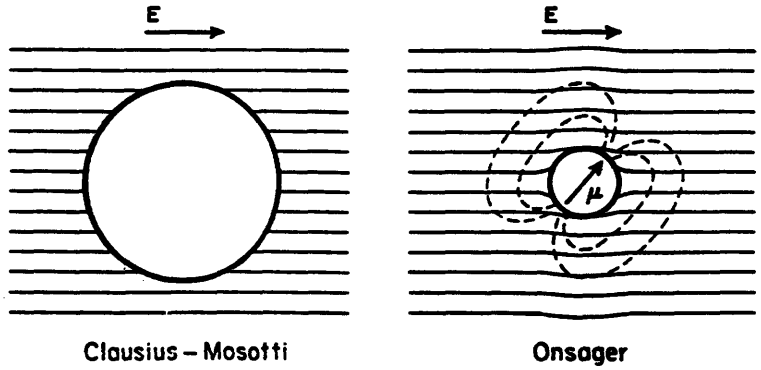


Figure 2-6: The Clausius-Mossotti and the Onsager cavities (after Van Vleck [188]).

- While the Clausius-Mossotti cavity contains a large number of molecules, the Onsager cavity encloses a single dipole molecule.
- While the center of the Clausius-Mossotti cavity is merely a mathematical point, the center of the Onsager cavity is marked by a point dipole which polarizes the surrounding medium. This polarization, acting back on the dipole in the cavity, creates the reaction field.

Based on these assumption, Onsager's theory arrives at the following expression linking the molecular dipole moment of the static dielectric constant [*cf.* Debye equation (2.17)]:

$$\frac{\varepsilon' - 1}{\varepsilon' + 2} - \frac{\varepsilon_\infty - 1}{\varepsilon_\infty + 2} = \frac{3\varepsilon'(\varepsilon_\infty + 2)}{(2\varepsilon' + \varepsilon_\infty)(\varepsilon' + 2)} \frac{N_d \mu^2}{9\varepsilon_0 kT}. \tag{2.18}$$

In Fig. 2-7, equations (2.17) and (2.18) are solved[9]. for the dipole moment μ. We see that, for a given "induced" dielectric constant ($\varepsilon_\infty = 4$ in this case), the dipole moment calculated from the Debye model is significantly smaller than that calculated from the Onsager model, especially for large values of ε'. This indicates that the Clausius-Mossotti local field was considerably overestimated — the very fact that causes the Mossotti catastrophe.

[9]Mathcad Plus 6.0 for Microsoft Windows (MathSoft Inc., Cambridge, Mass.), a numerical and symbolic calculation software package, was used throughout this work.

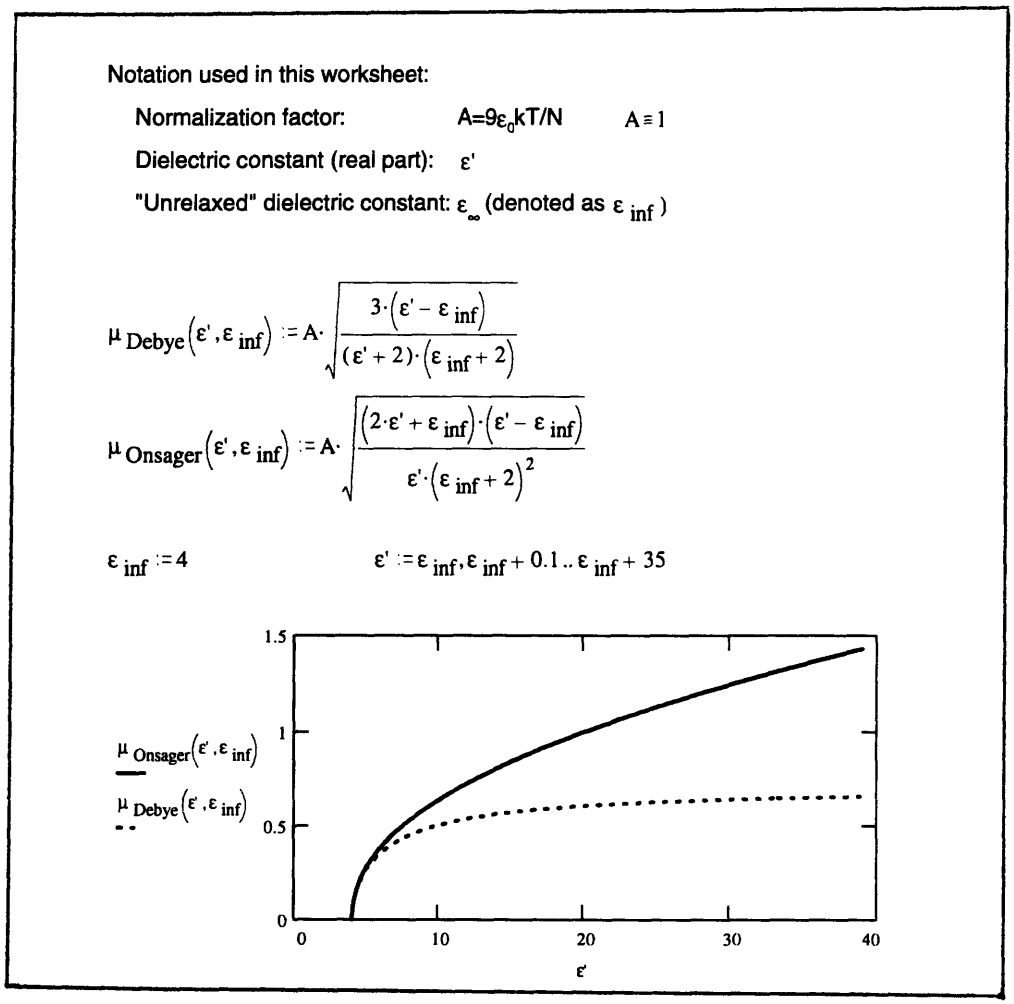


Figure 2-7: Mathcad worksheet illustrating the difference between Debye and Onsager results for the dipole moment μ. (Due to Mathcad's typesetting limitations, the dielectric constant due to induced polarization ε_∞ is shown as ε_{inf}.)

Space-Charge Polarization

Onsager's relation is quite well fulfilled for nonassociated polar liquids [189, p. 181], and can also be applied to weakly bound van der Waals solids, such as fullerites. In general, however, most solid dielectrics do not obey any of the local field expressions (Debye [187], Onsager [170], Kirkwood [171,172], etc.) at sufficiently low frequencies due to the charge carriers present in these materials — mostly ions, but possibly also electrons. This renders any meaningful measurement of the low-frequency dielectric permittivity very difficult, making the comparison with local field theory rather doubtful.

2.3 Dielectrics in Time-Dependent Fields: Dielectric Relaxation

2.3.1 Maxwell's Equations

The most general formulation of the laws of electricity and magnetism is due to Maxwell [191] who in 1864 unified observations of Faraday, Gauss, and Ampere in the following four equations:

$$\nabla \times \vec{E}(\vec{r},t) = -\frac{\partial \vec{B}(\vec{r},t)}{\partial t} \qquad \text{(Faraday's law)} \qquad (2.19)$$

$$\nabla \times \vec{H}(\vec{r},t) = \frac{\partial \vec{D}(\vec{r},t)}{\partial t} + \vec{J}(\vec{r},t) \qquad \text{(Ampere's law)} \qquad (2.20)$$

$$\nabla \cdot \vec{D}(\vec{r},t) = \rho(\vec{r},t) \qquad \text{(Gauss's law)} \qquad (2.21)$$

$$\nabla \cdot \vec{B}(\vec{r},t) = 0 \qquad \text{(Gauss's law)} \qquad (2.22)$$

where the field variables[10] are defined as:

[10]Here the Maxwell's equations are written in the MKS (SI) "rationalized" system of units, which has been used exclusively throughout this work.

$\vec{E}$:	electric field	(volts/meter; V/m)
$\vec{H}$:	magnetic field	(amperes/meter; A/m)
$\vec{B}$:	magnetic flux density	(tesla; T)
$\vec{D}$:	electric displacement	
	(electric flux density)	(coulombs/meter^2; C/m^2)
$\vec{J}$:	electric current density	(amperes/meter^2; A/m^2)
ρ:	electric charge density	(coulombs/meter^3; C/m^3)

Maxwell's equations (2.19)–(2.22) describe the relation of these electric and magnetic fields to each other and to the position and motion of charged particles. Taking the divergence of Ampere's law (2.20) and making use of the Gauss's law (2.21), we obtain the *continuity equation* for the conservation of charge and current:

$$\frac{\partial \rho}{\partial t} + \nabla \cdot \vec{J} = 0. \tag{2.23}$$

This equation states that charge distributions which change in time give rise to currents, and has the important consequence that $\rho(\vec{r}, t)$ and $\vec{J}(\vec{r}, t)$ may not be specified independently.

In order to solve electrodynamic problems, a further set of relationships among the field quantities $\vec{D}$, $\vec{E}$, $\vec{B}$, and $\vec{H}$ must be established as there are more variables than equations contained within Maxwell's equations (2.19)–(2.22). These additional equations are known as *constitutive relations,* and they arise from physical consideration of the media in the problem to be solved. One such constitutive relation for *linear media* in the static case was arrived at in Eqn. (2.6) on page 83:

$$\vec{D}(\vec{r}, t) = \varepsilon_0 \varepsilon'(\vec{r}) \vec{E}(\vec{r}, t). \tag{2.24}$$

A corresponding relation for the magnetic flux density is

$$\vec{B}(\vec{r},t) = \mu_0 \mu'(\vec{r}) \vec{H}(\vec{r},t), \tag{2.25}$$

where $\mu_0 = 4\pi \times 10^{-7}$ H/m is the *permeability of free space*, and $\mu'(\vec{r})$ is the *relative permeability* of the material under study.

In the linear media described by constitutive relations (2.24) and (2.25), the Maxwell's equations (2.19)–(2.22) are linear, and therefore we can use the *superposition principle* to decompose any time-varying fields into a series of time-harmonics, for which solutions can be readily obtained. This procedure amounts to taking a Fourier transform of equations (2.19)–(2.22), which yields Maxwell equations in the frequency domain:

$$\nabla \times \vec{\mathbf{E}}(\vec{r}) = -j\omega \vec{\mathbf{B}}(\vec{r}) \tag{2.26}$$

$$\nabla \times \vec{\mathbf{H}}(\vec{r}) = j\omega \vec{\mathbf{D}}(\vec{r}) + \vec{\mathbf{J}}(\vec{r}) \tag{2.27}$$

$$\nabla \cdot \vec{\mathbf{D}}(\vec{r}) = \rho(\vec{r}) \tag{2.28}$$

$$\nabla \cdot \vec{\mathbf{B}}(\vec{r}) = 0 \tag{2.29}$$

The field variables are now expressed as complex phasors $\vec{\mathbf{E}}$, $\vec{\mathbf{H}}$, $\vec{\mathbf{D}}$, $\vec{\mathbf{B}}$, $\vec{\mathbf{J}}$, and ρ, defined by $\vec{E}(\vec{r},t) = \mathrm{Re}\{\vec{\mathbf{E}}(\vec{r})e^{j\omega t}\}$, etc.

2.3.2 Complex Permittivity

Dielectric Response Function

In Section 2.2.3, the static polarizability of a linear medium was defined as $\vec{P} = \chi' \varepsilon_0 \vec{E}$, where χ' is the static dielectric susceptibility. In a time-varying electric field, the dielectric response of the medium is characterized by the *dielectric response function* $f(t)$ such that

$$P(t) = \varepsilon_0 (E_0 \delta t) f(t), \tag{2.30}$$

where $(E_0\delta t)$ is a delta-function excitation of strength E_0. For an arbitrary time-varying electric field $E(t)$, polarization $P(t)$ is then the result of the convolution integral

$$P(t) = f(t) \otimes \varepsilon_0 E(t) = \varepsilon_0 \int_0^\infty f(\tau) E(t-\tau) d\tau \tag{2.31}$$

Figure 2-8 shows a typical response of polarization $P(t)$ to a step-up excitation

$$\begin{aligned} E_{\text{up}}(t) &= E_0 \quad \text{for} \quad t \geq 0 \\ &= 0 \quad \text{for} \quad t < 0 \end{aligned}$$

and a corresponding step-down excitation $E_{\text{down}}(t)$. It is clear from the figure that, when the field E_0 is applied to the dielectric at time $t = 0$, the induced polarization P_{ind} is established very quickly — we can say instantaneously, compared with the time intervals of interest to us — but the remaining orientational part of the polarization takes time to reach its equilibrium (static) value P_{inf}.

Dielectric Susceptibility

While the dielectric response function $f(t)$ is an adequate and complete description of a dielectric, it is often more convenient to consider the dielectric response in the frequency domain. Equation 2.31 can generally be written

$$\vec{\mathbf{P}}(\omega) = \varepsilon_0 \boldsymbol{\chi}(\omega) \vec{\mathbf{E}}(\omega), \tag{2.32}$$

where $\vec{\mathbf{P}}(\omega)$ and $\vec{\mathbf{E}}(\omega)$ are the Fourier transforms of $\vec{P}(t)$ and $\vec{E}(t)$, respectively, while the frequency-dependent susceptibility $\boldsymbol{\chi}(\omega)$ is defined as the transform of the dielectric response function $f(t)$:

$$\boldsymbol{\chi}(\omega) = \chi'(\omega) - j\chi''(\omega) = \frac{1}{2\pi} \int_0^\infty f(t) e^{-j\omega t} dt. \tag{2.33}$$

We calculate the polarization $P_{up}(t)$ and $P_{down}(t)$ of a dielectric in response to the step excitations $E_{up}(t)$ and $E_{down}(t)$, respectively:

$$E_{up}(t) := \begin{cases} E_0 & \text{if } t \geq 0 \\ 0 & \text{otherwise} \end{cases} \qquad E_{down}(t) := \begin{cases} E_0 & \text{if } t < 0 \\ 0 & \text{otherwise} \end{cases}$$

As shown in the text, polarization is, in this case:

$$P_{up}(t) := P_{ind} + \varepsilon_0 \cdot E_0 \cdot \int_0^t f(\tau)\, d\tau \qquad P_{down}(t) := \left(P_{inf} - P_{ind}\right) - \varepsilon_0 \cdot E_0 \cdot \int_0^t f(\tau)\, d\tau$$

where P_{ind} is the "instantaneous" polarization due to induced polarizability, P_{inf} is the asymptotic (relaxed) polarization at infinitely long charging time, and $f(t)$ is the dielectric response function. The step-up and step-down polarization responses are plotted below for a typical dielectric response function

$$f(t) := \left(P_{inf} - P_{ind}\right) \cdot e^{-\left(\frac{t}{\tau_0}\right)}$$

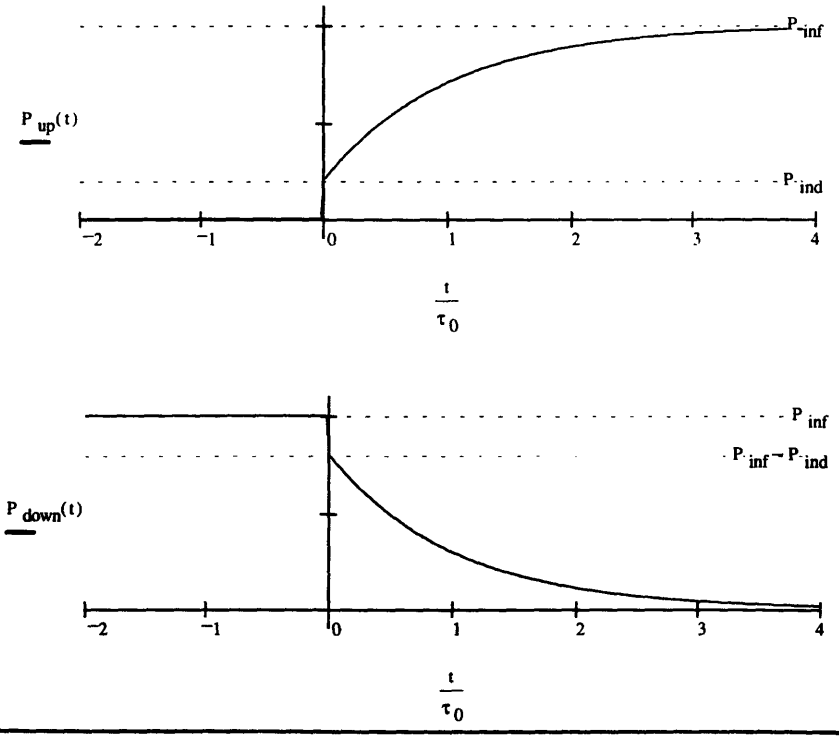


Figure 2-8: Mathcad worksheet showing the response of the polarization of a dielectric to the step-up and step-down excitations.

The susceptibility is a *complex* function of frequency, reflecting the fact that it contains information about both the amplitude and the phase angle of the components of the polarization. While the real part $\chi'(\omega)$ gives the amplitude of polarization in phase with the harmonic driving field, the imaginary part $\chi''(\omega)$ (also known as *dielectric loss*) gives the component in quadrature with the field.

Since, from the physical considerations, susceptibility $\chi(\omega)$ is a causal function, its real and imaginary parts can be expressed as Hilbert transforms of each other:

$$\chi'(\omega) = \frac{1}{\pi}\int_{\infty}^{\infty}\frac{\chi''(x)}{x-\omega}dx \tag{2.34}$$

$$\chi''(\omega) = -\frac{1}{\pi}\int_{\infty}^{\infty}\frac{\chi'(x)}{x-\omega}dx. \tag{2.35}$$

These integrals, known as *Kramers-Kronig relations*, are sometimes more conveniently written in the one-sided form:

$$\chi'(\omega) = \frac{2}{\pi}\int_{0}^{\infty}\frac{x\chi''(x)}{x^2-\omega^2}dx \tag{2.36}$$

$$\chi''(\omega) = -\frac{2\omega}{\pi}\int_{0}^{\infty}\frac{\chi'(x)}{x^2-\omega^2}dx. \tag{2.37}$$

One very immediate consequence of the Kramers-Kronig relations is their interpretation of the static susceptibility. Evaluation Eqn. 2.36 at $\omega = 0$ yields:

$$\chi'(0) = \frac{2}{\pi}\int_{0}^{\infty}\frac{\chi''(x)}{x}dx = \frac{2}{\pi}\int_{0}^{\infty}\chi''(x)d(\ln x). \tag{2.38}$$

This expression relates the polarization increment for a given polarization mechanism to the area of the loss curve plotted against the natural logarithm of the frequency. [177] This shows that a mechanism leading to a strong polarization must be associated with a correspondingly high loss.

Dielectric Permittivity

The frequency-domain response of a dielectric medium may also be written in terms of the *dielectric permittivity* $\varepsilon(\omega)$, which is defined by the constitutive relation (2.24) as

$$\vec{\mathbf{D}}(\omega) = \varepsilon_0 \varepsilon(\omega) \vec{\mathbf{E}}(\omega) = \varepsilon_0 \left[1 + \chi'(\omega) - j\chi''(\omega)\right] \vec{\mathbf{E}}(\omega). \tag{2.39}$$

The real part of $\varepsilon(\omega)$ consists of the contributions of free space and the real part of the susceptibility of the medium itself, while the imaginary component is entirely due to the medium. In the case where the medium has several polarization mechanisms coexisting and not significantly interacting among themselves, the permittivity can be expressed as the sum of the contributions of the individual mechanisms:

$$\varepsilon(\omega) = \varepsilon_0 \left[1 + \sum_\alpha \chi'_\alpha(\omega) - j \sum_\alpha \chi''_\alpha(\omega)\right] \equiv \varepsilon'(\omega) - j\varepsilon''(\omega) \tag{2.40}$$

where summation extends over all the separate polarization mechanisms labeled with the index α [177]. Figure 2-9 illustrates how the real part $\varepsilon'(\omega)$ of the permittivity is made up of contributions of all loss processes at frequencies higher than the frequency in question. The real part of the susceptibility $\chi'_\alpha(\omega)$ of every process adds to the sum of the contributions of all higher processes which define the "high frequency permittivity" $\varepsilon_{\infty\alpha}$ for that process.

Generally, the dielectric permittivity $\varepsilon'(\omega)$ of a material measures the polarization of the material per unit electric field. Interfacial, orientational, atomic, and electronic polarization mechanisms (see section 2.2.2) contribute to the total (static) dielectric constant $\varepsilon(0)$ at a frequency characteristic each mechanism. The time required for polarization to occur is directly related to the distance over which charge is being displaced, and the ease with which it can be displaced. (see Fig. 2-10). Interfacial polarization, which depends on the detailed electrode configuration, is generally not observed at frequencies above 1000 Hz [192]; orientational polarization typically takes place at frequencies below 1 MHz; atomic polarization arises with molecular vibrations

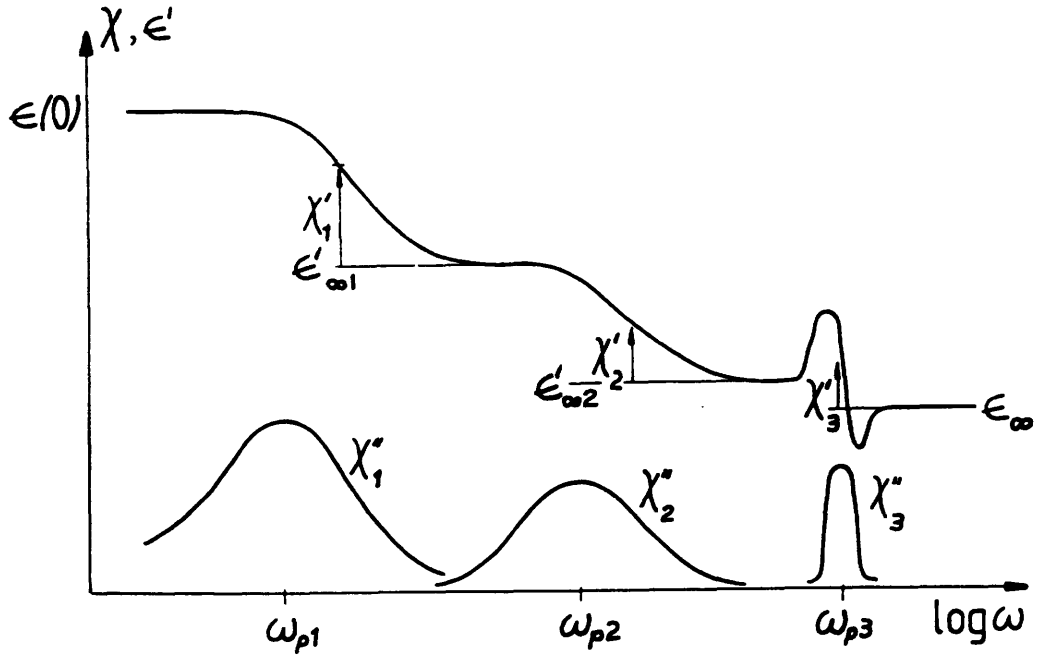


Figure 2-9: An illustration of the manner in which the static dielectric permittivity $\varepsilon(0)$ is made up of contributions of all loss processes. Three contributing processes are shown, denoted by the subscripts $\alpha = 1, 2, 3$ (the process associated with χ_3 being a resonance process). (after Jonscher [177]).

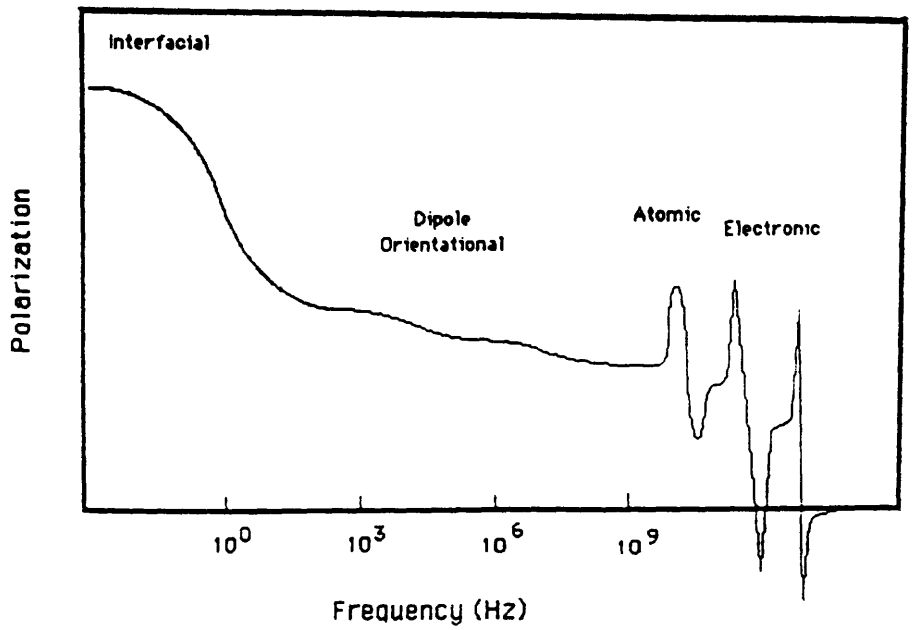


Figure 2-10: Dispersion of polarization in dielectric measurements is caused by four different polarization mechanisms (interfacial, dipole/orientational, atomic, and electronic) each contributing at its own characteristic frequency.

at frequencies around 10^9–10^{13} Hz, and electronic polarization shows up at optical frequencies (10^{14}–10^{16} Hz).

In our discussion of the dielectric relaxation, we shall constrain ourselves to the low frequency range of 10^{-3}–10^5 Hz, where orientational and interfacial polarization processes are the only contributors to $\varepsilon(0)$. The "unrelaxed," permittivity ε_∞ due to induced polarization will, therefore, be considered frequency-independent for the purposes of this study.

Effective Dielectric Constant

Since all actual dielectric media invariably possess a finite (although, possibly, very small) DC conductivity σ_0, this DC contribution will show up in any measurement of the dielectric response. Let us suppose that the dielectric medium under consideration is isotropic, and that, at $\omega = 0$, the *Ohm's law* (which is merely another

experimentally verified constitutive relation) holds:

$$\vec{\mathbf{J}} = \sigma_0 \vec{\mathbf{E}}. \tag{2.41}$$

By applying Ohm's Law (2.41) and using Eqn. (2.39), the Ampere's Law (2.27) can be written

$$\begin{aligned} \nabla \times \vec{\mathbf{H}}(\omega) &= j\omega\varepsilon_0\varepsilon(\omega)\vec{\mathbf{E}}(\omega) + \sigma_0\vec{\mathbf{E}}(\omega) \\ &= j\omega\varepsilon_0\varepsilon_{\text{eff}}(\omega)\vec{\mathbf{E}}(\omega), \end{aligned} \tag{2.42}$$

where $\varepsilon_{\text{eff}}(\omega)$ was chosen such that

$$\varepsilon_{\text{eff}}(\omega) = \varepsilon(\omega) - j\frac{\sigma_0}{\omega\varepsilon_0}. \tag{2.43}$$

By substituting Eqn.(2.40) we get:

$$\varepsilon_{\text{eff}}(\omega) = \varepsilon'(\omega) - j\left(\varepsilon''(\omega) + \frac{\sigma_0}{\omega\varepsilon_0}\right). \tag{2.44}$$

Eqn. (2.44) demonstrates that DC conductivity shows up as increased loss in a dielectric measurememnt. Furthermore, even if σ_0 is relatively small (as is the case in the insulators), it may dominate $\varepsilon_{\text{eff}}(\omega)$ at sufficiently low frequencies. In order to extract the actual permittivity of the material $\varepsilon(\omega)$ from the measured permittivity $\varepsilon_{\text{eff}}(\omega)$, an independent measurement of σ_0 is required.

2.3.3 Microscopic Models of Dielectric Relaxation

The motion of dipoles in the electric field gives rise to frequency-dependent contributions to the permittivity $\varepsilon'(\omega)$ and the loss factor $\varepsilon''(\omega)$. Figure 2-11 illustrates in a highly schematic manner the alignment of molecular dipoles in an applied electric field. Because the dipoles are rigidly attached to relatively large molecules in a

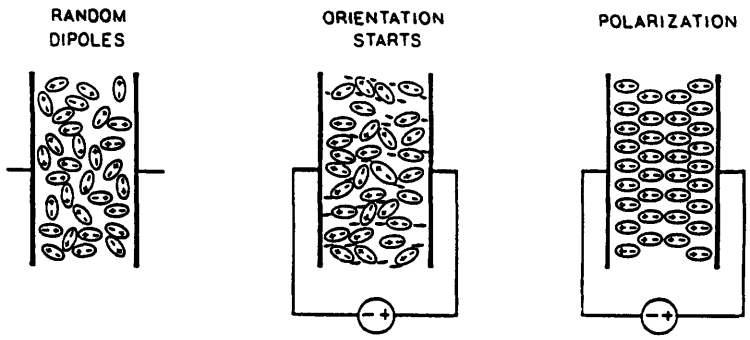


Figure 2-11: Idealized view of the polarization due to dipole orientation in the presence of an applied electric filed (after Day *et al.* [193]).

viscous medium, the orientation process can be characterized by a *dipole relaxation time* τ_d. Because of the hindering mechanism, there is energy loss associated with the orientation process.

The classical Debye theory: A single relaxation time

Debye [187] developed a model for the complex permittivity $\varepsilon(\omega)$ of a spherical polar molecule relaxing in a viscous medium, based on the assumption of a single relaxation time τ_d for all molecules:

$$\frac{\varepsilon(\omega) - \varepsilon_\infty}{\varepsilon(0) - \varepsilon_\infty} = \frac{1}{1 + j\omega\tau_d}, \tag{2.45}$$

where $\omega = 2\pi f$ is the angular frequency. The expression for the *normalized complex permittivity* $\frac{\varepsilon(\omega)-\varepsilon_\infty}{\varepsilon(0)-\varepsilon_\infty}$ is conventionally used to isolate the frequency dependence of complex permittivity for a particular polarization mechanism, where ε_∞ is used in the sense suggested by the Fig. 2-9. Separating Eqn. (2.45) into real and imaginary parts yields the relative permittivity $\varepsilon'(\omega)$ and loss factor $\varepsilon''(\omega)$, respectively:

$$\varepsilon'(\omega) = \varepsilon_\infty + \frac{\varepsilon(0) - \varepsilon_\infty}{1 + (\omega\tau_d)^2} \tag{2.46}$$

$$\varepsilon''(\omega) = \frac{(\varepsilon(0) - \varepsilon_\infty)\omega\tau_d}{1 + (\omega\tau_d)^2}. \tag{2.47}$$

Note that these equations assume that the material's DC conductivity $\sigma(0)$ is equal to zero. Ionic conductivity makes additional contribution to ε'', and can also lead to electrode polarization. These effects are discussed below in Sec. 2.3.4.

To explain the microscopic origins of the relaxation time τ_d, Debye developed a relationship between τ_d and the viscous friction η experienced by a spherical molecule of radius a:

$$\tau_d = \frac{4\pi a^3 \eta}{kT}. \tag{2.48}$$

The relaxation time is thus expected to be directly proportional to the microscopic viscosity experienced by the molecule. While this has been observed qualitatively [175], the quantitative calculations of the molecular size a from the relaxation time and viscosity measurements have not been very successful, because the macroscopic viscosity does not adequately describe the viscous friction experienced by the molecule [194].

The dependence of the permittivity and loss factor of the Debye model on the angular frequency ω is illustrated in Fig. 2-12. At frequencies much lower than $1/2\pi\tau_d$, when dipoles have sufficient time to orient along the applied field, the permittivity approaches the relaxed value $\varepsilon'(0)$ and the loss factor ε'' approaches zero. At high frequencies ($f \gg 1/2\pi\tau_d$), when dipoles are unable to orient, the permittivity approaches its unrelaxed value ε_∞ and the loss factor again approaches zero. At $f = 1/2\pi\tau_d$ the permittivity decreases from $\varepsilon'(0)$ to ε_∞ with increasing frequency, and the loss factor peaks out at $\varepsilon'' = \frac{1}{2}[\varepsilon'(0) - \varepsilon_\infty]$.

Deviations from the Debye behavior: A "distribution of relaxation times" approach

The width of the Debye relaxation at half maximum is only 1.4 decades. In real materials, however, the region of frequency dispersion extends over much larger frequency range than the Debye model predicts, because the dipolar hindering mechanisms are

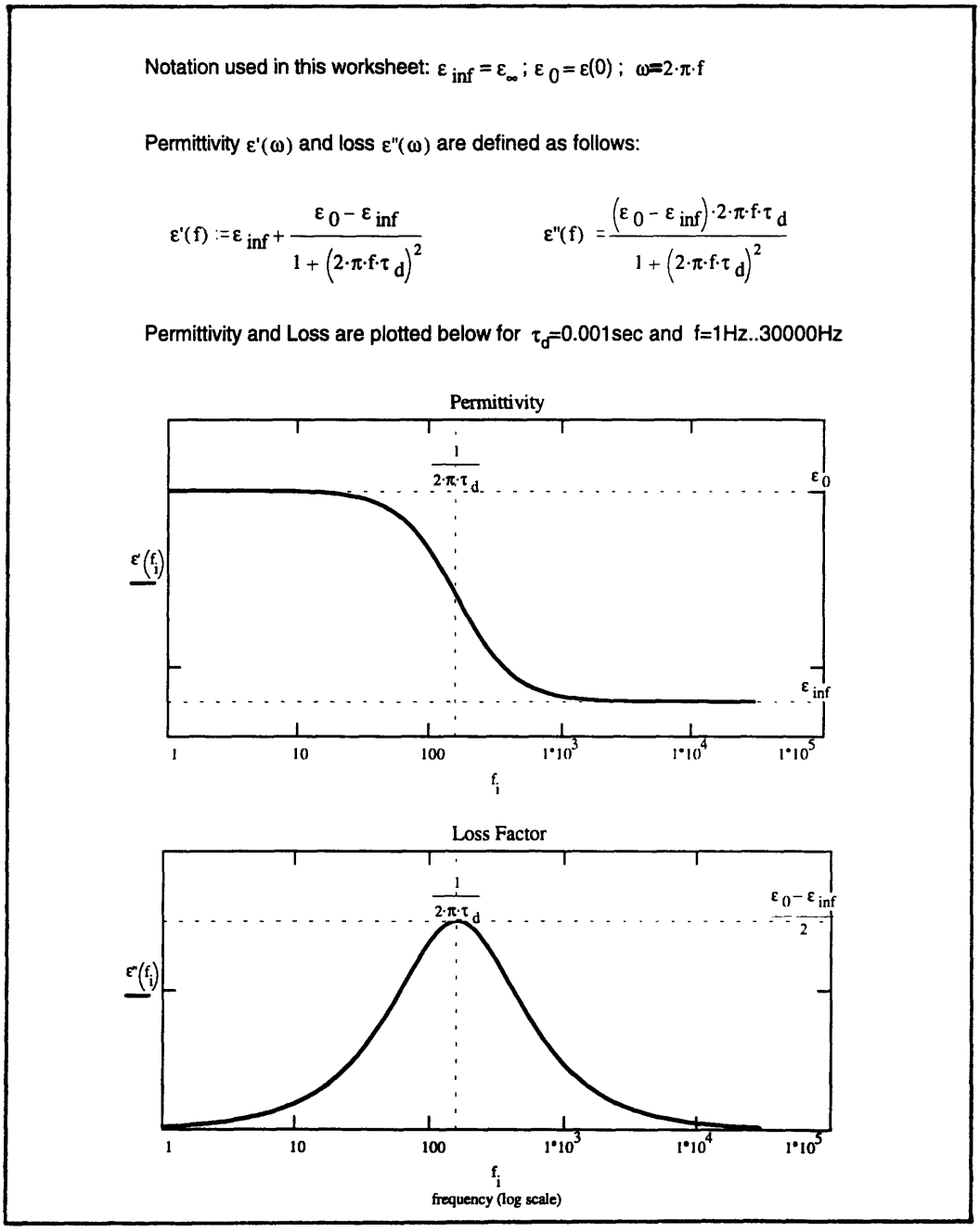


Figure 2-12: Mathcad worksheet showing the frequency dependence of the Debye single relaxation time model for dipole orientation.

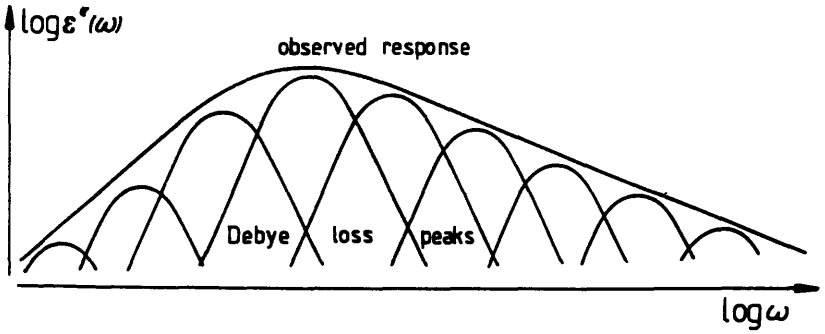


Figure 2-13: A schematic representation of the significance of the existence of a distribution of relaxation times in the application to the interpretation of a "non-Debye" loss peak in a dielectric material (after Jonscher [177]).

not characterized by a single τ_d but by a distribution of relaxation times $G(\tau)$. This broader dispersion characterized by $G(\tau)$ can be described in terms of the superposition of Debye-like relaxation processes as an integral (*cf.* Eqn. (2.45))

$$\frac{\varepsilon(\omega)-\varepsilon_\infty}{\varepsilon(0)-\varepsilon_\infty}=\int_{-\infty}^{\infty}\frac{G(\tau/\tau_d)}{1+j\omega\tau_d}d\ln(\tau/\tau_d), \tag{2.49}$$

where a normalized form $G(\tau/\tau_d)$ was used for the distribution function. This operation may be represented graphically by the construction show in Fig. 2-13. It is evident that, within very wide limits, any sufficiently slowly varying function of frequency $\varepsilon(\omega)$ may be represented by the integral in Eqn. (2.49), so that virtually all forms of relaxation behavior can be "explained" by this means [177].

The concept of a distribution of relaxation times was first proposed by von Schweidler [195]. Later Wagner [196] suggested the use of a Gaussian distribution, but the quantitative evaluation of this and other proposals that followed was prohibitively cumbersome until Cole and Cole [174] developed a method to evaluate how well the permittivity and loss factor agreed with the Debye model. Cole and Cole found [174] that a plot of $\varepsilon''(\omega)$ from Eqn. (2.47) versus $\varepsilon'(\omega)$ from Eqn. (2.46), with $\omega\tau_d$ as a parameter, results in a semicircle (Fig. 2-14), and that for most materials, the locus

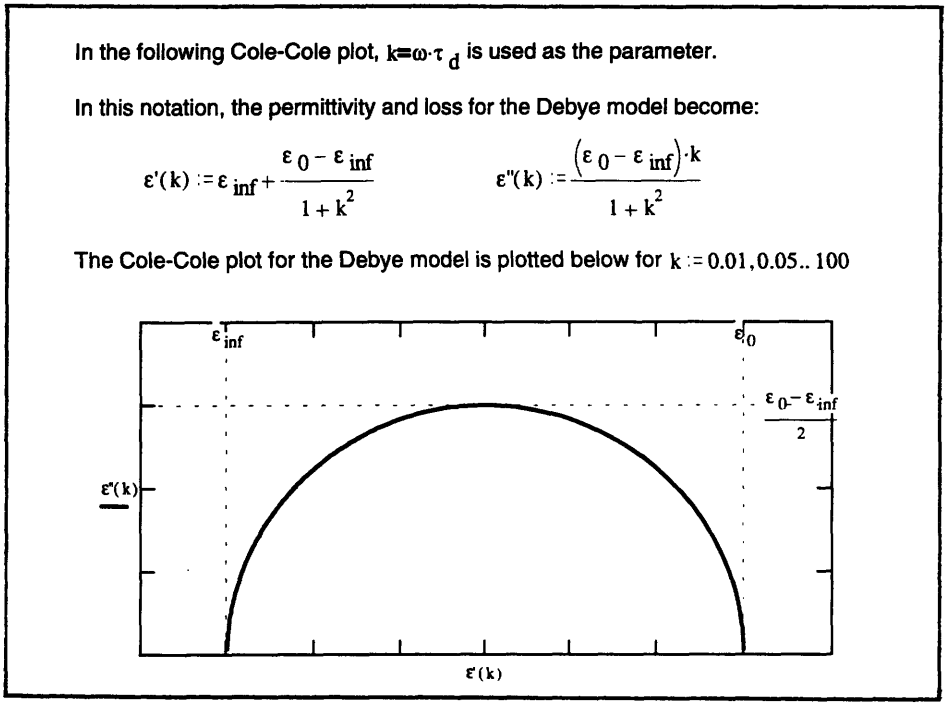


Figure 2-14: Mathcad worksheet showing a Cole-Cole plot of the Debye single relaxation time model for dipole orientation.

of experimental data fell *inside* this semicircle. Cole and Cole observed that the locus often formed the arc of a circle having a center depressed below the $\varepsilon'' = 0$ axis, and proposed that the data could be described empirically by a modified Debye equation,

$$\frac{\varepsilon(\omega) - \varepsilon_\infty}{\varepsilon(0) - \varepsilon_\infty} = \frac{1}{1 + (j\omega\tau_{CC})^{\beta_{CC}}}, \tag{2.50}$$

where the exponent β_{CC} is known as the distribution parameter that characterizes the breadth of the relaxation time distribution and ranges from 0 (infinitely broad distribution) to 1 (Debye's single relaxation time limit). This empirical function implicitly defines a functional form of the distribution of relaxation times,

$$G_{CC}(\tau/\tau_{CC}) = \frac{1}{2\pi} \frac{\sin[\pi(1-\beta_{CC})]}{\cosh[\beta_{CC}\ln(\tau/\tau_{CC})] - \cos[\pi(1-\beta_{CC})]}, \tag{2.51}$$

which is symmetrical and centered about the value τ_{CC} (see Fig. 2-17). The Cole-Cole

relaxation equation (2.50) is compared to the Debye model for $\beta = 0.7$ and $\beta = 0.4$ on Fig. 2-16.

Another empirical function describing some experimental dielectric relaxations was proposed by Davidson and Cole [175]. This function expresses the complex dielectric constant as

$$\frac{\varepsilon(\omega) - \varepsilon_\infty}{\varepsilon(0) - \varepsilon_\infty} = \frac{1}{(1 + j\omega\tau_{CD})^{\beta_{CD}}}, \tag{2.52}$$

where τ_{CD} is the Davidson-Cole time constant, and the distribution parameter β_{CD} is similar to that of the Cole-Cole distribution (see Fig. 2-16). The corresponding distribution of the relaxation times

$$\begin{aligned} G_{CD}(\tau/\tau_{CD}) &= \frac{\sin \pi\beta_{CD}}{\pi} \left(\frac{\tau}{\tau_{CD} - \tau}\right)^{\beta_{CD}}, \tau < \tau_{CD} \\ &= 0, \tau > \tau_{CD} \end{aligned} \tag{2.53}$$

is one-sided (see Fig. 2-17 and Table 2.3.3); there are no relaxation times below the value τ_{CD}. The maximum loss for this case occurs not at $\langle f \rangle = 1/2\pi\tau$ (as in the Debye and Cole-Cole distributions), but at

$$\langle f \rangle_{CD} = \frac{1}{2\pi\tau_{CD}} \tan\left(\frac{1}{\beta_{CD} + 1} \frac{\pi}{2}\right) \tag{2.54}$$

While the physical significance of this relaxation time distribution is unclear, a relaxation function of this form has been derived using a defect diffusion model [197].

Perhaps, the most popular empirical relaxation function was proposed by Williams and Watts [176, 198]. Like the Davidson-Cole function, the Williams-Watts relaxation gives rise to a skewed Cole-Cole diagram, which fits well to a large number of relaxation data for polymers and glasses. The Williams-Watts function is derived by assuming that the time decay of the polarization is expressed by the stretched exponential function,

$$P_{WW}(t) = e^{-(\frac{t}{\tau_{WW}})^{\beta_{WW}}}, \tag{2.55}$$

where τ_{ww} is the Williams-Watts time constant, and the distribution parameter[11] β_{ww} ranges from 0 to 1 (at $\beta_{ww} = 1$ the expression reduces to the Debye single relaxation time case; see Table 2.3.3 for more informations). Fourier-transforming the stretched exponential decay function, Williams and Watts [198] derived the following expression for the complex dielectric constant (see Fig. 2-16):

$$\frac{\varepsilon(\omega) - \varepsilon_\infty}{\varepsilon(0) - \varepsilon_\infty} = \sum_{n=1}^{\infty} \frac{(-1)^{n-1}}{(\omega\tau_{ww})^{n\beta_{ww}}} \frac{\Gamma(n\beta_{ww}+1)}{\Gamma(n+1)} \left[\cos\left(\beta_{ww}\frac{n\pi}{2}\right) - j\sin\left(\beta_{ww}\frac{n\pi}{2}\right)\right]. \quad (2.56)$$

The relaxation time distribution function for the Williams-Watts relaxation can also be solved in a closed form:

$$G_{ww}(\tau/\tau_{ww}) = -\frac{\tau_{ww}}{\pi\tau} \sum_{n=1}^{\infty} \frac{(-1)^n}{n!} \sin(\pi\beta_{ww}n)\Gamma(\beta_{ww}n+1)\left(\frac{\tau}{\tau_{ww}}\right)^{\beta_{ww}n+1}. \quad (2.57)$$

It is instructive to plot the Williams-Watts distribution function $G_{ww}(\tau/\tau_{ww})$ for different values of β_{ww} (see Fig. 2-15). It is asymmetric about $\tau/\tau_{ww} = 1$ when plotted *vs* $\log(\tau/\tau_{ww})$, has a greater fraction of relaxation times above the value τ_{ww}, and exhibits a maximum with an amplitude which tends to infinity as $\beta_{ww} \to 1$ when the distribution becomes a delta function, the situation corresponding to a single-time-constant Debye system. The location of the maximum occurs at $\tau/\tau_{ww} > 1$ for $\beta_{ww} < 1$, and gradually decreases towards its limiting value of $\tau/\tau_{ww} = 1$ when $\beta_{ww} = 1$.[12] While originally an empirical model, there have been attempts to explain the success of this function using models for relaxation based on diffusion [201, 202]. Recently, Phillips [203] has reviewed 125 papers on the subject of stretched exponential relaxation published since 1977 and proposed a microscopic theory of the

[11]The stretched exponential relaxation was, in fact, first proposed some 150 years ago by Kohlrausch [199] who, while investigating the discharge of a Leyden jar, discovered that decay of the *residual* charge associated with the dielectric relaxation of the glass body of the jar displayed a stretched exponential behavior. Although it is not clear if Williams and Watts [176] had known about Kohlrausch's work when they published their paper, the distribution parameter β_{ww} is often called Kohlrausch-Williams-Watts relaxation constant.

[12]A detailed comparison of the Davidson-Cole and Williams-Watts functions has been presented by Lindsey and Patterson [200].

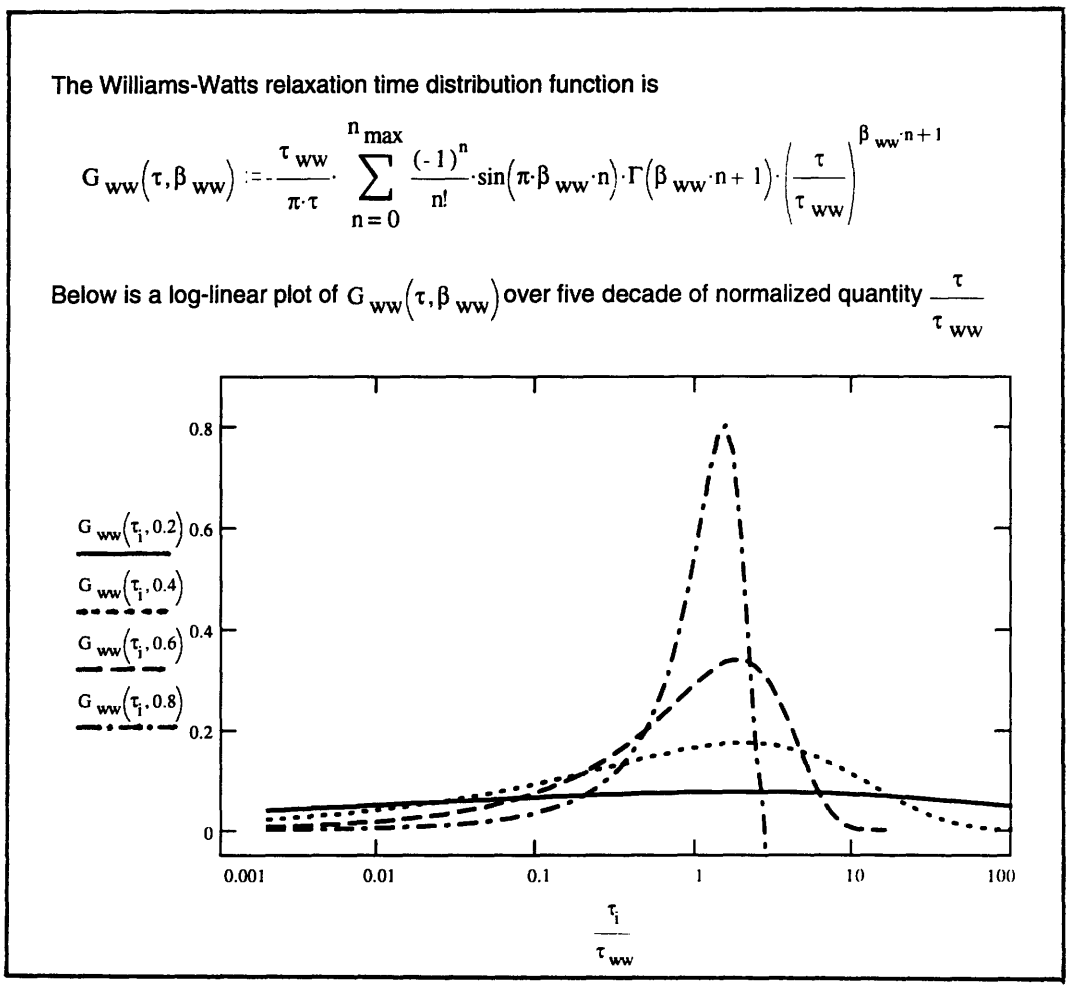


Figure 2-15: Mathcad worksheet calculating and displaying the Williams-Watts relaxation time distribution function for $\beta_{ww} = 0.2, 0.4, 0.6, 0.8$. The distribution function is very broad for the low values of β_{ww}, but tends asymptotically to a delta function at $\tau/\tau_{ww} = 1$ (Debye single-relaxation-time distribution) as $\beta_{ww} \rightarrow 1$.

In the following Cole-Cole plots, $k \equiv \omega \cdot \tau_d$ is used as the parameter, ranging over ten decades:

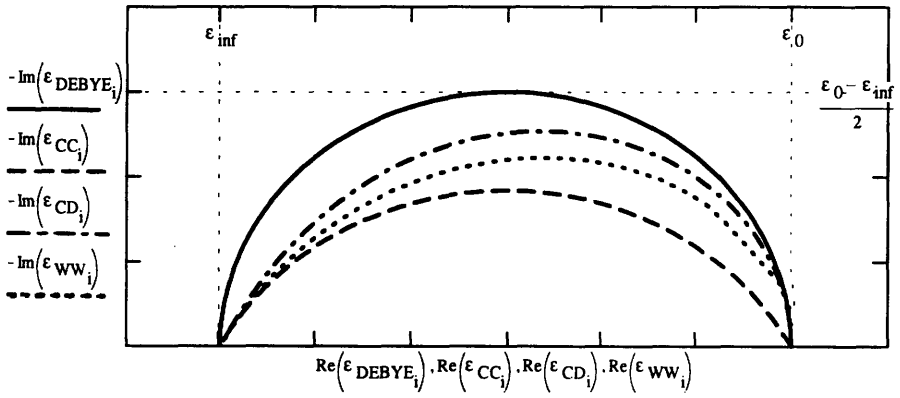
$k_{min} := 0.00001 \quad k_{max} := 10000 \quad N := 300 \quad i := 1..N \quad k := \text{LogRange}(k_{min}, k_{max}, N)$

In this notation, complex permittivities for the Debye, Cole-Cole, Davidson-Cole, and Williams-Watts models become:

$$\varepsilon_{DEBYE_i} := \varepsilon_{inf} + \frac{\varepsilon_0 - \varepsilon_{inf}}{1 + j \cdot k_i} \qquad \varepsilon_{CC_i} := \varepsilon_{inf} + \frac{\varepsilon_0 - \varepsilon_{inf}}{1 + (j \cdot k_i)^{\beta}} \qquad \varepsilon_{CD_i} := \varepsilon_{inf} + \frac{\varepsilon_0 - \varepsilon_{inf}}{(1 + j \cdot k_i)^{\beta}}$$

$$\varepsilon_{WW_i} := \varepsilon_{inf} + (\varepsilon_0 - \varepsilon_{inf}) \cdot \sum_{n=1}^{n_{max}} \frac{(-1)^{n-1}}{(k_i)^{n \cdot \beta}} \cdot \frac{\Gamma(n \cdot \beta + 1)}{\Gamma(n+1)} \cdot \left(\cos\left(\beta \cdot \frac{n \cdot \pi}{2}\right) - j \cdot \sin\left(\beta \cdot \frac{n \cdot \pi}{2}\right) \right)$$

First, we construct the Cole-Cole plots for each of the three models for $\beta := 0.7$



For comparison, the Cole-Cole plots for the same three models are shown below for $\beta := 0.4$

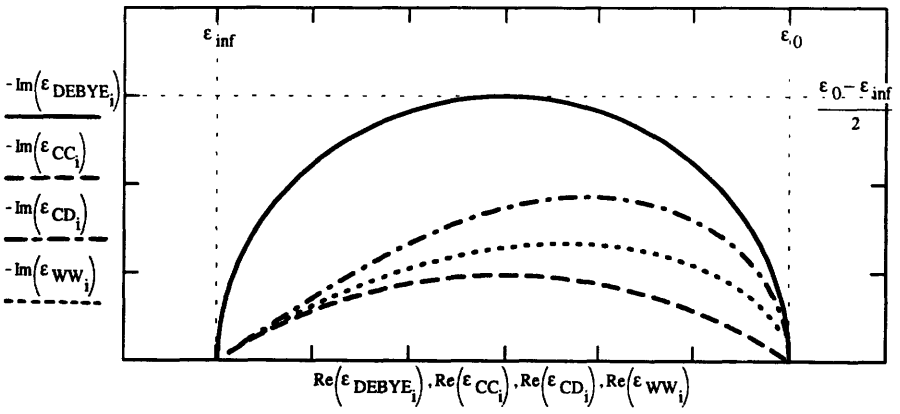


Figure 2-16: Mathcad worksheet calculating and displaying Cole-Cole plots of the Debye single relaxation time model (ε_{DEBYE}), Cole-Cole model (ε_{CC}), Davidson-Cole model (ε_{CD}), and Williams-Watts model (ε_{WW}).

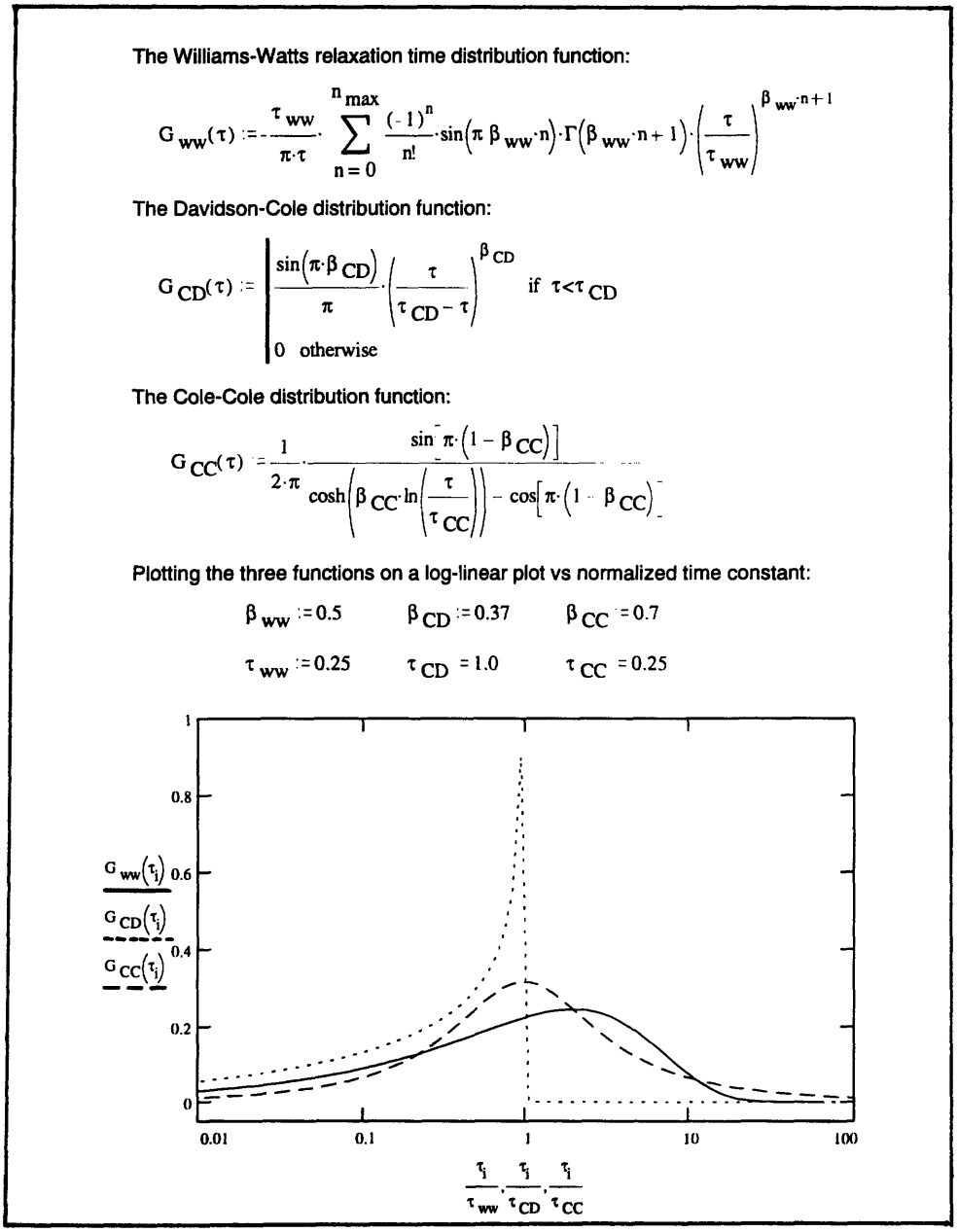


Figure 2-17: Mathcad worksheet calculating and displaying relaxation time distribution functions for Cole-Cole $G_{CC}(\tau/\tau_{CC})$, Davidson-Cole $G_{CD}(\tau/\tau_{CD})$, and Williams-Watts $G_{WW}(\tau/\tau_{WW})$ models. (The distribution function for the Debye single relaxation time model would appear as a delta function at $\tau/\tau_d = 1$ on the plot.) The constants (β's and τ's) for each models were chosen by a best fit of each function to a reliable set of experimental data [200].

Process	$\langle\tau\rangle$	$\langle\omega\rangle$
Debye	$\langle\tau\rangle_{\rm D} = \tau_d$	$\langle\omega\rangle_{\rm D} = \frac{1}{\tau_d}$
Cole-Cole	$\langle\tau\rangle_{\rm CC} = \tau_{\rm CC}$	$\langle\omega\rangle_{\rm CC} = \frac{1}{\tau_{\rm CC}} \tan\left(\frac{1}{\beta_{\rm CC}}\frac{\pi}{2}\right)$
Davidson-Cole†	$\langle\tau\rangle_{\rm CD} = \tau_{\rm CD}\beta_{\rm CD}$	$\langle\omega\rangle_{\rm CD} = \int_0^\infty \frac{G_{\rm CD}(\tau)}{\tau^2} d\tau$
Williams-Watts	$\langle\tau\rangle_{\rm WW} = \frac{\tau_{\rm WW}}{\beta_{\rm WW}}\Gamma\left(\frac{1}{\beta_{\rm WW}}\right)$	$\langle\omega\rangle_{\rm WW} \sim (d/dt)P_{\rm WW}(t)$ diverges‡

†The Davidson-Cole average relaxation frequency $\langle\tau\rangle_{\rm CD}$ can not be evaluated in closed form. To find it, a numerical integration of the relaxation times distribution function $G_{\rm CD}(\tau)$, as given by equation (2.53), must be performed.
‡As defined in Eqn. (2.55), $P_{\rm WW}(t) = e^{-(\frac{t}{\tau_{\rm WW}})^{\beta_{\rm WW}}}$.

Table 2.1: The average relaxation times $\langle\tau\rangle$ and the average relaxation frequencies $\langle\omega\rangle$ for various dielectric relaxation models considered in the text in terms of the parameters of those models.

Kohlrausch-Williams-Watts relaxation constant $\beta_{\rm WW}$ based on axiomatic set theory.

Deviations from the Debye behavior: A "many body interactions" approach

The dielectric relaxation models discussed thus far (Cole-Cole, Davidson-Cole, and Williams-Watts) have all taken the view that the nonexponential (non-Debye) relaxation behavior results from a superposition of exponentially relaxing processes with a particular distribution of relaxation times (Fig. 2-13). A completely different approach was taken by another group of researchers, lead by Jonscher [177, 204] who suggested that the relaxation behavior at the molecular level is intrinsically nonexponential, possibly resulting from cooperative molecular motions.

According to Jonscher [177, 205], the prevailing form of the frequency dependence of the dielectric loss peaks may be represented by the empirical law combining two power laws, respectively below and above the peak frequency ω_p

$$\varepsilon''(\omega) \sim \frac{1}{(\omega/\omega_p)^{-m} + (\omega/\omega_p)^{1-n}} \tag{2.58}$$

in which the exponents m and $1-n$ fall in the range $(0,1)$ and the peak frequency

ω_p is generally temperature dependent. The applicability of this empirical relation is limited at low frequencies by the onset of direct current conduction, while at the higher frequencies perturbing processes are often visible arising from the presence of some series resistance in the measuring system, or from the overlap of some other loss processes. Note that, while the relaxation models discussed previously all have only one parameter, the Jonscher model represented by Eqn. (2.58) is a two-parameter model.

To explain the two different and independent dielectric loss exponents to the left and to the right of the peak frequency ω_p (a feature characteristic of relaxation processes in many dielectric materials), Jonscher *et al.* developed the so-called *many-body universal model of dielectric relaxation* [205, 206], which was subsequently extended by the quantum-mechanical interpretation of Dissado and Hill [207, 208]. This model is based on a combination of single-particle and many-body transitions shown in the energy diagram of Fig. 2-18 which represents the potential energy of an assembly of a large number of interacting dipoles or charged particles in a two-level system. The large excitation energy Δ corresponds to the "large" transitions of single particles from an orientation or position corresponding to one of the two preferred states to the other allowed position or orientation. The bottoms of the potential wells are split by an energy $2B_{\text{eff}}$ which is determined by local conditions and by the externally applied field E. The shading of the bottoms of the potential wells represents the correlated states of width 2ζ shown in Fig. 2-18. The model recognizes three types of transitions denoted, respectively, by the arrows a, a', b, and c. Transitions a and a' correspond to the large single-particle transitions over the barrier height Δ, with thermal excitation in the case a and with partial tunneling in case a'. Transitions b and c, on the other hand, are configurational tunneling small transitions which do not involve thermal assistance.

The *small flip transitions* denoted by the arrow b in Fig. 2-18 represent a tunneling mode between different system configurations giving a net change of the total

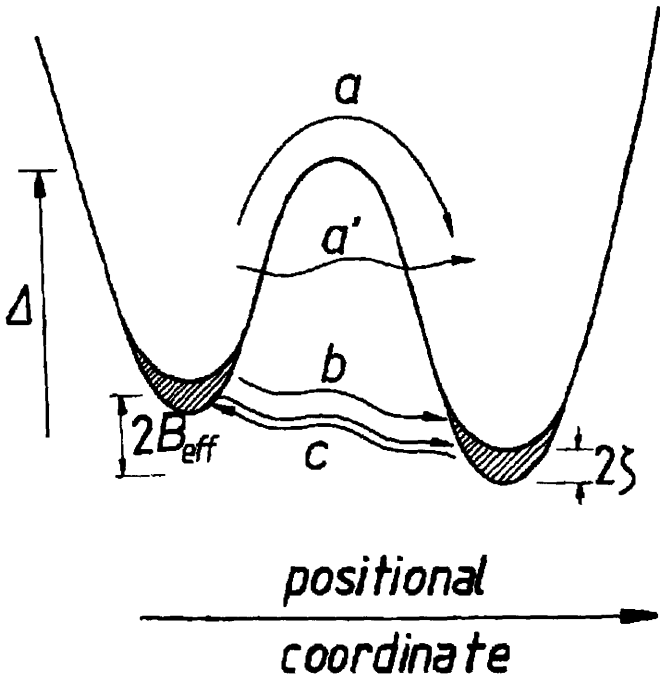


Figure 2-18: The potential energy diagram of a many-body two-level system representing the energy of a large number of interacting systems. The two wells correspond to the preferred orientations or positions. The splitting of the bottom by $2B_{\text{eff}}$ is shown; the shaded regions represent the energy states of width 2ζ resulting from particle interactions. Arrow a denotes large thermally assisted transitions over the barrier Δ, arrow a' is the same with tunnel assistance. Arrows b and c refer to configurational tunneling transitions of the *flip* and *flip-flop* types, respectively. (From Jonscher *et al.* [209].)

dipole moment. The *flip* transition constitutes the dominant polarization relaxation mechanism at high frequencies, $\zeta \ll \omega \ll \omega_p$, where $\zeta \simeq 10^{12}$ Hz is the phonon frequency of the system. These transition are thus the physical process behind the exponent n in Jonscher empirical "universal relaxation law" [Eqn. (2.58)]. On the other hand, the *flip-flop* processes denoted by the pair of arrows c in Fig. 2-18 represent the local fluctuations of the dipole moment which retain the average value of the total polarization. This mechanism, characterizing the response of the system at frequencies much lower than ω_p, is related to the exponent m in the empirical law of the dipolar response [Eqn. (2.58)].

The Dissado-Hill theory thus associates the exponent m in Eqn. (2.58) with the degree of correlation between the *flip-flop* transitions, and the exponent n with the degree of correlation of the *flip* transitions. In each case the value of unity corresponds to fully correlated transitions, and the value of zero — to uncorrelated transitions. The value $m = 0$ corresponds to completely uncorrelated *flip-flops*, giving the Davidson-Cole behavior [Eqn. (2.52).]

With increasing temperature, the correlation of the *flip* and *flip-flop* transitions is strengthened, increasing the values of the exponents m and n, as shown in Fig. 2-19. Note that the changes in the dielectric material itself (resulting, *e.g.*, from phase and structural transitions, diffusion of foreign species into the material, etc.) also alter the correlation of the *flip* and *flip-flop* transitions, and can thus affect the exponents m and n in a similar manner.

The sensitivity of the exponents m and n to the structure of the material represents one of the principal diagnostic uses of dielectric measurements. The shape of the loss spectrum represents a sensitive tool for the detection of order changes.

Summary

A summary of the various dielectric relaxation functions discussed in this section and their power-law exponents are displayed in Table 2.2.

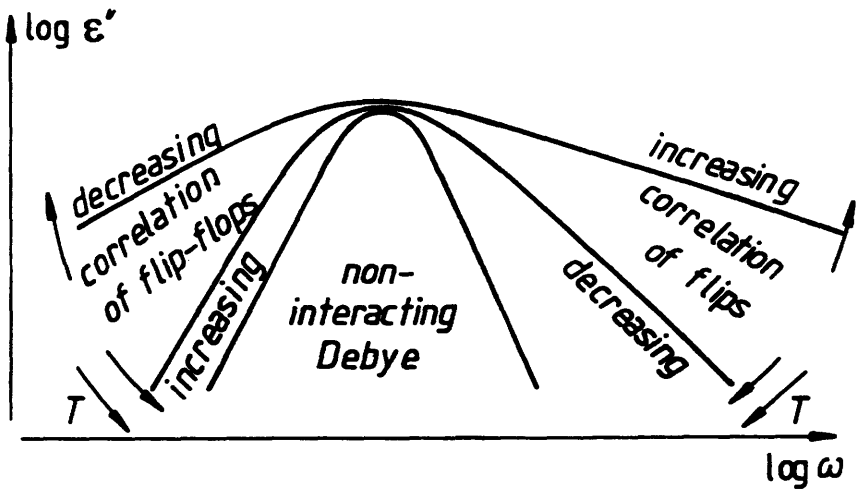


Figure 2-19: The effect of temperature on the shape of the loss peak of a dipolar material, as a consequence of changing correlations of *flip* and *flip-flop* transitions resulting from varying short-range order. The non-interacting Debye response is shown for comparison. (After Jonscher [210].)

Process	Normalized complex permittivity function	exponent for $\omega \ll \omega_p$		exponent for $\omega \gg \omega_p$	
		$\varepsilon'(\omega)$	$\varepsilon''(\omega)$	$\varepsilon'(\omega)$	$\varepsilon''(\omega)$
Debye (1929)	Eqn. (2.45)	2	1	-2	-1
Cole-Cole (1941)	Eqn. (2.50)	β_{cc}	β_{cc}	$-\beta_{cc}$	$-\beta_{cc}$
Davidson-Cole (1951)	Eqn. (2.52)	2	1	β_{cd}	β_{cd}
Williams-Watts (1970)	Eqn. (2.56)	2	1	$-\beta_{ww}$	$-\beta_{ww}$
Jonscher (1975)	Eqn. (2.58)	m	m	$n-1$	$n-1$

Table 2.2: A summary of various dielectric relaxation functions and their power-law exponents in the neighborhood of the peak frequency $\omega_p = \frac{2\pi}{\tau}$, where τ is the relaxation time parameter of the process in question.

2.3.4 Effect of Residual DC Conductivity

We saw from the Eqn. (2.44) on page 100 that the DC conductivity adds to the effective dielectric loss $\varepsilon''_{\text{eff}}(\omega)$ seen in a dielectric measurement:

$$\varepsilon_{\text{eff}}(\omega) = \varepsilon'(\omega) - j\left(\varepsilon''(\omega) + \frac{\sigma_0}{\omega\varepsilon_0}\right) \tag{2.59}$$

$$\varepsilon'_{\text{eff}}(\omega) = \varepsilon'(\omega) \tag{2.60}$$

$$\varepsilon''_{\text{eff}}(\omega) = \varepsilon''(\omega) + \frac{\sigma_0}{\omega\varepsilon_0}. \tag{2.61}$$

The frequency dependence of the loss factor described by Eqn. (2.59) is illustrated in Fig. 2-20. We see clearly that the DC conductivity σ_0 has a profound effect on the effective loss at low frequencies. Even a small σ_0 will dominate the dielectric response at sufficiently low frequencies because of the $1/\omega$ dependence. As σ_0 increases, it becomes increasingly difficult to discern the dipole loss peak. While it is still sometimes possible to extract the dipolar contribution to $\varepsilon''_{\text{eff}}$ even when σ_0 is large, an independent measurement of σ_0 is required.

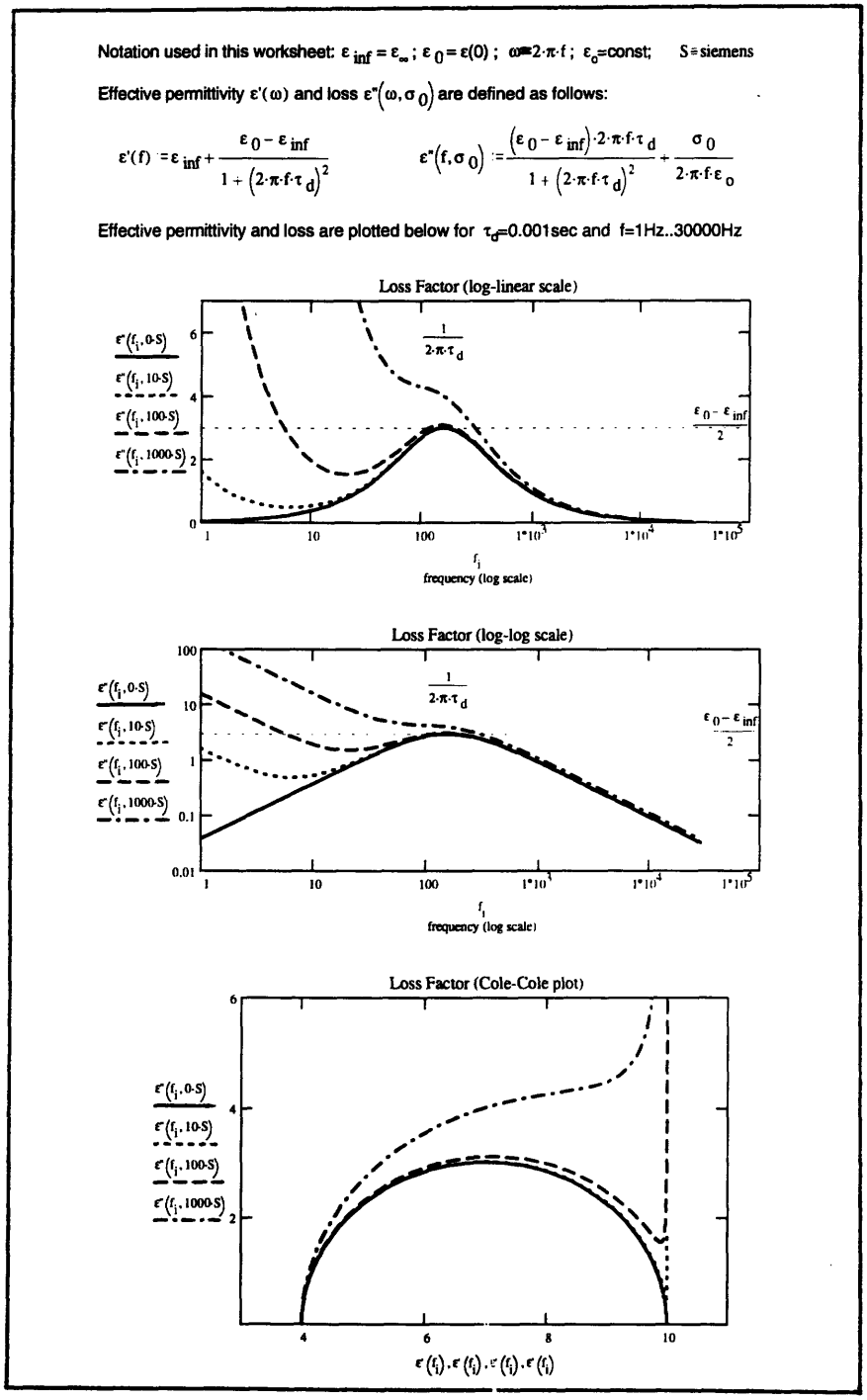


Figure 2-20: Mathcad worksheet illustrating the effective dielectric loss of a Debye dielectric having DC conductivity σ_0, for σ_0 equal to 0, 10, 100, and 1000 Siemens (solid, dotted, dashed, and dash-dotted traces, respectively). The frequency response of such a dielectric is shown here on the log-linear, log-log, and Cole-Cole plots. For each plot, the solid curves for which $\sigma_0 = 0$ S correspond to the ideal Debye dielectric similar to that of Figs. 2-12 and 2-14.

Chapter 3

Low frequency dielectric measurements

3.1 Introduction

After about sixty years of lingering development [3, 211], low-frequency (LF) dielectric measurements are finally emerging as an important materials characterization tool. In the last few years, they have become indispensable in such diverse fields as:

- mining industry — for monitoring the quality of coal [212];
- pharmacological industry — for estimating adsorption of drugs onto nanoparticles for novel drug delivery systems [213];
- polymer industry — for monitoring the kinetics of polymerization in polymerizing systems [214, 215];
- oil industry — for estimating the water content in crude oil [216];
- biology — for online monitoring of cell concentrations during yeast cultivation and other fermentation processes [217, 218];

- medicine — for non-invasive measurements of tissues and bones, possibly leading to the development of diagnostic techniques for early detection of such maladies as cancer and osteoporosis [219, 220];
- material science — for optimization of the cure cycle of composites [3, 221]; and
- food science — for prediction of the level of cholesterol in certain food ingredients [222].

The LF dielectric measurements are unequaled in their ability to *dynamically* monitor the many chemical and physical processes important in investigations of new materials — such as cure, polymerization, phase transitions, and diffusion.

In this Chapter, we shall review the LF dielectric measurement techniques that we used to investigate the dielectric properties of fullerenes. Section 3.2 describes the conventional parallel-plate technique for measuring the dielectric function $\varepsilon(\omega)$. Sec. 3.3 deals with theoretical and practical considerations of *microdielectrometry.* Finally, Sec.3.4 discusses special techniques for high-impedance transport measurements. In addition, Appendix A contains the LabView code for the software written to control the measurement systems and instruments described in this section.

3.2 Parallel-plate measurements

3.2.1 Overview

The conventional way for making low frequency (below $\sim$1 MHz) measurements of the dielectric properties of solids is to place a sample between closely spaced parallel conducting plates (Fig. 3-1), and to monitor the AC equivalent capacitance $C_m(\omega)$ and dissipation factor (also known as *loss tangent*) $D(\omega)$ of the resulting capacitor. Normally, one designs the plate spacing to be much less than the plate size, as this serves to minimize the effects of fringing field.

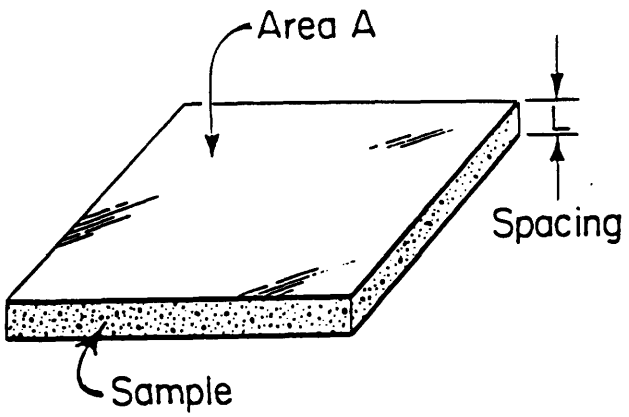


Figure 3-1: Parallel plate electrodes.

The material under test in the parallel-plate configuration (Fig. 3-1) can be modeled as a frequency-dependent capacitance $\mathbf{C}(\omega)$ in parallel with a frequency-independent resistor R_0 [Fig. 3-2(a)]. The DC resistance R_0 takes into account processes such as tunneling, thermally activated hopping, and ionic conduction. The capacitance $\mathbf{C}(\omega)$ is proportional to the complex dielectric function $\varepsilon(\omega) = \varepsilon'(\omega) - j\varepsilon''(\omega)$ of the sample material under test:

$$\mathbf{C}(\omega) = \varepsilon(\omega)\varepsilon_0 A/d, \tag{3.1}$$

where A is the cross sectional area of the capacitor, d is the separation between the plates, and $\varepsilon_0 = 8.85 \times 10^{-12}$ F/m is the absolute permittivity of free space. The capacitance $C_m(\omega)$ measured by a typical capacitance bridge (such as an HP 4274A by Hewlett Packard, Inc. that was used in this study) is equal to the real part of $\mathbf{C}(\omega)$:

$$C_m(\omega) = \varepsilon'(\omega)\varepsilon_0 A/d, \tag{3.2}$$

and so it can be used to extract the frequency-dependent real part of the dielectric function $\varepsilon'(\omega)$. The other measured quantity, the dissipation factor (the *loss tangent*)

given by

$$D(\omega) = \varepsilon''(\omega)/\varepsilon'(\omega) + \frac{d}{\omega\varepsilon_0\varepsilon'(\omega)AR_0}, \tag{3.3}$$

can then be used to extract the imaginary part of the dielectric function $\varepsilon''(\omega)$.

3.2.2 Special considerations

While the theory underlying the parallel-plate technique described above is quite simple, an actual measurement is complicated by a variety of additional constraints arising from the properties of the material being investigated, the nature of the interface, and the limitations of the measurement system. These three classes of constraints, as applied to the measurement of C_{60} solid films, are briefly discussed below.

Interfacial effects

In most actual measurements, the effect of *interfacial polarization* giving rise to the interfacial capacitance C_i needs to be taken into account. For a typical solid, the physics behind C_i includes:

1. The purely interfacial electronic effects influenced by the presence of electrons trapped with a finite lifetime in localized states near the interface [223], and

2. The "blocking layer" space-charge polarization effects due, *e.g.*, to the presence of mobile ions in the material [3, 193, 224] (see Fig. 3-3).

The measured capacitance C_m is then equal to the series combination of the interface capacitance C_i and the sample (bulk) capacitance C [225], as shown in Fig. 3-2(b). One thus expects the total reciprocal areal capacitance to have a linear dependence on thickness d of the sample with a *nonzero intercept* at $d = 0$, *i.e.*,

$$\frac{A}{C_m} = \frac{A}{C_i} + \frac{d}{\varepsilon_0\varepsilon'}. \tag{3.4}$$

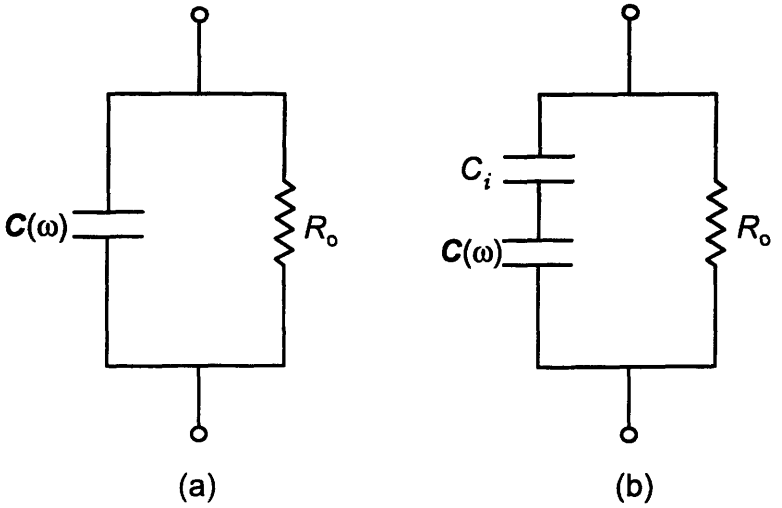


Figure 3-2: Equivalent circuits for the material under test in Fig. 3-1 with (b) and without (a) taking the interfacial capacitance into account.

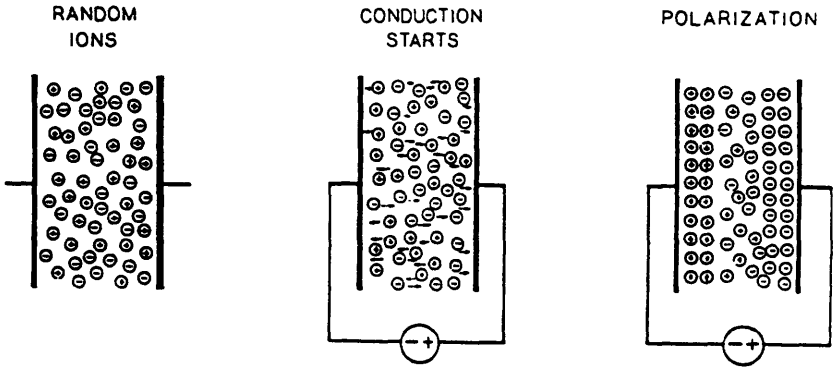


Figure 3-3: Idealized view of the polarization due to ions. Ion conduction in the presence of an applied electric field leads to electrode (interfacial) polarization and formation of a "blocking layer" (after Day *et al.* [193]).

Note that as the thickness d of the film gets smaller, the interfacial capacitance C_i may come to dominate the measured capacitance C_m. Hebard *et al.* have shown [225] that, in Al-Al_2O_3-Al trilayer structures, this happens when the oxide thickness falls below 50 Å. We, therefore, expect the bulk capacitance due to C_{60} to dominate the capacitive part of the impedance in the Al-C_{60}-Al trilayer structures with $d_{C_{60}} \sim 1000$ Å that were used in this study (see Sec. 4.6 and Fig. 4-13).

Linearity and time invariance

In addition to the interfacial effects, one needs to keep in mind that, in order to be able to reliably interpret a dielectric measurement, it needs to be performed in the *linear regime.* Whether or not a given sample is linear depends on the applied voltage. Most dielectrics become nonlinear at electric fields on the order of 10^5 V/cm, and experience catastrophic breakdown at electric fields on the order of 10^6 V/cm. Therefore, when dealing with films of thicknesses on the order of 1000 Å (a typical film thickness in our studies), the applied voltage must be kept at ~0.1 V or lower to keep a safe distance of two orders of magnitude or more away from the typical breakdown voltage.

The other important characteristic of a measured dielectric system is its *time invariance.* While usually not a problem at frequencies of 1 Hz and higher, this condition is very difficult to fulfill in very low frequency (VLF) measurements, when a single frequency scan may take hours, or even days. Temperature fluctuation, humidity, diffusion of ambient gases, and sample changes caused by other factors may complicate the interpretation of the results. Therefore, care should be taken to ensure that the sample changes only insignificantly during the interval required to make a single sample measurement.

Cable capacitance

Additional problems are introduced by cabling and shielding issues. In Fig. 3-4, the

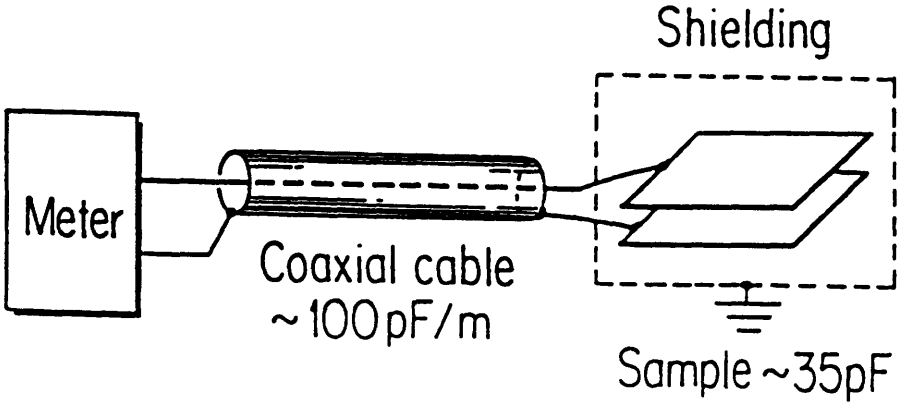


Figure 3-4: Schematic diagram of a measurement system illustrating the effect of cable capacitance and shielding.

parallel-plate sample is connected to a meter by a coaxial cable (~100 pF/m). A 2-meter cable introduces a capacitance of 200 pF in parallel with the sample capacitance, which must be subtracted from the measured capacitance C_m to determine the sample capacitance. Clearly, when the cable capacitance is comparable to the sample capacitance, the sensitivity and accuracy are reduced. It is, therefore, advisable to use the twisted-pair cables whenever possible, as they usually possess smaller capacitance per unit length than the coaxial cables.

Additionally, the cable and electrodes must be shielded, to prevent the pickup at 60 Hz and its harmonics which degrade measurements at or near those frequencies.

3.2.3 Measurement equipment

Whether using parallel plate or other types of electrodes, an AC measurement involves determining the admittance between the electrodes under sinusoidal steady-state conduction. Any AC measurement system thus includes a generator to produce the sinusoidal excitation fed to the sample, and an analyzer to compare the magnitude and phase of the output with the excitation input. The instruments and configurations used in this study are described below.

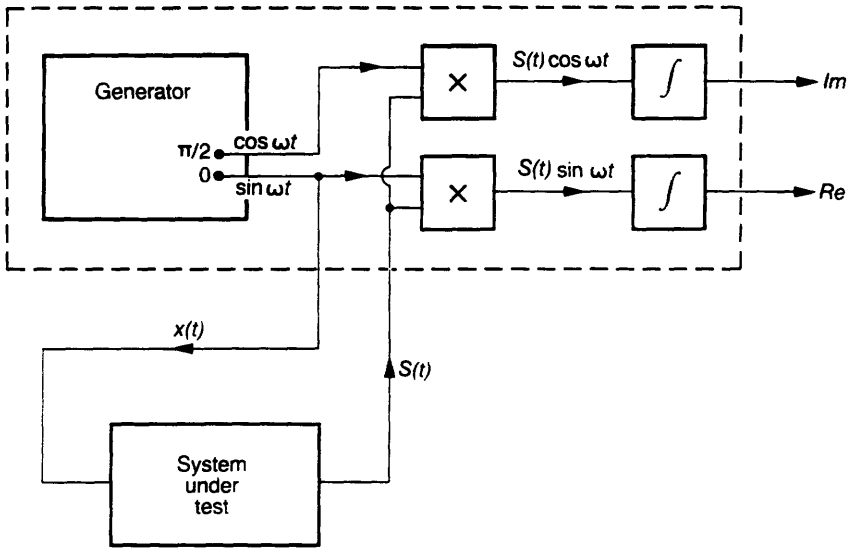


Figure 3-5: A schematic of the working principle of the SI 1254 Frequency Response Analyzer.

HP 4274A LCZ meter

Hewlett Packard's HP 4274A LCZ Meter is a general-purpose impedance-measuring instrument designed to measure circuit components such as capacitors and inductors in the frequency range from 100 Hz to 100 kHz. The magnitude of the sinusoidal input excitation can be varied from 0.01 V to 10 V, and was usually fixed at 0.1 V to ensure that the measurement stays in the linear regime, as discussed above. The instrument is equipped with the standard IEEE 488 computer bus, which facilitates interfacing and control from a lab computer. Appendix A.1 describes the LabView software interfacing the instrument with an IBM-compatible PC.

SI 1254 Frequency Response Analyzer

The Digital Frequency Response Analyzer (FRA) SI 1254 by Solartron Instruments (a division of Schlumberger Ltd.) is an example of the digital correlator system. The principle of transfer function measurement is shown schematically in Fig. 3-5. The sample response $S(t)$ to the perturbing signal $x(t) = X_0 \sin \omega t$ is correlated with two

synchronous reference signals, one in phase with $x(t)$ and the other 90° out of phase, in order to calculate the real and imaginary parts of the sample's transfer function $\mathbf{S}(\omega)$:

$$Re\{\mathbf{S}(\omega)\} \sim \frac{1}{T}\int_0^T S(t)\sin\omega t\,dt \tag{3.5}$$

$$Im\{\mathbf{S}(\omega)\} \sim \frac{1}{T}\int_0^T S(t)\cos\omega t\,dt \tag{3.6}$$

where T, the integration time, is an integer number of periods of the perturbing signal. The FRA thus yields directly the real and imaginary parts of the transfer function of the sample, which, in SI 1254, can alternatively be displayed in the phase–magnitude notation.

Since the input impedance of the SI 1254 FRA is relatively low (100 MΩ), the output signal $S(t)$ needs to be channeled through a high-bandwidth amplifier, such as the SR 570 current amplifier described in Sec. 3.4.[1] Because the FRA is a *digital* instrument, it can be used to perform measurements at arbitrarily low frequencies. In this study, we have measured the dielectric properties of C_{60} films at frequencies as low as 1 mHz. Appendix A.2 presents the LabView software interfacing the SI 1254 FRA with a personal computer.

Other equipment

All of the functions of the FRA can alternatively be implemented directly in a modern personal computer equipped with appropriate Input/Output hardware using digital signal processing techniques. Work has been started on a digital computer-based data acquisition system (DAQ) based on the National Instruments' AT-MIO-16E-3 multifunction I/O board. The board features two analog output channels for generation of the excitation signal, and 16 analog input channels for output detection. The 500 kSamples/s, 12-bit (1 in 4,096) resolution, and 100 GΩ input impedance pro-

[1] The SI 1286 Electrochemical Interface by Solartron Instruments, with input impedance exceeding 10 GΩ, can also be used for signal conditioning.

vide the operational parameters better than those of the SI 1254 FRA. A LabView implementation of the frequency analysis system is currently in progress.

3.3 Microdielectrometry

Clearly, the calibration of the parallel-plate measurements described in Sec. 3.2 will be affected if the plate spacing d changes in the course of the measurements, as it will, for instance, at the C_{60} phase transition point $T_{01} \approx 260$ K (Sec. 1.3.2 and Fig. 1-11), or during intercalation of oxygen and other species into the interstitial spaces of C_{60} solid (Sec. 4.7), or during photopolymerization of a C_{60} film (Sec. 1.3.2).

To avoid this problem, we have used the microdielectrometry technique [226–228] to measure dielectric properties of C_{60} at low frequencies. Instead of using a parallel plate geometry, both electrodes used in the microdielectric measurement are placed on the same surface of an integrated circuit (see Fig. 3-6), and the medium to be studied (C_{60} film) is placed over the electrodes by thermal sublimation in vacuum (Sec. 4.5). The comb electrodes in Fig. 3-6, in contrast to parallel plates, provide a fixed calibration for both ε' and ε'', because electrode size and spacing remain constant even when the sample itself is changing. However, the interdigitated electrode geometry is less efficient than parallel plates in terms of coupling the electric field through the sample medium. To increase the signal to an easily measurable level, some microdielectrometer sensors provide amplification in the form of an integrated field-effect transistor, whose gate electrode is one of the two interdigitated electrodes (called the floating gate; see Fig. 3-6). To compensate for the transistor amplification factor, which would require a complex calibration procedure at each operating temperature, a second identical field-effect transistor is simultaneously fabricated on the same integrated circuit. The second field-effect transistor serves as a reference in a differential feedback circuit, the details of which have been published elsewhere [229]. The net effect of the two-transistor plus feedback circuit combination is that when

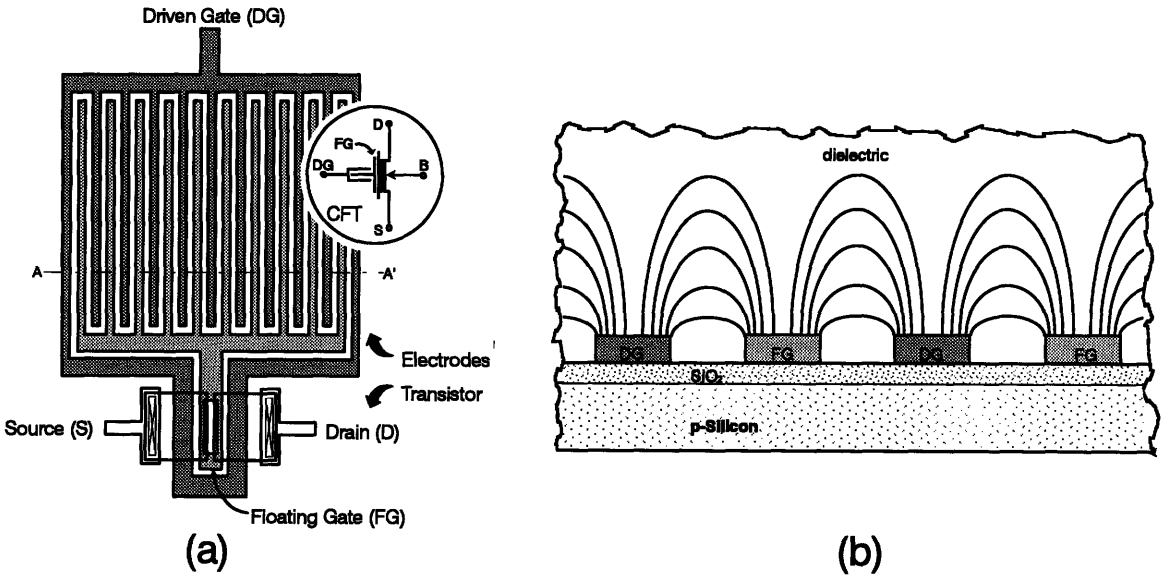


Figure 3-6: (a) Schematic view of active portion of microdielectrometer sensor chip. CFT refers to "floating-gate charge-flow transistor," of which the microdielectrometer is an example. (b) Schematic cross-section through the electrode region (AA′) showing interdigitated driven gate (DG) and floating gate (FG) electrodes, and the electric field coupling them through the dielectric (C_{60}) sample.

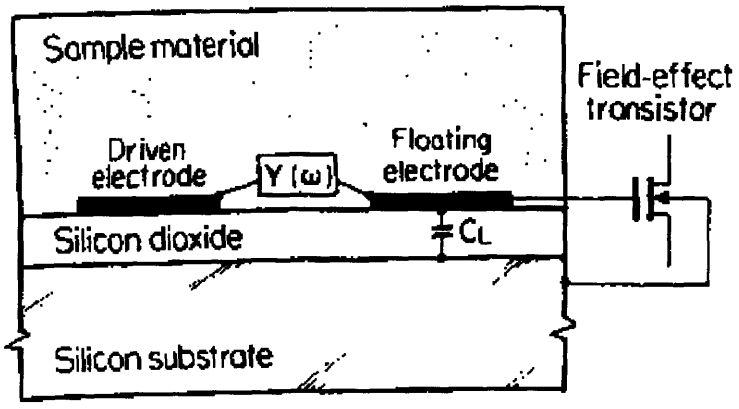


Figure 3-7: Cross section of microdielectrometer sensor. The silicon dioxide insulator is much thinner than the electrode spacing. $\mathbf{Y}(\omega)$ is the comb electrode admittance; C_L is the capacitance between the floating electrode and the substrate [3].

a sinusoidal signal is applied to the driven electrode, the corresponding sinusoidally varying voltage that appears on the floating gate can be measured independent of the transistor amplification factor. This floating-gate voltage has an amplitude and phase relative to the drive signal that depends on the geometry of the device and on the dielectric properties of the sample medium. The fact that the sensing electrode is electrically floating, combined with the proximity of the amplifier to that electrode, means that a good signal-to-noise ratio can be achieved at very low frequencies (down to $\sim 10^{-3}$ Hz).

As the device geometry is both stable and reproducible, the task of calibrating the measurement reduces to relating the measured amplitude and phase for a particular device geometry to the specific values of ε' and ε'' for the sample. To derive this relationship, consider a cross section of the microdielectrometer sensor shown in Fig. 3-7. The cross section shows the electrodes separated from a conducting ground plane (the silicon substrate) by a silicon dioxide insulating layer whole thickness is much less than the electrode spacing. One of the electrodes is driven with a signal, while the other is connected to the input gate of one of the field-effect transistors,

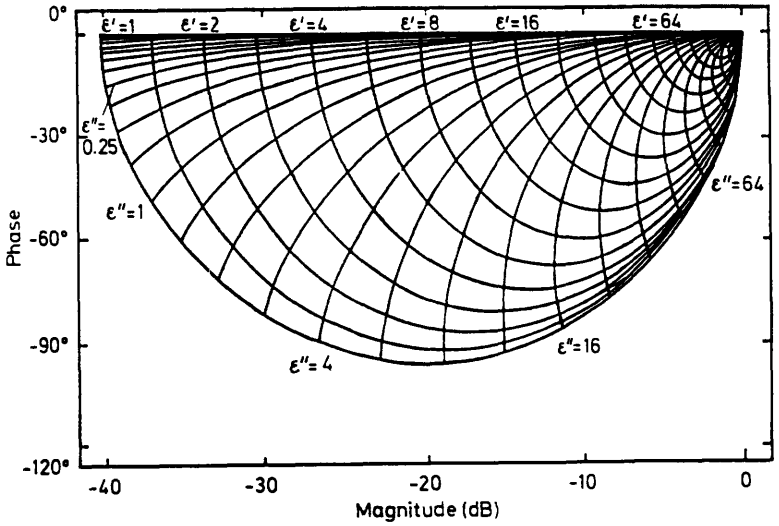


Figure 3-8: Calibration of the microdielectric sensor, showing contours of constant permittivity and loss factor as a function of the measured magnitude and phase [230, 231].

as described above. Except for a capacitance C_L between it and the ground plane, this latter electrode is electrically floating. The capacitance C_L integrates the current reaching the floating electrode through the comb electrode admittance $\mathbf{Y}(\omega)$, and develops a voltage which depends on the charge rather than the current [3]. Therefore, instead of providing a direct measurement of $\mathbf{Y}(\omega)$, the microdielectrometer measures this voltage, or, equivalently, the complex transfer function defined as follows:

$$\mathbf{H}(\omega) = \frac{\mathbf{Y}(\omega)}{1 + j\omega C_L \mathbf{Y}(\omega)}. \tag{3.7}$$

Like the admittance $\mathbf{Y}(\omega)$, the transfer function $\mathbf{H}(\omega)$ has a magnitude and phase which can be interpreted in terms of an assumed homogeneous dielectric medium with permittivity ε' and loss factor ε'', in accordance with a particular model for admittance $\mathbf{Y}(\omega)$ appropriate for the material under study. Figure 3-8 illustrates such a calibration as a contour plot, for the case of $\mathbf{Y}(\omega)$ corresponding to the simple model of Fig. 3-2.

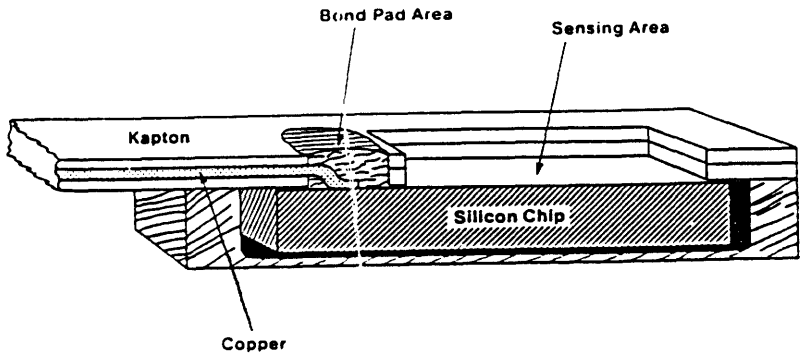


Figure 3-9: Schematic of "ribbon cable" packaging of the Micromet Instruments' integrated sensor (such as the one shown in Fig. 3-6.) The bonds from the package to the chip are completely passivated, and thus are not exposed either to the material under test or to the ambient environment.

Two types of sensors have been used in this study, both supplied by Micromet Instruments Inc. (Newton, MA). The first, used for characterization of the dielectric properties of C_{60} films as function of oxygen diffusion (see Sec 4.4.2), was an integrated sensor shown in Fig. 3-6, having an electrode spacing of 12.5 μm, and oxide (SiO_2) thickness of approximately 1.5 μm, and approximately 7.5 cm of total electrode meander (see Table 3.1). The sensors of this type are preassembled in a "ribbon cable" package, as shown in Fig. 3-9.

The other type of sensor, the so-called "Micron Sensor" that was introduced by Micromet Instruments in 1995, was used for transport and photoconductivity studies of the C_{60} films. It is comprised of two chromium interdigitated electrodes deposited on a quartz substrate (Fig. 3-10). Unlike the sensor in Fig. 3-6, the new Micron Sensor does not have the integrated on-chip electronics, but compensates for the loss of amplification with a more closely packed geometry, featuring 1 μm interelectrode spacing and a 1 m meander length (see Table 3.1). It is configured so that a variety of material deposition techniques, including spin-coating, spraying, printing, and thermal sublimation, may be used to apply films to the surface of the sensor.

A measurement system that determines the real and imaginary parts of the di-

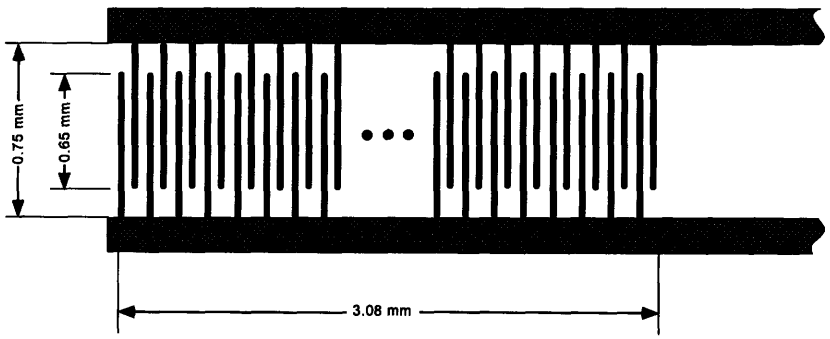


Figure 3-10: The Micron Sensor geometry. Chromium electrodes (1500 Å) are deposited on quartz substrate. [Courtesy of Huan Lee (Micromet Instruments, Newton, MA) and David Day (Auburn International, Denvers, MA).]

Specification	Integrated sensor	Micron sensor
Sensor Dimensions	$14'' \times 0.375'' \times 0.02''$	$1 \times 1 \times 0.04$ cm
Active Face Dimensions	$0.2'' \times 0.1''$	3.08×0.75 mm
Electrode Spacing D_μ	12.5 μm	1 μm
Meander Length L_μ	$\sim$7.5 cm	1 m
Electrode Thickness H_μ	N/A	1500 Å (chromium)
Permittivity Range	1 to 40	1 to 20
Log Loss Factor Range	–2 to 3	–2 to 2
Log Conductivity Range (S/cm)	–16 to –5	–13 to –5.5
A/D Ratio	N/A	35
Temperature Range	–100 to 250°C	–150 to 200°C

Table 3.1: Microdielectric sensor specifications. (Source: Micromet Instruments, Inc.)

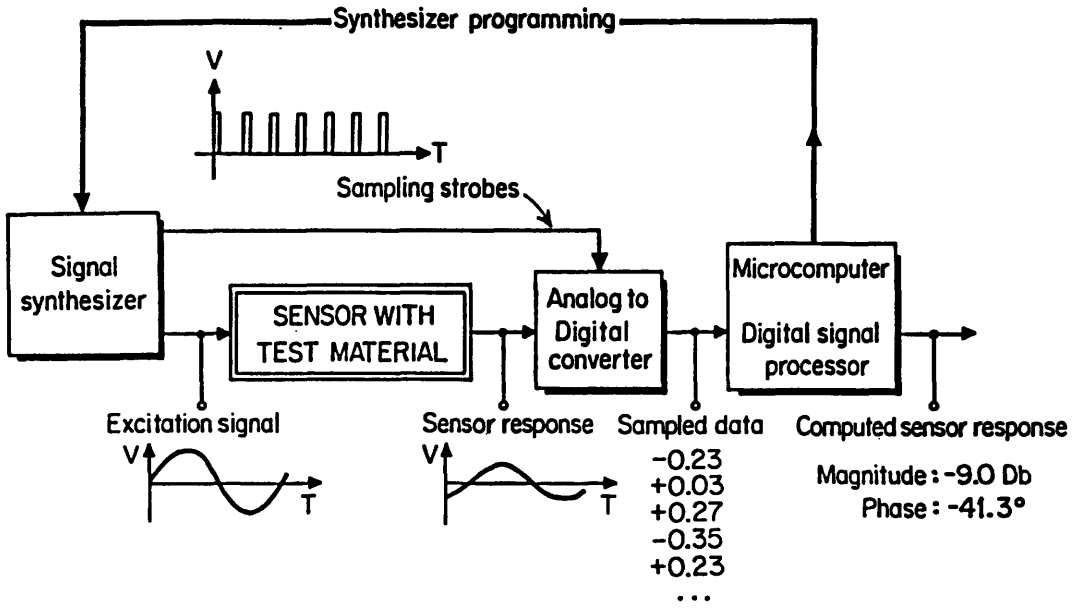


Figure 3-11: Functional block diagram of sampled data system used in microdielectrometry measurements [231].

electric constant of the material coating the sensor consists of a frequency response analyzer (similar to the one described in Sec. 3.2.3) and a device (that can be implemented either in hardware on in software) for converting the measured gain and phase into the real and imaginary parts of the dielectric constant. A calibration table (different for each type of sensor), such as the one shown in Fig. 3-8, is used for the conversion.

For most of our sensor-based dielectric measurements, we used the commercially available *Eumetric® System II Microdielectrometer* by Micromet Instruments, Inc. (Newton, MA) that combines both the FRA and the lookup functions in a single apparatus. It contains a digital correlator [232] that supplies the sinusoidal drive signal to the driven gate electrode and determines the relative amplitude and phase of the comparator output signal. A functional block diagram of the digital correlator is shown in Fig. 3-11. A master clock synchronizes the digitally synthesized drive

waveform and the sampling of the comparator output. A discrete Fourier transform (implemented in software) is used to determine the amplitude and phase of the sampled waveform. Based on the accuracy of the amplitude and phase measurement electronics, the ε'' sensitivity of the microdielectrometer is about 0.01 [232], which for a medium having a dielectric permittivity of 4 corresponds to the loss tangent D sensitivity of less than 0.003. At a frequency of 0.01 Hz, an ε'' sensitivity of 0.01 corresponds to a conductivity sensitivity of about 10^{-16} S/cm.

The microdielectrometer was interfaced with an IBM-compatible computer via RS-232 serial port using a versatile LabView software presented in Appendix A.3.

Both the integrated sensor and the Micron Sensor include an on-chip temperature indicator. Since all dielectric and transport properties are temperature dependent, the ability to make a temperature measurement at the same point as the dielectric measurement is a useful feature of the microdielectrometry technique. Together with other unique characteristics of this technique described above (*e.g.*, open-faced electrodes, fixed calibration, good sensitivity), microdielectrometry is particularly appropriate for performing in-situ measurements, investigating the dynamics of diffusion and adsorption, and monitoring the phase transition and cure processes. The results obtained by using this technique for the dielectric and transport studies of C_{60} films are presented in Sections 4.7 and 4.4.2, respectively.

3.4 Transport Measurements

As detailed in Sec. 2.3.4, an independent measurement of the DC conductivity σ_0 is necessary in order to recover the dielectric function $\varepsilon(\omega)$ from the effective dielectric function $\varepsilon_{\text{eff}}(\omega)$ obtained from an AC dielectric measurement. In addition, there are a number of situations where a transport measurement itself provides valuable information about the structure of the sample. For instance, since the resistivity of fullerites has been shown to be extremely sensitive to the presence of oxygen in the

interstitials of their fcc lattice (see Sec. 4.4.2), transport measurements can be an effective tool for ascertaining the oxygen content of C_{60} films.

We have seen in Chapter 1 that, in their pristine state, fullerene solids are insulating. The resistivity of pure crystalline C_{60} is $\sim 10^7$ Ω·cm (see Table 1.2), and it can rise by as much as three orders of magnitude as a result of oxygen adsorption. It can easily be shown using Table 3.1 and Fig. 3-10 that, if a Micron sensor is used to measure the resistivity of such an oxygenated C_{60} film, the DC resistance being measured will exceed 1 GΩ. Measuring resistances of this magnitude reliably requires special techniques, which are considered below.

As always in high-resistance measurements, a known voltage should be applied to the sample, and the resulting current should be measured. This approach is commonly referred to as SVMC (Source Voltage Measure Current).[2]

The naïve way of measuring an unknown large resistance R_s is to terminate the circuit with a well-calibrated resistor R_0 of known value, and to amplify the resulting voltage with a voltage preamplifier, as shown in Fig. 3-12(a). In this configuration, R_0 serves both as a reference resistor whose value is known precisely, and as a current-limiting component of the circuit ensuring that, regardless of the value of the test resistor R_s (which may change by many orders of magnitude, as a result of, *e.g.*, oxygen diffusion and temperature changes) the current in the circuit is limited to V_s/R_0. Using a simple voltage divider formula and solving for R_s, we derive the formula for calculating the unknown resistance R_s from the circuit parameters of Fig. 3-12(a):

$$R_s = R_0 \left(G \frac{V_s}{V_m} - 1 \right), \tag{3.8}$$

where G is the differential amplifier gain, and V_m is the measured voltage. While, under certain conditions, this method may yield satisfactory results, it has a number of drawbacks. Most importantly, to get a large voltage from the current I_s, a large

[2]Note that, when dealing with low-resistance (high-conductivity) samples, the Source Current Measure Voltage (SCMV) approach should instead be used.

resistor R_0 is necessary,[3] which, in combination with cable capacitance and other stray capacitance (see below), can lead to unacceptable penalties in frequency response and phase accuracy.

A much better amplitude and phase accuracy in the presence of stray capacitance can be achieved by using a current amplifier, as shown in Fig. 3-12(b). Assuming an ideal (infinite input impedance) linear OpAmp, the unknown resistance R_s is simply

$$R_s = -R_f \frac{V_s}{V_m}, \tag{3.9}$$

where R_f is the feedback resistor. For our measurements, we used the SR570 Low Noise Current Amplifier from Stanford Research (Sunnyvale, CA). A block diagram of the SR570 amplifier is reproduced in Fig. 3-13.

A few special consideration for high-resistance measurements [233] are outlined below:

Settling time. The settling time of the circuit is particularly important when making high-resistance measurements. To illustrate, suppose that a 10 GΩ resistive sample is connected to the measuring instrument with a coaxial cable. Considering that a typical coaxial cable has capacitance of ~100 pF/m, the circuit's settling time will be 10 GΩ × 100 pF/m = 1 s.

Instrument Loading. Whenever an ohmmeter is used for high resistance measurements, its input impedance must be considered. If an ohmmeter with input resistance R_I is connected to the resistance under test R_s, then the indicated (measured) resistance R_m is

$$R_m = R_s \left(\frac{R_I}{R_s + R_I} \right).$$

[3] In the instances when the configuration depicted in Fig. 3-12(a) was used (in particular, in all transport experiments conducted at MIT), the high precision film resistors from Caddock Electronics, Inc. (Roseburg, Oregon) were utilized. Available in denominations as high as 100 MΩ, these resistors are remarkably robust both with respect to temperature fluctuations and in their frequency response.

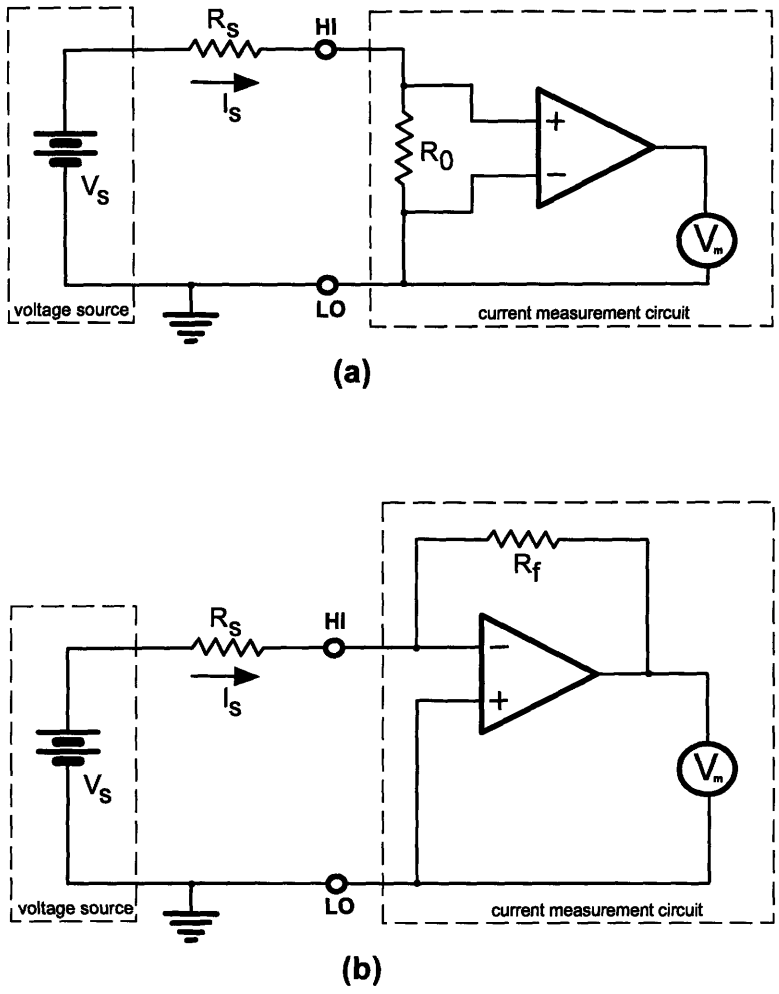


Figure 3-12: (a) A schematic of the current measurement circuit using a large terminating resistor R_0. The voltage drop over R_0 is amplified by a differential OpAmp of gain G, and measured using a voltmeter V_m. (b) A schematic of the current measurement circuit using a current amplifier. The current to voltage conversion gain is controlled by the feedback resistor R_f.

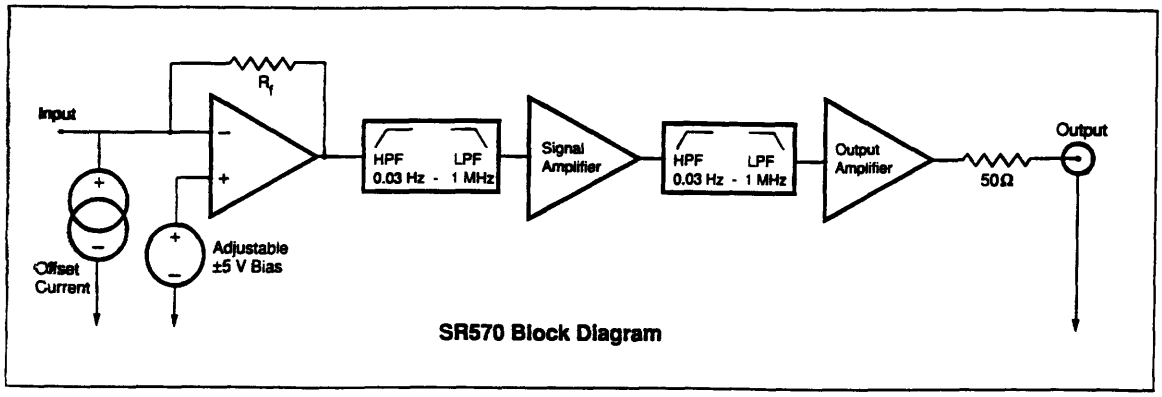


Figure 3-13: A block diagram of the SR570 Low Noise Current Amplifier. The input current can be offset to suppress any undesired background currents. The voltage at the "+" terminal of the amplifier is controlled by an adjustable ±5 V bias source (0 V at the "+" terminal makes the SR570's input a virtual null). The current to voltage conversion gain is controlled by the feedback resistor R_f. Sensitivities from 1 pA/V to 1 mA/V can be selected in a 1-2-5 sequence. As the sensitivity increases and R_f gets larger, any capacitance present will cause the bandwidth of the instrument to suffer. The SR570 provides a choice between a "high bandwidth" mode, where R_f is chosen as small as possible and the gain is made up later in the amplifier chain, and a "low noise" mode, where R_f is chosen as large as possible to optimize noise performance. The noise performance and frequency response of the instrument can be further adjusted using two identical first order RC filters that can be configured as lowpass, highpass, or bandpass, with the cutoff frequencies controlled from the front panel of the instrument.

Thus, if an ohmmeter with input resistance of 1 GΩ is used to measure a 100 MΩ sample, the resulting measurement will be off by 9%.

Guarding. Guarding high-resistance test connections can significantly reduce the effects of leakage resistance, increase measurement accuracy, and improve time response (bandwidth) of the instrument. Under this technique, the measurement cable shield is driven with a unity gain amplifier to maintain the same potential as the wire inside the shield. Since both the shield and the wire are then at the same potential, the leakage current is eliminated. Most modern instruments provide a guard terminal facilitating this technique.

Leakage Currents. In the SVMC configurations, such as the one pictured in Fig. 3-12(b), care should be taken to suppress any leakage currents present in the system. The *baseline suppression* feature of the SR570 amplifier (see Fig. 3-13) is available to offset the input current so as to suppress any undesired background currents.

Provided that the difficulties outlined above are addressed and a successful measurement has been performed, the output of the current amplifier (ranging from -5 V to +5 V for SR570) needs to be converted to the resistivity of the sample being measured. For samples in the parallel-plate configuration (Fig. 3-1), this is merely a matter of plugging in the electrode area A and separation distance d into the formula

$$\rho = R_s \frac{A}{d}, \tag{3.10}$$

where R_s is the sample resistance calculated using Eqn. (3.9). In practice, instead of the Eqn. (3.9), amplifier gain G_{amp} and output voltage V_{amp} are used to calculate R_s:

$$R_s = \frac{V_s}{G_{\text{amp}} V_{\text{amp}}}. \tag{3.11}$$

Note that the amplifier gain G_{amp} is expressed in *amperes per volt* (A/V).

The situation gets somewhat more complex when the Micron sensor (see Sec. 3.3) is utilized to measure the resistivity. The sensor's geometrical parameters listed in Table 3.1 should then be used to calculate the geometrical factor A/d of Eqn. (3.10). For films thicker than the sensor electrode thickness H_μ,

$$\frac{A}{d} = \frac{L_\mu H_\mu}{D_\mu}, \tag{3.12}$$

where L_μ and H_μ are, respectively, the meander length and the electrode spacing of the sensor. Given the parameters in Table 3.1, we calculate

$$\frac{A}{d} = 15\text{cm}.$$

Clearly for films thinner than H_μ, the film thickness d_{film} should be used in place of H_μ in Eqn. (3.12).

Note that, when the Micron sensor is used to measure the dielectric properties of materials, the geometrical parameter A/d can be used to calculate the dielectric constant ε' from the measured capacitance C_m:

$$\varepsilon' = \frac{C_m}{A/d}. \tag{3.13}$$

However, the simple-minded way of calculating A/d utilized in Eqn. (3.12) is no longer adequate, since it does not take into account the fringing fields imposed by the geometry of the sensor (see Figs. 3-6 and 3-10), which cannot be neglected in AC measurements. Micromet Instruments recommends using $A/d = 35$ cm, a value determined from experimental calibrations. In assessing the merits of this value relative to the approximation of Eqn (3.12), it is important to keep in mind that, in dielectric measurements, the fringe fields extend not only above the surface of the sensor into the bulk of the measured material, but also into the quartz substrate, whose dielectric constant $\varepsilon'_{\text{quartz}} = 3.75$ contributes additional polarization (which we

consider to be frequency-independent) that gets internalized in the A/d geometrical parameter.

Chapter 4

Dielectric Properties of Pristine and Modified C_{60} Films

4.1 Introduction

Since the discovery by Krätschmer *et al.* [7] of the method for bulk synthesis of fullerene C_{60} (see Section 1.2), the complex dielectric function $\varepsilon(\omega) = \varepsilon'(\omega) - j\varepsilon''(\omega)$ of solid C_{60} films has been studied over a broad frequency range using a wide variety of techniques [24, 25, 45, 61, 76, 234].

In this chapter, we present the results of our studies of the C_{60} dielectric function $\varepsilon(\omega)$ at the low end of the frequency spectrum (0.01 Hz–100 kHz). We shall start, however, by giving an overview of $\varepsilon(\omega)$ at optical frequencies (Sec. 4.2). Experimental difficulties in obtaining intrinsic properties of C_{60}-based solids are discussed in Sec. 4.3. In Sec. 4.4, we explain the motivation underlying the efforts to improve the dielectric properties of C_{60} films by intercalation of various foreign species into the interstitial spaces of the solid. The justification for molecular oxygen intercalation is given in Sec. 4.4.1, and the feasibility of using other gases (Cl_2, NO) as intercalants is discussed. Sec. 4.5 is devoted to techniques of fullerene thin film sample preparation and characterization. The results of the measurements of $\varepsilon(\omega)$ as a function of impu-

rity diffusion and as a function of temperature are presented in Sections 4.7 and 4.8, respectively.

4.2 Optical dielectric function of C_{60}

The optical dielectric function $\varepsilon(\omega)$ of C_{60} has been mapped out in the range of 10^{13}–10^{16} Hz (corresponding to 0.05–40 eV) using infrared, vis-UV, and electron energy loss spectroscopies. Figure 4-1 presents a summary of experimental data reported for the real $\varepsilon'(\omega)$ and imaginary $\varepsilon''(\omega)$ parts of the dielectric function at 300 K over the entire optical frequency range from the infrared through the ultraviolet.

In Fig. 4-1, the features in the optical dielectric function below ~0.3 eV are due to molecular vibrations (see Sec. 1.6), and can be associated with the four strong first-order F_{1u} intramolecular modes (at 526, 576, 1183, and 1428 cm^{-1}, as detailed in Table 1.3) and two strong combination ($\omega_1+\omega_2$) modes (at 1539 cm^{-1} and 2328 cm^{-1}) first observed by Krätschmer *et al.* [7] from measurements of the infrared absorption spectrum of a C_{60} film. Transmission experiments carried out on thicker (~2-3 μm) films reveal numerous (~100) additional features attributed to other intramolecular combination modes [108], which also enter into $\varepsilon(\omega)$. The IR peaks in Fig. 4-1 have been successfully fit [235] to the standard Drude-Lorentz model [236], in which the complex dielectric function $\varepsilon(\omega)$ is given by the sum of contributions from a background core real constant ε_∞, a Drude (or free carrier) term $\varepsilon_{\text{Drude}}(\omega)$ and a phonon term $\varepsilon_{\text{phonon}}(\omega)$ [235].

$$\varepsilon(\omega) = \varepsilon'(\omega) - j\varepsilon''(\omega) = \varepsilon_\infty + \varepsilon_{\text{Drude}}(\omega) + \varepsilon_{\text{phonon}}(\omega) \tag{4.1}$$

where

$$\varepsilon_{\text{Drude}}(\omega) = \frac{-\omega_p^2}{\omega(\omega - j/\tau)} \tag{4.2}$$

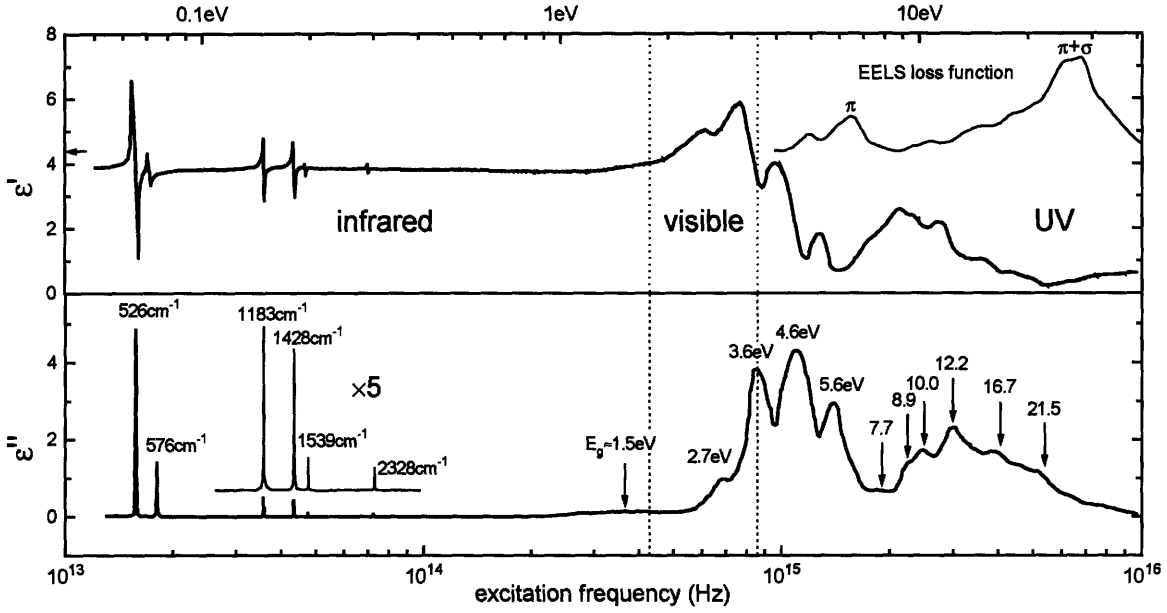


Figure 4-1: Summary of real $\varepsilon'(\omega)$ and imaginary $\varepsilon''(\omega)$ parts of the dielectric function for C_{60} vacuum-sublimed solid films at room temperature over all optical frequencies. The data between 0.05 and 0.5 eV (mid- to near-infrared) were collected using the Fourier transform infrared (FTIR) transmission technique [45]. The vis-UV range was investigated by variable angle spectroscopic ellipsometry (VASE) [25] and near-normal-incidence reflection and transmission experiments [61]. UV data above ~7 eV were obtained using electron energy loss spectroscopy (EELS) [234] by Kramers-Kronig analysis of the EELS loss function (inset). The arrow at the left axis points to $\varepsilon' = 4.4$, the observed low frequency value of the dielectric constant [24].

and

$$\varepsilon_{\text{phonon}}(\omega) = \sum_{i=1}^{n} \frac{f_i \omega_i^2}{\omega_i^2 - \omega^2 + j\Gamma_i \omega}. \tag{4.3}$$

In the Drude term, ω_p is the free carrier plasma frequency and τ is the free carrier scattering time. For the i^{th} phonon contribution, f_i, ω_i and Γ_i are the oscillator strength, frequency and damping, respectively, for each IR mode (see Ref. [235] for a listing of oscillator parameters).

As the absorption edge of C_{60} solid has been determined to be $\sim$1.5 eV [85], the structure in $\varepsilon(\omega)$ in the visible-UV range below $\sim$7 eV (see Fig. 4-1) is primarily of electronic origin, and may be assigned to electronic transitions between carbon π (bonding) and π^* (antibonding) electron states (Sec. 1.4). The data in this range were obtained by Ren *et al.* [25] for films vacuum deposited on Si(100) using variable angle spectroscopic ellipsometry (VASE), and by Wang *et al.* [61] on films deposited on quartz (Suprasil) from near-normal-incidence reflection and transmission experiments. The four broad peaks in this range (at 2.7, 3.6, 4.6, and 5.6 eV [25, 61]) are identified with dipole-allowed electronic transitions, and can also be described by a sum of Lorentz oscillators (see Ren *et al.* [25], Wang *et al.* [61], and Kelly *et al.* [237] for a table of oscillator parameters). In this case, each oscillator function corresponds to a transition between narrow electronic energy bands derived from C_{60} molecular orbitals. The core dielectric constant ε_∞, used to approximate interband absorption well beyond the range of the data [61], has been found to equal $\varepsilon_\infty \approx 2.4$ [25, 61]. The success of the Lorentz oscillator fits at both infrared and vis-UV frequencies corroborates the strong molecular character of the C_{60} solid (Sec. 1.3.2).

To obtain the dielectric function $\varepsilon(\omega)$ in the UV range above $\sim$7 eV not easily accessible by optical techniques, the electron energy loss spectroscopy (EELS) has been successfully employed [234, 238]. In the inset to Fig. 4-1, the two dominant peaks in the frequency dependence of the EELS loss function $\mathcal{I}m\{-1/\varepsilon(\omega)\}$ for small momentum transfer ($q = 0.1$ Å^{-1}) occur at $\sim$6 eV for the π-plasmon and an even more prominent peak at $\sim$26 eV is observed for the $\pi + \sigma$-plasmon. The shoulders

between ~8 and ~25 eV have been attributed to transitions between bonding σ and antibonding σ^* levels, and partially also to mixed $\pi - \sigma^*$ or $\sigma - \pi^*$ transitions [234]. Through the Kramers-Kronig analysis (see Sec. 2.3.2), these, as well as other less pronounced details of the EELS loss spectrum, enter into the complex dielectric function $\varepsilon(\omega)$ as features between 7 eV and 40 eV. It should be noted that the peak positions in $\varepsilon''(\omega)$ (at 7.7, 8.9, 10.0, and 12.2 eV) obtained by analyzing the EELS data are in agreement with the optical UV results reported by Kelly *et al.* [237] using a synchrotron radiation ellipsometer. The higher energy feature at 21.5 eV may be associated with the *giant optical absorption* that was detected around 21 eV in the gas phase of both C_{60} and C_{70}, via photoionization spectroscopy using synchrotron radiation [239]. Not shown on Fig. 4-1 are the results of XPS and UPS experiments at much higher frequencies (~300 eV) probing the core electrons of C_{60} solid and thus contributing to the core dielectric constant ε_∞.

From Fig. 4-1, it is clear that, as we move towards lower and lower frequencies, for every loss process represented by a peak in the $\varepsilon''(\omega)$, there is a rise (sometimes accompanied by a small oscillation) in $\varepsilon'(\omega)$, as prescribed by the Kramers-Kronig relations. As we move below 10^{13} Hz, all electrons and most phonons have already responded, and $\varepsilon'(\omega)$ is approaching its DC value. The small difference between $\varepsilon'(10^{13}\,\text{Hz}) \approx 3.9$ [61] and $\varepsilon'(10^{5}\,\text{Hz}) \approx 4.4$ [24] (shown by an arrow in Fig. 4-1) is probably due to the losses associated with C_{60} molecules rapidly rotating at room temperature ($T > T_{01}$) at ~10^9 Hz, as evidenced by NMR [73], ultrasound attenuation [52], and other experiments sensitive to phenomena in this frequency range (see Sec. 1.3.2).

From the Kramers-Kronig relations, it follows [see Eqn. (2.38)], for the case of zero frequency:

$$\varepsilon'(0) - 1 = \frac{2}{\pi}\int_0^\infty \frac{\varepsilon''(\omega)}{\omega}\,d\omega = \frac{2}{\pi}\int_0^\infty \varepsilon''(\omega)\,d(\ln\omega). \tag{4.4}$$

This tells us that the DC dielectric constant $\varepsilon'(0)$ includes *all* contributions from the higher frequency loss processes, and is proportional to the area under the $\varepsilon''(\omega)$ curve plotted on a logarithmic scale [177]. The rest of this chapter reports the measurements of the dielectric function $\varepsilon(\omega)$ of C_{60} thin films for frequencies *below* 10^5 Hz, where new, previously unreported, polarization mechanisms come into play.

4.3 Experimental difficulties in obtaining intrinsic electrical characteristics of C_{60} solids

One of the fascinating peculiarities of solid fullerene materials is the fact that their properties can be greatly affected by a host of external factors — from ambient gases to ambient light. These effects are important for both optical and electrical measurements. In particular, the results of electrical measurements (*e.g.*, transport, dielectric properties, photoconductivity) can be affected by many orders of magnitude.

The realization of the importance of external factors when measuring electrical and optical properties of fullerites has not always been appreciated by the fullerene research community, which led to the appearance of dozens of erroneous reports in the literature on electrical and other properties (particularly, photoconductivity) of C_{60} and other fullerites. After three years of experimental research into the properties of solid C_{60}, we have identified the following four major effects peculiar to fullerene solids that tend to skew the results of electrical and optical measurements:

Large Interstitial Volume: A large amount of interstitial volume (26% for close-packed spheres) leads to rapid uptake of molecular oxygen and other impurities from the ambient environment. Such impurities quench carrier transport and photoconductivity in solid C_{60}, greatly affecting the measurements of these properties. Due to the possibility of charge transfer from an impurity to a C_{60} ball, large dipole moments are created that affect the dielectric measurements.

In addition, the mobile impurities complicate many electrical measurements by lowering the breakdown voltage of the C_{60} films, so that these measurements need to be performed at low voltage levels, which results in decreasing the signal-to-noise ratio.

Phototransformation: As was described in Sec. 1.3.2 (page 37), C_{60} films photopolymerize easily when irradiated with vis-UV light. Any experiments involving high-intensity light (*e.g.*, photoconductivity, pump-probe reflectivity or transmission [240], etc.) should, therefore, be performed with caution, so as to avoid polymerization of the film. In addition, UV light facilitates adsorption of oxygen into the bulk of the film (see Sec. 4.4.1), leading to the undesirable consequences outlined above.

Long-lived excited states: It has been shown by Hamed *et al.* [241] that C_{60} films exhibit *persistent photoconductivity,* the effect which consists of a metastable increase in dark conductivity caused by brief exposure to light. This points to the existence of long-lived (with time constants on the order of days) excited states in solid C_{60} (attributed to the distortions that the C_{60} molecules experience in the presence of localized charge [241]). Occupation of these excited states increases the effective conductivity of C_{60} films by many orders of magnitude.

Crystallinity: The properties of C_{60} films change substantially depending on their degree of crystallinity. Single-crystal films would come closest to the intrinsic bulk properties of crystalline C_{60}. However, the difficulties in manufacturing such films (MBE or Langmuir-Blodgett techniques are necessary to obtain films of high crystallinity), prompted us to turn to vacuum-deposited polycrystalline films (see Sec. 4.5 and the HRTEM photo in Fig. 1-14) for our investigations. The degree of crystallinity can be monitored using X-ray diffraction (see Fig. 4-11). It should be noted that the crystallite size distribution of the polycrystalline films is strongly affected by the nature of the substrate [112], and under certain

conditions, the films can even be made completely amorphous.[1]

From the preceding discussion, it might appear that it is virtually impossible to obtain the properties of pristine C_{60} by investigating a C_{60} film. Indeed, any C_{60} experiment calls for a C_{60} film to be made and kept in vacuum (to avoid impurities "polluting" the fullerite's large interstitial regions), in complete darkness (to avoid phototransformations), for days prior to the start of and during the experiment (to allow the long-lived excited states to die out). The experiment itself needs, of course, to be performed in vacuum to protect the films from contamination with ambient impurities.

The practical reality rules out the possibility of such a complicated experimental setup. While we tried to keep exposure to the ambient light and atmosphere to a minimum, it was practically impossible to completely eliminate either of the two. Instead, we directed our efforts toward developing methods to continually monitor the status of the film (impurity concentration, degree of polymerization, etc.) and then use this information to deduce the behavior of the pristine film. Microdielectrometry (described in Chapter 3) is one method particularly suitable for this task.

4.4 Film modification: Motivation and justification

While C_{60} may be a desirable material for use in electronic devices (*e.g.*, as a gate dielectric — see Sec. 1.7), its dielectric properties are easily compromised by the presence of large interstitial spaces which can be easily filled with mobile polar impurities, as described in Sec. 4.3 above. The need to prevent the diffusion of such impurities

[1] Crystallinity of the vacuum-grown films is also strongly affected by the temperature of the substrate during deposition. In a systematic investigation of this substrate temperature effect, Rusakova *et al.* [242, 243] found that a relatively small change in substrate temperature from 40°C to 200°C can increase the grain size by an order of magnitude from 25 nm to 250 nm.

into the bulk of a C_{60} solid prompted us to attempt to engineer a C_{60}-based material in which most of the interstitial spaces are closed (filled), and thus are inaccessible to external impurities.

We devised and tested two different ways for filling the interstitials of a C_{60} film.

In one approach, an external "filler" or "glue" molecular species is forced into the interstitials of a C_{60} solid. Oxygen (O_2) is one molecular agent that is known to diffuse into C_{60} films either under pressure [244, 245] or with the assistance of UV irradiation [116, 117, 246, 247], as described in Sec. 4.4.1 below. Some species, when forced into a C_{60} solid's interstitials, will react with surrounding C_{60} balls, forming compounds extending through (and thereby "sealing off") the interstitial spaces of a fullerite. Direct reactive oxygenation (*e.g.*, using ozone) is one method belonging to this class of techniques. Other related methods include chlorination [248], bromination [248], and fluorination [92]. Another molecule that shows much promise as a molecular "glue" yielding a range of electrically remarkable C_{60}-based materials is NO (nitric oxide) [139]. Its small size (1.1508 Å) allows it to easily diffuse into the bulk of the fullerite, and its substantial dipole moment (0.16 Debye) enhances the dielectric constant of the resulting compound considerably. The results obtained by intercalation of these species into C_{60} films are presented in Sec. 4.10.

A completely different method of "sealing off" the interstitials of a fullerene solid is to use C_{60}'s propensity to crosslink and polymerize when exposed to intensive UV-vis irradiation [45], thereby reducing (or, perhaps, even eliminating) the interstitials into which impurities may diffuse. We measured the dielectric properties of UV-polymerized C_{60} films, as well as those grown (deposited) in the presence of UV radiation, and compared them to the results obtained with pristine C_{60} films (see Sec. 4.10).

4.4.1 NMR and ESR evidence for oxygen diffusion

Since oxygen has proved to be one of the most important intercalants affecting the electrical properties of C_{60} films, it is worthwhile to discuss the evidence for oxygen intercalation into the bulk of C_{60} solid in more detail.

It was mentioned in Sec. 1.5 that oxygen can be an exohedral intercalant of C_{60} solids (see Fig. 4-2). Unlike the alkali-metal intercalants, which can transfer a large amount of charge (the outer shell electron for each alkali-metal atom) to the C_{60} balls, virtually no such charge transfer can be assumed for the case of oxygen intercalation. However, some charge transfer does indeed occur, giving rise to the enhanced polarization effects described in Sec. 4.7. It will be shown in Sec. 4.7 that the amount of charge transferred by oxygen molecules is between 20 and 100 times less than that transferred by alkali-metal atoms.

A variety of experiments provide evidence for oxygen diffusion in fullerites. Assink *et al.* [244] have used ^{13}C NMR spectroscopy to show that molecular oxygen diffuses readily into the octahedral interstitial sites of the fcc lattice of C_{60}. As shown in Fig. 4-3, exposure of C_{60} to 1 kbar oxygen for 1.75 hours at room temperature resulted in a spectrum of seven evenly spaced resonances corresponding to the filling of 0 to 6 of the adjacent octahedral interstitial sites with oxygen molecules. Oxygen pressure was found to substantially accelerate the rate of oxygen diffusion [Fig. 4-3(b)], but it was also observed that, even at ambient conditions, oxygen eventually fills much of the octahedral sites of a fullerite. The exact proportion of the sites filled depends very substantially on the crystallinity of the sample, as discussed in Sec. 4.3. Crystalline powders with micron-sized crystallites, such as those used by Assink *et al.* [244], tend to have considerably lower diffusion rates than the vacuum-deposited polycrystalline films composed of much finer crystallites that were used in our study (see Sec. 4.5 for the details of sample preparation and characterization).

While forcing oxygen into the interstitials of a fullerite under pressure is an obvious method of speeding up the diffusion, its practical significance is quite limited. UV-

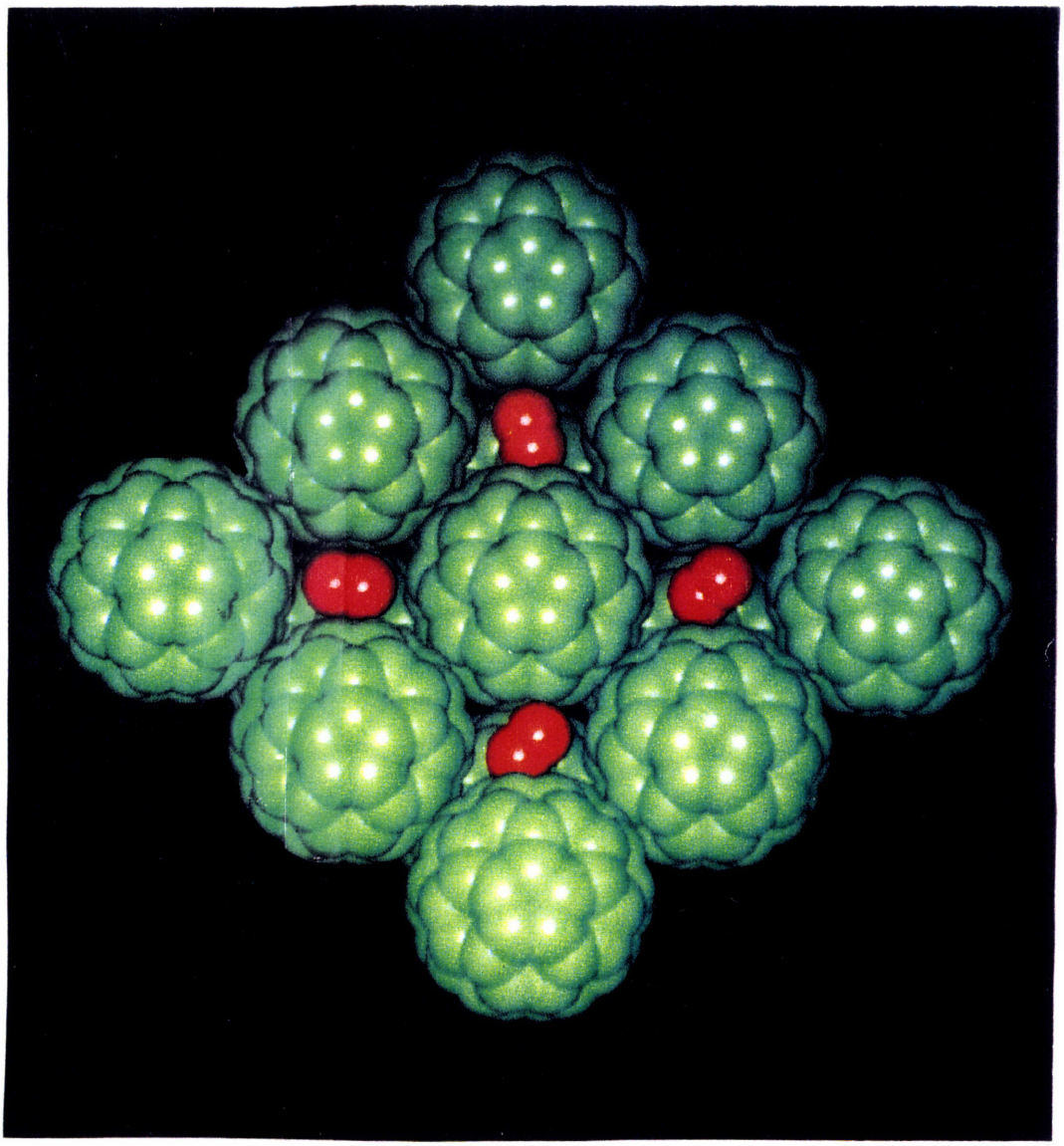


Figure 4-2: C_{60} molecules (green) arranged in a face-centered cubic lattice. Oxygen molecules (O_2, red) occupy octahedral interstitial sites of the C_{60} solid. The carbon atoms (green) and oxygen atoms (red) are represented by spheres of radii corresponding to the van der Waals radii of carbon and oxygen, respectively. This figure was created on a Silicon Graphics Indy^{TM} workstation running *Cerius*^{2} software by Molecular Simulations, Inc.

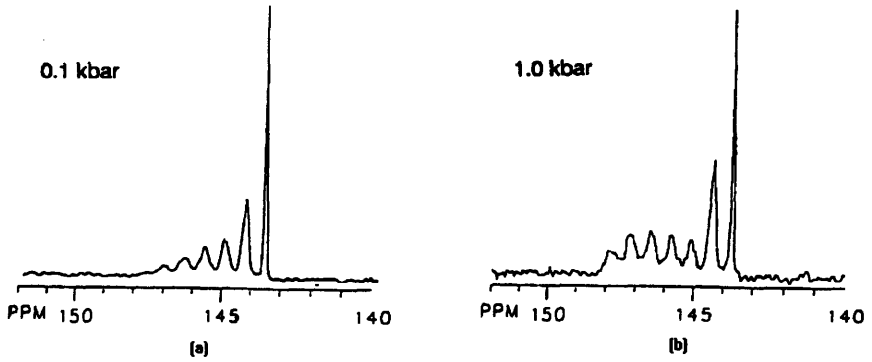


Figure 4-3: NMR evidence for pressure-assisted oxygen diffusion into C_{60} films. The largest peak in both (a) and (b) corresponds to the primary resonance at 143.7 ppm corresponding to an fcc C_{60} solid at $T > T_{01}$. The other six peaks correspond to the C_{60} molecules in the lattice surrounded by 1, 2, 3, 4, 5, and 6 oxygen molecules, respectively. Spectra (a) and (b) were taken for samples exposed for 1.75 hours to 0.1 and 1.0 kbar oxygen, respectively [244].

assisted oxygen diffusion [117, 247] provides a more expedient means of forcing the oxygen into the bulk of C_{60} solid. (Indeed, this method has been used in a C_{60}-based negative-photoresist photolithography process, as described in Sec. 1.7.6.) Eloi *et al.* [117] verified the increase in the diffusion rate of O_2 into the fcc C_{60} lattice by direct measurement of the oxygen uptake via resonant alpha particle scattering experiments, as shown in Fig. 4-4. The broadening of the resonance scattering peak in Fig. 4-4(b) indicates that a thin (20 nm) oxygen layer with a composition of $C_{60}O_{0.6}$ (corresponding to about one oxygen molecule per two C_{60} balls) was formed on the surface of the C_{60} film upon UV irradiation in 1 atm of O_2. Eloi *et al.* [117] showed that, depending on the intensity of the UV irradiation, the stoichiometry of the surface layer of a C_{60} film can reach oxygen concentrations as high as $C_{60}O_{4.8}$. Since there is only one octahedral site ($R_{\text{octahedral}} = 2.07$ Å; see Table 1.2) per C_{60} molecule in the fcc lattice (see Fig. 4-2), *physisorption* of molecular oxygen in the lattice would result in a maximum oxygen stoichiometry $C_{60}O_2$. Furthermore, the possibility of molecular oxygen occupying the tetrahedral sites ($R_{\text{tetrahedral}} = 1.12$ Å; see Table 1.2)

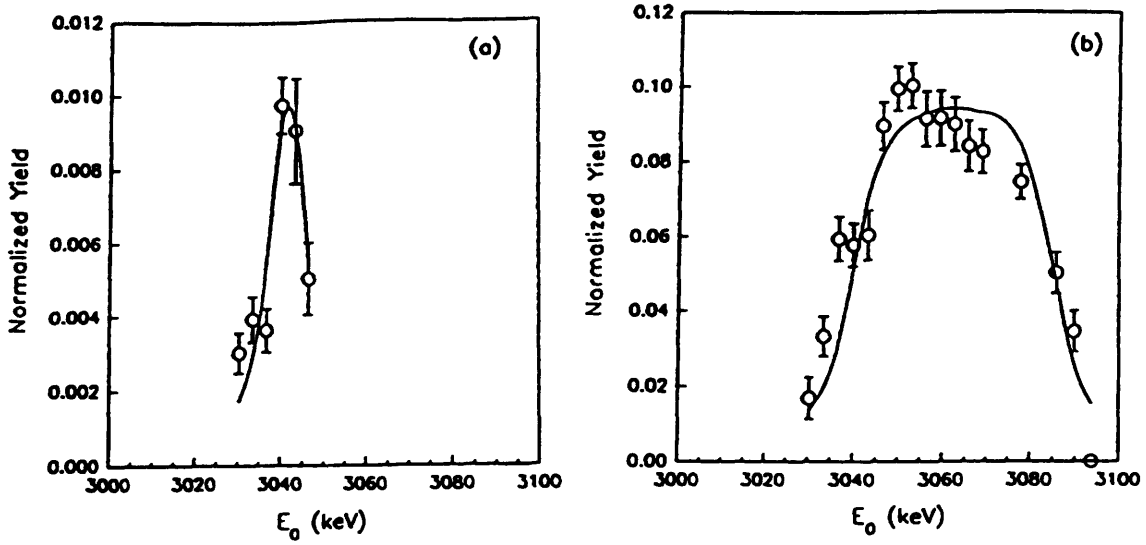


Figure 4-4: Resonant alpha particle backscattering evidence for UV-assisted oxygen diffusion into C_{60} films. Oxygen excitation yields obtained from a resonance scan of a 1400 Å thick C_{60} film exposed to 1 atm O_2 for 1 hr in the absence of light (a), and from a 2400Å thick film which was simultaneously exposed to 1 atm O_2 and light from a Xe lamp for 1 hr (b) [117].

is eliminated by considering that the van der Waals radius of an oxygen molecule is 1.4 Å, too large to fit into a tetrahedral site. Stoichiometries higher than those expected from simple physisorption (*e.g.*, pressure-induced diffusion, as described above) can be attributed to a subsequent chemical reaction between the C_{60} and oxygen under continued irradiation.

Electron Spin Resonance (ESR) spectroscopy is another method for assessing the oxygen content of C_{60} films. Neutral fullerenes (C_{60}) in their ground state are in a singlet state. Compensated spins are also expected in CO, CO_2, $C_{60}O$, $C_{60}O_2$, $C_{60}O_4$. In principle, this inhibits the use of ESR. Nonetheless, it was noted that the "as-grown" fullerenes are weakly ESR-active [249, 250], and also that unpairing of the electron spins occurs in C_{60}:O_2 solid mixtures under UV irradiation [251]. This makes ESR a good method for studying the oxygen content of UV-irradiated films. Figure 4-5 follows the evolution of the unpaired spin concentration in a typical 914 Å-thick C_{60} film used in our dielectric studies. As seen in Fig. 4-5, the spin concentration increases rapidly under UV-exposure in 1 atm of oxygen, reaching near-saturation levels within about 3 hours. Subsequent exposure in vacuum partially reverses this effect, expelling about a third of adsorbed oxygen within an hour. Annealing the film in vacuum at 175°C reverses the effect completely. (The effect of annealing on the transport properties of C_{60} films is discussed in Sec. 4.4.2.)

It is important to emphasize that, while oxygen does indeed diffuse into the bulk of fullerites, profoundly affecting their electrical and optical properties, many other molecular intercalants that have been investigated do not. In particular, it has recently been reported [252] that considerably more O_2 is intercalated into the C_{60} lattice than in the case of N_2 under identical experimental conditions, despite the fact that the sizes of the two molecules are quite similar. This real difference in the behavior of O_2 from that of N_2 has significant technological implications, as it could lead to techniques for separating these two gases — a goal of considerable practical

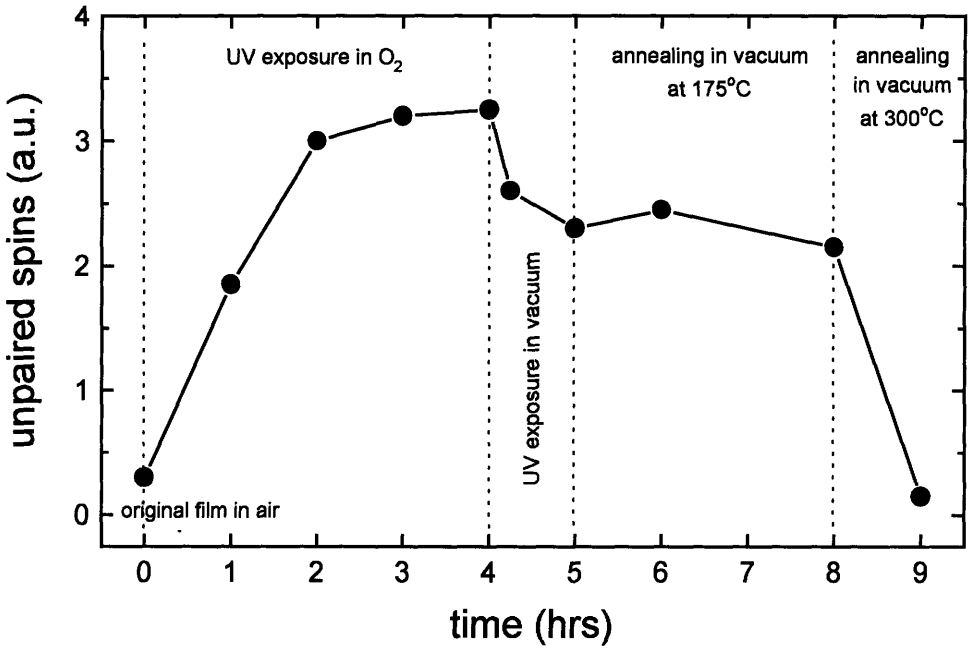


Figure 4-5: ESR evidence for UV-assisted oxygen diffusion into a 914 Å C_{60} film. (Data courtesy Dr. S. Glarum of AT&T Bell Labs.)

importance.[2]

4.4.2 Transport Evidence of Oxygen Diffusion

Given the exponential dependence of conductivity on the position of the Fermi level in a semiconductor, conductivity measurements can provide an extremely sensitive way of monitoring the density of electronic states in the gap or near the band edges of crystalline C_{60} caused by oxygen, light, or other agents. In particular, as mentioned in Sec. 4.3, oxygen decreases the intrinsic conductivity of fullerites by as much as four orders of magnitude. The magnitude of this effect, together with C_{60} solid's

[2]While not quite as technologically important — and indeed not quite as unexpected, — we have also found that Xe, a heavy noble gas with a van der Waals radius comparable to that of C_{60} lattice interstitials, can be made to diffuse into a C_{60} crystalline powder, as evidenced by the weight uptake. By subjecting C_{60} powder to a Xe environment at $T = 200°C$ and $p = 850$ psi for 2 days, the composition of $C_{60}Xe_{0.203}$ was achieved. However, Xe atoms were found to promptly pop out of the C_{60} interstitials once the pressure is removed.

σ at 300 °C (S/cm)	E_a (eV)	Ref.
$\sim 10^{-6}$	0.26	[253]
1.7×10^{-7}	0.58	[60]
4×10^{-7}	0.36	[254]
$\sim 10^{-4}$	0.26	[255]
$\sim 10^{-8}$	0.43	[256]
$\sim 10^{-14}$	1.1 ($\downarrow$)	[257]
8.3×10^{-7}	0.54 ($\uparrow\downarrow$)	[258]
$\sim 10^{-11}$	1.0 ($\uparrow$), 0.5 ($\downarrow$)	[121]
2×10^{-8}	0.51	[122]
5.4×10^{-10}	$\sim$1 ($\uparrow\downarrow$)	[259]
$\sim 10^{-14}$	0.82	[260]
3×10^{-10}	0.51	[261]

Table 4.1: Intrinsic conductivity σ and activation energy E_a reported for C_{60} single crystals and highly crystalline films (top portion), and for polycrystalline and amorphous films (bottom portion). E_a is the activation energy for temperatures above the structural transition $T_{01} > 260$°C, measured on heating ($\uparrow$) and/or on cooling ($\downarrow$), when specified by the data source.

propensity for adsorbing oxygen from the surrounding atmosphere, is responsible for the wide dispersion of values for the conductivity of C_{60} reported in the literature.

Table 4.1 summarizes the results for experimental values of C_{60} conductivity reported in 12 papers on the subject. These papers were chosen so as to exclude those whose authors displayed lack of awareness about the profound effect of oxygen on the electronic properties of solid C_{60}. All of the values in the Table 4.1 are purported to display the *intrinsic* conductivity of C_{60} films and crystals. Still, a quick glance at Table 4.1 confirms that the reported results for σ vary by as much as ten orders of magnitude.

To characterize the conductivity (and, by inference, the oxygen content) of our C_{60} films, we have performed transport measurements using the Micron sensor and the measurement technique described in Sec. 3.3 and 3.4, respectively. Typically, a 2000 Å-thick C_{60} film was deposited on the sensor as described in Sec. 4.5, and its conductivity was measured for temperatures ranging from 25 °C to 250 °C, as

shown in Fig. 4-6(a). The average temperature scanning rate was ~1 °C for every five minutes. The arrows in Fig. 4-6 indicate the direction of the temperature sweep. The current amplifier setup described in Sec. 3.4 allowed us to monitor the change in conductivity over seven decades. The measurement was performed at $V = 1$ V, and the conductivity σ was calculated using Equations (3.10) and (3.12).

We notice right away that annealing increases the conductivity of C_{60} film, probably both by improving the crystallinity of the film and by driving the oxygen out of the interstitial regions.

Typically, the conductivity is activated in accordance with the Arrhenius equation of the form

$$\sigma = \sigma_0 \exp\left(-\frac{E_a}{kT}\right), \tag{4.5}$$

where σ_0 is the conductivity prefactor, k is the Boltzmann constant, T is the absolute temperature, and E_a, the activation energy, is a measure of the energy distance between the Fermi level and the band edge in the semiconductor. In the case of a crystalline solid, the conductivity is determined by thermal excitation of charge carriers over the energy gap, and the activation energy should be approximately half of the value of the band gap. Figure 4-6(b) displays an Arrhenius plot of the conductivity.

The kink in the curve at $T \approx 120$ °C during the temperature up-sweep probably corresponds to the onset of oxygen effusion. Region 1 of the curve thus corresponds to the oxygen-filled C_{60}, which has a conductivity exhibiting an activation energy of $E_a = 0.44$ eV. Above $T \approx 120$°C (region 2 of the curve), oxygen is expelled out of the C_{60} solid. This process is also activated in temperature, and it affects the conductivity of the film, thus the activation energy of the effusion adds to the activation energy of oxygenated C_{60}, yielding a relatively high (in the view of the C_{60}'s HOMO-LUMO gap of ~1.6 eV) value $E_a = 1.90$ eV.[3]

[3]Since oxygen molecules leaving C_{60} film no longer participate in the C_{60} transport mechanisms (*e.g.*, as carrier traps), the number $E_a = 1.90$ eV for the combined activation energy of transport

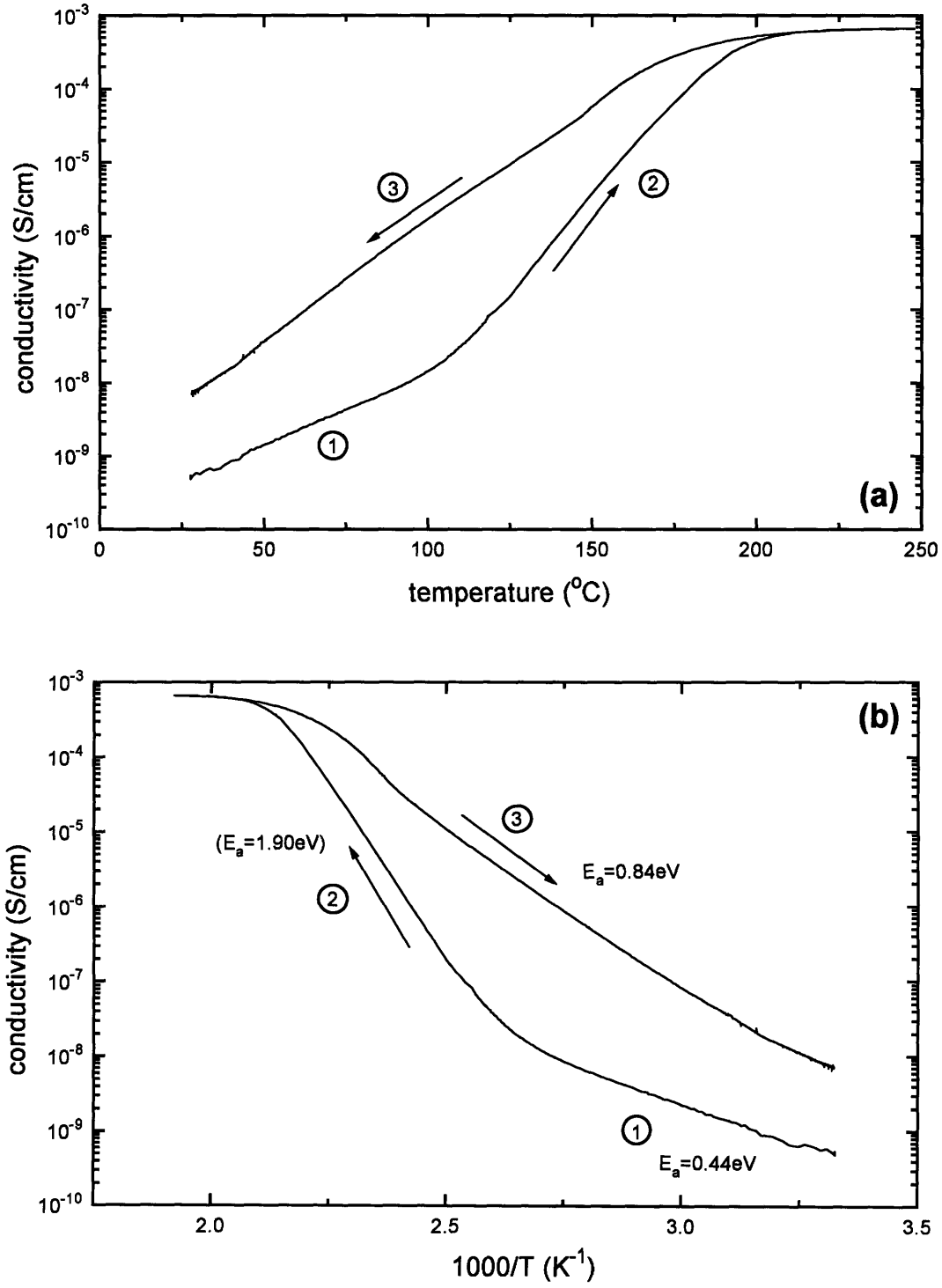


Figure 4-6: Transport measurements of C_{60} film. The measured Conductivity of C_{60} is plotted versus temperature (a) and vs 1000/T on an Arrhenius plot (b). Arrows indicate the direction of temperature scan.

The curves in Fig. 4-6 level off at ~220°C, as C_{60} molecules start to sublimate from the substrate (a first-order phase transition). Although the accepted value for the sublimation temperature of C_{60} is ~350°C [63] (see Table 1.2), it has been our experience that the onset of sublimation occurs at temperatures as low as 200°C. Region 3 of the curves in Fig. 4-6 following the annealing, where the conductivity is activated with $E_a = 0.84$ eV, corresponds to de-oxygenated C_{60} rapidly adsorbing oxygen. Since this is a transient process, no reliable determination of the intrinsic activation energy of C_{60} can be made from these data.

Note that those conductivity studies listed in Table 4.1 reporting conductivities lower than the average also report activation energies higher than the average. It is fairly certain that the amount of adsorbed oxygen played a large role in those studies, rendering their conclusions highly questionable. While not providing the final word on the role of oxygen in the electronic transport, our study yields results consistent with the accepted conductivity value of 1.7×10^{-7} S/cm [60] (see Table 1.2), supports the observations of reversibility of oxygen diffusion with annealing [244, 255], and provides an explanation for the erroneous values for the conductivity and the corresponding activation energy reported in the literature (see Table 4.1).[4]

It has been speculated [255] that oxygen affects the transport properties of the C_{60} films in at least two distinct ways. In the first few minutes of exposure, oxygen diffuses through the inter-grain boundaries, rapidly quenching electronic transport, and decreasing the intrinsic conductivity of C_{60} by one or two orders of magnitude. Then, in a slow process that can run for hours or even days, oxygen diffuses into the interstitial spaces of the fullerite crystallites, lowering the conductivity of the material by about two more orders of magnitude. While this theory appears plausible and consistent with our study, more experiments are needed to ascertain the effect of

and effusion has no straightforward interpretation.

[4]After the present work had been completed, an excellent paper by Asakawa *et al.* [262] came to our attention, in which our conclusions regarding oxygen effects on conductivity and activation energy have been confirmed in a careful *in-situ* experiment.

oxygen on electronic transport in the fullerite. Additional evidence supporting and extending this theory is provided by our studies of low frequency dielectric properties of fullerene thin films reported in Sec. 4.7.

4.5 Sample preparation and characterization

All samples used in this study were prepared at AT&T Bell Laboratories at Murray Hill, NJ, in the lab of Dr. Arthur Hebard. In this section we review the general techniques and considerations related to preparing and characterizing thin film fullerite samples.

Generally, when planning a thin-film experiment extending to cryogenic temperatures, particular attention should be paid to choosing the substrates.[5] Ideally, the substrate used for measuring the electrical properties of a material versus temperature should possess the following properties:

1. High electrical resistivity, to prevent parasitic currents and capacitances arising between the sample and the substrate from skewing the measurements.

2. High thermal conductivity, to afford good cryogenic control, particularly in situations when external incident radiation is present (such as in *in situ* optical measurements of C_{60} — photoconductivity, pump-probe experiments, and polymerization experiments).

3. The thermal expansion coefficient matched with that of the film being measured, to avoid cracking and tearing apart the film.

For our C_{60} experiments, we have used quartz, fused quartz, and glass (pyrex) substrates, all of which are excellent insulators. From Fig. 4-7, it is evident that, when

[5]This discussion is limited to choosing substrates suitable for electrical measurements. A different set of criteria for choosing a substrate should be applied in preparing a spectroscopy experiment. In this context, the ideal substrate (for a transmission experiment) is one that is transparent to the incident radiation. For example, KBr or Si substrates are usually used in infrared spectroscopy; quartz substrates — in UV-vis spectroscopy, and sapphire substrates — in X-ray diffraction experiments.

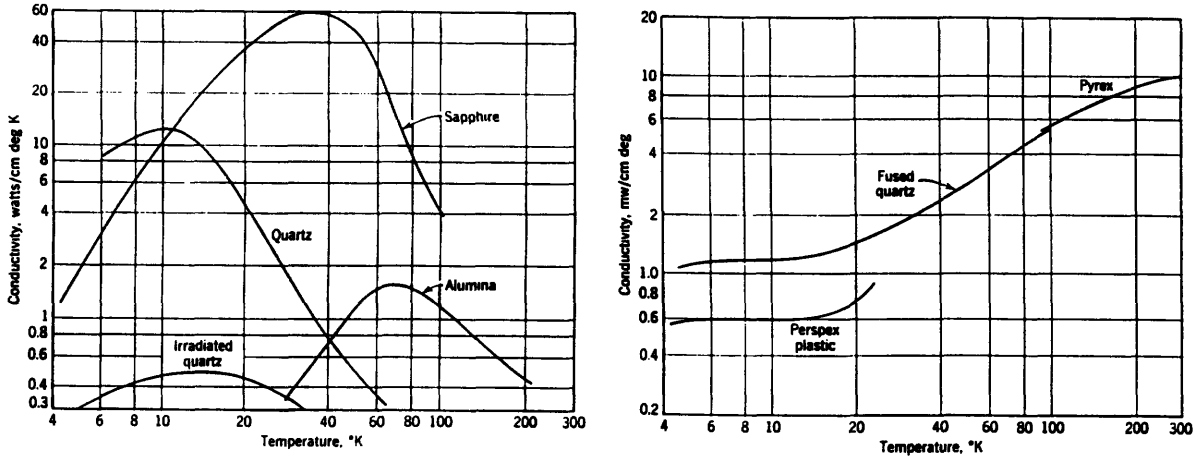


Figure 4-7: (a) Thermal conductivity of a number of electrically insulating solids as a function of temperature, plotted on a log-log scale. The log-temperature scale is used to emphasize the practically important behavior of the thermal conductivity at cryogenic temperatures. (b) Thermal conductivity for glass (pyrex), fused quartz, and Perspex plastic, plotted on a log-log scale. Note the change in scale of the ordinate.

high thermal conductivity is important (*e.g.*, in optical experiments), a quartz substrate is much preferable, as its thermal conductivity can be up to four orders of magnitude higher that that of pyrex or fused quartz (at $\sim$10 K).[6]

As described in Sec. 3.3, the integrated and 1-micron interdigitated sensors, which were used for some of the dielectric and transport experiments described below, are patterned on silicon and quartz, respectively. From Table 3.1, their operating temperature ranges are -100–250°C and -150–200°C, respectively, with the 1-micron sensor capable of sustaining temperatures as low as 10 K.

For thin-film deposition, 10–15 mg of 99.9% purified C_{60} (most batches were supplied by Dr. Robert Haddon of AT&T Bell Laboratories, with the rest coming from

[6]The substrate thermal conductivity considerations are even more important in optical measurements of superconducting samples, such as the alkali-metal-doped M_3C_{60} (M=K,Rb,Cs) films that turn superconducting with critical transition temperatures T_c ranging from 18 K to 40 K (see Sec. 1.5). A pump-probe measurement on such films is currently being performed by us at MIT [240, 263], with films prepared at Bell Labs on sapphire substrates. As is clear from the Fig. 4-7(a), sapphire is the best available insulating material (as far as thermal conductivity is concerned) in the temperature range of 10–100 K.

Hoechst AG, a commercial supplier) were loaded into alumina crucibles. The rotating substrate (either at ambient or at elevated temperature, up to ~200°C), was located approximately 10 cm from the crucibles, and a quartz-crystal microbalance was used to monitor the rate of deposition and final film thickness (see Fig. 4-8). A 200°C soak cycle with shutter closed over the substrate prevented high vapor pressure solvent residues from reaching the substrate. Using a diffusion pump connected to the deposition chamber, a base pressure of 1.5×10^{-6} torr was maintained during the deposition. Deposition rates in the range of 5–30 Å/min were typical for source temperatures of ~350°C. After the deposition, the thickness of the films was determined by ellipsometry (or by profilometry, for thicker films), and was generally found to be in good agreement with the readings of the thickness monitor (see Fig. 4-9).

Confirmation that the deposited films comprise C_{60} molecules has been obtained from the infrared transmission and UV-vis absorbance spectra shown in Figs. 4-10(a) and 4-10(b), respectively. X-ray powder diffraction (Fig. 4-11) was used to ascertain the fcc structure of the C_{60} crystallites comprising the film. Small crystallites on the order of 100 Å in diameter were typical. High resolution transmission electron microscopy (HRTEM) was utilized to further visualize the morphology of the film (see Fig. 1-14).

Raman spectroscopy was also employed for film characterization, with results similar to those presented in Fig. 1-21. In particular, it was confirmed that our films did indeed phototransform (polymerize) when irradiated with high intensity 488 nm light (Fig. 4-12).

In order to assess the oxygen content of our films, electron spin resonance (ESR) and weight uptake techniques were used, as discussed in Sec. 4.4.

To investigate the electrical properties of our C_{60} films, we fabricated Al-C_{60}-Al trilayer structures for electrical characterization (Fig. 4-13). These sandwich structures were made by depositing in succession on glass: 200 μm-wide aluminum down stripes, a known thickness of C_{60}, and finally, 200 μm-wide aluminum cross stripes.

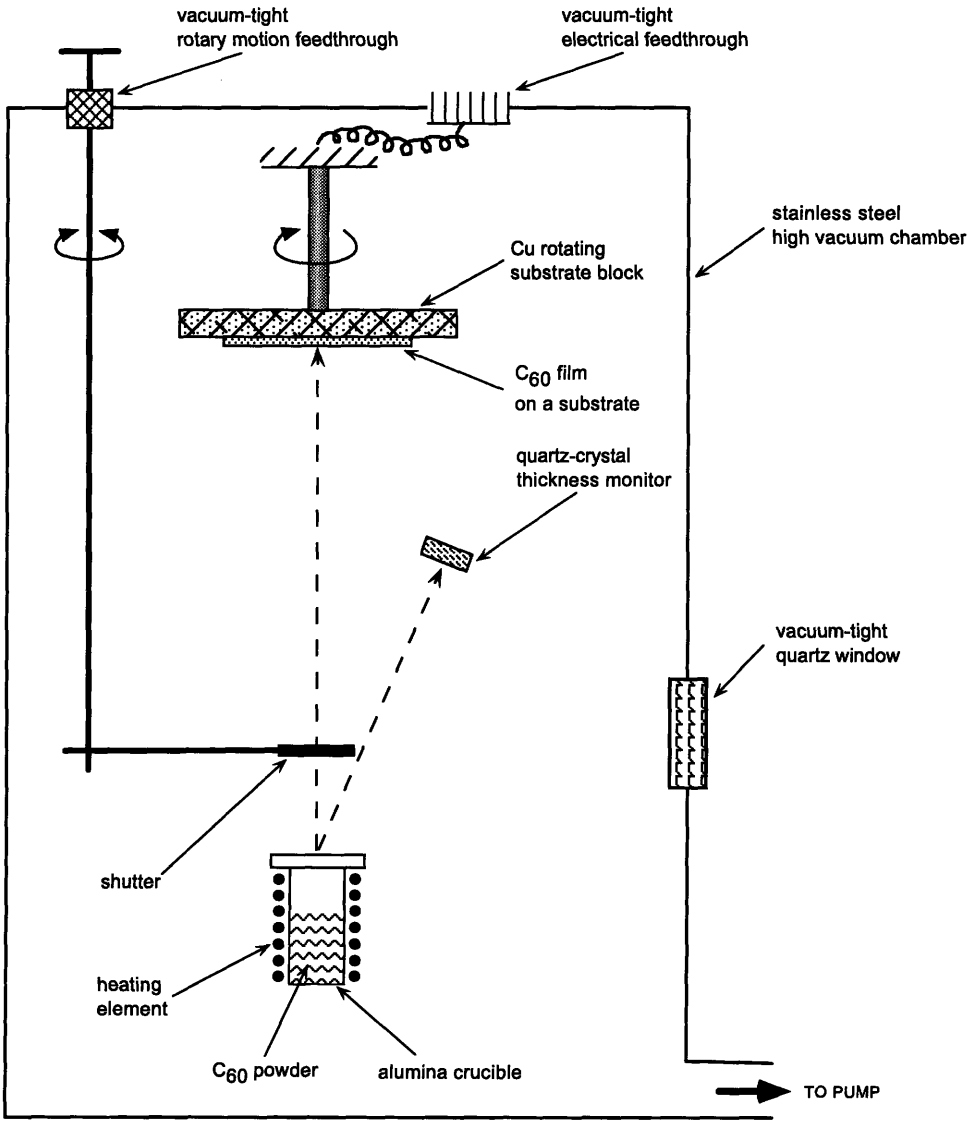


Figure 4-8: A schematic of the vacuum deposition system used to grow the C_{60} films for all experiments described herein. The system is located at AT&T Bell Labs, in the laboratory of Dr. Arthur Hebard.

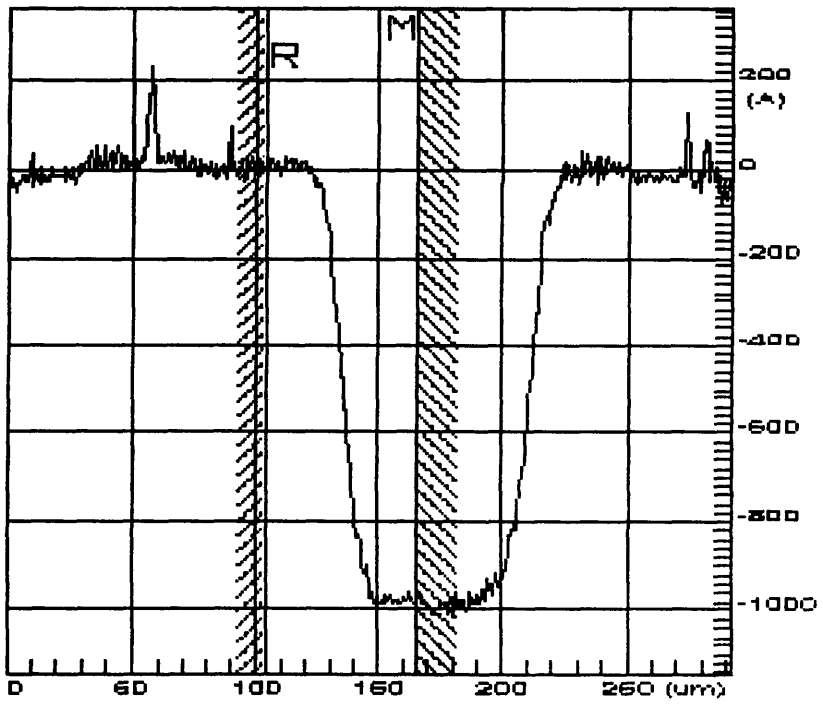


Figure 4-9: A Dektak 8000 profilometer measurement of a 1000 Å C_{60} film (as indicated by the crystal monitor in the deposition system depicted in Fig. 4-8). A narrow ($\sim 70\mu$m) channel was masked on the surface of the substrate with a thin gold wire prior to the C_{60} deposition. After the deposition, a profilometer scan was taken across the resulting gap in the film. To avoid scratching the film, a light profilometer stylus was used, exerting the force of only 12 mg on the surface of the film. The depth measurement taken between the two vertical diagonally shaded bars shown on the plot indicated a film thickness of 989 Å, in close agreement with the expected thickness of 1000 Å. [The Dektak 8000 profilometer used for these measurements is located at the Microfabrication Shared Educational Facility of the MIT Center for Material Science and Engineering (CMSE).]

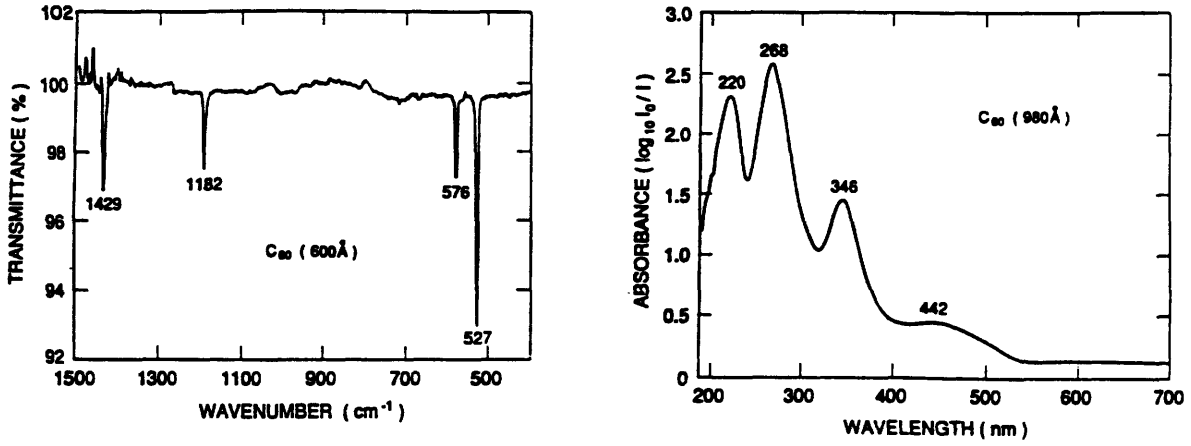


Figure 4-10: (a) Infrared transmission of a 600 Å-thick C_{60} film deposited on a KBr substrate. The frequencies of the four absorption peaks labeled on the figure [*cf.* Fig. 1-21(a)] coincide with other published values for sublimed films [7, 45] and are also seen for C_{60} in solution, pointing to the molecular character of the C_{60} solid films. (b) Wavelength-dependent absorbance of a 930 Å-thick C_{60} film deposited onto quartz. The four prominent absorption peaks arise from interband transitions among the molecular orbitals [24].

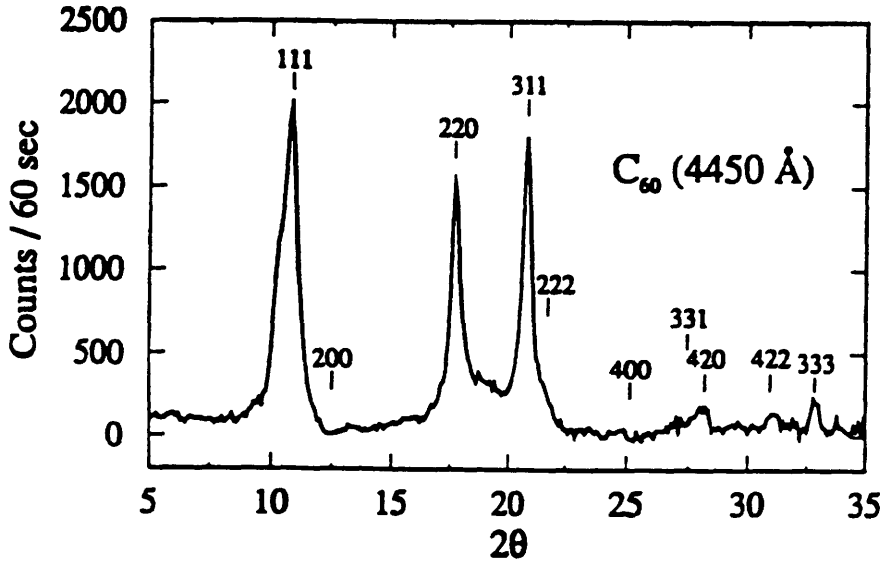


Figure 4-11: X-ray scan of a 4450 Å-thick C_{60} film deposited onto an off-axis cut single-crystal sapphire substrate. The markers indicate the calculated diffraction lines from a face-centered cubic cell seen in diffraction from bulk C_{60} powder. The flat background indicates that the film does not have a significant amorphous fraction. The width of the peaks indicates that the crystalline domains do not have long-range order (the film is polycrystalline), with the coherence length on the order of 60 Å, or about four unit cells [24].

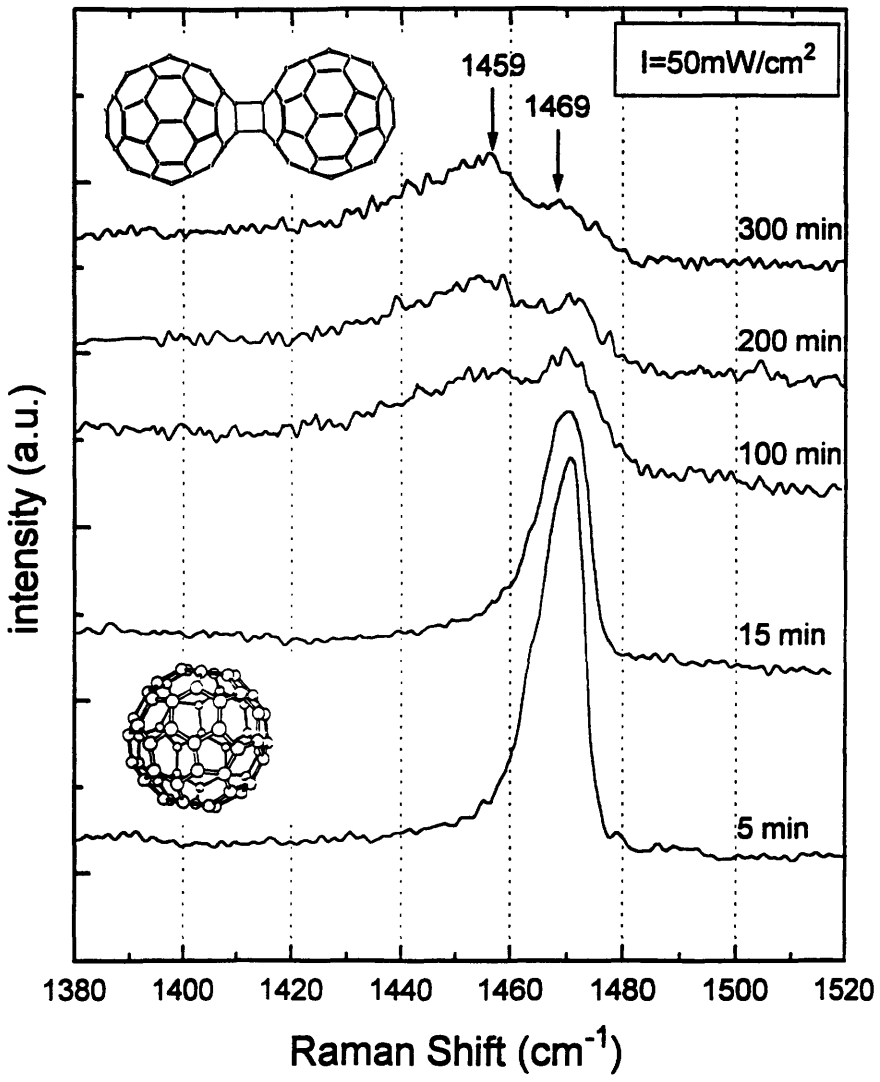


Figure 4-12: The characteristic signature of the C_{60} photopolymerization process is the gradual shift of the 1469 cm^{-1} Raman $A_g(2)$ line (corresponding to the pentagonal-pinch vibrational mode in C_{60} before polymerization, see Sec. 1.6) to 1459 cm^{-1}. This figure follows the decay of the 1469 cm^{-1} Raman peak and the development of the 1459 cm^{-1} peak in a vacuum-sublimed 1000 Å-thick C_{60} film subjected to 50 mW/cm^2 argon-ion laser irradiation at 488 nm. The decreased magnitude of the Raman peak at 1459 cm^{-1} in photopolymerized C_{60} film compared to the original 1469 cm^{-1} peak in pristine C_{60} points to increased disorder due to polymerization. This Raman study was performed at the Francis Bitter National Magnet Laboratory (M.I.T.)

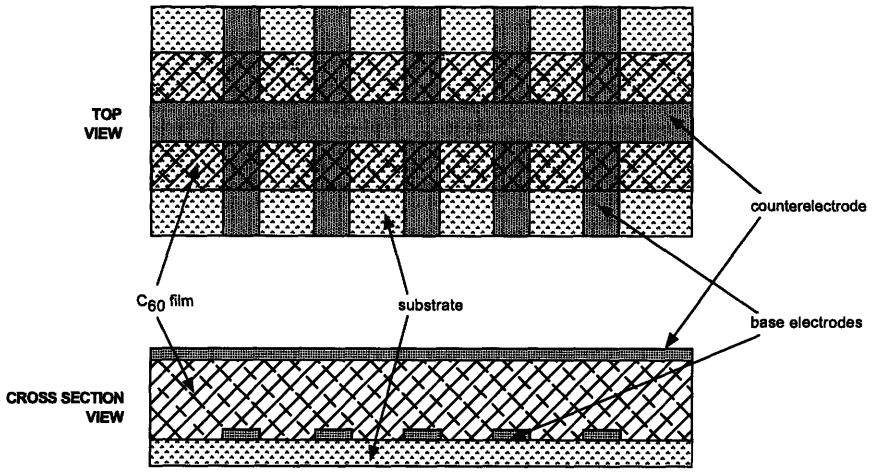


Figure 4-13: A typical trilayer ("sandwich") structure is composed of five identical Al-C_{60}-Al junctions, each of which can be used independently in a dielectric (or transport) experiment.

The sample was briefly handled in the ambient while being transferred from the aluminum deposition system into the C_{60} deposition system — but long enough for a thin (~10–20 Å) layer of aluminum oxide (Al_2O_3) to grow on the Al down stripes. While this oxide layer is too thin, in comparison with the thickness of the C_{60} film, to affect the bulk capacitance of the structure, it contributes significantly to the interfacial capacitance C_i (see Sec. 3.2.2). In addition, since Al_2O_3 is an excellent insulator, it blocks much of the DC current through the structure, rendering this configuration unusable for transport measurements.[7] Note that, in the context of semiconductor measurements, the bottom interface of the structure shown in Fig. 4-13 would be considered an MIS (metal–insulator–semiconductor) interface. Indeed, the behavior of such an interface in an Al-Al_2O_3-C_{60}-Al "sandwich" structure has been investigated by Yonehara and Pac [129] and others [264], who found such a structure to be strongly

[7]It is instructive to keep in mind the estimate for the resistance expected from a typical trilayer structure similar to that shown in Fig. 4-13. Assuming a typical C_{60} film thickness of 1000 Å and a typical width of 200 μm for both the down stripes and the cross stripes, we calculate that, as the conductivity σ of C_{60} varies from 10^{-7} Ω·cm to 10^{-10} Ω·cm as a result of oxygen exposure, the resistance of the C_{60} layer varies from ~1 MΩ to ~1 GΩ. The resistance of the entire structure will be further increased by the presence of the Al_2O_3 layer at the bottom interface.

rectifying (see Sec. 1.7.3). In the context of the dielectric measurements presented in this work, however, it is sufficient to treat the Al_2O_3 layer[8] as a frequency-independent capacitance C_i in series with the bulk capacitance due to C_{60}.

The microdielectric sensor with interdigitated electrodes (see Figs. 3-6 and 3-10) was utilized for some of the experiments, in which case a C_{60} film of known thickness was deposited directly onto the surface of the sensor.

4.6 Measurement of the intrinsic dielectric constant of C_{60}

In order to ascertain the intrinsic dielectric constant ε' of C_{60}, the dielectric measurement needs to be performed at frequencies low enough to include the intrinsic relaxation processes of the material, but high enough to escape the effect of impurities. We have determined experimentally that the effects of oxygen and other impurities occupying the interstitials of solid C_{60} on the dielectric relaxation of C_{60} films are confined to frequencies below $\sim$5 kHz. A measurement at 100 kHz would thus yield the intrinsic dielectric constant ε' of the material.

Such measurements were performed on trilayer ("sandwich") structures similar to the one shown in Fig. 4-13. Figure 4-14 plots the reciprocal capacitance $1/C$ normalized to the area A of the cross stripes vs film thickness. The linear dependence of the reciprocal capacitance on the film thickness, with finite positive intercept on the ordinate, is consistent with the model described in Sec. 3.2, in which the measured capacitance is equal to the series combination of the interface capacitance and a geometrical capacitance [225]. From the slope of the linear fit through the C_{60} data in Fig. 4-14 (solid circles), a value $\varepsilon' = 4.4 \pm 0.2$ for the relative dielectric constant is

[8]It is important to remember that C_i here includes a contribution due to the Al_2O_3 layer (geometrical), as well as a Al_2O_3-independent component due purely to the interfacial effects discussed in Sec. 3.2.2.

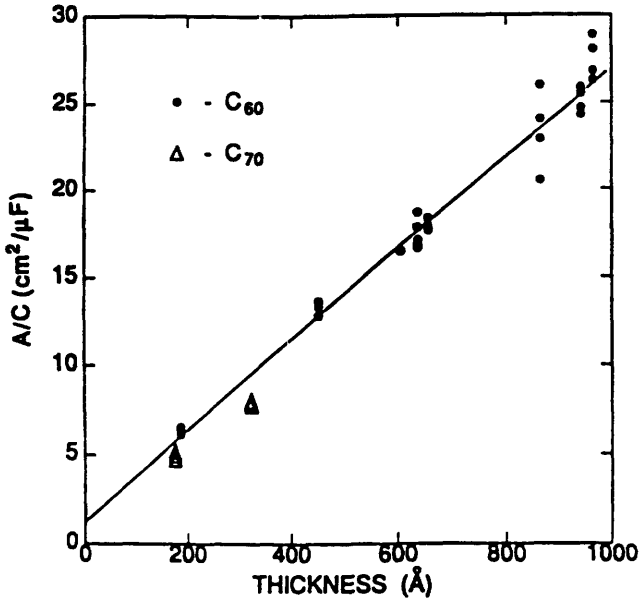


Figure 4-14: Plot of the reciprocal areal capacitance of Al-C_{60}-Al (●) and Al-C_{70}-Al (△) trilayer structures as a function of fullerene film thickness, measured at 100 kHz. A relative permittivity of 4.4±0.2 for C_{60} is calculated from the solid line regression fit to the C_{60} data [24].

calculated. This value is comparable to that of thin-film amorphous SiO_2 which itself is on the low end of the range for thin-film oxide dielectrics [24].

Note that, since the measurements depicted in Fig. 4-14 were performed at 100 kHz, the enhanced polarization effects due to hopping impurities (which make a large contribution to the polarization below 5 kHz) do not interfere with the measurement, and thus the dielectric constant $\varepsilon' \approx 4.4$ is a good approximation of the "true" static dielectric constant of pristine C_{60}. This value is somewhat higher than the value of $\varepsilon' \approx 3.9$ obtained from the optical measurements [61] (see Fig. 4-1.) As noted in Sec. 4.2, this small difference is probably due to the additional losses associated with the rapid molecular rotation motion of C_{60} at room temperature ($T > T_{01}$) and at a frequency of $\sim 10^9$ Hz, as evidenced by NMR [73], ultrasound attenuation [52], and other experiments sensitive to phenomena in this frequency range (see Sec. 1.3.2).

4.7 Dielectric properties as a function of oxygen diffusion

As was discussed above, the interstitial spaces of the fcc C_{60} solid are large enough to accommodate almost any element of the Periodic Table. In this section, we shall investigate how molecular oxygen affects the dielectric properties of C_{60} films (discussion of effects of other species will be deferred to Sec. 4.10). First, we demonstrate that some impurities are present in the lattice by observing nonlinear effects in the dielectric function at low frequencies (Sec. 4.7.1). We then hypothesize that these impurities consist mainly of molecular oxygen, and demonstrate the development of a dielectric loss peak (accompanied by an increase in polarization) with prolonged exposure to ambient oxygen (Sec. 4.7.2). Sec. 4.7.3 demonstrates that very little charge transfer is necessary in order to achieve polarization enhancements reported in Sec. 4.7.2, which makes the oxygen diffusion model of dielectric relaxation in oxygenated C_{60} increasingly plausible. In Sec. 4.7.4, we follow the dielectric loss peak as a function of oxygen content, and propose the model of a *diffusion-controlled relaxation mechanism* for low frequency dielectric relaxation of oxygenated C_{60}, and Sec. 4.7.5 describes how to obtain both tracer and chemical diffusion constants for oxygen diffusion into C_{60} purely from dielectric measurements.

4.7.1 Low-frequency nonlinearities in the dielectric data

In addition to ensuring that the frequency at which the measurement is performed is sufficiently high to avoid impurity contributions to the dielectric function, it is also important to conduct the measurement at voltage levels low enough to avoid nonlinearities, particularly at low frequencies. From the arguments outlined in Sec. 3.2.2, we concluded that a 1000 Å-thick dielectric film measured at 100 mV (corresponding to a field strength of 10^4 V/cm) should stay well within its linear region.

Figure 4-15 displays the real and imaginary parts of the dielectric function of a

500 Å-thick C_{60} film measured at 10 mV (open dots) and 100 mV (solid dots). Clearly, the behavior of the C_{60} film at low frequencies (below $\sim$1 kHz) is *nonlinear*, despite the relatively modest electric field strength of 2×10^4 V/cm. This nonlinearity strongly suggests the presence of weakly bound dipoles in the interstitials of the film. Combining this observation with the evidence from the magnetic studies (Sec. 4.4.1) and transport measurements (Sec. 4.4.2), we hypothesize that these dipoles are created via a charge transfer between the C_{60} balls and the oxygen molecules (O_2) occupying interstitial spaces of the C_{60} lattice. However, the charge transfer may not necessarily be an integral charge, as shown below.

4.7.2 Development of the dielectric loss peaks as a result of oxygen diffusion

The presence of electric dipoles in an oxygenated C_{60} solid is further confirmed by dielectric studies of C_{60} thin films. These studies were performed using either the trilayer sample configuration (shown in Fig. 4-13) for capacitance measurements, or a Micron sensor (Fig. 3-10) using the microdielectrometry technique.

The main feature that shows up consistently in the dielectric measurements of all C_{60} films we have studied is a significant increase in permittivity ε', accompanied by a peak in the dielectric loss ε'', at frequencies on the order of $\sim$100 Hz at room temperature. These features are dependent on both the concentration of oxygen in the interstitials of the film and on temperature. These relationships are investigated in this section and in Sec. 4.8, respectively.

Figure 4-16 displays a representative "snapshot" of the evolution of a 1000 Å C_{60} film after 16 hours of exposure to the ambient environment at room temperature ($T \approx 296$°C). The figure shows the real (a) and imaginary (b) parts of the dielectric function, as well as the loss tangent (c) and the Cole-Cole representation (d). The data for the C_{60} film (solid lines) are compared to the Debye single-relaxation-time model (see Sec. 2.3.3) described by Equations (2.46) and (2.47). We notice right away that

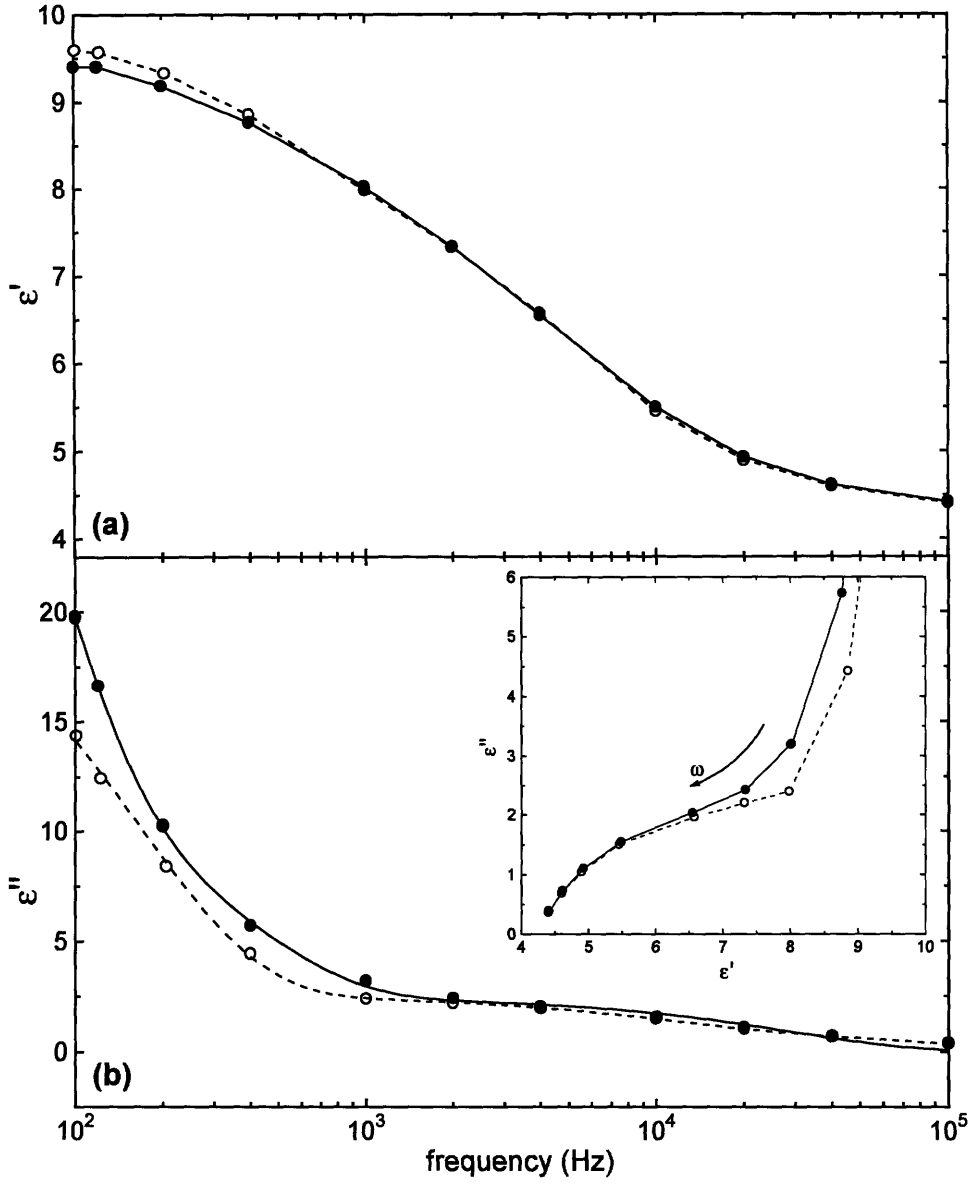


Figure 4-15: Evidence of nonlinear behavior of a C_{60} film at low frequencies (below ~1 kHz) due to the presence of weakly bound dipoles. A 500 Å-thick C_{60} film was measured at 10 mV excitation (o, dashed lines) and 100 mV excitation (●, solid lines). The real (a) and imaginary (b) parts of the dielectric function are displayed. The inset shows the Cole-Cole plot of the sample, with the arrow indicating the direction of the frequency increase. The shape of the Cole-Cole plot suggests a Debye-like dielectric relaxation mechanism combined with a DC conductivity effect (see Fig. 2-20).

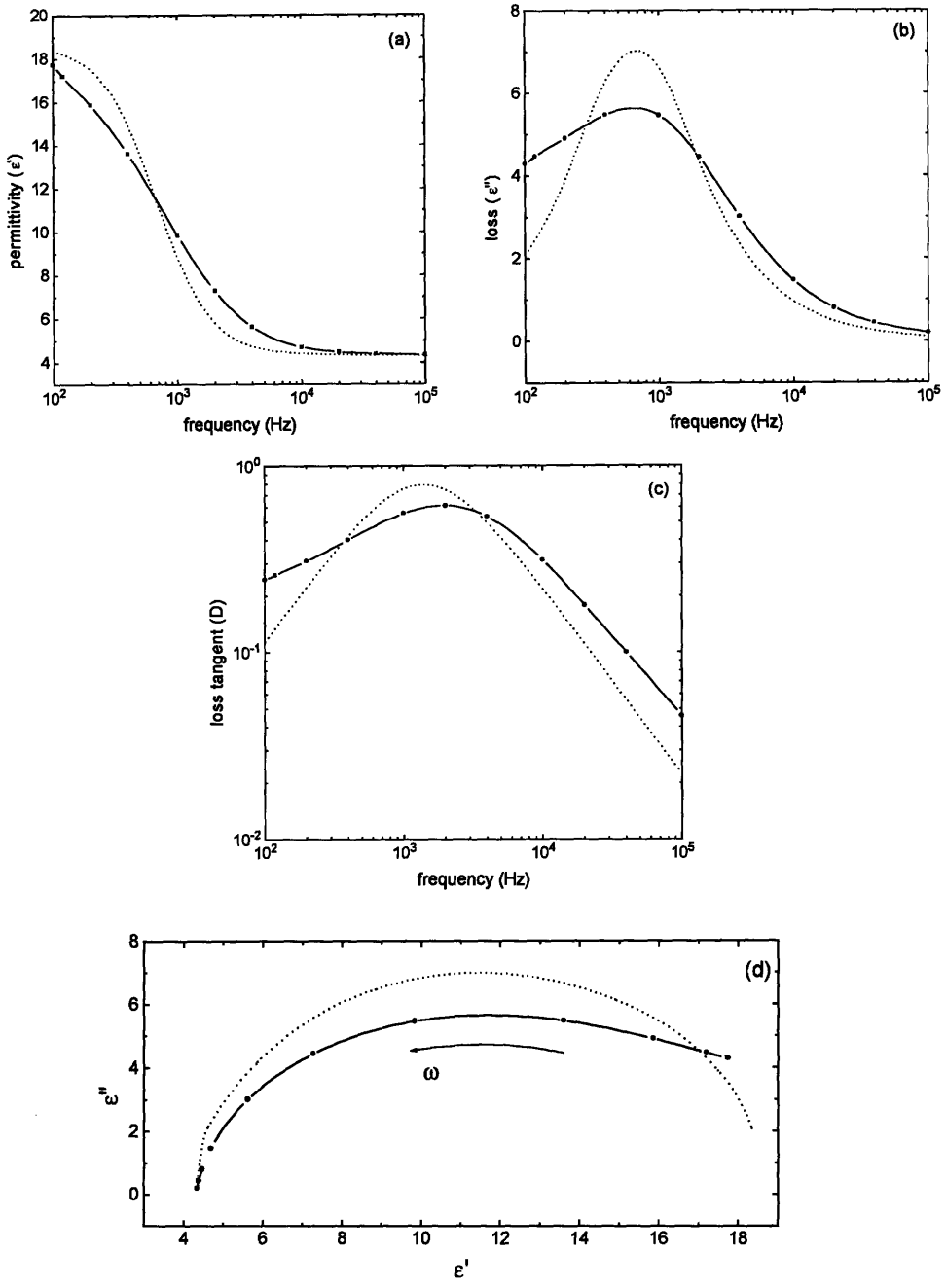


Figure 4-16: Dielectric response of a 1000 Å C_{60} film after 16 hours of exposure to the ambient environment at room temperature ($T \approx 296°C$). The real (a) and imaginary (b) parts of the dielectric function are plotted on a log-linear scale, whereas the loss tangent (c) is shown on a log-log scale. Plot (d) displays the Cole-Cole representation of the data. The dotted lines correspond to the Debye relaxation function [Equations (2.45)] with the following parameters: $\varepsilon_\infty = 4.34$, $\varepsilon(0) = 18.66$, $f_{\text{peak}} = 674\,\text{Hz}$, $\tau_d = 1/2\pi f_{\text{peak}} = 236\mu\text{s}$.

our system cannot be adequately described by a simple Debye relaxation mechanism. The linear fits to the log-log plot of the loss tangent data in Fig. 4-16(c) suggest the high-frequency and low-frequency exponents of 0.87 and 0.19, respectively. Referring to Table 2.2, we discover that no single-parameter models (Cole-Cole, Davidson-Cole, or Williams-Watts) are able to fit the data. We shall, therefore, utilize Jonscher's "many-body interactions" approach leading to the two-parameter model of dielectric relaxation [177] described in Sec. 2.3.3.

4.7.3 Calculation of added polarization

The development of the dielectric peaks, such as the one shown in Fig. 4-16, after oxygen exposure provides further evidence of the presence of dipoles in oxygenated C_{60} films. The fact that both C_{60} and molecular oxygen (O_2) molecules are non-polar, together with the evidence for reversible oxygen diffusion into the bulk of C_{60} solid (Sec. 4.4.1-4.4.2), strongly suggests that these dipoles arise due to a charge transfer between oxygen molecules and C_{60} balls. On the other hand, the amount of this charge transfer is bound to be very small, reflecting the fact that the electron affinities of both C_{60} and molecular oxygen are relatively high. The direction of charge transfer can be ascertained by comparing the electron affinities of these two molecules. Since the electron affinity of C_{60} molecule (2.65$\pm$0.05 eV [40]) is considerably higher than the electron affinity of molecular oxygen (0.451$\pm$0.007 eV [265]), we expect oxygen to be the donor and C_{60} the acceptor of electrons.[9]

Even though the amount of charge transferred from an oxygen molecule to a C_{60} molecule may be small, it can create a relatively large effective dipole moment if the charge is transferred over a large distance. To calculate the amount of charge that needs to be transferred in order to achieve the added polarization evident in

[9]One should be careful when using the values for electron affinity for making prediction regarding the direction of charge transfer, as these numbers are modified by the lattice screening effects in the solid. In the case of C_{60}, these are good estimates, however, because C_{60} forms a loosely bound *molecular* solid (Sec. 1.3.2).

Fig. 4-16(a), we shall use the Clausius-Mossotti equation (2.11). As discussed in Section 2.2.3, the relative permittivity ε' of a solid is linked to the dipole moment μ of the permanent dipoles contained in the solid and to the molecular polarizability α_m via the Clausius-Mossotti formula

$$\frac{\varepsilon' - 1}{\varepsilon' + 2} = \frac{N_d \mu^2}{9\varepsilon_0 kT} + \frac{4\pi N_m \alpha_m}{3}, \tag{4.6}$$

where N_m is molecular density of the solid, N_d is the density of permanent dipoles, T is temperature, and the fundamental constants are $\varepsilon_0 = 8.85 \times 10^{-12}\,\mathrm{F/m}$ and $k = 1.38 \times 10^{-23}\,\mathrm{J/K}$, the permittivity of free space and the Boltzmann constant, respectively. In the absence of permanent dipoles, the molecular polarizability is, therefore,

$$\alpha_m = \frac{3}{4\pi N_m} \frac{\varepsilon' - 1}{\varepsilon' + 2}. \tag{4.7}$$

Setting $\varepsilon = 4.4$ and $N = 1.44 \times 10^{21}\,\mathrm{cm^{-3}}$ (molecular density for C_{60} solid), we get $\alpha_m = 90\,\mathrm{Å^3}$ for the polarizability at $\omega = 10^5\,\mathrm{Hz}$. This value compares well with other determinations of the low-frequency molecular polarizability of C_{60} [235, 266–268].

We explain the dramatic increase in the dielectric function $\varepsilon'(\omega)$ from 4.4 at 10^5 Hz to 18.4 at 100 Hz by polarization caused by the interstitial oxygen. We determine the strength μ of a permanent dipole at room temperature by solving equation (4.6) with $\varepsilon = 18.4$, $\alpha_m = 90\,\mathrm{Å^3}$, and $T = 300\,\mathrm{K}$, which yields $\mu \approx 0.9$ Debye. We then represent each C_{60} molecule as a conducting sphere of radius $R \approx 5$ Å, and each oxygen molecule as a point-charge q transferring a fractional charge onto the C_{60} molecule (Fig. 4-17). From an image charge calculation, we obtain the dipole moment

$$\mu = -qa\left[1 - \left(\frac{R}{a}\right)^3\right] \tag{4.8}$$

created by the transfer of a charge q onto a sphere of radius R located distance a away from the charge q (see Fig. 4-17). For the C_{60} solid with O_2 in the octahedral

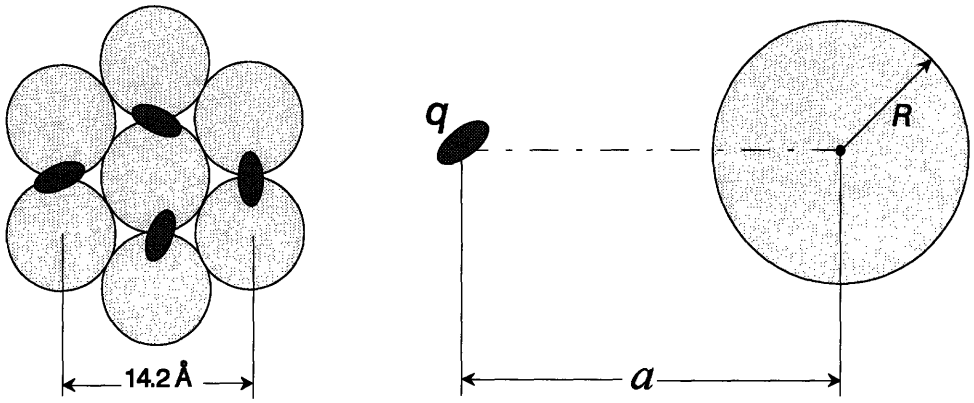


Figure 4-17: A schematic drawing (2D projection) showing oxygen molecules (represented by ellipses) located in the interstitials of the C_{60} solid (with buckyballs represented by spheres). The fcc C_{60} lattice constant is 14.2 Å. The figure to the right is used in the image charge calculation to obtain Eqn. (4.8) for the dipole moment. The reader should refer to Fig. 4-2 for a more realistic rendition of the three-dimensional C_{60}/O_2 compound.

sites, $R \approx 5$ Å and $a \approx 7$ Å, and so q is determined to be

$$q \sim 0.04 q_{\bar{e}},$$

where $q_{\bar{e}} = 1.6 \times 10^{-19}$ Coulomb is the elementary charge on an electron. Clearly, it is very plausible to expect this small amount of charge transfer to occur between a C_{60} molecule and an interstitial oxygen molecule through a hybridization mechanism.[10] This validates our assumption[11] regarding the origin of the dipoles in oxygenated C_{60}.

[10]Note that this calculation ignores the contribution from other C_{60} molecules surrounding a particular oxygen molecule (see Fig. 4-17). The dipole moment μ will only arise if the oxygen molecule is displaced from the center of the interstitial site.

[11]See Sec. 4.7.6 for a discussion of other plausible dipole-forming mechanisms related to various interface effects.

4.7.4 Dynamics of the dielectric loss peaks as a function of oxygen diffusion

In one of the most fascinating results of our studies of low-frequency dielectric properties of C_{60} films, we found that the dielectric loss peaks described above (see Fig. 4-16 in Sec. 4.7.2) change their magnitude, shape, and frequency position as a function of oxygen diffusion onto the bulk of the film. Figure 4-18 illustrates schematically the dynamics of the loss peak as a function of exposure to ambient oxygen. The top trace in Fig. 4-18 shows that as-prepared films display very little anomalous dielectric dispersion, resulting in the absence of the dielectric loss peak. The $1/\omega$ rise in the dielectric loss toward low frequencies is due to the finite DC conductivity of the sample, as discussed in Sec. 2.3.4. With prolonged exposure to oxygen, the dielectric loss peak becomes more pronounced, and gradually moves towards higher frequencies by about an order of magnitude (middle traces in Fig. 4-18). With additional exposure, however, the dielectric loss peak decreases again, until it finally disappears completely after about two weeks of exposure. After heat treatment in vacuum, the dielectric peak reappears, as illustrated by the bottom trace in Fig. 4-18.

We explain the dynamics of the dielectric loss peak in terms of the oxygen diffusion and O_2-C_{60} charge transfer models described in Sec. 4.7.3 above. Since no oxygen is present in the as-prepared C_{60} film (top trace in Fig. 4-18), no charge transfer occurs, and thus no dipoles are present. Therefore, no anomalous dielectric dispersion occurs in the material.

Once the sample is placed in the ambient environment, molecular oxygen starts diffusing into the bulk of the film, transferring charge to the neighboring C_{60} balls, and thus creating electrical dipoles, as described in Sec. 4.7.3. As the oxygen molecule diffuses through the C_{60} lattice, it "drags" this transferred charge from one C_{60} ball to the next along its path. Thus diffusion of an oxygen molecule through the lattice, which, on the microscopic level, is a random walk-like process (see Sec. 4.7.5), has the effect of flipping the O_2-C_{60} dipoles at some rate determined by the oxygen diffusion

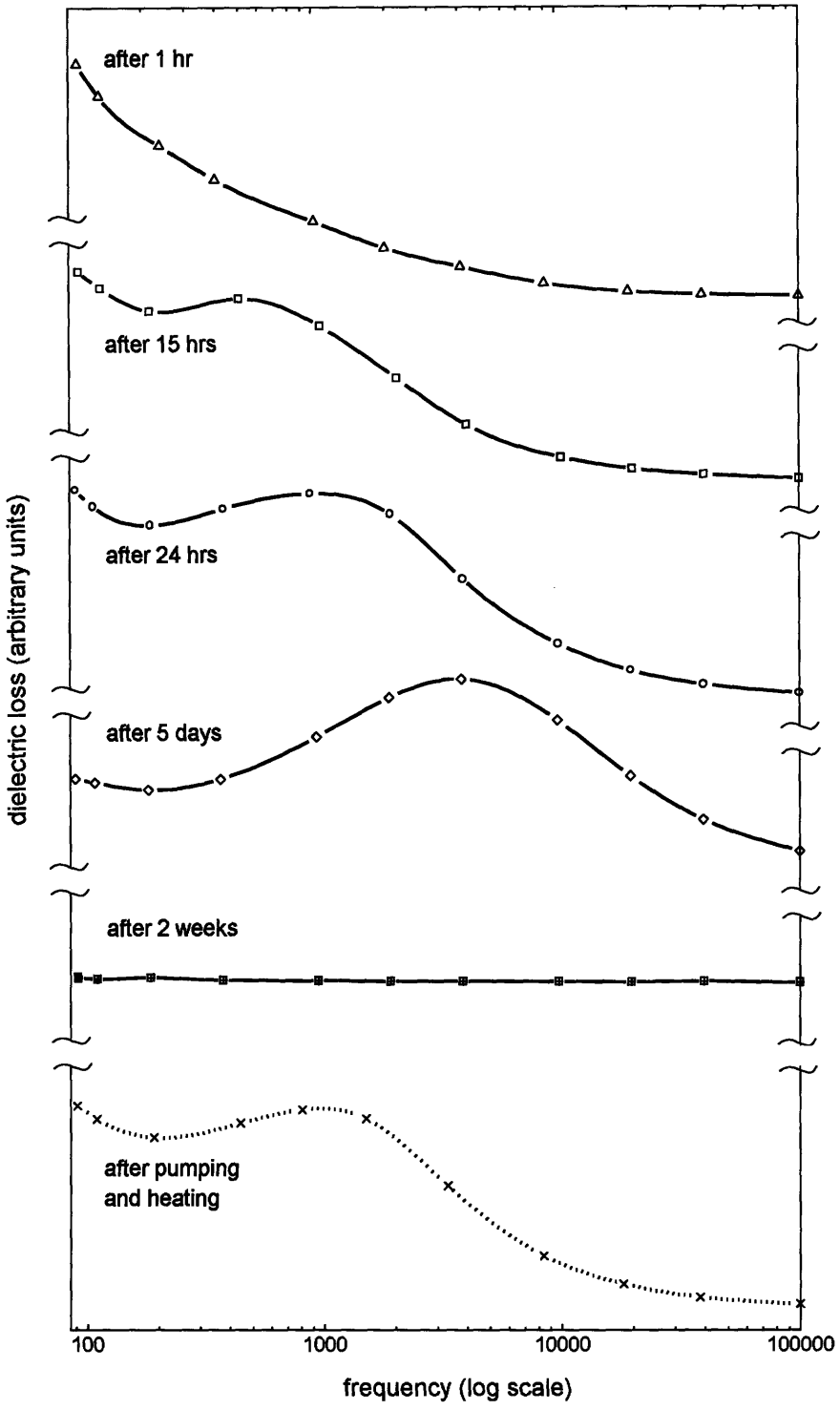


Figure 4-18: A schematic plot of dielectric loss vs frequency for a 1000 Å C_{60} film, prepared initially without exposure to oxygen, showing peaks moving after various durations of oxygen exposure. The y-axis scale is the same for all traces. The traces have been stacked vertically for clarity.

constant and the hopping distance. An applied AC electric field can couple to this process, yielding a loss peak at some frequency determined by the rate of oxygen hopping, which, in turn, is controlled by the diffusion constant of oxygen in its C_{60} host.

We, therefore, propose a *diffusion-controlled relaxation* mechanism for low frequency dielectric relaxation in oxygenated C_{60}.

In the pristine C_{60} film, in the absence of a charge-transferring diffusant (such as O_2), no enhanced polarization [Fig. 4-19(a)] or anomalous dielectric dispersion [Fig. 4-19(b)] is observed. As a greater fraction of the interstitial sites gets filled by diffusion, more dipoles are created via charge transfer, which results in increased polarization and the development of a dielectric loss peak at the characteristic hopping frequency of the molecules. As the number of empty sites decreases, oxygen molecules may need to hop to the second nearest neighbor sites, which requires more energy, and is therefore much less likely to occur, resulting in a decrease in the additional polarization and in the magnitude of the loss peak. With increasing oxygenation, a nearly full occupancy of the interstitial sites is eventually achieved, interstitial hopping is inhibited, and the loss peaks, together with the enhanced polarization, disappear.

To exclude the possibility that the observed enhanced polarization behavior is due to some kind of an electrode effect, we also manufactured trilayer structures qualitatively similar to those in Fig. 4-13, but with the electrodes made of metals other than aluminum (Ag, Au, Cr). A representative result of dielectric measurements performed on a Al-C_{60}-Ag trilayer structure is shown in Fig. 4-20. Clearly, this result is similar to those obtained with Al-C_{60}-Al trilayers. We tentatively conclude that the enhanced polarization effects that we observe are due to intrinsic properties of the C_{60}-O_2 system, and not to the electrode effects.[12]

[12]A thickness dependence study with Al-C_{60}-Al trilayers is needed to further clarify the significance of electrode effects. By varying the thickness of the C_{60} layer, it should be possible to reliably isolate bulk C_{60} properties from the interface effects. Preparations for such a study are currently under way. See Sec. 4.7.6 for additional discussion of possible interface-related sources of polarization in this system.

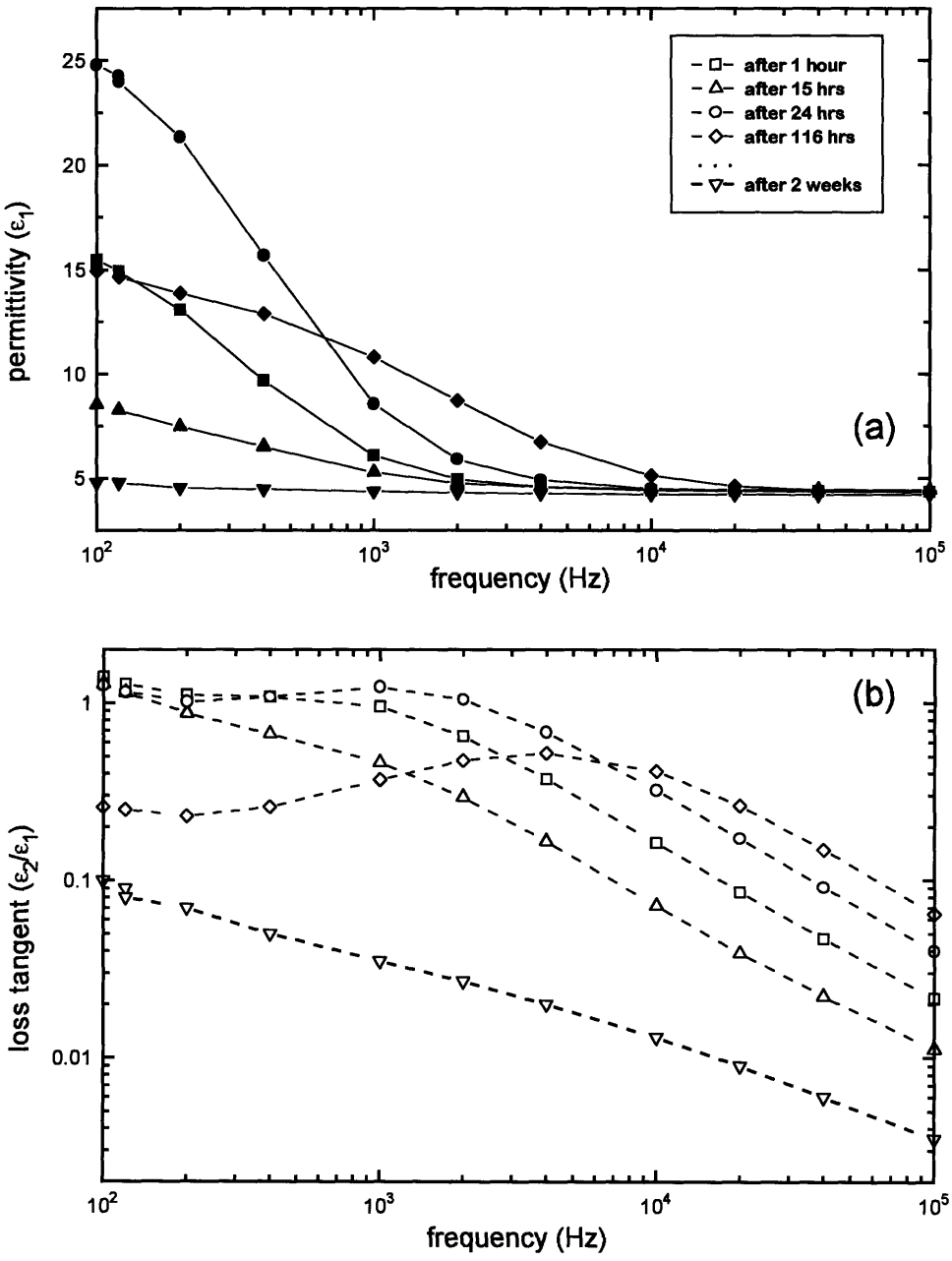


Figure 4-19: Evolution of the dielectric peaks in an oxygenated 857 Å-thick C_{60} film with exposure to the ambient atmosphere. Note that, while the permittivity is plotted on a log-linear scale (a), the dielectric loss tangent is plotted on a log-log scale (b).

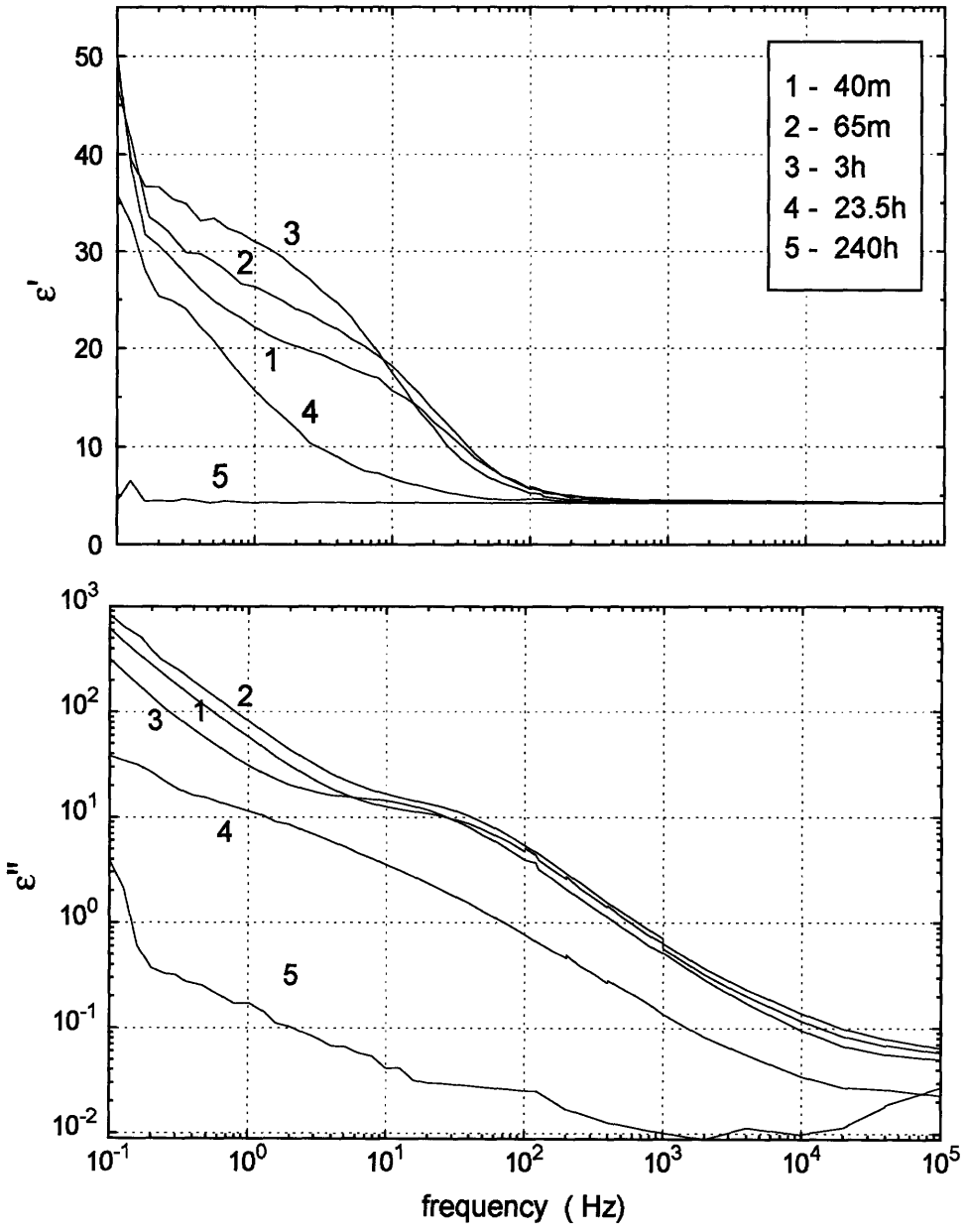


Figure 4-20: Enhanced polarization and anomalous dispersion effects observed in a Al-C_{60}(650Å)-Ag trilayer structure. Note that the data were taken over an extended frequency range, compared to that of Fig. 4-19.

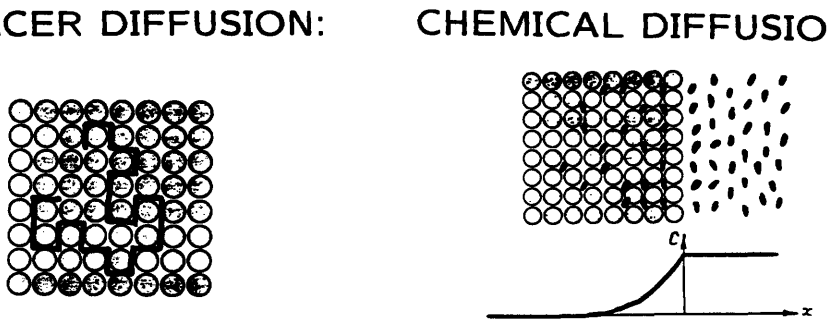


Figure 4-21: Illustration of the tracer and chemical diffusion processes in two dimensions. The hollow circles represent atoms or molecules of the host material arranged in a regular lattice, into which the diffusant is diffusing. Tracer diffusion is a random walk-like process. The graph for the case of chemical diffusion shows a snapshot concentration of the material as a function of position x at some time t. The concentration of the diffusant outside the sample is constant, and it decreases with x into the bulk of the material.

4.7.5 Obtaining the chemical and tracer diffusion constants from the dielectric loss data

There are two different diffusion constants that are important in thermodynamics: a tracer diffusion constant, D_{tracer}, and a chemical diffusion constant, D_{chem} (the latter usually being simply designated as D)[13]. To our knowledge, both of them have never been obtained at the same time using dielectric measurements either on C_{60} or on any other material. Our dielectric measurement techniques (see Chapter 3), spanning nine orders of magnitude in frequency, allowed us to obtain both of the constants simultaneously for the C_{60}-O_2 system.

The tracer and chemical diffusion processes are illustrated in Fig. 4-21. Tracer diffusion is usually described as a random walk of the diffusing species (diffusant)

[13]Both D_{tracer} and D_{chem} can vary with temperature, concentration, and other factors, so it would be more precise to call them diffusion *coefficients*, rather than *constants*. The name *diffusion constant* is still often used, however, implying the diffusion coefficient measured at some assumed point in the phase space (usually, at room temperature, with diffusion coefficient presumed to be concentration-independent, unless noted otherwise).

in the lattice of the host material. The tracer diffusion constant is defined by the *Einstein relation:*

$$D_{\text{tracer}} = \frac{\langle d^2 \rangle}{2\tau}, \tag{4.9}$$

where d is the average hopping distance, and τ represents the time required for a single *hop* in the random walk chain.

The chemical diffusion constant D_{chem} describes the distribution of a diffusant in the host material. D_{chem} can be thought of as a *macroscopic* diffusion constant, and it relates to the *microscopic* tracer diffusion constant D_{tracer} via the following equation

$$D_{\text{chem}} = F D_{\text{tracer}} \tag{4.10}$$

where

$$F = \frac{C}{k_B T} \frac{\partial \mu}{\partial C}, \tag{4.11}$$

C is composition (in number of particles per volume), μ is the chemical potential, T is the temperature, and $k_B = 1.38 \times 10^{-23}$ J/K is the Boltzmann constant.

The distribution of a diffusant in a given film during absorption (or desorption) is governed by the one-dimensional differential equation for diffusion due to Fick [269] (Fick's First Law), with the space coordinate x taken in the direction of the film thickness (see Fig. 4-21):

$$\frac{\partial C(x,t)}{\partial t} = -\frac{\partial J}{\partial x}, \tag{4.12}$$

where $C(x,t)$ is the concentration and J is the flux of the diffusant. For a description of nonsteady-state problems, it is necessary to combine Fick's first law (4.12) with a differential mass balance equation stating that a change in the diffusant's concentration $C(x)$ results in a flux $J(x)$:

$$J = -D \frac{\partial C}{\partial x} \tag{4.13}$$

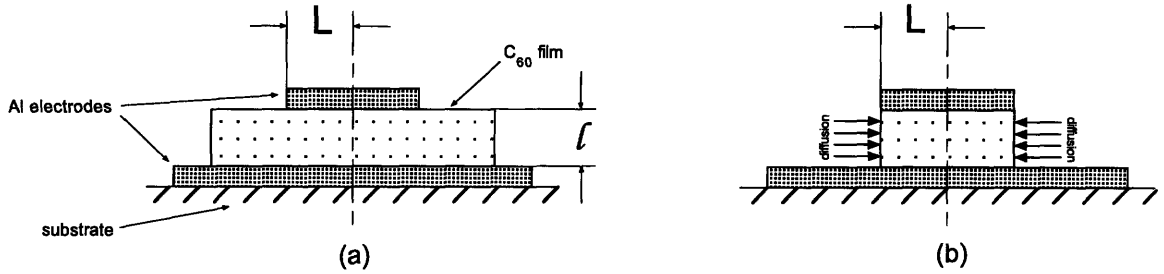


Figure 4-22: (a) A single M-C_{60}-M (M=metal) junction similar to those shown in Fig. 4-13, where ℓ represents the thickness of the C_{60} film, and L is one half of the electrode width. (b) An approximation used in deriving Eqns. (4.15) and (4.16) assumes that the initial concentration is equal to C_1 across the C_{60} film's edges. This approximation requires that $\ell \ll L$. For typical values of $\ell \sim 1000$ Å and $L \sim 100\,\mu$m, this requirement is clearly fulfilled, and the use of this approximation is justified.

where D is the (chemical) diffusion coefficient. Combining Eqns. (4.12) and (4.13), we arrive at Fick's Second Law:

$$\frac{\partial C(x,t)}{\partial t} = D\frac{\partial C^2}{\partial^2 x} + \frac{\partial D}{\partial C}\left(\frac{\partial C}{\partial x}\right)^2, \tag{4.14}$$

where we allowed for the possibility that the diffusion coefficient D is a function of concentration C.

Solutions of Fick's second law (4.14) for various geometries and initial conditions have been compiled by Crank [270]. For the case of lateral diffusion into the film of the kind expected in our Al-C_{60}-Al trilayer structures (see Fig. 4-13), the concentration of diffusant (*e.g.*, molecular oxygen) at distance x into the film after time t is found as [270]

$$\frac{C(x,t) - C_0}{C_1 - C_0} = 1 - \frac{4}{\pi}\sum_{n=0}^{\infty}\frac{(-1)^n}{2n+1}\cos(\alpha_n x)e^{-D\alpha_n^2 x} \tag{4.15}$$

where C_0 is the initial concentration of the diffusant in the film (zero), C_1 is the concentration at surface (saturated), D is the diffusion coefficient, $\alpha_n = \frac{(2n+1)\pi}{2L}$, and L is equal to one half of the electrode width (see Fig. 4-22). Figure 4-23 presents a plot of $C(x,t)$ as a function of t for several values of x (top), and a plot of $C(x,t)$ as a

function of x for several values of t (bottom). Together, these plots demonstrate that, as $t \rightarrow \infty$, the diffusant concentration becomes the same (uniform) throughout the film. (Note also that n only need to be carried to about $n_{\max} = 20$ for convergence of the summation.)

If $M(t)$ denotes the total amount of diffusing substance which has entered the film at time t, and M_∞ is the amount at equilibrium ($t \rightarrow \infty$), then the solution to Fick's second law can be written as [270]

$$\frac{M(t)}{M_\infty} = 1 - \frac{8}{\pi^2} \sum_{n=0}^{\infty} \frac{1}{(2n+1)^2} \exp\left[-D(2m+1)^2\pi^2 \frac{t}{4L^2}\right]. \tag{4.16}$$

The value of t/L^2 for which $M(t)/M_\infty = \frac{1}{2}$, conveniently written as $t_{1/2}/L^2$, is given approximately by

$$\frac{t_{1/2}}{L^2} = -\frac{1}{\pi^2 D} \ln\left[\frac{\pi^2}{16} - \frac{1}{9}\left(\frac{\pi^2}{16}\right)^9\right], \tag{4.17}$$

the error being about 0.001% for typical values of the parameters [271]. Thus the approximation

$$D = 0.04919 \left(\frac{L^2}{t_{1/2}}\right) \tag{4.18}$$

can be used so that if the half-time of the sorption process $t_{1/2}$ is observed experimentally, the value of the diffusion coefficient, assumed constant, can be determined.

In a remarkable illustration of the power and usefulness of dielectric measurements, we were able to measure both the tracer and chemical diffusion constants of oxygen in C_{60} in a single measurement. Figure 4-24 displays the results of this measurement, plotting both the real $\varepsilon'(\omega)$ and imaginary $\varepsilon''(\omega)$ parts of the dielectric function over a broad frequency range. The measurement was performed on a 1000 Å-thick C_{60} film in the "sandwich" configuration (see Fig. 4-13). To map the dielectric function over nine decades in frequency, we had to utilize both the HP 4274A LCZ meter (for measurements from 100 Hz to 100 kHz) and the SI 1254 Frequency Response Analyzer (for measurements below 30 Hz), in configurations described in Sec. 3.2.3.

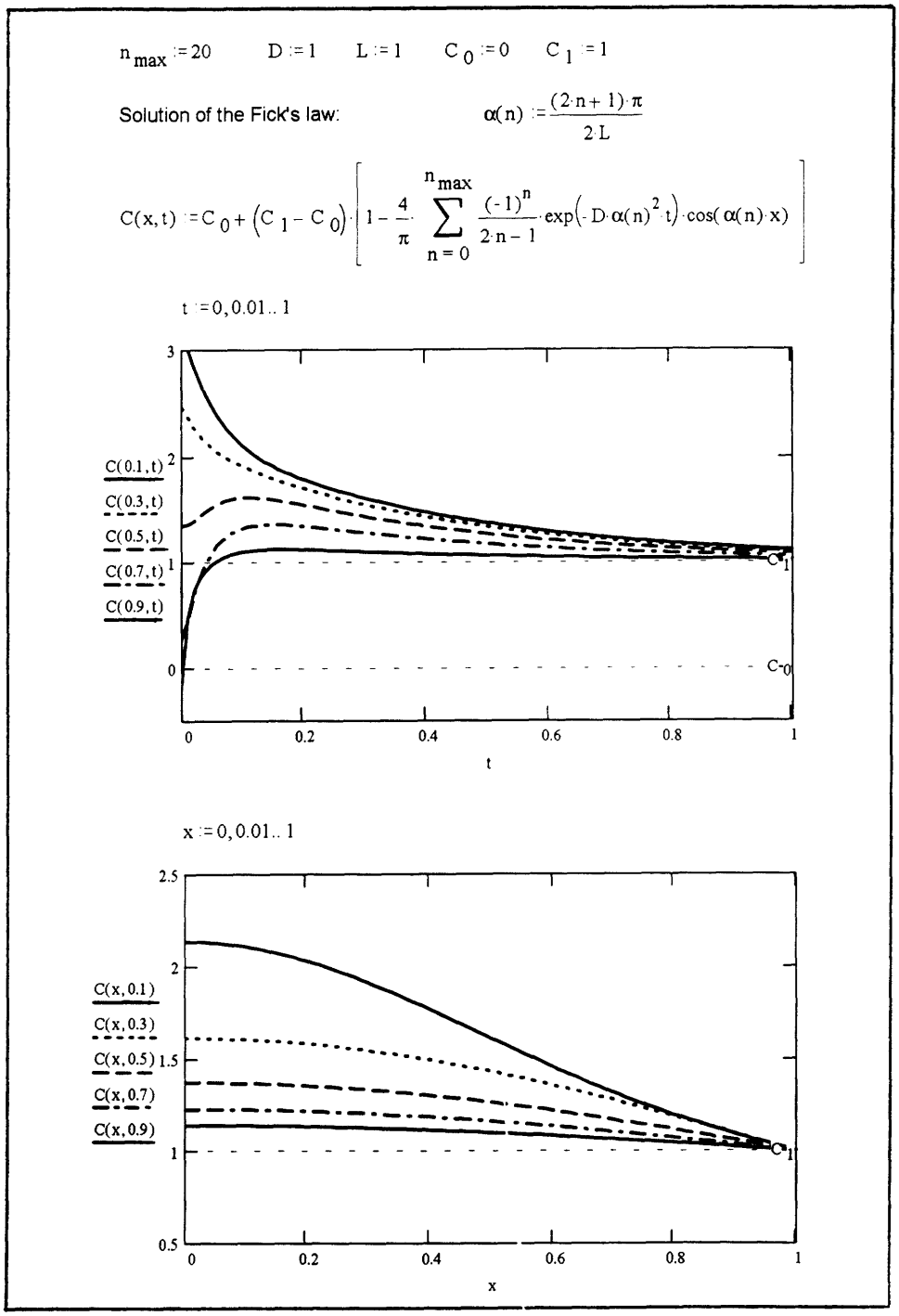


Figure 4-23: Mathcad worksheet calculating Fick's law solutions for the concentration $C(x,t)$ as a function of time t (top plot) and coordinate x (bottom plot).

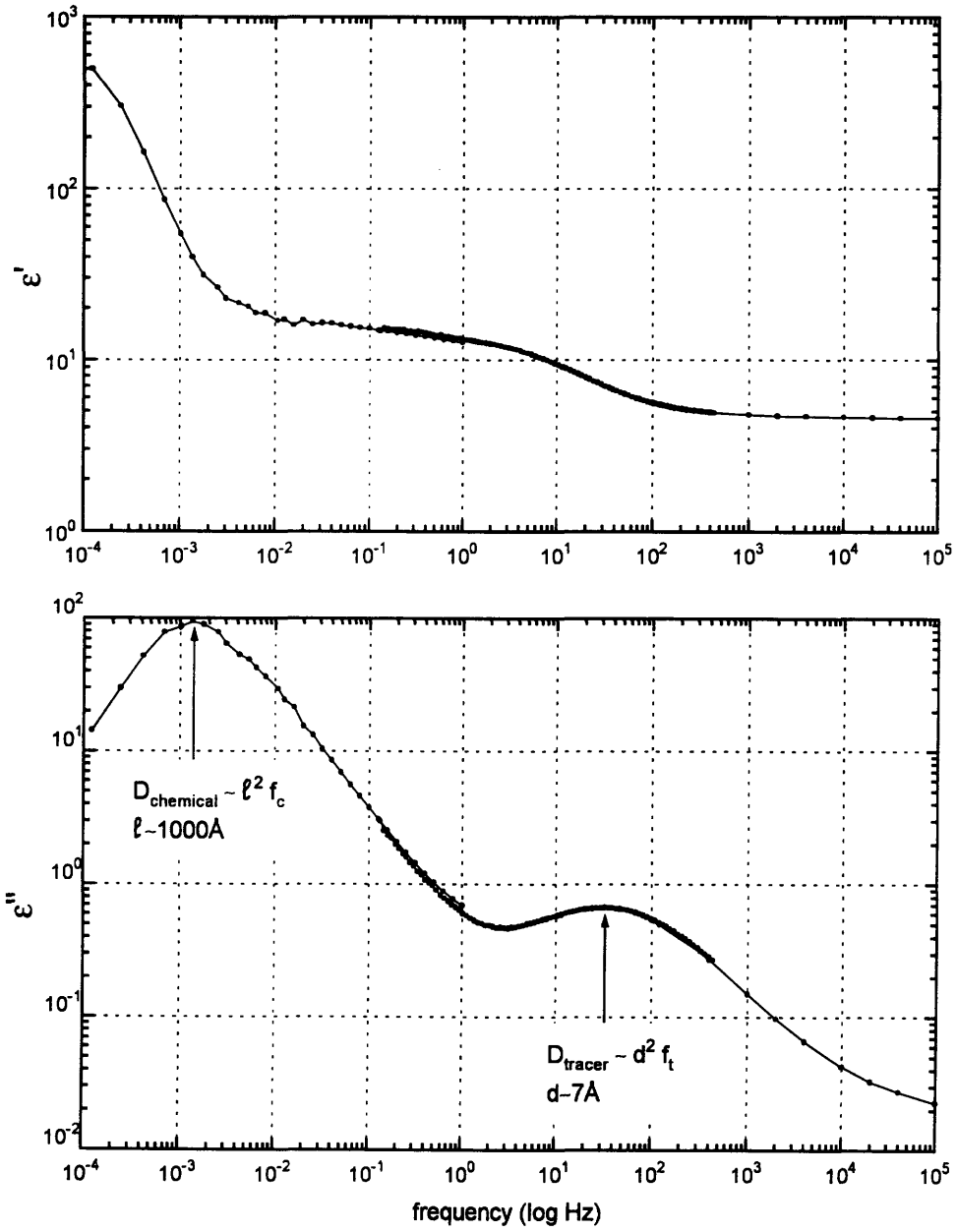


Figure 4-24: Plot of $\varepsilon'(\omega)$ and $\varepsilon''(\omega)$ used to determine the molecular oxygen diffusion into a C_{60} film. Both tracer and chemical diffusion processes are indicated.

An additional preamplifier stage was necessary for measurements below 1 Hz, due to the increased effective conductivity of the sample at low frequencies. The excellent overlap of the data in the three measurement regions confirms the validity of our measurement technique.

In addition, the DC resistance has been subtracted from the dielectric data, as described in Sec. 2.3.4. Therefore, only dielectric polarization and loss, not obscured by the DC conductivity, are shown in Fig. 4-24.

The Einstein relation [Eqn. (4.9)] can be written in the frequency domain as

$$D_{\text{tracer}} = \frac{1}{2}\langle d \rangle^2 f_t, \tag{4.19}$$

where $\langle d \rangle \approx 7$ Å is the average oxygen molecule hopping length corresponding to the distance between two neighboring octahedral sites (see Figs. 4-17 and 4-2), and $f_t = 1/\tau \approx 35$ Hz is the hopping frequency determined from the position of the dielectric loss peak in Fig. 4-24. The tracer diffusion constant can thus be determined from Eqn. (4.19) as

$$D_{\text{tracer}} \approx 10^{-13}\text{cm}^2 \cdot \text{sec}^{-1}.$$

To find the chemical diffusion coefficient D_{chem}, we first refer to Fig. 4-19 following the evolution of the polarization and dielectric loss as a function of oxygen diffusion. As is evident from the figure, both polarization and loss achieve their maximum positions after ~24 hrs of exposure to the ambient environment, corresponding to half-occupancy of the sites that are eventually occupied by oxygen, as described in Sec. 4.7.4. This gives $t_{1/2} \sim 24$ hrs for the half-time of the sorption process of Eqn. (4.18).

On the other hand, the same diffusion process that leads to the development and subsequent disappearance of the tracer diffusion (molecular hopping) dielectric loss peak in Fig. 4-19, should also show up as a "relaxation" of the interfacial polarization in the dielectric measurements. We can thus extend Eqn. (4.18) to incorporate the

chemical diffusion values obtained from dielectric measurements (Fig. 4-24):

$$D \approx 0.05 \left(\frac{L^2}{t_{1/2}} \right) \approx \ell^2 f_c, \tag{4.20}$$

where f_c is the frequency position of the chemical diffusion-related loss peak in Fig. 4-24, corresponding to millihertz frequencies. The origins of the chemical diffusion-related apparent polarization increase and the accompanying loss peak in Fig. 4-24 should be attributed to the interfacial polarization due to oxygen ions drifting back and forth between the plates of the capacitor under the applied very-low-frequency electric field. We estimate the chemical diffusion of molecular oxygen in C_{60} at room temperature as

$$D_{\text{chem}} \approx 10^{-14} \text{cm}^2 \cdot \text{sec}^{-1},$$

approximately an order of magnitude lower than the tracer diffusion constant.

We have, therefore, demonstrated that the chemical diffusion constant can be determined by dielectric measurements either by following the evolution of the *tracer* diffusion (hopping) loss peak and detecting the half-time of the sorption process $t_{1/2}$, or by direct measurement of $f \sim 1/t_{1/2}$ via detecting the dielectric loss peak at very low frequencies due to *interfacial* polarization.

4.7.6 Alternative dipole-forming mechanisms

The oxygen-induced charge transfer mechanism presented above explains very well the main features of the dielectric behavior of C_{60} films that we observe:

1. development of a low frequency polarization increase accompanied by a dielectric loss peak;

2. evolution of this loss peak with increasing oxygen content; and

3. eventual disappearance of the loss peak and additional polarization with full oxygenation of the specimen (once the majority of the interstitial lattice sites

is occupied).

In addition, there is ample evidence to support the proposition that oxygen does indeed diffuse into the interstitials of a fullerite (see Sections 4.4.1 and 4.4.2).

Still, it would not be prudent to neglect mentioning other possible sources of additional polarization that would cause the films to exhibit similar dielectric behavior.

One such effect relates to the interaction of C_{60} with the top and bottom Al interfaces in an Al-C_{60}-Al trilayer structure, such as those used in our dielectric measurements. Diffusion of Al atoms during and after the deposition of the top electrode is of particular concern, since charge transfer between an Al atom and a C_{60} molecule may be quite considerable, resulting in a large additional polarization. While no definitive study of Al-C_{60} surface interaction has been conducted to date, there are indications that strong surface interaction, with possible formation of surface dipoles, does exist:

- Using Auger electron spectroscopy (AES) and temperature-programmed desorption (TPD), Hamza *et al.* [272] demonstrated that a monolayer coverage of C_{60} passivates aluminum surfaces, preventing formation of aluminum oxide after exposure to oxygen and water vapor from room temperature up to 600 K.

- As mentioned in Sec. 4.5, the behavior of Al-C_{60} interfaces in an Al-Al_2O_3-C_{60}-Al "sandwich" structure has been investigated by Yonehara and Pac [129] and others [264], who found such an MIS (metal–insulator–semiconductor) structure to be strongly rectifying (see Sec. 1.7.3).

- By studying $\{\text{Al-C}_{60}\}_n$ $(1 < n < 20)$ multilayer structures, Hebard *et al.* [273] showed that up to six electrons per C_{60} can be transferred from the Al to the C_{60} surface layer.

- McNally *et al.* [274] observed electric field-induced diffusion of Al into the bulk of C_{60} when studying thin-film Al-C_{60}-Al trilayer structures. According to

their report the diffusion occurs very rapidly at field strengths on the order of 3.5×10^4 V/cm, which is considerably below the expected C_{60} dielectric breakdown field of $\sim10^6$ V/cm. Indeed, no structural breakdown of the C_{60} layer has been observed in this study [274].

- Most recently, Owens *et al.* [275] used photo-electron spectroscopy (PES) to study the electronic properties and morphologies of aluminum-C_{60} interfaces. They reported the formation of an interface dipole between the first layer of C_{60} and the Al surface, reflecting the transfer of approximately 0.2 electrons per first-layer fullerene. Deposition of Al onto C_{60} at 300 K resulted in formation of Al clusters on the surface and also in limited Al diffusion into the fullerene lattice. These interstitial Al atoms are believed to create a solid solution and to form donor levels that are thermally ionized [275]. Aluminum overlayer growth at 60 K results in smaller islands and suppressed doping because both surface and bulk diffusion are thermally-activated processes. Owens *et al.* [275] found no evidence of bulk Al-C_{60} compound formation, however.

In all cases, the nature of the fullerene-surface interaction is attributed to an electron charge transfer mechanism from the metal surface to the fullerenes. One would then expect that other metals should interact with the fullerene surface layer in a manner similar to that of aluminum. Indeed, many published reports corroborate this conclusion:

- A number of Scanning Tunneling Microscopy (STM) results show that C_{60} interacts strongly with metal surfaces, such as Al [272], Cu (111) [276], Ag (111) [277], Au (111) [278], Au (001) and Au (100) [279]. The interaction with these metal surfaces is much stronger than the C_{60}–C_{60} interaction.

- Surface-enhanced Raman scattering (SERS) provides yet another informative probe of the interaction between fullerenes and substrates. For a monolayer

of C_{60} on noble metal substrates, downshifts in the Raman-active mode frequencies were generally observed, with some modes downshifting more than others. Using the strong Raman $A_g(2)$ pentagonal pinch mode as a calibration standard, downshifts between 15–18 cm^{-1} were observed on Au surfaces, between 26–28 cm^{-1} on Ag surfaces, and 23 cm^{-1} on Cu surfaces, indicative of the increasing interaction between C_{60} and the Au, Cu, and Ag surfaces in that order, and consistent with the sequence of work functions for the substrates Ag (4.3 eV), Cu (4.7 eV), and Au (5.1 eV) [280].

- Sarkar and Halas [281] have demonstrated a pronounced diffusion of silver (Ag) atoms into C_{60} thin films. The diffusion process was observed to be significant at temperatures just above room temperature, with an activation energy of 2.5 ± 0.5 eV. Temperature-dependent conductivity measurements indicate [281] that silver atoms form an impurity band in solid C_{60} with an activation energy of 0.26 eV.

- We have also found that C_{60} trilayers structures with gold electrodes (Au-C_{60}-Au) always yield samples that appear to be shorted, with measured resistance values on the order of Ohms. (This result has been corroborated by reports from other groups [282, 283].) This suggests that gold is penetrating into the bulk of C_{60} (perhaps, by forming pinholes, rather than by diffusion).

In general, the bonding of fullerenes to some substrates is strong while to others it is weak. Furthermore, metals tend to have a lower work function than semiconductors. Because of the band gap between the occupied valence band and the empty conduction band in semiconductors, more energy is usually required to remove an electron from its highest-lying occupied state to the vacuum level, as compared to a metal. Thus it is expected that charge is more easily transferred between a fullerene and the substrate in the case of a metal. Consequently, fullerenes should bind more strongly to metal surfaces than to semiconductor or insulating surfaces [23]. This argument is

in general applicable to real C_{60} interfaces with substrates, except in cases where the semiconductor has a high density of surface bonds, such as the Si (111) and Si (100) surfaces. The binding of C_{60} to oxides such as SiO_2 and sapphire (α-Al_2O_3) is weak, while the binding to metals such as Al, Au, Ag, and Cu is strong [23].

Having established that a dipole moment due to a C_{60}/metal interface resulting in additional polarization is possible, we must still explain how it accounts for the dynamics of the dielectric loss peak that we observe. Recalling that the loss peak develops and then decays with oxygen exposure, we must rule out the possibility of a mere interfacial polarization, for such polarization would simply add a constant to the permittivity, without affecting dielectric loss at all. However, if we allow for the possibility of diffusion of metal atoms from the electrodes into the bulk of C_{60} (as indicated by some of the studies outlined above), then a charge transfer mechanism similar to that developed for oxygen diffusion (Sec. 4.7.3) would apply, resulting in frequency-dependent polarization and a dielectric loss peak at low frequencies. One might then account for the peak's dynamics (similar to that described in Sec. 4.7.4) by proposing that, as metal (*e.g.*, Al) atoms oxidize, they become less mobile, which prevents them from hopping between adjacent C_{60} interstitials, thereby eliminating dielectric dispersion.

While not impossible, this mechanism appears rather far-fetched. However, further controlled experiments are necessary to fully discount this possibility.[14] In the next Section, we shall concentrate on the oxygen-based mechanism developed in Sec. 4.7.2–4.7.5.

[14]It should be noted, however, that all of our reasoning would apply to the interfacial metal diffusion-induced polarization in exactly the same way that it applies to the oxygen diffusion-induced effect.

4.8 Temperature dependence of the dielectric function in oxygenated C_{60}

4.8.1 Dielectric behavior at $T > T_{01}$

The preceding discussion indicates rather strongly that the long range transport related to chemical diffusion and the reorientation of the induced dipoles due to tracer diffusion are two aspects of the same physical process. Since most of the electron charge carriers in oxygenated C_{60} are trapped, and thus not available for conduction (as evidenced by variations in conductivity of C_{60} by as much as ten orders of magnitude as a function of oxygenation — see, *e.g.*, Table 4.1), it is possible that ionic conduction due to oxygen diffusion contributes significantly to the DC conduction in oxygenated C_{60}. This would suggest that the magnitude of the activation energy of the peak dielectric loss frequency E_τ related to dielectric relaxation due to oxygen hopping is close to the magnitude of the activation energy of the DC conductivity E_σ, which we have measured to be ~0.5 eV (see Sec. 4.4.2).

To test this hypothesis, we measured the dielectric properties of C_{60} films (0.1Hz< f <100kHz) versus temperature (100K< T <300K). The results of this study are presented in Fig. 4-25. The highest-frequency dielectric loss peak in Fig. 4-25(b) corresponds to 290 K, and the loss peak moves down in frequency, as the temperature is lowered in steps of 5 K to 215 K. As demonstrated in Sec. 4.7.2, the peaks that we observe are not Debye-like, as evidenced by the higher-frequency slope of $1 - n = 0.7$ (on the log scale) in the dielectric loss peak [Fig. 4-25(b)]. This indicates that our system is somewhat correlated [177] [a slope of unity ($n = 0$) in the Debye loss peaks corresponds to uncorrelated systems], so that an oxygen molecule hopping from one interstitial site to the next is likely to increase the hopping probability of a neighboring oxygen molecule (see Fig. 2-19 and accompanying discussion in Sec. 2.3.3). This is consistent with our observation that, as a greater fraction of the interstitial sites gets

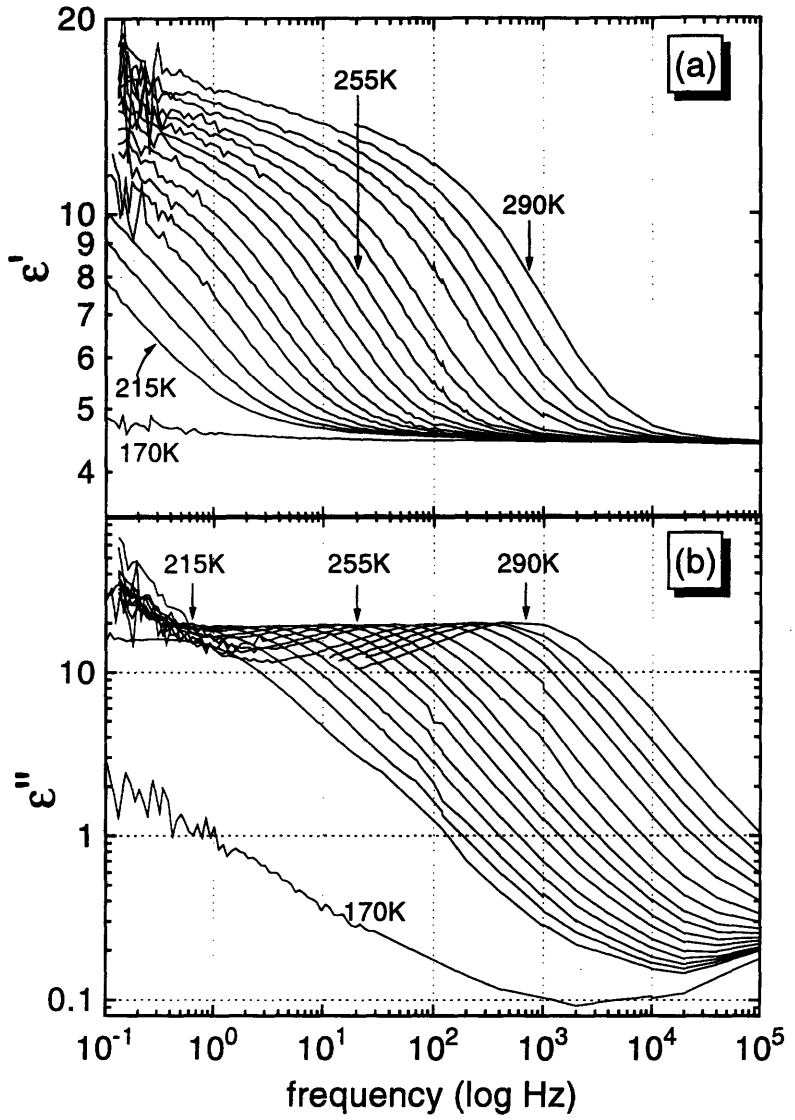


Figure 4-25: Frequency dependence of the real (a) and imaginary (b) parts of the dielectric function of a 840 Å-thick C_{60} film plotted on the log-log scale for temperatures 215–290 K in 5 K intervals. The loss (ε'') peak is activated with a $E_a = 0.5$ eV energy barrier and a frequency prefactor of 2×10^{12} Hz (as found from the Arrhenius plot in Fig. 4-26). The loss peak in the ε'' vs ω plot is not Debye-like, as evidenced by the higher-frequency slope of –0.7 (on the log scale), indicative of a correlated system. The broad increase in the loss function beyond 100 kHz for the low temperature $\varepsilon''(\omega)$ traces is due to residual rotations of C_{60} molecule below the $T_{01} \approx 260$ K structural "freeze-out" transition. The hopping of the oxygen molecules also freezes out below ~190 K, resulting in a decrease of the slope of the dielectric loss (ε'') and in a leveling off of the polarization (ε') [see also Sec. 4.8.2].

filled by the oxygen diffusion, the system becomes increasingly more correlated, until the loss peak disappears completely.

An Arrhenius plot of the frequency position of the dielectric loss peaks shown in Fig. 4-25 is plotted in Fig. 4-26. We find that the peaks are indeed temperature activated with

$$f = f_0 \exp\left(-\frac{E_a}{k_B T}\right), \tag{4.21}$$

where E_a is the activation energy, and f_0 is the frequency prefactor. From Fig. 4-26 we find that the activation energy of the loss peak below the phase transition at $T_{01} = 260$ K is 0.35 eV whereas the activation energy above the phase transition is 0.49 eV, with a frequency prefactor $f_0 = 2 \times 10^{12}$ Hz comparable to the phonon frequencies. Comparing the high temperature ($T > T_{01}$) activation energy of the peak frequency E_τ to the activation energy of the DC conductivity E_σ of our C_{60} films (Fig. 4-6 in Sec. 4.4.2), we find that the two are about the same and equal to $\sim$0.5 eV. This result has been confirmed for several samples of various geometries, but we are not yet completely convinced that $E_\tau = E_\sigma$ holds universally for this system. More experiments are needed to confirm this point. If this relationship holds in subsequent investigations, it will add much credibility to our hypothesis linking oxygen ions to the long-range charge transport in C_{60} films.

Since the suggestion that the activation energy of the DC conductivity of the film E_σ may be the same as the activation energy of the dielectric loss peak E_τ is one of the more intriguing results of our study, it is worthwhile to review the literature for other examples and theories where the same has been shown to be the case.

There are two basic kinds of theories that have been use to explain this behavior. In the first, the separate ionic hopping events are independent and have a broad distribution of relaxation times, while in the second, collective effects occur so that each hopping ion has strong interactions (usually of the Coulombic type) with surrounding ions. These two types of mechanisms have been called *parallel* and *series* conduction processes, respectively, by Elliott [284].

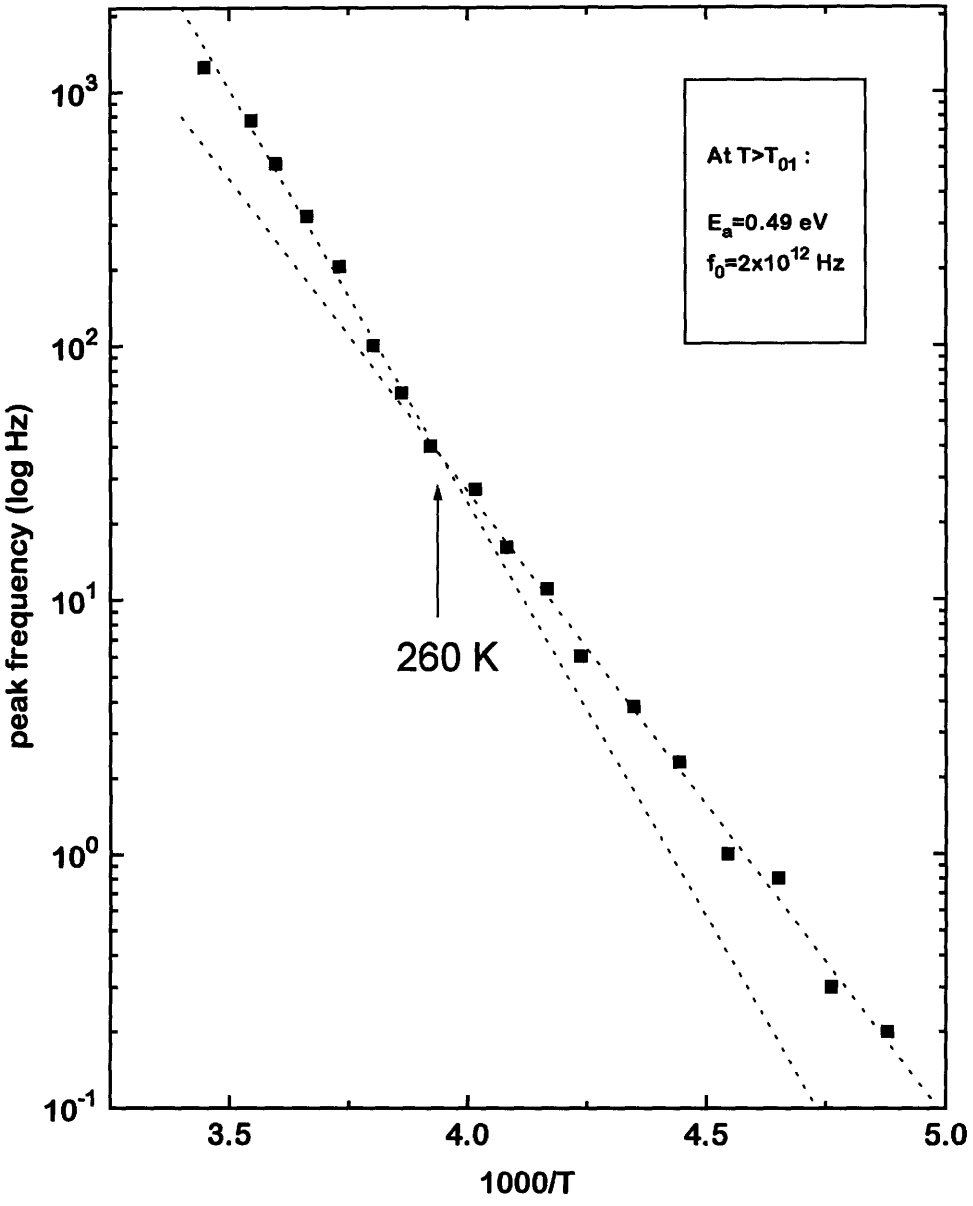


Figure 4-26: Arrhenius plot of the position of the (tracer) dielectric loss peak frequency shown in Fig. 4-25.

The series-type theories have received considerable attention recently, and they appear to explain the $E_\sigma = E_\tau$ effect rather well. In the macroscopic approach by Ngai *et al.* [285–288], called the "coupling model," the cooperative adjustment of the environment of the migrating ions leads to a stretching out of the relaxation process to times much larger than the primitive relaxation time for a non-interactive jump. Here it is implicitly assumed that the DC conductivity and AC relaxation are coupled (derived from the same underlying process).

In a more microscopic theory, called the "jump relaxation model," Funke [289–291] points out that the influence of a "cage effect potential" due to surrounding ions can lead to a high probability of return of the jumping ion ("unsuccessful jump"), which contributes to the AC relaxation, and not to the DC conductivity. This theory can explain why $E_\sigma = E_\tau$ by the fact that both successful and unsuccessful jumps involve the same potential barrier. It would seem, however, that this statement would be valid only for strong electrolytes, since it is difficult to see how E_τ can include an energy that determines the increase in the number of carriers with increasing temperature in this model.

Still another theory of the *series* type is the "diffusion-controlled relaxation" model of Elliott [284], which incorporates cooperative ionic motions, and has some formal similarity to Funke's model. This model, too, predicts that $E_\sigma = E_\tau$ only for strong electrolyte materials.

In all of these theories, the important point is that the AC relaxation process and the DC conductivity are both parts of the same process of interactive ion jumping. In the O_2/C_{60} system considered in our study, this would imply that oxygen diffusion through the C_{60} lattice contributes substantially to the DC conduction process in C_{60}. Since electrons in oxygenated C_{60} are trapped by the deep trap states, and are largely unavailable for DC conduction (as evidenced by extremely low conductivity of oxygenated C_{60} — see Table 4.1 in Sec. 4.4.2), we should consider this proposition increasingly plausible.

We briefly mention an alternative approach that involves a model of hopping conductivity [292]. This approach was originally developed to explain electronic conduction in disordered systems, but it is also applicable to ionic hopping processes. In it, the AC hopping conductivity is described by an equivalent circuit consisting of a random-resistor network with capacitors. At high frequencies, the jumps occur only between nearest sites, corresponding to an AC response that is mostly capacitive. At lower frequencies, multiple hopping can be described in terms of more highly conducting regions (clusters) surrounded by regions of poorer conductivity. Finally, as $\omega \rightarrow 0$, all capacitor-related impedances become infinite, and the conductivity is controlled by an infinite critical cluster of resistors. An analogous model was developed by Efros and Shklovskii [293] and by Balagurov [294] to describe the conductivity of a system consisting of randomly distributed metallic particles in a dielectric matrix near the percolation threshold. Another prominent theory of this kind, developed for ionic conducting glass systems, results in the Barton [295]-Nakajima [296]-Namikawa [297] (BNN) relation, which links the DC (static) dielectric constant $\varepsilon'(0)$ to the DC conductivity $\sigma_{\rm DC}$ as

$$\varepsilon'(0) \propto \frac{\sigma_{\rm DC}}{\omega_t}, \tag{4.22}$$

where ω_t is the frequency of the (tracer) dielectric loss peak. The BNN model has recently been popularized by Hunt [298–305]. If $\varepsilon'(0)$ is independent of T (as it seems to be in the case of C_{60}), then Eqn. (4.22) requires that both ω_t and $\sigma_{\rm DC}$ have the same temperature dependence. This model, therefore, also predicts $E_\sigma = E_\tau$, and it has an added benefit of not being limited to strong electrolytes, as is the case for some of the other theories.

4.8.2 Dielectric behavior at $T < T_{01}$

Let us now return to Fig. 4-25 and consider the dielectric behavior of our system below the C_{60} structural transition.

At temperatures below the $T_{01} \approx 260$ K transition, the C_{60} molecules are not free to rotate any more (see Sec. 1.3.2) and the losses associated with their rotational motion ($\omega_{rot} \sim 10^9$ Hz at $T \sim 300$ K [73]) are moving into our frequency range ($\omega_{rot} \sim 10^5 - 10^6$ Hz at $T \sim 160$ K [52, 72]) and appear as a broad increase in the loss function above 100 kHz. Below ~190 K the absolute value of the slope of the dielectric loss curve is starting to decrease as well, reaching $n - 1 = 0.37$ at 170 K [the bottom curve on Fig. 4-25(b)]. This shows that at low temperatures the hopping motion of the oxygen molecules freezes out, and the system becomes more strongly correlated, which, in turn, results in a leveling off of the polarization [see the bottom curve on Fig. 4-25(a) corresponding to the frequency response at 170 K].

An argument can be made that the decrease in the $n-1$ exponent below 190 K is the result of the second-order phase transition in C_{60}, which is frequency dependent. The results of measurements of T_{02} by various methods at different frequencies are presented in Fig. 4-27 [306]. Following the linear dependency demonstrated in Fig. 4-27, and given that 100 kHz is the highest frequency we can access, we can expect the onset of the second order transition at $T \approx 200$ K, which is precisely what we observed in Fig. 4-25.

Additionally, in Fig. 4-28 we plot the capacitance C and loss tangent D of a 655 Å-thick C_{60} film versus temperature at 100 kHz. We recall that, at 100 kHz, no additional polarization due to oxygen occurs, and all of the dielectric properties measured are those of intrinsic C_{60}. A large anomaly, with an onset at ~ 230 K and reaching maximum at ~ 190 K, is clearly seen in the capacitance plot in Fig. 4-28(a). It is likely that this anomaly is indicative of the second-order phase transition, and is associated with the frozen-in orientational disorder [69, 76]. It can be inferred from Fig. 4-28 that the ratcheting motion of the C_{60} molecules responsible for the increased polarization decreases for temperatures from ~190 K down to ~65 K, and dies down completely for $T < 65$ K, as discussed in Sec. 1.3.2.

For comparison, we also show in Fig. 4-29 the data for the real and imaginary

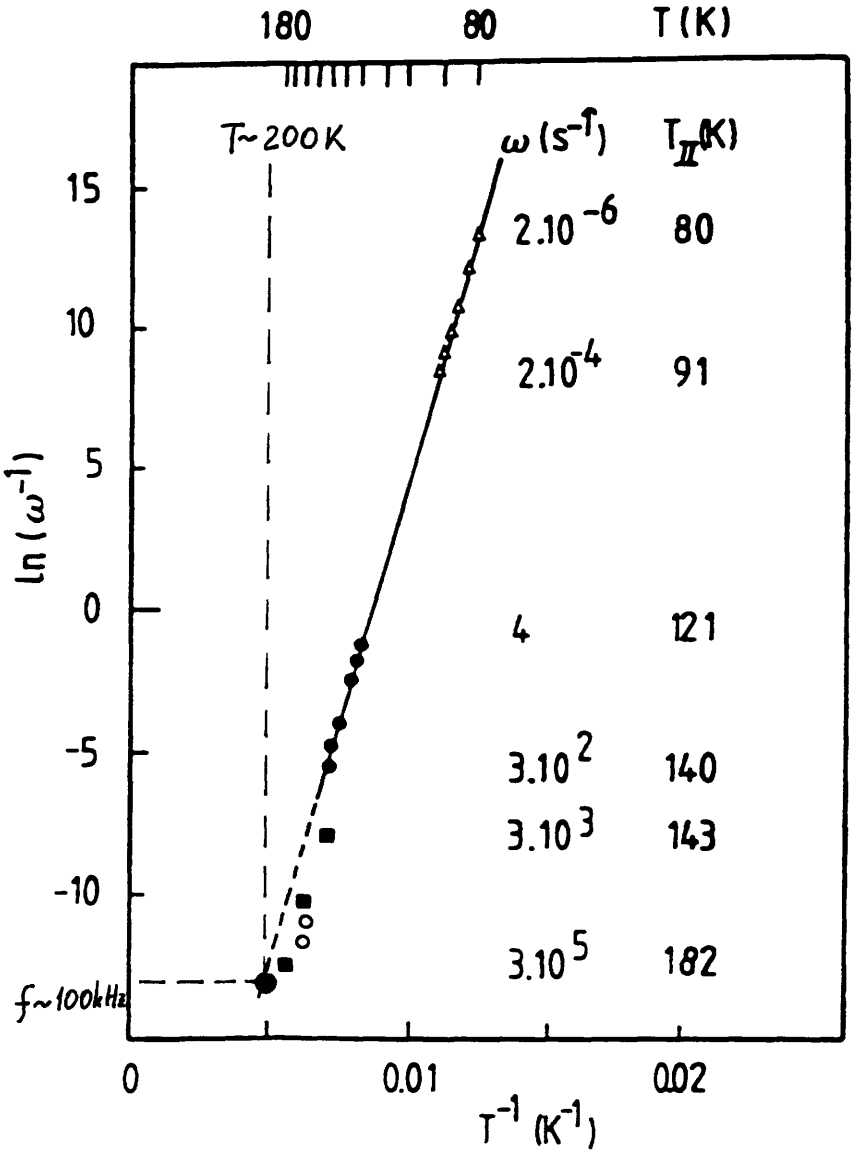


Figure 4-27: Plot of $\ln(\omega^{-1})$ vs T^{-1} for different measurement frequencies. The points, triangles, full squares, and open circles are taken from elastic constant [306], thermal expansion [307], dielectric [76], and sound velocity [52], measurements, respectively. The T_{02} values for each frequency are listed [306].

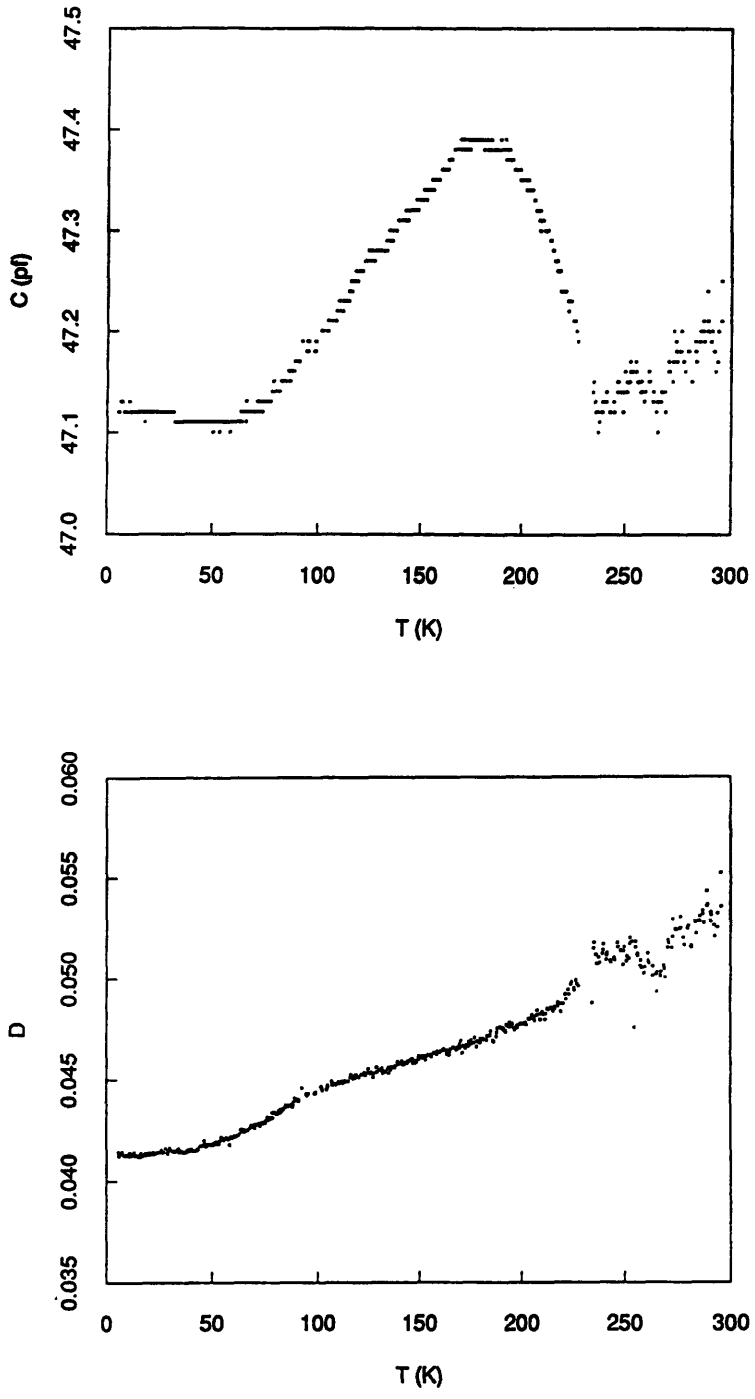


Figure 4-28: Capacitance (a) and dielectric loss tangent (b) vs temperature, for a 655 Å-thick C_{60} film. The measurement was conducted at 100 kHz to avoid the effect of oxygen and other impurities.

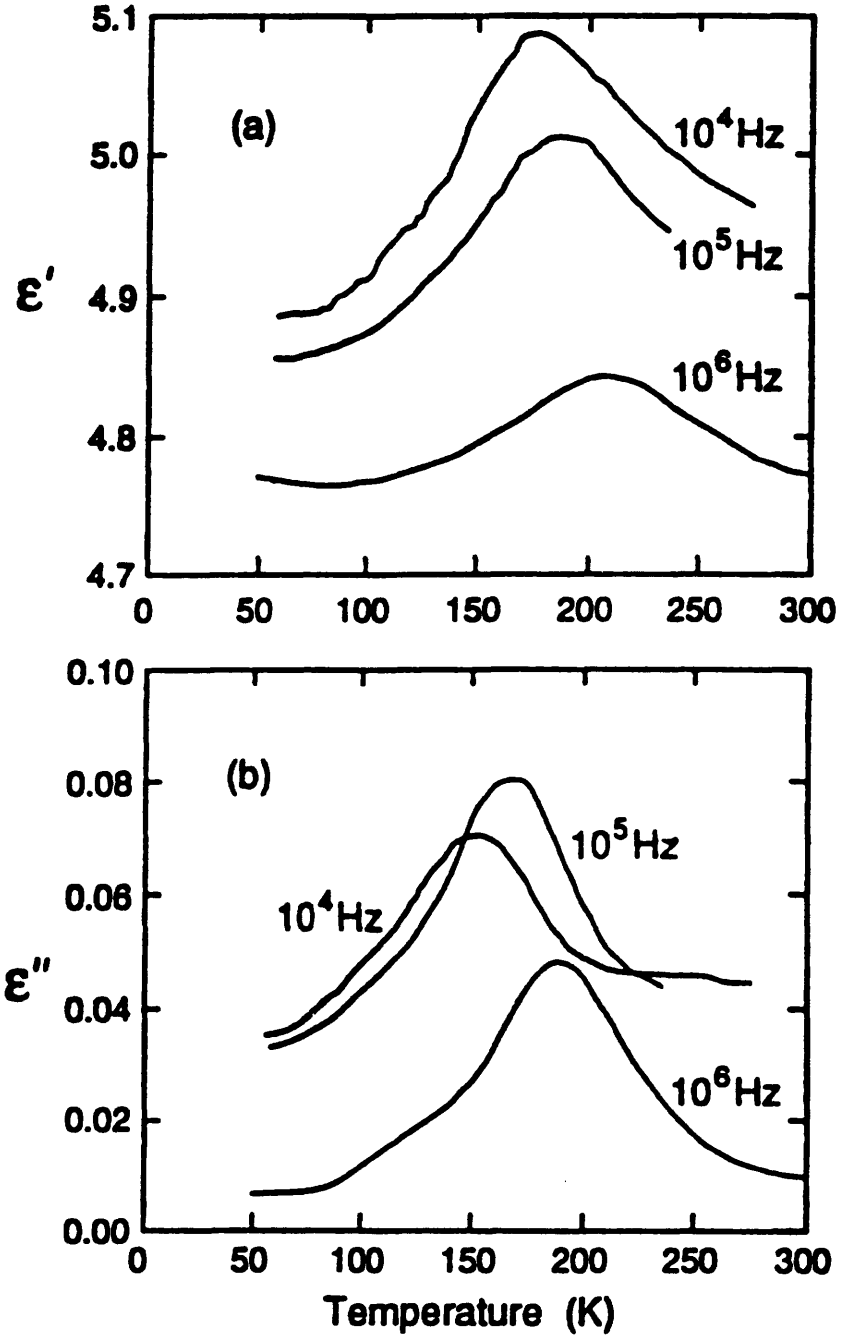


Figure 4-29: Real (a) and imaginary (b) parts of the dielectric function of a C_{60}/C_{70} mixture pellet plotted as a function of temperature at different frequencies [308].

parts of the dielectric constant of C_{60} plotted as a function of temperature at different frequencies that has recently been reported by Chern *et al.* [308]. We can see that the position of the peak in the 10^5 Hz trace for $\varepsilon'(T)$ in Fig. 4-29(a) agrees very well with our capacitance data reported in Fig. 4-28(a). The agreement in the dielectric loss data is less apparent, however, perhaps due to the fact that Chern *et al.* [308] present the imaginary part of the dielectric function $\varepsilon''(T)$ in Fig. 4-29(b), while we plot the dielectric loss tangent $D(T)$ in Fig. 4-28(b). Note also that Chern *et al.* [308] used a C_{60}/C_{70} mixture pellet in their work, rather than a pure C_{60} thin film that was utilized in our experiments.

4.9 Effect of humidity

As mentioned before, interstitial spaces in the weakly bound van der Waals lattice of the C_{60} solid are large enough to accommodate any of the chemical elements, and many of the smaller molecules (*e.g.*, molecular oxygen). We have verified that nitrogen gas (N_2) does not affect the dielectric and transport properties of fullerites, and this is consistent with evidence obtained from the NMR experiments [244, 252]. The other molecular species present in the ambient environment is water (H_2O), whose concentration can be measured in terms of the humidity of the environment.

There are a number of reasons why water molecules are an extremely unlikely source for the polarization increases in C_{60} films that we observe at low frequencies:

1. None of the sample characterization techniques reported in Sec. 4.5 (including the highly accurate infrared probe) were able to detect any amount of water present in our samples after days of storage in an ambient environment with variable humidity.

2. Hamza *et al.* [272] found that multilayer and monolayer coverages of C_{60} on aluminum passivated the surface such that exposure of the surface to water at room temperature led to no oxidation of the surface. This suggests very strongly

that water does not penetrate a polycrystalline C_{60} film in any way — either along the grain boundaries or via diffusion into the interstitial spaces.

3. While the permittivity of water ($\varepsilon' \approx 78.5$ at $T = 300$ K [309]) is certainly high enough to affect the permittivity of the host material that water diffuses into, this increase in permittivity (as usual, accompanied by a loss peak in ε'') would occur at gigahertz frequencies[15], rather than at $\sim 100 - 1000$ Hz frequencies, as is the case in our experiments.

Taken together, these arguments rule out the importance of water as the source for an increase in permittivity and the associated dielectric loss peak in C_{60} at low frequencies. If anything, the presence of water might be responsible for the small discrepancy[16] between the $\varepsilon' = 3.9$ value for permittivity of C_{60} observed in optical experiments [61] and the $\varepsilon' = 4.4$ value observed at 100 kHz [24].

While not participating in dielectric relaxation, water, when accumulated on the surface of the measured film, can increase the conductivity of the film, affecting the measured dielectric properties at low frequencies, as described in Sec. 2.3.4. While a sample in the "sandwich" configuration (Fig. 4-13) does not have an open surface for water condensation, a sample prepared on a microdielectric sensor (Figs. 3-6 and 3-10) does, and dielectric properties measured with dielectrometry can, therefore, be affected by ambient humidity, as demonstrated below.

A microdielectric sensor with 1 μm inter-electrode spacing and 1 m meander length (see Fig. 3-10) was used for this experiment. After the deposition of a 1.88 μm-thick

[15]The large losses in water-containing materials at gigahertz frequencies (corresponding to the onset of the dipole-flipping process, as described in Sec. 2.3) are, in fact, utilized in such diverse applications as food cooking (microwave ovens) and geological surveying (which relies on variations in water content — and, thus, the dielectric constant — of different kinds of soils to map out the geological profile of the land without digging.)

[16]As was mentioned in Sec. 4.6, the other — and considerably more likely — possible reason for this discrepancy is losses associated with rotational motion that C_{60} molecules experience at $T > T_{01}$, reported to center at frequencies on the order of 100 MHz [52, 73]. Surface Acoustic Wave (SAW) experiments in this frequency range should be able to quantitatively ascertain the losses associated with this rotational motion. Preparations for such a study, to be conducted in cooperation with a Raytheon, Inc. research facility, are currently under way.

C_{60} film onto the surface of the sensor, the device was taken out in the air, and the dielectric function of the C_{60} was measured as a function of oxygen diffusion using the Eumetric® System II Microdielectrometer apparatus (Micromet Instruments, Newton, MA), as described in Sec. 3.3.

In Fig. 4-30, we show the evolution of the dielectric properties of the film as a function of exposure to the ambient environment at room temperature. The uppermost dotted line represents the measurement taken within the first minute of exposure. Clearly, in an oxygen-free C_{60} sample, the static dielectric constant is dominated by conduction, since the conductivity of oxygen-free C_{60} films at room temperature is $\sim 10^{-6}$ S·cm^{-1} or less (see Table 4.1). However, in polycrystalline films, oxygen rapidly diffuses into the grain boundaries isolating C_{60} grains (crystallites) one from another and thus quenching the conductivity, reducing it by as much as seven orders of magnitude [257, 260] within a few hours of exposure. (A similar rapid quenching of the photoconductivity by oxygen in C_{60} films has been reported by Minami [310], Asakawa [262], and many others). The increased resistivity due to oxygen causes both the polarization and dielectric loss (decaying dotted curves in Fig. 4-30) to decrease dramatically within 13 hours [see inset to the Fig. 4-30(b)].

The big loss peak accompanied by a polarization increase re-appears again after 13 hours of exposure (solid lines in Fig. 4-30), signaling another increase in sample conduction. We have linked this effect to an increase in ambient relative humidity from ~35% to ~60%. With increased humidity, the moisture condenses on the surface of the sample, "shorting out" the electric field lines of the microdielectric sensor (Fig. 3-6(b)). This underscores the importance of making the sample thick enough (at least on the order of the inter-electrode spacing) when using the microdielectrometry technique.

As the humidity decreases back to its initial value (~35%) during the 28–45 hours of exposure [inset to Fig. 4-30(b)], the conduction-related loss decreases as well [dashed lines in Fig. 4-30(b,c)], and then disappears completely, leaving behind

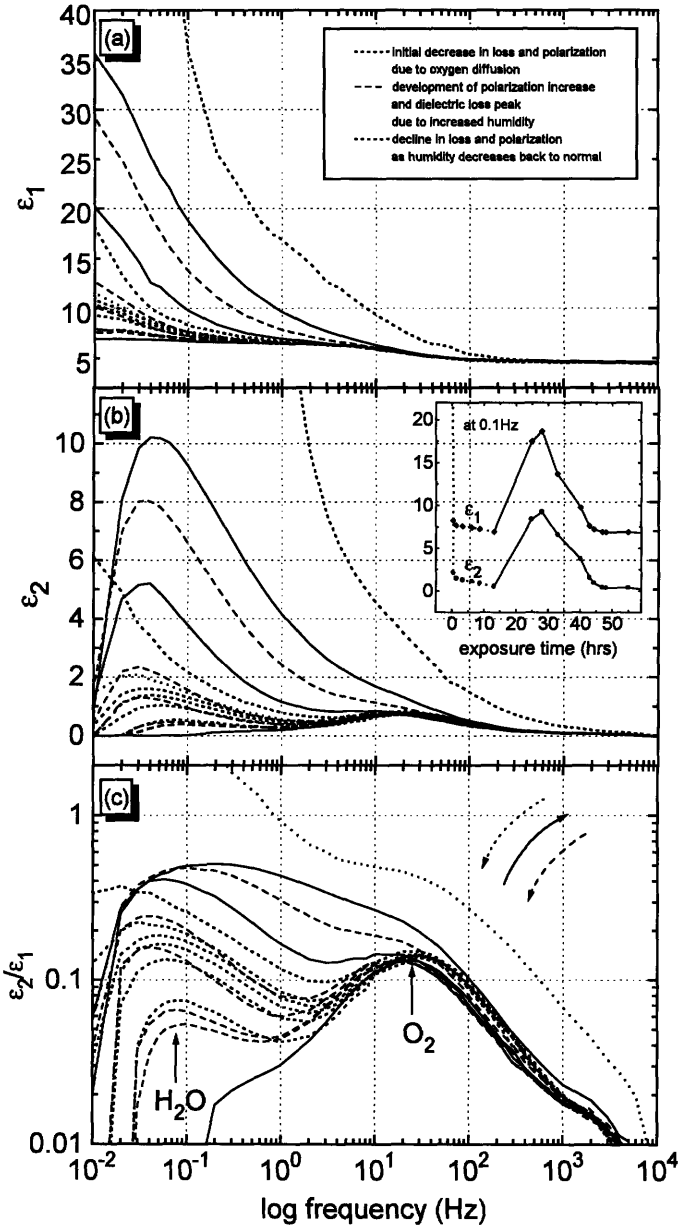


Figure 4-30: Frequency dependence of the real (a) and imaginary (b) parts of the dielectric function of a C_{60} polycrystalline film plotted on a log-linear scale, and the loss tangent (c) plotted on a log-log scale. Water (H_2O) and oxygen (O_2) related loss peaks are identified. The initial decrease in loss and polarization due to quenching of the conduction by inter-grain oxygen is shown by the dotted lines. The solid lines and the inset to plot (b) show the development, and dashed lines show the decay of the loss peak due to the surface moisture (see text). As the humidity decreases back to its initial value (~35%) during hours 28–45 of exposure (inset), the conduction-related loss decreases as well (dashed lines), and then disappears completely, leaving behind the Debye-like dielectric loss peak at ~30 Hz, corresponding to the lowest solid line.

the familiar dielectric loss peak at ~30 Hz due to interstitial oxygen hopping [the dashed line in Fig. 4-30(b,c)].

Note also that, regardless of the low frequency phenomena relating to water and oxygen effects, the relative permittivity ε' of C_{60} films measured with microdielectrometry at 10^5 Hz is in close agreement with $\varepsilon'(10^5\,\text{Hz}) \approx 4.4$ determined from the capacitance measurements of M/C_{60}/M (M=metal) trilayer structures (Sec. 4.6).

From the fact that the oxygen-related dielectric loss peak is not affected by humidity changes, we conclude that, as expected, water does not penetrate into the bulk of C_{60} lattice, but instead condenses on the surface of the film, resulting in large surface conductivity, which appears as a large low frequency loss peak in dielectric measurements (Fig. 4-30). This process is fully reversible and, as the ambient humidity decreases, so does the conductivity-related loss peak.

4.10 Effect of other film treatments

Keeping in mind that the original objective of this study was to produce a high-quality thin-film dielectric out of C_{60}, we have tried a variety of other film treatments, following the general philosophy for film modification outlined in Sec. 4.4. We briefly mention the results here, as they may be important in the future for technological reasons.

As demonstrated in Fig. 4-31, a ten-minute exposure of a ~1000 Å-thick C_{60} film to chlorine improved the film's dielectric properties considerably by both increasing the permittivity by ~15% and reducing the dielectric loss by as much as an order of magnitude. It is almost certain that, unlike oxygen, chlorine reacts with C_{60}, opening up C_{60}'s double bonds and attaching itself to the resulting free radicals [96]. Since the resulting compound appears to have intriguing dielectric properties, as evidenced by the data in Fig. 4-31, its chemical composition merits further investigations.

Similar improvements have been achieved by infusing nitric oxide (NO) into the

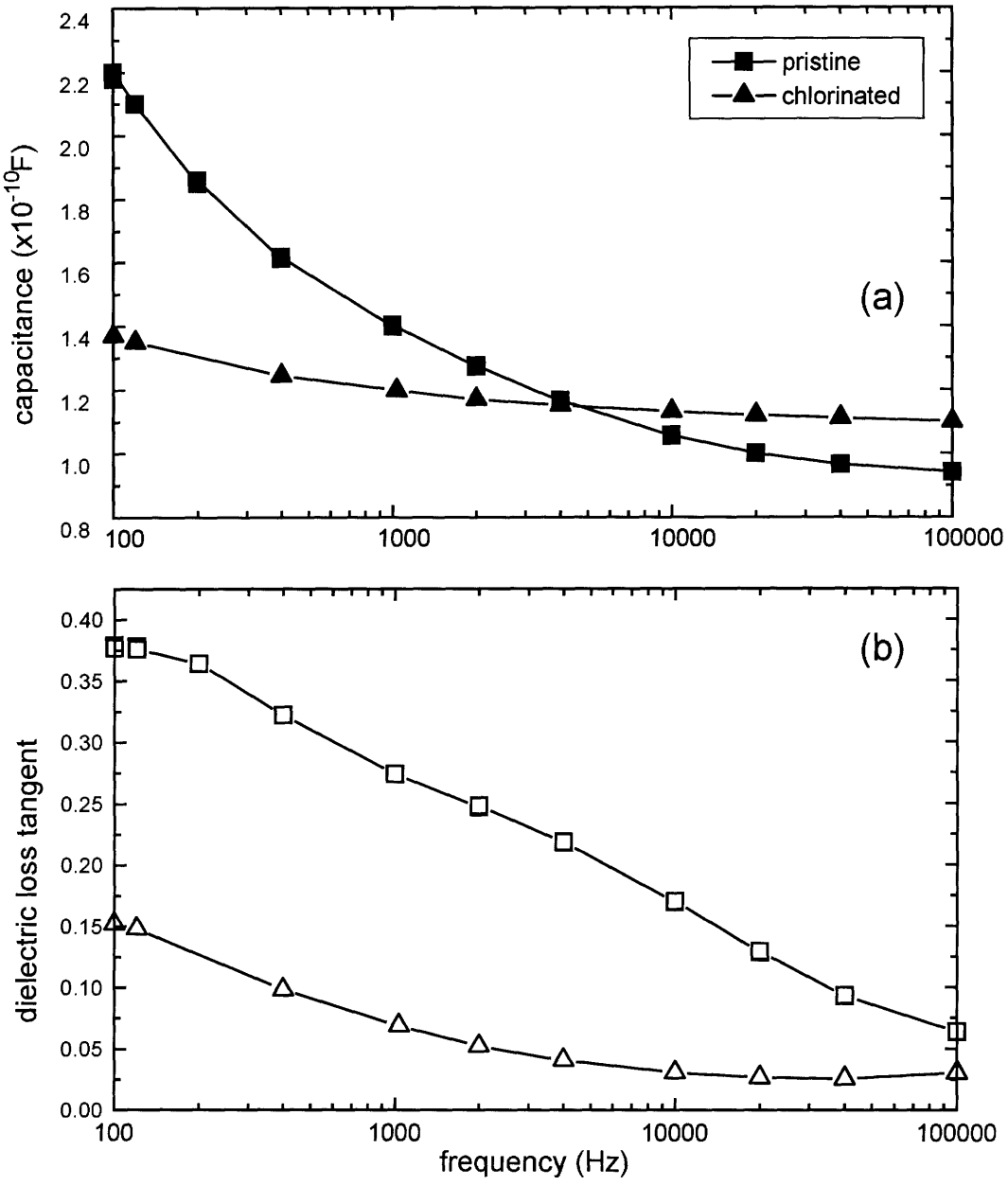


Figure 4-31: (a) Capacitance C and (b) dielectric loss tangent D vs frequency on a log scale showing the effect of 10-minute exposure of a 410 Å-thick C_{60} film to chlorine. A ~15% increase in permittivity and a large reduction in dielectric loss can be inferred from these data, indicating a significant improvement of dielectric properties of the C_{60} film.

C_{60} lattice.[17] By subjecting C_{60} crystalline powder to an NO environment at $T = 100°C$ and $p = 300$ psi for 4 hours, a film composition of $C_{60}(NO)_{0.88}$ has been achieved,[18] as determined by weight uptake measurements. Since NO is dipolar on its own, additional polarization due to NO simply adds to that of the C_{60} intrinsic polarization without introducing any additional loss mechanisms over the frequency range that we are dealing with. The result is a good low-loss dielectric less susceptible to oxygen-induced degradation (because most interstitials are already filled with NO). This achievement would have been of potential practical importance,[19] had it not been for the fact that NO is a highly toxic gas that is usually avoided in industrial environments.

In the two previous examples (Cl_2 and NO), we attempted introduce a "glue" or "filler" material into the interstitials of the fullerite that would make the solid more stable in the ambient environment, while at the same time enhancing its dielectric properties. A different way of achieving the same goal would be to attempt to "seal off" the interstitial spaces of the fullerene lattice by modifying the host material itself. As Fig. 4-32 demonstrates, we have achieved some success with reducing the dielectric loss of C_{60} films by growing them in the presence of UV light. While the physical reason for this effect is unclear, we hypothesize (and X-ray diffraction experiments confirm) that the improvement is due to the fact that the UV-grown films are more disordered (perhaps, cross-linked via photopolymerization, as described in Sec. 1.3.2), thus making it harder for oxygen or other impurities to diffuse into the bulk of the material and compromise its dielectric properties.

Another method to "seal off" the film is to cross-polymerize it, as described in Sec. 1.3.2. In Fig. 4-33, we compare the dielectric functions of pristine and pho-

[17]Using IR spectroscopy, Fastow *et al.* [311] have studied NO adsorption on C_{60} and demostrated that NO interacts relatively strongly with C_{60}. Similarly, a strong interaction has been reported between C_{60} and adsorbed CO [311] and CO_2 [312].

[18]The $C_{60}(NO)_{0.88}$ composition corresponds to the highest NO content that has ever been obtained. More typically, C_{60}/NO composites with somewhat lower NO content are produced [313].

[19]See also Sec. 1.7.6 outlining the possible use of NO to enhance the photosensitivity of C_{60} as a photoresist in microelectronic fabrication applications [139].

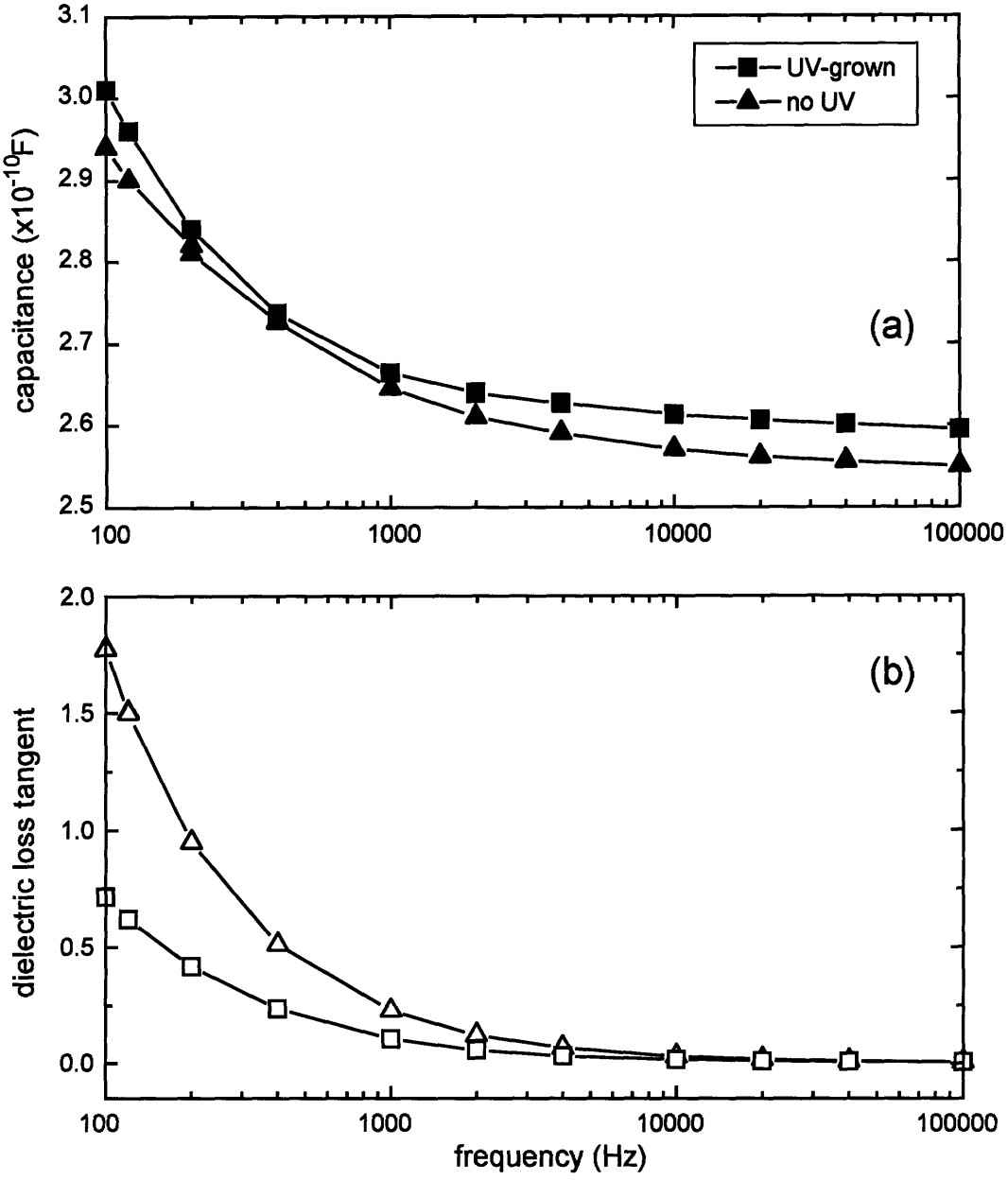


Figure 4-32: Plot of capacitance (a) and dielectric loss tangent (b) vs frequency (on the log scale) for C_{60} films of 1600 Å thickness grown in the absence (triangles) and in the presence (squares) of UV light during deposition. The data display evidence of lower dielectric loss at low frequency in UV-grown C_{60} films.

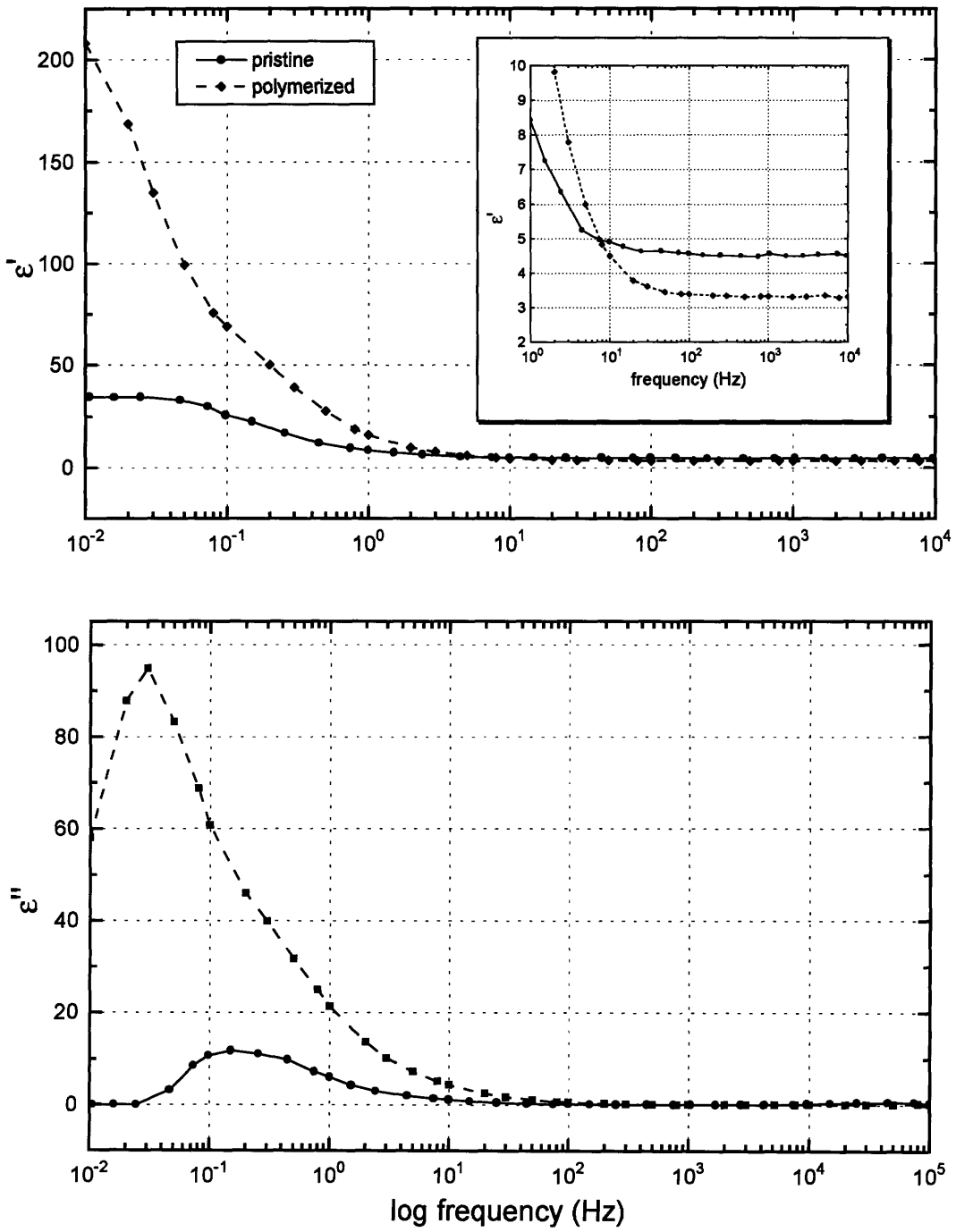


Figure 4-33: Real (ε') and imaginary (ε'') parts of the dielectric function of a 1191 Å C_{60} film before and after photopolymerization with a 488 nm Ar-ion laser source in vacuum for 10 hours at an average fluence of 1 W/cm^2. The measurement was performed using the Micron sensor.

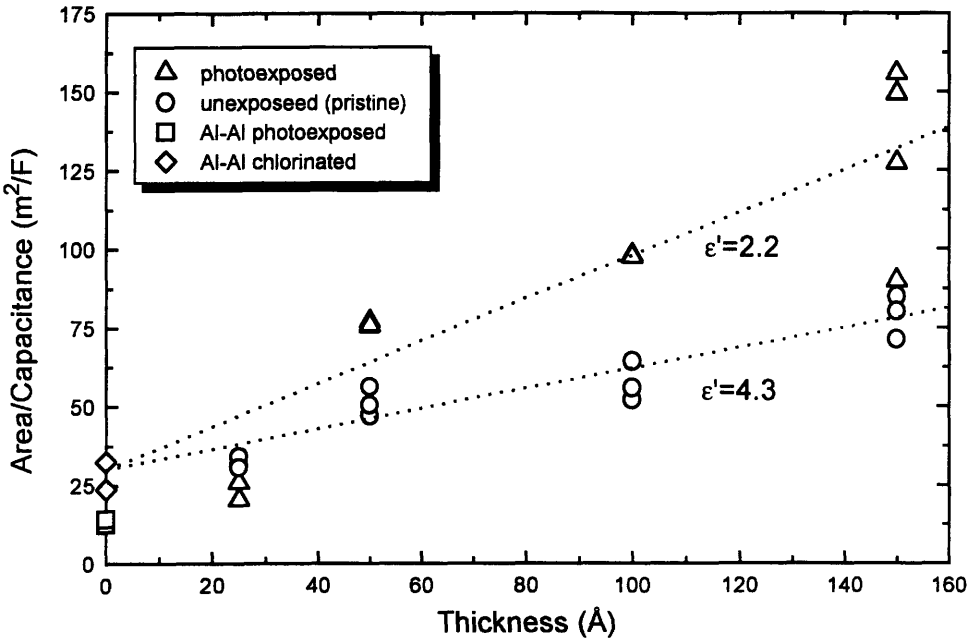


Figure 4-34: Plot of the reciprocal areal capacitance A/C vs thickness for pristine (circles) and UV-polymerized (triangles) C_{60} films demonstrating that UV-polymerization decreases the real part of the dielectric constant ε'. Control data points for photoexposed (squares) and chlorinated (diamonds) Al-Al_2O_3(ML)-Al junctions (without any C_{60}) are shown for reference.

topolymerized 1191 Å-thick C_{60} films measured with the Microdielectrometer. The most interesting finding, shown in the inset plot, is that the intrinsic dielectric constant of the polymerized C_{60} film ($\varepsilon' \approx 2.3$) is *lower* than that of the pristine C_{60} film ($\varepsilon' \approx 4.5$). This finding is consistent with the thickness dependence study presented in Fig. 4-34, in which we compare the dielectric constants of pristine and photoexposed fullerene films by showing a linear dependence of the inverse capacitance $1/C$ on thickness ℓ for each film.

Chapter 5

Conclusions and Future Work

5.1 Conclusions

We used dielectric spectroscopy to measure the frequency and temperature dependence of the low frequency dielectric function $\varepsilon(\omega)$ of thin C_{60} films. We found that oxygen rapidly diffuses into the grain boundaries of the C_{60} polycrystalline film, increasing its resistivity by about seven orders of magnitude. Water, on the other hand, does not penetrate into the bulk of C_{60} solid, and the increase in conduction resulting from its presence on the surface of a C_{60} film is fully reversible.

In order to explain the Debye-like dielectric loss peak and the accompanying increase in polarization observed at $\sim$35 Hz, a small charge transfer is inferred between the C_{60} and O_2 molecules which occupy interstitial spaces of C_{60} solid exposed to oxygen (or ambient air). Due to the large size of the C_{60} molecules, this small charge transfer creates large dipole moments, which in turn are coupled to the applied AC electric field via a *diffusion-controlled relaxation* mechanism. These dipole moments are responsible for a significant increase of permittivity ε' at low frequencies.

With increasing oxygenation, the interstitial sites become nearly fully occupied, interstitial hopping is inhibited, and the loss peaks, together with the enhanced polarizations, disappear.

We note that C_{60} can be thought of as a rather potent "charge sponge." In M_3C_{60} (M=alkali metal), this leads to fascinating superconducting compounds (Sec. 1.5); in thin-film $\{Al\text{-}C_{60}\}_n$ multilayer structures, charge transfer leads to interesting interface effects [273]; and in our study, charge transfer leads to extraordinary additional polarization.

We conclude that dielectric and, especially, microdielectric spectroscopy can be used to assess the content of oxygen or other impurities in the interstitial spaces of C_{60} solid. Both tracer and chemical diffusion coefficients can be determined. We have used this technique to ascertain the effect of various intercalants on the dielectric properties of C_{60} films.

5.2 Possible Applications

The original goal of our research has been to engineer a good, low-loss thin-film dielectric material out of C_{60}. We have shown that, by treating the film with certain agents (molecular oxygen, nitric oxide, and chlorine), the dielectric properties of C_{60} films can indeed be improved. This may lead to potentially technologically important uses of C_{60}-derived materials in thin film electronic applications.

Much of this work was devoted to the development of scientific background for understanding the mechanism of diffusion of oxygen and other species through the bulk of the fullerite. This enhanced understanding may also prove to be technologically important, as suitable fullerene structures may provide the means to selectively separate gas mixtures. For identical time duration, pressure, and temperature conditions, while significant quantities of oxygen or NO can be incorporated into the lattice, there is no evidence that either methane [244] or nitrogen (N_2) [252] gases diffuse into the lattice. The selectivity is controlled by the channel size between interstitial sites. The channel size is, in turn, precisely determined by the fullerene size and crystal structure. Thus, extremely high levels of selectivity may be expected if the effective

channel size is intermediate to the diameters of the molecules being separated. The separation process could be based on the selectivity of fullerenes to gas sorption, or, if the fullerenes are formed in a membrane [67], could be based on their selectivity to gas permeation.

A related possible application is using fullerene materials as gas adsorbants for gas storage, as well as for controlled gas release over time. Finally, with increasing interest in using fullerenes in advanced batteries, low frequency AC measurements of fullerene materials are becoming increasingly important.

5.3 Future Work

As mentioned in Sec. 4.7.4, a thickness dependence study with Al-C_{60}-Al trilayers is needed to further clarify the significance of electrode effects in our dielectric measurements. By varying the thickness of the C_{60} layer, it should be possible to reliably isolate bulk C_{60} properties from the interface effects. Preparations for such a study are currently under way.

Also, the hypothesis that the activation energy of the dielectric loss peak frequency E_τ is equal to the activation energy of the DC conductivity E_σ for C_{60} at $T > T_{01}$ (Sec. 4.8.1) needs further confirmation. More temperature dependence studies similar to that described in Sec. 4.8.1 are therefore needed.

Much of the fullerene-related work that the author has performed both at MIT and at Bell Labs is beyond the scope of this thesis. Some of the topics not mentioned here include:

- Molecular dynamics simulations of fullerene vibrational modes.
- Monte-Carlo simulation of oxygen diffusion in C_{60} lattice.
- Extensive investigations of photoconducting properties of pristine and photopolymerized C_{60}.

- Dielectric, transport, and photoconductivity measurements of C_{70}. There are indications that C_{70} may outperform C_{60} as a host material for many of the applications mentioned above. C_{70}-based compounds, therefore, merit further investigation.

- NO/C_{60} compounds looks very promising for both dielectric and microelectronics applications, and should be studied more rigorously.

- It has been observed that C_{60} interfaces with various metals may be fractal in nature. If so, the AC properties of such interfaces may exhibit interesting scaling behavior.

- Endohedral fullerenes are almost certain to have a very high dielectric constant due to their large intrinsic dipole moments. Unfortunately, the study of their bulk properties has so far been hampered by their unavailability in anything but trace amounts.

Appendix A

LabView Software Listings

The following pages contain listings of LabVIEW [314] virtual instrument (VI) drivers that we developed for the experimental configurations described in Sections 3.2.3 and 3.3. For each instrument, both the virtual instrument's front panel and the wiring diagram are presented. In some cases, the VI's position in hierarchy is also shown.

A.1 HP 4274A Impedance Bridge

See Figures A-1 through A-3.

A.2 SI 1254 Frequency Response Analyzer

See Figures A-4 and A-5.

A.3 Microdielectrometer

See Figures A-6 through A-8.

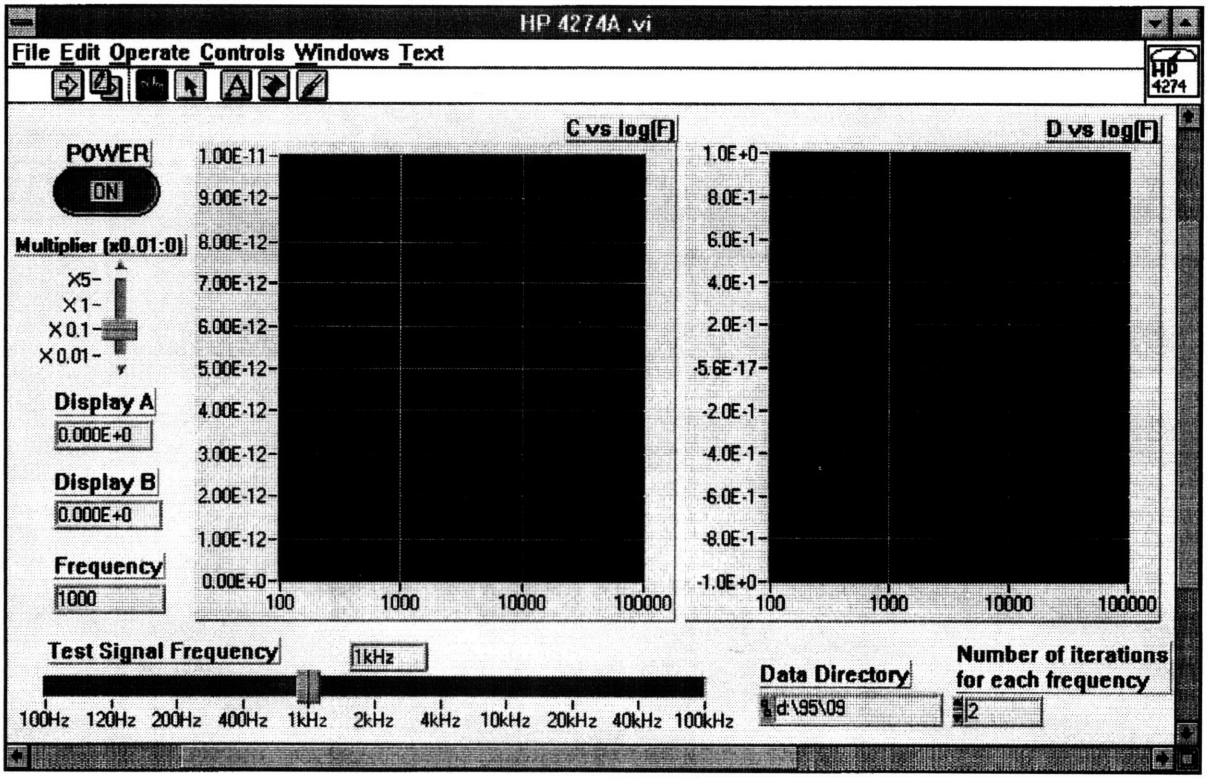


Figure A-1: HP 4274A VI's front panel.

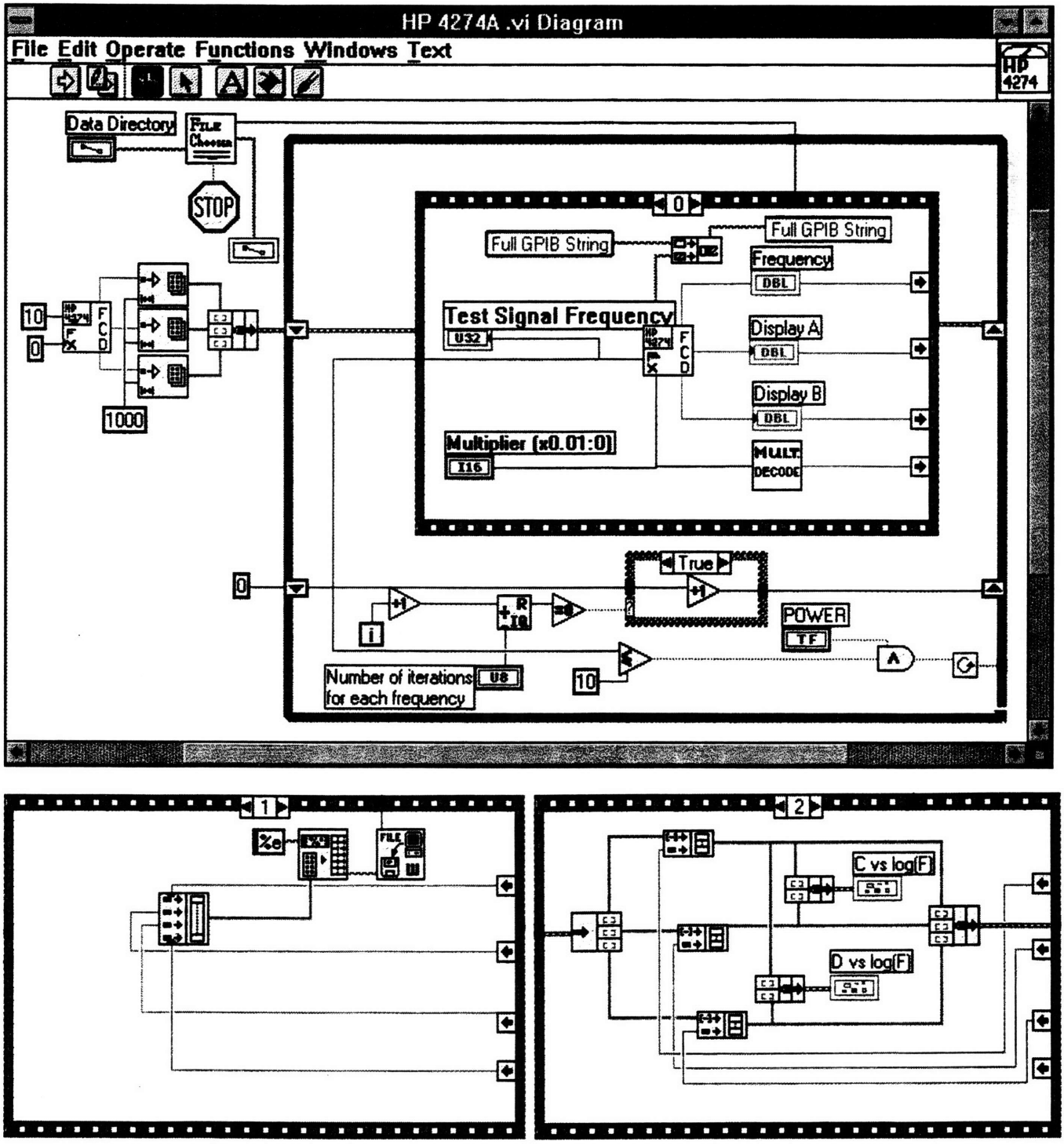


Figure A-2: HP 4274A VI's wiring diagram. The two embedded frames of the sequence structure are shown separately.

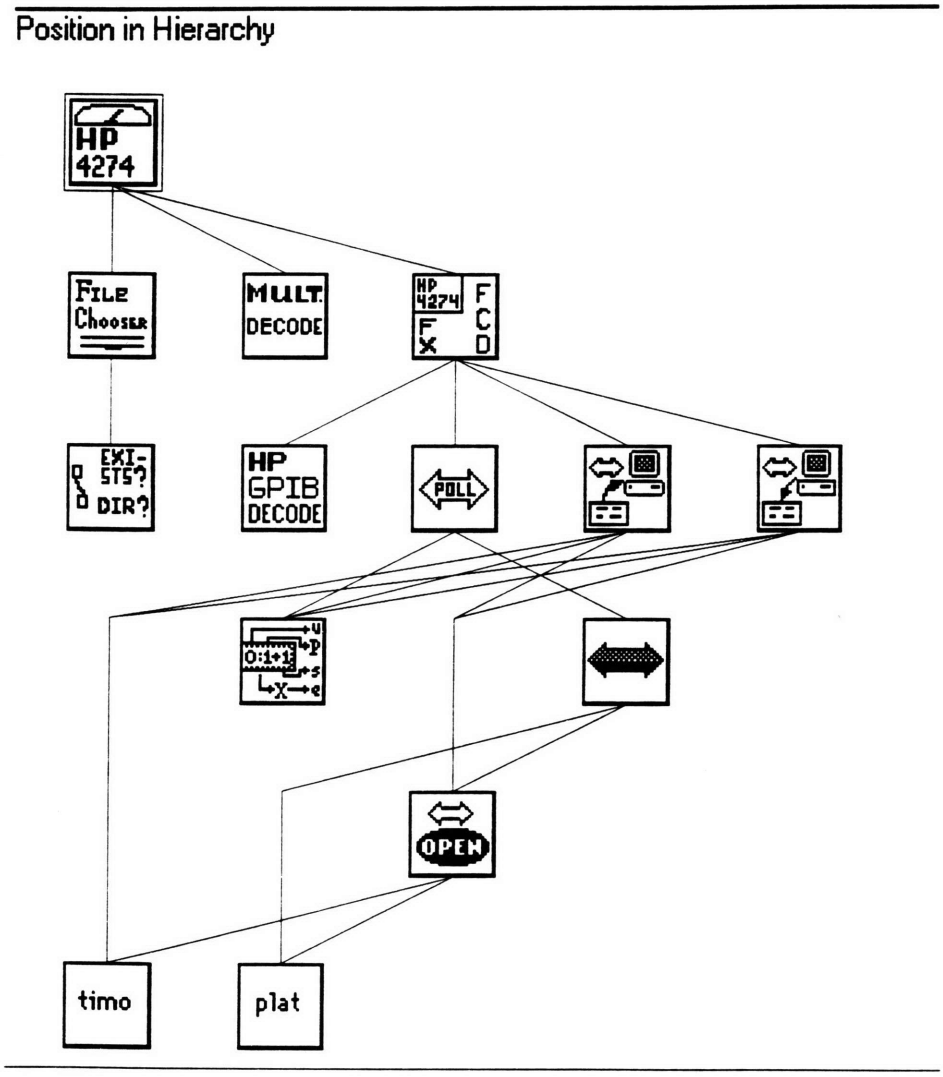


Figure A-3: HP 4274A VI's position in hierarchy.

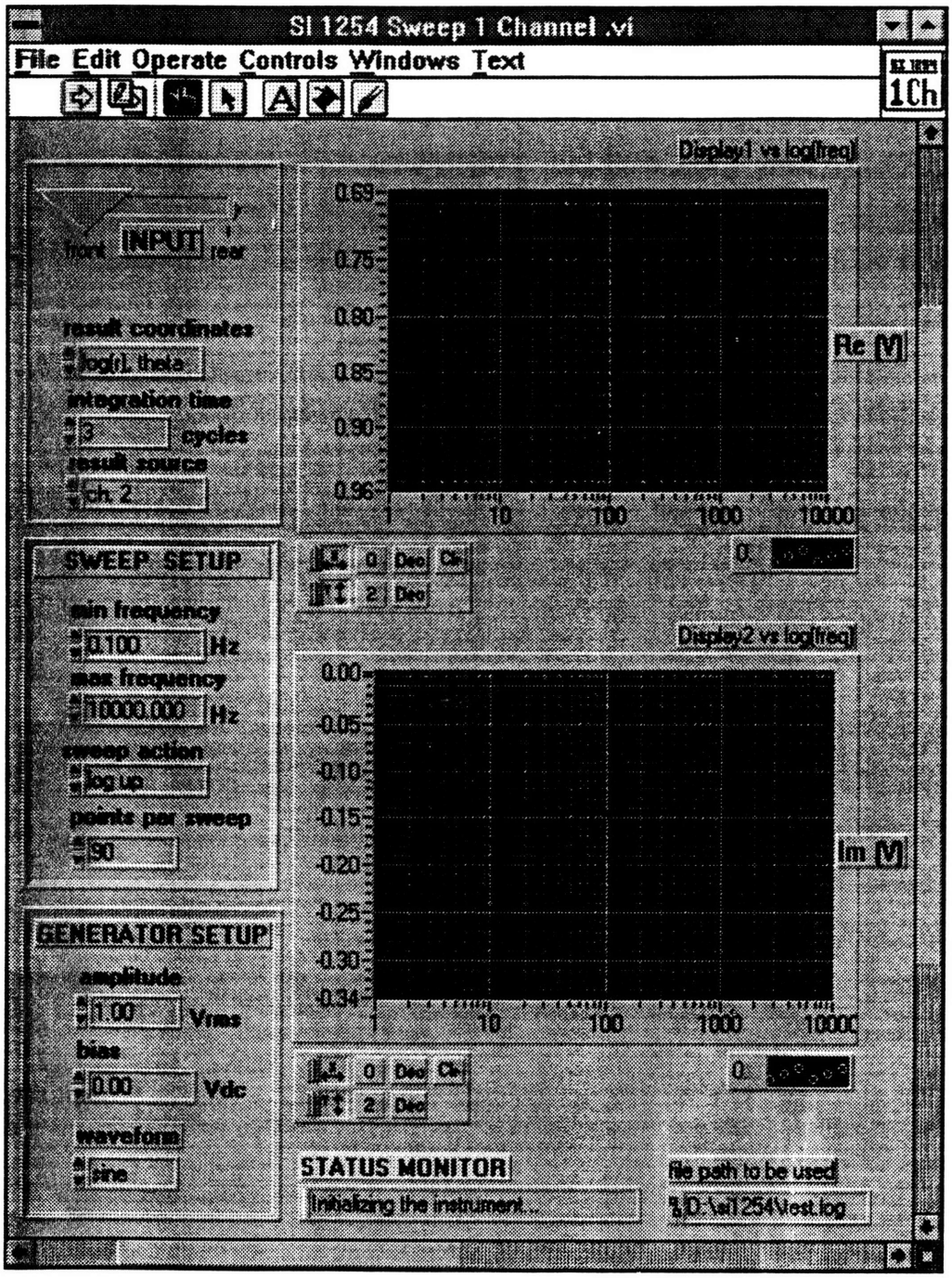


Figure A-4: SI 1254 VI's front panel.

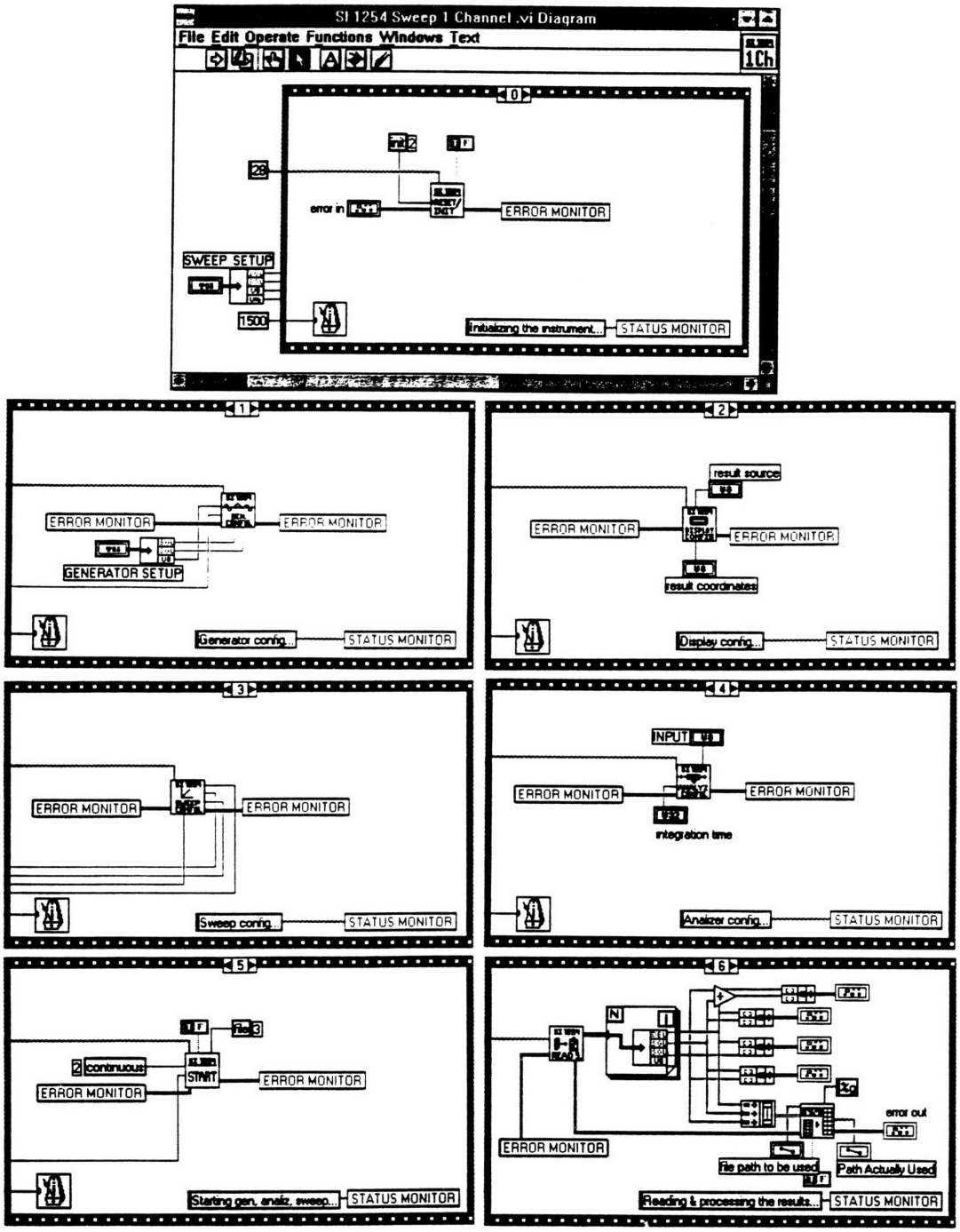


Figure A-5: SI 1254 VI's wiring diagram. The six embedded frames of the sequence structure are shown separately.

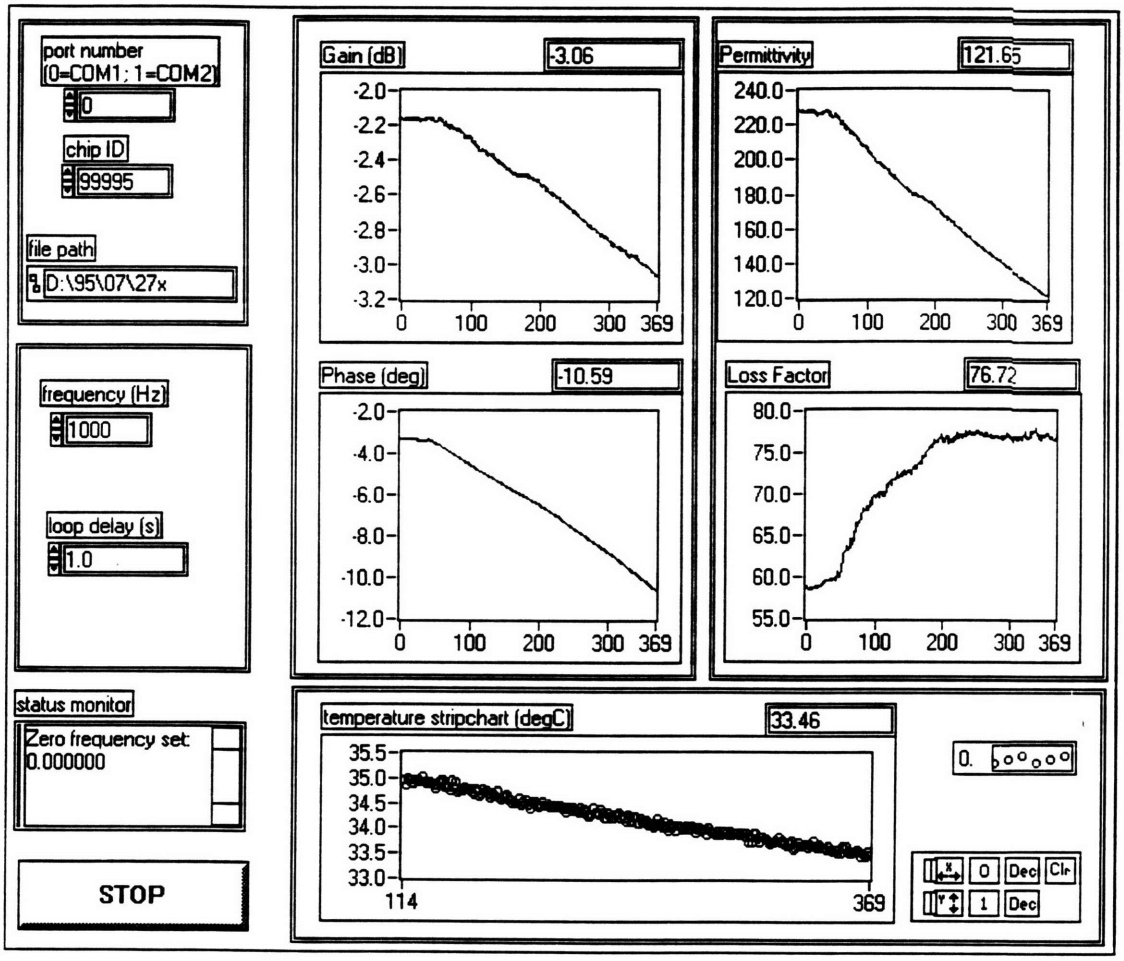


Figure A-6: The Microdielectrometer VI's front panel displaying results of a representative data acquisition run.

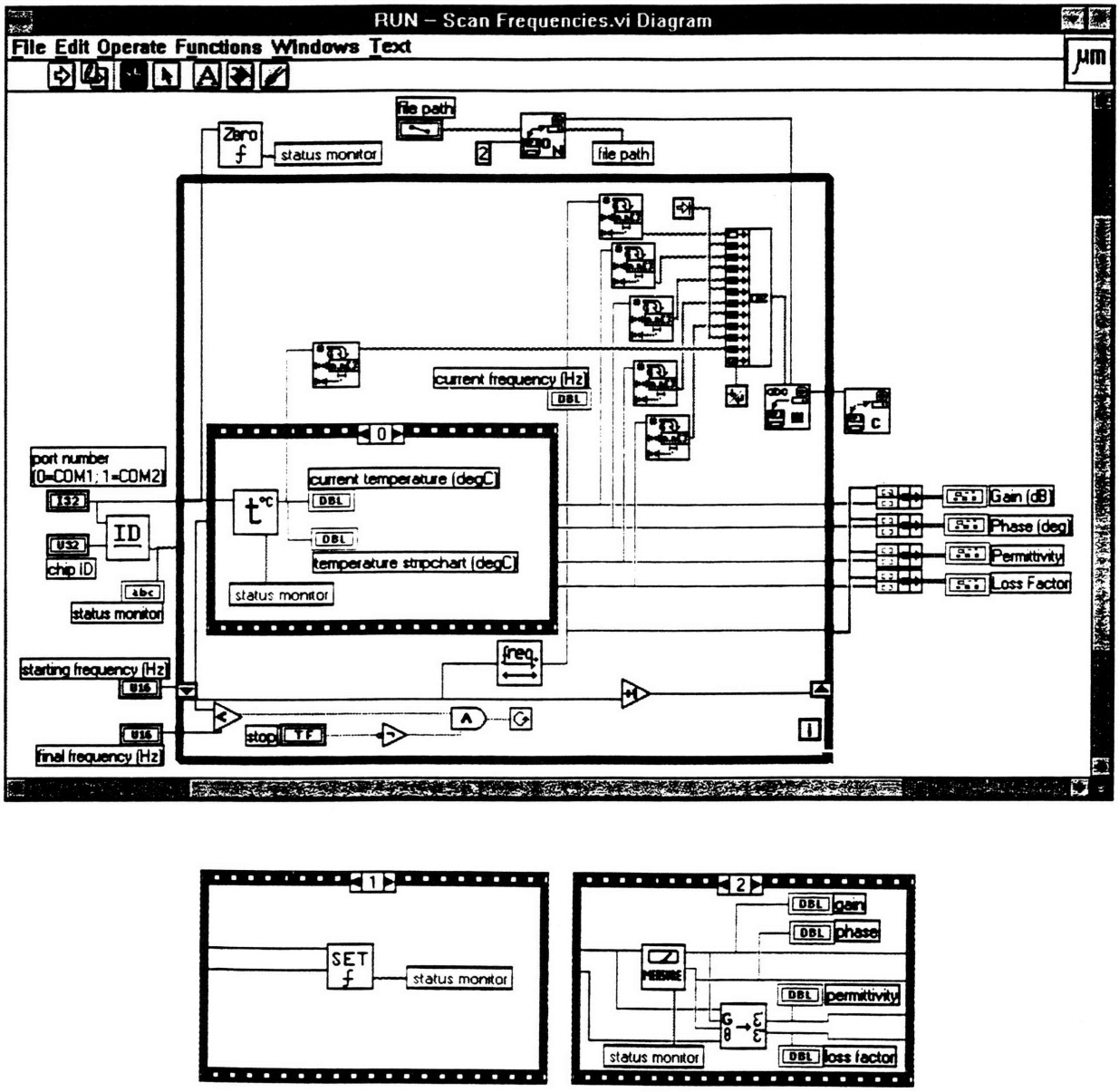


Figure A-7: The Microdielectrometer VI's wiring diagram. The two embedded frames of the sequence structure are shown separately.

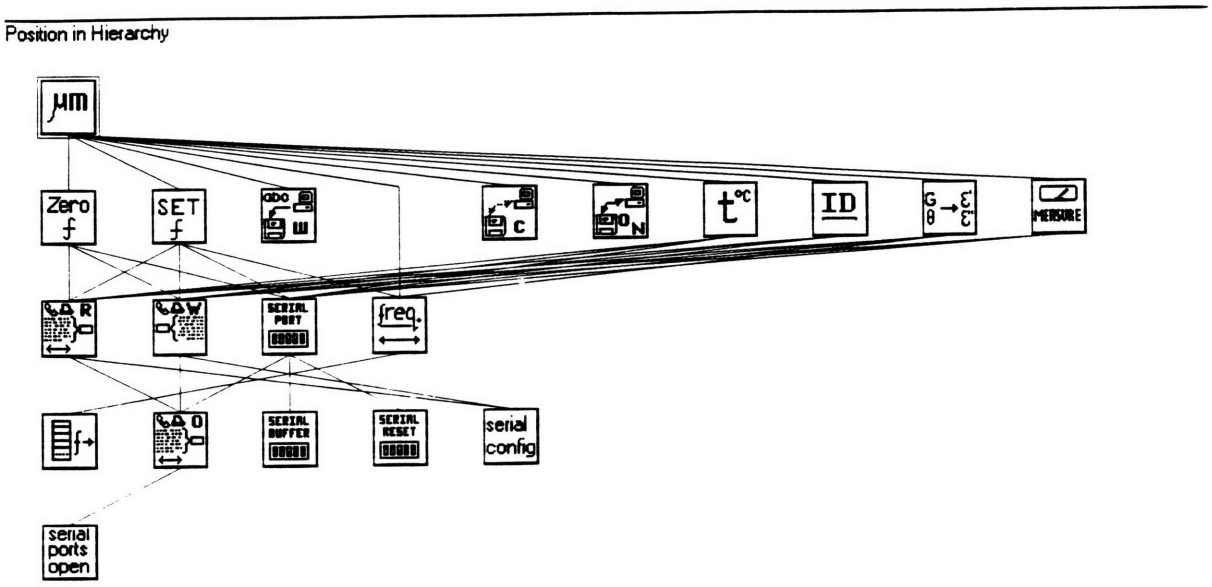


Figure A-8: The Microdielectrometer VI's position in hierarchy.

Bibliography

[1] H. W. Kroto, J. R. Heath, S. C. O'Brien, R. F. Curl, and R. E. Smalley. Space, stars, C_{60} and soot. *Nature (London)*, 318:162–163, 1985.

[2] D. E. Koshland. *Science*, 254(5039):1705–1707, 20 Dec 1991.

[3] S. D. Senturia and N. F. Sheppard. *Dielectric Analysis of Thermoset Cure*, volume 80 of *Advances in Polymer Science*, pages 1–47. Springer-Verlag, Berlin, 1986.

[4] R. Buckminster Fuller. *Inventions: The Patented Works of R. Buckminster Fuller.* St. Martin's Press, New York, 1983.

[5] R. Buckminster Fuller. In W. Marlin, editor, *The Artifacts of R. Buckminster Fuller: A Comprehensive Collection of His Designs and Drawings*, New York, 1984. Garland Publishing.

[6] A. F. Hebard. Buckminsterfullerene. *Annual review of materials science, V23*, 23:159–191, 1993.

[7] W. Kratschmer, Lowell D. Lamb, K. Fostiropoulos, and D. R. Huffman. Solid C_{60}: a new form of carbon. *Nature (London)*, 347:354–358, 1990.

[8] H. W. Kroto, A. W. Allaf, and S. P. Balm. C_{60}: Buckminsterfullerene. *Chem. Rev.*, 91:1213–1235, 1991.

[9] H. W. Kroto. Space, stars, C_{60} and soot. *Science*, 242:1139–1145, 1988.

[10] R. S. Lewis, T. Ming, J. F. Wacker, E. Anders, and E. Steel. *Nature (London)*, 326:160, 1987.

[11] P. R. Buseck, S. J. Tsipursky, and R. Hettich. Fullerenes from the geological environment. *Science*, 257(5067):215–217, 1992.

[12] Ivan Amato. Materials science: A first sighting of buckyballs in the wild. *Science*, 257(5067):167, 1992.

[13] R.F. Curl and R.E. Smalley. *Science*, 242:7779, 1988.

[14] E.A. Rohlfing, D.M. Cox, and A. Kaldor. *J. Chem. Phys.*, 81:3322, 1984.

[15] R. F. Curl and R. E. Smalley. Fullerenes. *Scientific American*, pages 54–63, October 1991.

[16] S. Iijima. Helical microtubules of graphitic carbon. *Nature (London)*, 354:56–58, 1991.

[17] C. H. Kiang, W. A. Goddard, III, R. Beyers, J. R. Salem, and D. S. Bethune. Catalytic synthesis of single-layer carbon nanotubes with a wide range of diameters. *J. Phys. Chem.*, 98:6612–6618, 1994.

[18] C. H. Kiang, W. A. Goddard III, R. Beyers, and D. S. Bethune. Carbon nanotubes with single-layer walls. *Carbon*, 33:903, 1995.

[19] M. S. Dresselhaus, G. Dresselhaus, and P. C. Eklund. Fullerenes. *Journal of Materials Research*, 8(8):2054–2097, 1993.

[20] H. W. Kroto. C_{60}: Buckminsterfullerene, the celestial sphere that fell to earth. *Angewandte Chemie (International Edition in English)*, 31(2):111–129, 1992.

[21] R. Taylor and D. R. M. Walton. The chemistry of fullerenes. *Nature (London)*, 363(6431):685–693, 1993.

[22] J. H. Weaver and D. M. Poirier. Solid state properties of fullerenes and fulleride. In H. Ehrenreich and F. Spaepen, editors, *Solid State Physics*, volume 48, page 1, New York, 1994. Academic Press. Chapter 1.

[23] M. S. Dresselhaus, G. Dresselhaus, and P. C. Eklund. *Science of Fullerenes and Carbon Nanotubes.* Academic Press, New York, 1995.

[24] A. F. Hebard, R. C. Haddon, R. M. Fleming, and A. R. Kortan. Deposition and characterization of fullerene films. *Appl. Phys. Lett*, 59(17):2109–2111, 21 Oct 1991.

[25] S. L. Ren, Y. Wang, A. M. Rao, E. McRae, J. M. Holden, T. Hager, K. Wang, W.-T. Lee, H. F. Ni, J. P. Selegue, and P. C. Eklund. Ellipsometric determination of the optical constants of C_{60} (buckminsterfullerene) films. *Appl. Phys. Lett.*, 59(21):2678–2680, 1991.

[26] R. L. Meng, D. Ramirez, X. Jiang, P. C. Chow, C. Diaz, K. Matsuishi, S. C. Moss, P. H. Hor, and C. W. Chu. Growth of large, defect free pure C_{60} single crystals. *Appl. Phys. Lett.*, 59(26):3402–3403, 1991.

[27] H. E. Huntley. *The divine proportion.* Dover Publications, New York, 1970.

[28] F. Chung and S. Sternberg. Laplacian and vibrational spectra for homogeneous graphs. *Journal of Graph Theory*, 16(6):605–627, 1992.

[29] F. Chung and S. Sternberg. Mathematics and the buckyball. *American Scientist*, 81(1):56–71, 1993.

[30] F. Chung, B. Kostant, and S. Sternberg. *Groups and the buckyball.* Birkhäuser, 1994.

[31] B. Kostant. Structure of the truncated icosahedron (such as Fullerene or viral coatings) and a 60-element conjugacy class in PSl(2,11). *Proc. Natl. Acad. Sci.*, 91:11714–11717, 1994.

[32] B. Kostant. Structure of the truncated icosahedron (e.g. Fullerene or C_{60}, viral coatings) and a 60-element conjugacy class in PSl(2,11). *Selecta Mathematica, New Series*, 1:163–195, 1995.

[33] B. Kostant. The graph of the truncated icosahedron and the last letter of Galois. *Notices of the AMS*, 42(9):959–968, 1995.

[34] W. I. F. David, R. M. Ibberson, J. C. Matthewman, K. Prassides, T. J. S. Dennis, J. P. Hare, H. W. Kroto, R. Taylor, and D. R. M. Walton. *Nature (London)*, 353:147, 1991.

[35] R. D. Johnson, G. Meijer, and D. S. Bethune. *J. Am. Chem. Soc.*, 112:8983–8984, 1990.

[36] R. D. Johnson, D. S. Bethune, and C. S. Yannoni. Fullerene structure and dynamics: A magnetic resonance potpourri. *Accounts of Chemical Research*, 25(3):169–175, 1992.

[37] C. Christides, T. J. S. Dennis, K. Prassides, R. L. Cappelletti, D. A. Neumann, and J. R. D. Copley. Rotational dynamics of solid C_{70}: A neutron scattering study. *Phys. Rev. B*, 49(4):2897–2903, 1994.

[38] S. Saito and A. Oshiyama. Electronic and geometric structures of C_{70}. *Phys. Rev. B*, 44:11532, 1991.

[39] H. D. Beckhaus, C. Rüchardt, M. Kao, F. Diederich, and C. S. Foote. The stability of buckminsterfullerene (C_{60}): Experimental determination of the heat of formation. *Angewandte Chemie (International Edition in English)*, 31(1):63–64, 1992.

[40] D. L. Lichtenberger, K. W. Nebesny, C. D. Ray, D. R. Huffman, and L. D. Lamb. Valence and core photoelectron spectroscopy of C_{60} buckminsterfullerene. *Chem. Phys. Lett.*, 176(2):203–208, 1991.

[41] A. Tokmakoff, D. R. Haynes, and S. M. George. *Chem. Phys. Lett.*, 186:450, 1991.

[42] G. Dresselhaus, M. S. Dresselhaus, and J. G. Mavroides. Spin-orbit interaction in graphite. *Carbon*, 4:433, 1966.

[43] J. DeVries, H. Steger, and B. Kamke et al. Single photon ionization of C_{60}-fullerene and C_{70}-fullerene with synchrotron radiation: Determination of the ionization potential of C_{60}. *Chem. Phys. Lett.*, 188(3-4):159–162, 1992.

[44] H. Steger, J. DeVries, and B. Kamke et al. Direct double ionization of C_{60} and C_{70} fullerenes using synchrotron radiation. *Chem. Phys. Lett.*, 194(4-6):452–456, 1992.

[45] A. M. Rao, P. Zhou, K. A. Wang, G. T. Hager, J. M. Holden, Y. Wang, W.-T. Lee, X.-X. Bi, P. C. Eklund, D. S. Cornett, M. A. Duncan, and I. J. Amster. Photoinduced polymerization of solid C_{60} films. *Science*, 259(5097):955–957, 1993.

[46] A. R. Kortan, N. Kopylov, S. Glarum, E. M. Gyorgy, A. P. Ramirez, R. M. Fleming, F. A. Thiel, and R. C. Haddon. Superconductivity at 8.4K in calcium-doped C_{60}. *Nature (London)*, 355(6360):529–532, 1992.

[47] P. W. Stephens, L. Mihaly, P. L. Lee, R. L. Whetten, S. M. Huang, R. Kaner, F. Diederich, and K. Holczer. Structure of single-phase superconducting K_3C_{60}. *Nature (London)*, 351:632, 1991.

[48] M. B. Jost, N. Troullier, D. M. Poirier, J. L. Martins, J. H. Weaver, L. P. F. Chibante, and R. E. Smalley. Electronic states of solid C_{60}. *Phys. Rev. B*, 44:1966–1969, 1991.

[49] J. E. Fischer, P. A. Heiney, A. R. McGhie, W. J. Romanow, A. M. Denenstein, J. P. McCauley, Jr., and A. B. Smith III. *Science*, 252:1288, 1991.

[50] S. J. Woo, S. H. Lee, E. Kim, K. H. Lee, Y. H. Lee, S. Y. Hwang, and I. C. Jeon. Bulk modulus of the C_{60} molecule via the tight binding method. *Physics Letters A*, 162(6):501–505, 1992.

[51] S. J. Duclos, K. Brister, R. C. Haddon, A. R. Kortan, and F. A. Thiel. *Nature (London)*, 351:380, 1991.

[52] X. D. Shi, A. R. Kortan, J. M. Williams, A. M. Kini, B. M. Saval, and P. M. Chaikin. Sound velocity and attenuation in single crystal C_{60}. *Phys. Rev. Lett.*, 68(6):827–830, 1992.

[53] J. E. Fischer. Structure and dynamics of solid C_{60} and its intercalation compounds. *Materials Science and Engineering Pt B, Solid State Materials for Advanced Technology*, 19(1-2):90–99, 1993.

[54] G. Kriza, J. C. Ameline, J. Jerome, A. Dworkin, H. Szwarc, C. Fabre, D. Schutz, A. Rassat, and P. Bernier. *J. Phys. I, France*, 1:1361, 1991.

[55] G. A. Samara, J. E. Schirber, B. Morosin, L. V. Hansen, D. Loy, and A. P. Sylwester. *Phys. Rev. Lett.*, 67:3136, 1991.

[56] P. A. Heiney, G. B. M. Vaughan, J. E. Fischer, N. Coustel, D. E. Cox, J. R. D. Copley, D. A. Neumann, W. A. Kamitakahara, K. M. Creegan, D. M. Cox, J. P. McCauley, Jr., and A. B. Smith III. Discontinuous volume change at the orientational ordering transition in solid C_{60}. *Phys. Rev. B*, 45(8):4544–4547, 1992.

[57] E. Grivei, B. Nysten, M. Cassart, A. Demain, and J. P. Issi. Specific heat of fullerenes extract. *Solid State Commun.*, 85(2):73–75, 1993.

[58] E. Grivei, M. Cassart, J. P. Issi, L. Langer, B. Nysten, J. P. Michenaud, C. Fabre, and A. Rassat. Anomalous specific heat of C_{60}. *Phys. Rev. B*, 48(11):8514–8516, 1993.

[59] R. C. Yu, N. Tea, M. B. Salamon, D. Lorens, and R. Malhotra. Thermal conductivity of single crystal C_{60}. *Phys. Rev. Lett.*, 68(13):2050–2053, 1992.

[60] C. Wen, J. Li, K. Kitazawa, T. Aida, I. Honma, H. Komiyama, and K. Yamada. Electrical conductivity of a pure C_{60} single crystal. *Appl. Phys. Lett.*, 61(18):2162–2163, 1992.

[61] Y. Wang, J. M. Holden, A. M. Rao, W. T. Lee, X. X. Bi, S. L. Ren, G. W. Lehman, G. T. Hager, and P. C. Eklund. Interband dielectric function of C_{60} and M_6C_{60} (M = K, Rb, Cs). *Phys. Rev. B*, 45(24):14396–14399, 1992.

[62] J. E. Fischer, D. E. Luzzi, and K. Kniaz et al. Existence of high order superlattices in orientationally ordered C_{60}. *Phys. Rev. B*, 47(21):14614–14617, 1993.

[63] J. Abrefah, D. R. Olander, M. Balooch, and W. J. Siekhaus. Vapor pressure of buckminsterfullerene. *Appl. Phys. Lett.*, 60(11):1313–1314, 1992.

[64] C. Pan, M. P. Sampson, Y. Chai, R. H. Hauge, and J. L. Margrave. Heats of sublimation from a polycrystaline mixture of C_{60} and C_{70}. *J. Phys. Chem.*, 95:2944, 1991.

[65] E. J. Kim, Y. H. Lee, and J. Y. Lee. Fragmentation of C_{60} and C_{70} clusters. *Phys. Rev. B*, 48(24):18230–18234, 1993.

[66] A. Lundin and B. Sundqvist. Compressibility of C_{60} between 150 and 355K and up to 1GPa. *Europhys. Lett.*, 27:463, 1994.

[67] C. B. Eom, A. F. Hebard, L. E. Trimble, G. K. Celler, and R. C. Haddon. Fabrication and properties of freestanding C_{60} membranes. *Science*, 259(5103):1887–1890, 1993.

[68] K. Prassides, H. W. Kroto, and R. Taylor et al. Fullerenes and fullerides in the solid state: Neutron scattering studies. *Carbon*, 30(8):1277–1286, 1992.

[69] W. I. F. David, R. M. Ibberson, T. J. S. Dennis, J. P. Hare, and K. Prassides. Structural phase transitions in the fullerene C_{60}. *Europhysics Letters*, 18(3):219–225, 1992.

[70] A. Dworkin, H. Szwarc, S. Leach, J. P. Hare, T. J. Dennis, H. W. Kroto, R. Taylor, and D. R. M. Walton. *C.R. Acad. Sci., Paris Serie II*, 312:979, 1991.

[71] Y. Maruyama, T. Inabe, H. Ogata, Y. Achiba, S. Suzuki, K. Kikuchi, and I. Ikemoto. *Chem. Lett.*, 10:1849, 1991.

[72] R. Tycko, G. Dabbagh, R. M. Fleming, R. C. Haddon, A. V. Makhija, and S. M. Zahurak. Molecular dynamics and the phase transition in solid C_{60}. *Phys. Rev. Lett.*, 67(14):1886, 1991.

[73] C. S. Yannoni, R. D. Johnson, G. Meijer, D. S. Bethune, and J. R. Salem. ^{13}C NMR study of the C_{60} cluster in the solid state: Molecular motion and carbon chemical shift anisotropy. *J. Phys. Chem.*, 95:9–10, 1991.

[74] P. H. M. van Loosdrecht, P. J. M. van Bentum, and G. Meijer. Rotational ordering transition in single crystal C_{60} studied by Raman spectroscopy. *Phys. Rev. Lett.*, 68(8):1176–1179, 1992.

[75] W. P. Beyermann, M. F. Hundley, and J. D. Thompson et al. Low temperature specific heat of C_{60}. *Phys. Rev. Lett.*, 68(13):2046–2049, 1992.

[76] G. B. Alers, B. Golding, A. R. Kortan, R. C. Haddon, and F. A. Theil. Existence of an orientational electric dipolar response in C_{60} single crystals. *Science*, 257(5069):511–514, 1992.

[77] G. Vantendeloo, S. Amelinckx, and M. A. Verheijen et al. New orientationally ordered low temperature superstructure in high purity C_{60}. *Phys. Rev. Lett.*, 69(7):1065–1068, 1992.

[78] D. S. Cornett, I. J. Amster, and M. A. Duncan et al. Laser desorption mass spectrometry of photopolymerized C_{60} films. *Journal of Physical Chemistry*, 97(19):5036–5039, 1993.

[79] M. Menon, K. R. Subbaswamy, and M. Sawtarie. Structure and properties of C_{60} dimers by generalized tight binding molecular dynamics. *Phys. Rev. B*, 49(19):13966–13969, 1994.

[80] G. B. Adams, J. B. Page, O. F. Sankey, and M. O'Keeffe. Polymerized C_{60} studied by first principle molecular dynamics. *Phys. Rev. B*, 50:17471, 1994.

[81] P. C. Eklund P. Zhou and P. W. Stephens. Unpublished results.

[82] J. Li, M. Ozawa, N. Kino, T. Yoshizawa, T. Mitsuki, H. Horiuchi, O. Tachikawa, K. Kishio, and K. Kitazawa. Photopolymerized skins of C_{60} crystals. *Chem. Phys. Lett.*, 227(6):572, 1994.

[83] P. Zhou, Z. H. Dong, A. M. Rao, and P. C. Eklund. Reaction mechanism for the photopolymerization of solid fullerene C_{60}. *Chem. Phys. Lett.*, 211(4-5):337–340, 1993.

[84] P. C. Eklund, A. M. Rao, P. Zhou, Y. Wang, and J. M. Holden. Photochemical transformation of C_{60} and C_{70} films. *Thin Solid Films*, 257:185–203, 1995.

[85] S. Saito and A. Oshiyama. Cohesive mechanism and energy bands of solid C_{60}. *Phys. Rev. Lett.*, 66(20):2637–2640, 1991.

[86] R. E. Smalley. Doping the fullerenes. In G. S. Hammond and V. J. Kuck, editors, *Large Carbon Clusters*, page 199, Washington, DC, 1991. American Chemical Society.

[87] R. E. Smalley. Self assembly of the fullerenes. *Accounts of Chemical Research*, 25(3):98–105, 1992.

[88] J. N. Liu, B. L. Gu, and R. S. Han. Electronic structures of doped fullerenes with boron and nitrogen atoms. *Solid State Commun.*, 84(8):807–810, 1992.

[89] T. Pradeep, V. Vijayakrishnan, and A. K. Santra et al. Interaction of nitrogen with fullerenes: Nitrogen derivatives of C_{60} and C_{70}. *Journal of Physical Chemistry*, 95(26):10564–10565, 1991.

[90] C. N. R. Rao, T. Pradeep, and R. Seshadri et al. Nitrogen derivatives of C_{60} and C_{70}: Interaction of fullerenes with nitrogen in gas phase and with amines in solution phase. *Indian Journal of Chemistry Section A-Inorgancic Physical Theoretical and Analytical*, 31(5):F27–F31, 1992.

[91] R. Seshadri, A. Govindaraj, and R. Nagarajan et al. Addition of amines and halogens to fullerenes C_{60} and C_{70}. *Tetrahedron Letters*, 33(15):2069–2070, 1992.

[92] H. Selig, C. Lifshitz, T. Peres, J. E. Fischer, A. R. McGhie, W. J. Romanow, Jr. J. P. McCauley, and III A. B. Smith. Fluorinated fullerenes. *J. Am. Chem. Soc.*, 113:5475–5476, 1991.

[93] J. H. Holloway, E. G. Hope, R. Taylor, G. J. Langley, A. G. Avent, T. J. Dennis, J. P. Hare, H. W. Kroto, and D. R. M. Walton. *J. Chem. Soc., Chem. Commun.*, page 966, 1991.

[94] R. E. Haufler, J. J. Conceicao, L. P. F. Chibante, Y. Chai, N. E. Byrne, S. Flanagan, M. M. Haley, S. C. O'Brien, C. Pan, Z. Xiao, W. E. Billups, M. A. Ciufolini, R. H. Hauge, J. L. Margrave, L. J. Wilson, R. F. Curl, and R. E. Smalley. Matrix isolation spectroscopy of C_{60}. *J. Phys. Chem.*, 94:8634, 1990.

[95] P. R. Birkett, P. B. Hitchcock, H. W. Kroto, R. Taylor, and D. R. M. Walton. Preparation and characterization of $C_{60}Br_6$ and $C_{60}Br_8$. *Nature (London)*, 357(6378):479–481, 1992.

[96] P. R. Birkett, A. G. Avent, and A. D. Darwish et al. Preparation and C-13 NMR spectroscopic characterization of $C_{60}Cl_6$. *Journal of the Chemical Society (London Chemical Communications)*, (15):1230–1232, 1993.

[97] R. C. Haddon, A. F. Hebard, M. J. Rosseinsky, D. W. Murphy, S. J. Duclos, K. B. Lyons, B. Miller, J. M. Rosamilia, R. M. Fleming, A. R. Kortan, S. H. Glarum, A. V. Makhija, A. J. Muller, R. H. Eick, S. M. Zahurak, R. Tycko, G. Dabbagh, and F. A. Thiel. Conducting films of C_{60} and C_{70} by alkali-metal doping. *Nature (London)*, 350(6316):320–322, 1991.

[98] R. M. Fleming, A. P. Ramirez, M. J. Rosseinsky, D. W. Murphy, R. C. Haddon, S. M. Zahurak, and A. V. Makhija. *Nature (London)*, 352:787, 1991.

[99] G. P. Kochanski, A. F. Hebard, R. C. Haddon, and A. T. Fiory. Electrical resistivity and stoichiometry of K_xC_{60} films. *Science*, 255(5041):184–186, 1992.

[100] A. F. Hebard, , M. J. Rosseinsky, R. C. Haddon, D. W. Murphy, S. H. Glarum, T. T. M. Palstra, A. P. Ramirez, and A. R. Kortan. Superconductivity at 18K in potassium-doped C_{60}. *Nature (London)*, 350:600–601, 18 April 1991.

[101] K. Holczer, O. Klein, G. Grüner, S.-M. Huang, R. B. Kaner, K.-J. Fu, R. L. Whetten, and F. Diederich. Alkali-fulleride superconductors: Synthesis, composition, and diamagnetic shielding. *Science*, 252:1154–1157, 1991.

[102] M. J. Rosseinsky, A. P. Ramirez, S. H. Glarum, D. W. Murphy, R. C. Haddon, A. F. Hebard, T. T. M. Palstra, A. R. Kortan, S. M. Zahurak, and A. V. Makhija. Superconductivity at 28K in Rb_xC_{60}. *Phys. Rev. Lett.*, 66(21):2830–2832, 1991.

[103] K. Tanigaki, T. W. Ebbesen, S. Saito, J. Mizuki, J. S. Tsai, Y. Kubo, and S. Kuroshima. *Nature (London)*, 352:222, 1991.

[104] T. T. M. Palstra, O. Zhou, Y. Iwasa, P. Sulewski, R. Fleming, and B. Zegarski. High pressure superconducting phase of Cs_3C_{60} with T_c=40K. *Solid State Commun.*, 93:327, 1995.

[105] Q. Zhu, D. E. Cox, J. E. Fischer, K. Kniaź, A. R. McGhie, and O. Zhou. Intercalation of solid C_{60} with iodine. *Nature (London)*, 355(6362):712–714, 1992.

[106] Arthur F. Hebard. Superconductivity in doped fullerenes. *Physics Today*, 45(11):26–32, 1992.

[107] Z. H. Dong, P. Zhou, J. M. Holden, P. C. Eklund, M. S. Dresselhaus, and G. Dresselhaus. Observation of higher order Raman modes in C_{60} films. *Phys. Rev. B*, 48(4):2862–2865, 1993.

[108] K. A. Wang, A. M. Rao, P. C. Eklund, M. S. Dresselhaus, and G. Dresselhaus. Observation of higher order infrared modes in solid C_{60} films. *Phys. Rev. B*, 48(15):11375–11380, 1993.

[109] S. Guha, J. Menendez, J. B. Page, G. B. Adams, G. S. Spencer, J. P. Lehman, P. Giannozzi, and S. Baroni. Isotopically resolved Raman spectra of C_{60}. *Phys. Rev. Lett.*, 72(21):3359–3362, 1994.

[110] R. A. Jishi, R. M. Mirie, and M. S. Dresselhaus. Force constant model for the vibrational modes in C_{60}. *Phys. Rev. B*, 45(23):13685–13689, 1992.

[111] R. A. Jishi, M. S. Dresselhaus, G. Dresselhaus, K.-A. Wang, P. Zhou, A. M. Rao, and P. C. Eklund. Vibrational mode frequencies in C_{70}. *Chem. Phys. Lett.*, 206(1-4):187–192, 1993.

[112] A. F. Hebard, O. Zhou, Q. Zhong, R. M. Fleming, and R. C. Haddon. C_{60} films on surface-treated silicon: Recipes for amorphous and crystalline growth. *Thin Solid Films*, 257, 1994.

[113] Q.-Y. Tong, C. B. Eom, U. Gösele, and A. F. Hebard. Materials with a buried C_{60} layer produced by wafer direct bonding. *J. Electrochem. Soc.*, 141(10):L137–L138, 1994.

[114] A. V. Hamza, M. Balooch, R. J. Tench, M. A. Schildbach, R. A. Hawley-Fedder, H. W. H. Lee, and C. McConaghy. Patterning of C_{60} films. *Journal of Vacuum Science Technology B*, 11(3):763–765, 1993.

[115] A. F. Hebard, C. B. Eom, R. M. Fleming, Y. J. Chabal, A. J. Muller, S. H. Glarum, G. J. Pietsch, R. C. Haddon, A. J. Mujsce, M. A. Paczkowski, and G. P. Kochanski. Enhanced cohesion of photo oxygenated fullerene films: A new opportunity for lithography. *Applied Physics Part A. Solids and Surfaces.*, 57(3):299–303, 1993.

[116] P. Zhou, A. M. Rao, K. A. Wang, J. D. Robertson, C. Eloi, M. S. Meier, S. L. Ren, X.-X. Bi, P. C. Eklund, and M. S. Dresselhaus. Photo-assisted structural transition and oxygen diffusion in solid C_{60} films. *Appl. Phys. Lett.*, 60(23):2871–2873, 1992.

[117] C. C. Eloi, J. D. Robertson, A. M. Rao, P. Zhou, K-A. Wang, and P. C. Eklund. An investigation of photoassisted diffusion of oxygen in solid C_{60} films using resonant alpha scattering. *Journal of Materials Research*, 8(12):3085–3089, 1993.

[118] H. G. Busmann, H. Gaber, H. Strasser, and I. V. Hertel. Hard amorphous carbon coatings on soft epitaxial fullerite films by fullerene beam deposition. *Appl. Phys. Lett.*, 64(1):43–45, 1994.

[119] R. F. Pierret. *Field Effect Devices*, volume 4 of *Modular Series on Solid State Devices.* Addison-Wesley, 1983.

[120] J. Kastner, J. Paloheimo, and H. Kuzmany. Fullerene field-effect transistors. In *Proc. of the Int. Winter School on Electronic Properties of High Temperature Superconductors (IWEPS'92)*, Kirchberg, Austria, 1992.

[121] J. Paloheimo, H. Isotalo, J. Kastner, and H. Kuzmany. Conduction mechanisms in undoped thin films of C_{60} and $C_{60/70}$. *Synthetic Metals*, 56(2-3):3185–3190, 1993.

[122] K. Hoshimono, S. Fujimori, and S. Fujita et al. Semiconductor like carrier conduction and its field effect mobility in metal doped C_{60} thin films. *Japanese Journal of Applied Physics Part 2, Letters*, 32(8A):L1070–L1073, 1993.

[123] R. C. Haddon, A. S. Perel, R. C. Morris, T. T. M. Palstra, A. F. Hebard, and R. M. Fleming. C_{60} thin film transistors. *Appl. Phys. Lett.*, 67:121, 1995.

[124] D. Sarkar and N. J. Halas. Dember effect in C_{60} thin films. *Solid State Commun.*, 90(4):261–265, 1994.

[125] E. Frankevich, Y. Maruyama, H. Ogata Y. Achiba, and K. Kikuchi. Mobilities of charge carriers in C_{60} orthorhombic single crystal. *Solid State Commun.*, 88(2):177–181, 1993.

[126] E. Frankevich, Y. Maruyama, and H. Ogata. Mobility of charge carriers in vapor phase grown C_{60} single crystal. *Chem. Phys. Lett.*, 214(1):39–44, 1993.

[127] K. M. Chen, Y. Q. Jia, K. Wu, X. D. Zhang, W. B. Zhao, C. Y. Li, and Z. N. Gu. The bias-temperature effect in a rectifying Nb/C_{60}/p-Si structure: Evidence for mobile negative charges in the solid C_{60} film. *J. Phys. Condensed Matter*, 6:L367–L372, 1994.

[128] K. M. Chen, Y. Q. Jia, S. X. Jin, K. Wu, W. B. Zhao, C. Y. Li, Z. N. Gu, and X. H. Zhou. Heterojunctions of solid C_{60} and crystalline silicon: rectifying properties and energy-band models. *Abstract of spring MRS*, H7.3:169, 1995.

[129] H. Yonehara and C. Pac. Dark and photoconductivity behavior of C_{60} thin films sandwiched with metal electrodes. *Appl. Phys. Lett.*, 61(5):575–576, 1992.

[130] K. Pichler, M. G. Harrison, R. H. Friend, and S. Pekker. Charge injection, electric field modulation and spectroscopy of charged states of fullerene in metal insulator semiconductor devices. *Synthetic Metals*, 56(2-3):3229–3234, 1993.

[131] N. S. Sariciftci, D. Braun, and C. Zhang et al. Semiconducting polymer buckminsterfullerene heterojunctions: Diodes, photodiodes, and photovoltaic cells. *Appl. Phys. Lett.*, 62(6):585–587, 1993.

[132] N. S. Sariciftci, A. J. Heeger, and F. Wudl. *J. Appl. Phys., Jpn. Solid State Devices and Materials, Intl. Conf. on Solid State Devices and Materials*, pages 781–784, 1993. (25th International Conference, Chiba, Japan).

[133] L. Smilowitz, A. W. Hays, G. Wang, A. J. Heeger, and J. E. Bowers. *Synthetic Metals*, in press, 1994.

[134] N. S. Sariciftci and A. J. Heeger. Reversible, metastable, ultrafast photoinduced electron transfer from semiconducting polymers to buckminsterfullerene and in the corresponding donor acceptor heterojunctions. *International Journal of Modern Physics B*, 8(3):237–274, 1994.

[135] J. B. Camp and R. B. Schwarz. Use of fullerene films as surfaces of uniform electric potential. *Appl. Phys. Lett.*, 63(4):455–457, 1993.

[136] Y. B. Zhao, D. M. Poirier, R. J. Pechman, and J. H. Weaver. Electron stimulated polymerization of solid C_{60}. *Appl. Phys. Lett.*, 64(5):577–579, 1994.

[137] Y. Wang, J. M. Holden, X. X. Bi, and P. C. Eklund. Thermal decomposition of polymeric C_{60}. *Chem. Phys. Lett.*, 217(4):413–417, 1994.

[138] A. F. Hebard, T. T. M. Palstra, and R. C. Haddon et al. Absence of saturation in the normal state resistivity of thin films of K_3C_{60} and Rb_3C_{60}. *Phys. Rev. B*, 48(13):9945–9948, 1993.

[139] K. B. Lyons, A. F. Hebard, D. Inniss, R. L. Opila, Jr., H. L. Carter, Jr., and R. C. Haddon. Photo-induced cross linking and decomposition of C_{60} in the presence of NO. *J. Phys. Chem.*, 99:16516, 1995.

[140] R. S. Ruoff. *Interface*, 3(1):30, 1994.

[141] A. W. Synowczyk and J. Heinze. Application of fullerenes as sensor materials. volume 117, pages 73–77, Berlin, 1993. Springer-Verlag. (Springer Series in Solid-State Sciences).

[142] R. P. Feynman. *There's plenty of room at the bottom.* John Wiley & Sons, New York, 1961.

[143] Von Hippel. Molecular designing of materials. *Science*, 138(12):91–108, 1962.

[144] K. E. Drexler. Molecular engineering: An approach to the development of general capabilities for molecular manipulation. *Proc. Natl. Acad. Sci. USA*, 78(9):5275–5278, 1981.

[145] K. E. Drexler. *Engines of Creation: The Coming Era of Nanotechnology.* Anchor Press/Doubleday, New York, 1986.

[146] K. E. Drexler. *Nanosystems: Molecular Machinery, Manufacturing, and Computation.* John Wiley & Sons, 1992.

[147] J. A. Stroscio and D. M. Eigler. *Science*, 254:1319, 1991.

[148] J. Viitanen. Proposal for precise manipulation of C_{60} molecules. *Journal of Vacuum Science Technology B: Microelectronics Processing, Phenomena*, 11(1):115–116, 1993.

[149] R. Lüthi, E. Meyer, H. Haefke, L. Howald, W. Gutmannsbauer, and H.-J. Güntherodt. Sled-type motion on the nanometer scale: Determination of dissipation and cohesive energies of C_{60}. *Science*, 266:1979–1981, 1994.

[150] R. F. Schinazi, R. Sijbesma, and G. Srdanov et al. Synthesis and virucidal activity of a water soluble, configurationally stable, derivatized C_{60} fullerene. *Antimicrobial agents and chemotherapy*, 37(8):1707–1710, 1993.

[151] S. H. Friedman, D. L. Decamp, and R. P. Sijbesma et al. Inhibition of the HIV-1 protease by fullerene derivatives: Model building studies and experimental verification. *J. Am. Chem. Soc.*, 115(15):6506–6509, 1993.

[152] S. Saito, S. I. Sawada, N. Hamada, and A. Oshiyama. Electronic and geometric structures of fullerenes. *Mater. Sci. Eng.*, B19:105, 1993.

[153] R. Saito, M. Fujita, G. Dresselhaus, and M. S. Dresselhaus. Electronic structure and growth mechanism of carbon tubules. *Materials Science and Engineering*, 19(1-2):185–191, 1993.

[154] H. Schmid and H. W. Fink. Mechanical and electronic manipulation of nanometer-sized wires. *Nanotechnology*, 5:26–32, 1994.

[155] C. M. Jin, T. Guo, Y. Chai, A. Lee, and R. E. Smalley. Fullerene nanowires. In C. Taliani, G. Ruani, and R. Zamboni, editors, *Proceedings of the First Italian Workshop on Fullerenes: Status and Perspectives*, volume 2 of *World Scientific Advanced Series in Fullerenes*, pages 21–29, Singapore, 1992. World Scientific.

[156] R. E. Smalley. From dopyballs to nanowires. *Materials Science and Engineering Pt. B*, 19(1-2):1–7, 1993.

[157] T. W. Ebbesen. Making bucks. how to profit from fullerenes: Winning strategies for emerging markets. *Nature (London)*, 361(6409):218–218, 1993.

[158] D. R. Huffman. Applications of fullerenes. *Materials letters*, 21(2):127, 1994.

[159] Mitsubishi forms a venture to commercialize fullerenes. *Chemical Marketing Reporter*, 245(20):3, 16 May 1994.

[160] R. M. Baum. Commercial uses of fullerenes and derivatives slow to develop. *Chemical and Engineering News*, 71(47):8–18, 22 Nov 1993.

[161] Stephen Moore. The shape of things to come? *Chemical Engineering*, 99(7):41–45, July 1992.

[162] P. van Musschenbroek. *Introductio ad Philosophiam Naturalem.* Luchtmans, Leiden, 1762.

[163] M. Faraday. *Phil. Trans.*, 128:1, 79, 265, 1837–1838.

[164] C. J. F. Böttcher. *Theory of electric polarization*, volume 1. Elsevier, Amsterdam, 1973.

[165] O. F. Mossotti. *Bibl. Univ. Modena*, 6:193, 1847.

[166] O. F. Mossotti. *Mem. di mathem. e di fisica in Modena*, 24(2):49, 1850.

[167] R. Clausius. volume 2. Vieweg, Braunschweig, 1879.

[168] P. Debye. *Phys. Z.*, 13:97, 1912.

[169] J. J. Berzelius. *Essai sur la Theorié des Proportions Chimique et sur l'Influence Chimique de l'Electricité.* Paris, 1819.

[170] L. Onsager. Electric moments of molecules in liquids. *J. Amer. Chem. Soc.*, 58:1486–1493, 1936.

[171] J. G. Kirkwood. The dielectric polarization of polar liquids. *Journal of Chemical Physics*, 7:911–919, 1939.

[172] J. G. Kirkwood and R. M. Fuoss. Anomalous dispersion and dielectric loss in polar polymers. *Journal of Chemical Physics*, 9:329–340, 1941.

[173] P. Drude. Zwei methoden zur messung der dielektrizitätskonstante und der elektrischen absorption bei schnellen schwingungen. *Z. Phys. Chem.*, 23:267–325, 1897.

[174] K. S. Cole and R. H. Cole. Dispersion and absorption in dielectrics. *Journal of Chemical Physics*, 9:341–351, 1941.

[175] D. W. Davidson and R. H. Cole. Dielectric relaxation in glycerol, propylene glycol, and *n*-propanol. *The Journal of Chemical Physics*, 19(12):1484–1490, 1951.

[176] G. Williams and D. C. Watt. Non-symmetrical dielectric relaxation behavior arising from a simple empirical decay function. *Trans. Faraday Soc.*, 66:80–85, 1970.

[177] A. K. Jonscher. *Dielectric Relaxation in Solids.* Chelsea Dielectrics Press, London, 1983.

[178] P. P. Jenkins, A. N. MacInnes, M. Tabib-Azar, and A. R. Barron. Gallium Arsenide transistors: Realization through a molecularly designed insulator. *Science*, 263:1751–1753, 25 March 1994.

[179] J. T. Yount, P. M. Lenahan, and J. T. Krick. Comparison of defect structure in N_2O- and NH_3-nitrided oxide dielectrics. *Appl. Phys. Lett.*, 76(3):1754–1758, 1994.

[180] D. S. Shukert. Design and processing of low-dielectric-constant polymeric composites. Master's thesis, M.I.T., Cambridge, MA, 1987. MIT MS ME'87.

[181] T.-M. Lu, S. P. Murarka, T. S. Kuan, and C. H. Ting, editors. *Low-Dielectric Constant Materials — Synthesis and Applications in Microelectronics*, volume 381 of *Mat. Res. Soc. Symp. Proc.* Materials Research Society, 1995.

[182] G. M. Sessler. *Electrets.* Springer, Berlin, 1980.

[183] A. R. von Hippel, editor. *Dielectric materials and applications.* John Wiley & Sons, New York, 1954.

[184] August Chełkowski. *Dielectric physics*, volume 9 of *Studies in Physical and Theoretical Chemistry*. Elsevier, 1980.

[185] H. A. Lorentz. *Ann. Physik*, 9:641, 1880.

[186] L. Lorenz. *Ann. Physik*, 11:70, 1880.

[187] P. Debye. *Polar Molecules*. Dover, New York, 1929.

[188] J. H. Van Vleck. *Ann. N. Y. Acad. Sci.*, 40:289, 1940.

[189] A. R. von Hippel. *Dielectrics and Waves*. John Wiley & Sons, New York, 1954.

[190] D. H. Staelin, A. W. Morgenthaler, and J. A. Kong. *Electromagnetic Waves*. Prentice Hall, 1994.

[191] J. C. Maxwell. *A Treatise on Electricity and Magnetism*. Clarendon Press, Oxford, 1892.

[192] N. F. Sheppard. *Dielectric analysis of the cure of thermosetting epoxy/amine systems*. PhD thesis, Massachusetts Institute of Technology, Cambridge, MA, 1986.

[193] D. R. Day, T. J. Lewis, H. L. Lee, and S. D. Senturia. The role of boundary layer capacitance at blocking electrodes in the interpretation of dielectric cure data in adhesives. *J. Adhesion*, 18:73–90, 1985.

[194] C. P. Smyth. *Dielectric Behavior and Structure*. McGraw-Hill, New York, 1955.

[195] E. von Schweidler. Studien über die Anomalien im Verhalten der Dielektrika. *Annalen der Physik*, 24:711–770, 1907.

[196] K. W. Wagner. *Ann. d. Physik*, c1910.

[197] S. H. Glarum. Dielectric relaxation of isoamyl bromide. *J. Chem. Phys.*, 33:639, 1960.

[198] G. Williams, D. C. Watt, S. B. Dev, and A. M. North. Further considerations of non-symmetrical dielectric relaxation behaviour arising from a simple empirical decay function. *Trans. Faraday Soc.*, 67:1323–1335, 1977.

[199] R. Kohlrausch. *Ann. Phys. (Leipzig)*, 12:393, 1847.

[200] C. P. Lindsey and G. D. Patterson. Detailed comparison of the Williams-Watts and Cole-Davidson functions. *J. Chem. Phys.*, 73(7):3348–3357, 1980.

[201] E. W. Montroll and J. T. Bendler. On levy (or stable) distributions and the williams-watts model of dielectric relaxation. *J. Stat. Phys.*, 34:129, 1984.

[202] M. F. Shlesinger. Williams-Watts dielectric relaxation: A fractal time stochastic process. *J. Stat. Phys.*, 36:117, 1984.

[203] J. C. Phillips. Kohlrausch explained: A partial solution to a problem that is 150 years old. *AT&T Technical Memorandum ITD-94-22968P*, 1994.

[204] A. K. Jonscher. The 'universal' dielectric response. *Nature*, 267:673–679, 1977.

[205] A. K. Jonscher. A new model of dielectric loss in polymers. *Colloid & Polymer Sci.*, 253:231–250, 1975.

[206] A. K. Jonscher. Physical basis of dielectric loss. *Nature*, 253:717–719, 1975.

[207] L. A. Dissado and R. M. Hill. *Nature*, 279:685, 1979.

[208] L. A. Dissado and R. M. Hill. *Phil. Mag.*, B41:625, 1980.

[209] A. K. Jonscher. *J. Phys. D: Applied Physics*, 13:L137, 1980.

[210] A. K. Jonscher. *J. Mater. Sci.*, 16:2037, 1981.

[211] R. H. Kienle and H. H. Race. The electrical, chemical and physical properties of alkyd resins. *Trans. Electrochem. Soc.*, 65:87, 1934.

[212] A. J. Mackinnon, P. J. Hall, D. Hayward, and R. A. Pethrick. Low-frequency dielectric measurements on argone premium coals. *Fuel*, 72(7):1077–1078, 1993.

[213] E. Benoit, P. Maincent, and J. Bessiere. Applicability of dielectric measurements to the adsorption of drugs onto nanoparticles. *International Journal of Pharmaceutics*, 84(3):283–286, 1992.

[214] D. E. Kranbuehl. Continuous dielectric measurements of polymerizing systems. *Journal of Non-Crystalline Solids*, 131–133:930–934, 1991.

[215] M. Orczyk, E. Pater, and J. Sworakowski. Kinetics of polymerization of mixed diacetylene single-crystals determined from dielectric measurements. *Makromolekulare Chemie*, 193(5):1135–1146, 1992.

[216] P. Mauret and J. P. Fayet. Calculation method of crude water-content by dielectric measurements. *Revue de l'Institut Francais du Petrole*, 47(2):285–288, 1992.

[217] K. Mishima, A. Mimura, Y. Takahara, K. Asami, and T. Hanai. Online monitoring of cell concentrations by dielectric measurements. *Journal of Fermentation and Bioengineering*, 72(4):291–295, 1991.

[218] K. Mishima, A. Mimura, and Y. Takahara. Online monitoring of cell concentrations during yeast cultivation by dielectric measurements. *Journal of Fermentation and Bioengineering*, 72(4):296–299, 1991.

[219] R. Pethig. Dielectric properties of biological materials: Biophysical and medical applications. *IEEE Trans. on Electrical Insulation*, EI-19(5):453–474, 1984.

[220] K. R. Foster and H. P. Schwan. Dielectric properties of tissues and biological materials: A critical review. *Crit. Rev. Biomed. Eng.*, 17(1):25–104, 1989.

[221] M. Ungarish, R. Joseph, J. Vittoser, and S. Kenig. Cure cycle optimization of composites by dielectric measurements. *Composites*, 21(6):481–486, 1990.

[222] W. B. Zhang and P. B. Addis. Prediction of levels of cholesterol oxides in heated tallow by dielectric measurement. *Journal of Food Science*, 55(6):1673–1675, 1990.

[223] J. Halbritter. *Z. Physik*, B31:19, 1978.

[224] J. F. Johnson and R. H. Cole. Dielectric polarization of liquid and solid formic acid. *J. Am. Chem. Soc.*, 73:4536, 1951.

[225] A. F. Hebard, S. A. Ajuria, and R. H. Eick. Interface contribution to the capacitance of thin-film Al-Al_2O_3-Al trilayer structures. *Appl. Phys. Lett.*, 51(17):1349–1351, 1987.

[226] S. D. Senturia and S. L. Garverick. Method and apparatus for microdielectrometry. U.S. Patent No. 4,423,371, Dec. 27, 1983.

[227] S. D. Senturia, Jr. N. F. Sheppard, H. L. Lee, and D. R. Day. *In-situ* measurements of the properties of curing systems with microdielectrometry. *J. Adhesion*, 15:69–90, 1982.

[228] N. F. Sheppard, D. R. Day, H. L. Lee, and S. D. Senturia. Microdielectrometry. *Sensors and Actuators*, 2:263–274, 1982.

[229] S. L. Garverick and S. D. Senturia. An MOS device for AC measurements of surface impedance with application to moisture monitoring. *IEEE Transactions on Electron Devices*, ED-29(1):90–94, Jan 1982.

[230] H. L. Lee. *Optimization of a Resin Cure Sensor.* PhD thesis, M.I.T., Cambridge, MA, 1982.

[231] M. C. W. Coln and S. D. Senturia. The application of linear system theory to parametric microsensors. In *Proc. Transducers '85*, page 118. IEEE, 1985.

[232] M. C. W. Coln. *A high performance dielectric measurement system.* PhD thesis, Massachusetts Institute of Technology, Cambridge, MA, 1985.

[233] *Low Level Measurements: Precision DC Current, Voltage and Resistance Measurements.* Keithley Instruments, Inc., Cleveland, OH, 4th edition, 1992.

[234] E. Sohmen, J. Fink, and W. Krätschmer. Electron energy-loss spectroscopy studies on C_{60} and C_{70} fullerite. *Z. Phys. B – Condensed Matter*, 86:87–92, 1992.

[235] P. C. Eklund, A. M. Rao, Y. Wang, P. Zhou, K. A. Wang, J. M. Holden, M. S. Dresselhaus, and G. Dresselhaus. Optical properties of C_{60} and C_{70} based solid films. *Thin Solid Films*, 257:211–232, 1995.

[236] F. Wooten. *Optical Properties of Solids.* Academic, New York, 1972.

[237] M. K. Kelly, P. Etchegoin, D. Fuchs, W. Krätschmer, and K. Fostiropoulos. Optical transitions of C_{60} films in the visible and ultraviolet from spectroscopic ellipsometry. *Phys. Rev. B*, 46(8):4963–4968, 1992.

[238] A. Lucas, G. Gensterblum, J. J. Pireaux, P. A. Thiry, R. Caudano, J. P. Vigneron, Ph. Lambin, and W. Krätschmer. Elementary excitations of C_{60} from the far infrared to the far vacuum ultraviolet studied by high resolution electron-energy loss spectroscopy. *Phys. Rev. B*, 45(23):13694–13702, 1992.

[239] I. V. Hertel, H. Steger, J. de Vries, B. Weisser, C. Menzel, B. Kamke, and W. Kamke. Giant plasmon excitation in free C_{60} and C_{70} molecules studied by photoionization. *Phys. Rev. Lett.*, 68(6):784–787, 1992.

[240] S. B. Fleischer, B. Pevzner, D. Dougherty, M. S. Dresselhaus, E. P. Ippen, and A. F. Hebard. Visible and near-IR femtosecond low-excitation pump-probe studies on C_{60} and alkaline doped C_{60} films. In *MRS Abstracts, 1995 Fall meeting*, page 739. Materials Research Society Press, Pittsburgh, PA, 1995.

[241] A. Hamed, Rasmussen, and P. H. Hor. Existence of persistent photoconductivity at high temperatures in C_{60}. *Phys. Rev. B*, 48(19):14760–14763, 1993.

[242] I. Rusakova, A. Hamed, and P. H. Hor. Effects of deposition temperature and thermal treatment on the structure of C_{60} and C_{70} films. In C. L. Renschler, D. M. Cox, J. J. Pouch, and Y. Achiba, editors, *Novel Forms of Carbon II*, volume 349 of *Mat. Res. Soc. Symp. Proc.*, pages 101–106, Pittsburgh, Pennsylvania, 1994. Materials Research Society.

[243] I. Rusakova, A. Hamed, and P. H. Hor. TEM study of C_{70} polycristalline films. *Journal of Materials Research*, 9(11):2814–2822, 1994.

[244] R. A. Assink, J. E. Schirber, D. A. Loy, B. Morosin, and G. A. Carlson. Intercalation of molecular species into the interstitial sites of fullerene. *Journal of Materials Research*, 7(8):2136–2143, 1992.

[245] D. E. Morris, K. K. Singh, and A. P. B. Sinha. A novel stable solid formed by C_{60}+Oxygen at high $P(O_2)$. *Journal of Materials Research*, 8(9):2273–2276, 1993.

[246] G. H. Kroll, P. J. Benning, Y. Chen, T. R. Ohno, J. H. Weaver, L. P. F. Chibante, and R. E. Smalley. Intercaction of O_2 with C_{60}: photon-induced oxidation. *Chem. Phys. Lett.*, 181(2-3):112–116, 1991.

[247] A. M. Rao, K. A. Wang, J. M. Holden, Y. Wang, P. Zhou, P. C. Eklund, C. C. Eloi, and J. D. Robertson. Photoassisted oxygen doping of C_{60} films. *Journal of Materials Research*, 8(9):2277–2281, 1993.

[248] F. N. Tebbe, J. Y. Becker, D. B. Chase, L.E. Firment, E.R. Holler, B.S. Malone, P.J. Krusic, and E. Wasserman. Multiple, reversible chlorination of C_{60}. *J. Am. Chem. Soc.*, 113(26):9900–9901, 1991.

[249] S. G. Kukolich and D. R. Huffman. Epr spectra of C_{60} anion and cation radicals. *Chem. Phys. Lett.*, 182:263–265, 1991.

[250] S. Kawata, K. Yamauchi, and S. Suzuki et al. The origin of the ESR signal of C_{60} seen in the powder and in benzene solution: The indication of the reaction of C_{60} with oxygen induced by photoexcitation. *Chemistry Letters*, (9):1659–1662, 1992.

[251] D. Leporini, L. Andreozzi, C. Callegari, and F. Fuso. Photoassisted interactions in C_{60}/O_2 mixtures: an ESR, calorimetric and mass spectroscopy investigation. *Physics Letters A*, 189(4):322–326, 1994.

[252] J. E. Schirber, R. A. Assink, G. A. Samara, B. Borosin, and D. A. Loy. Negative pressure effects in high-pressure oxygen-intercalated C_{60}. *Phys. Rev. B*, 51(21):15552–15554, 1995.

[253] T. Arai, Y. Murakami, H. Suematsu, K. Kikuchi, Y. Achiba, and I. Ikemoto. Resistivity of single crystal C_{60} and effect of oxygen. *Solid State Commun.*, 84(8):827–829, 1992.

[254] P. M. He, Y. B. Xu, and X. J. Zhang et al. Electrical conductivity studies of a pure C_{60} single crystal. *Journal of Physics Condensed Matter*, 5(37):7013–7016, 1993.

[255] A. Zahab and L. Firlej. Resistivity in C_{60} thin films of high crystallinity. *Solid State Commun.*, 87(10):893–897, 1993.

[256] D. Barančok, M. Haluška, V. Nádaždy, and J. Vajda. Strong influence of the phase transition on the electrical properties of C_{60} single crystals. *Solid State Comm.*, 94(8):597–600, 1995.

[257] J. Mort, R. Ziolo, M. Machonkin, D. R. Huffman, and M. I. Fegurson. Electrical conductivity studies of undoped solid films of $C_{60/70}$. *Chem. Phys. Lett.*, 186(2-3):284–286, 1991.

[258] A. Hamed, Y. Y. Sun, Y. K. Tao, R. L. Meng, and P. H. Hor. Effects of oxygen and illumination on the *in situ* conductivity of C_{60} thin films. *Phys. Rev. B*, 47(16):10873–10880, 1993.

[259] N. Takahashi, H. Dock, and N. Matsuzawa et al. Plasma polymerized C_{60}/C_{70} mixture films: Electric conductivity and structure. *Journal of Applied Physics*, 74(9):5790–5798, 1993.

[260] M. Hosoya, K. Ichimura, Z. H. Wang, G. Dresselhaus, M. S. Dresselhaus, and P. C. Eklund. Dark conductivity and photoconductivity in solid films of C_{70}, C_{60}, and K_xC_{70}. *Phys. Rev. B*, 49(7):4981–4986, 1994.

[261] S. Fujimori, K. Hoshimono, and S. Fujita et al. Variation of conductivity and activation energy in metal doped and undoped C_{60} films under oxygen exposure. *Solid State Commun.*, 89(5):437–440, 1994.

[262] T. Asakawa, M. Sasaki, T. Shiraishi, and H. Koinuma. Dark and photoconductivity behaviors of amorphous and crystalline C_{60} films. *Japanese Journal of Applied Physics (Part 1)*, 34(4A):1958–1962, Apr 1995.

[263] S. B. Fleischer, E. P. Ippen, G. Dresselhaus, and M. S. Dresselhaus. Femtosecond optical dynamics of C_{60} and M_3C_{60}. *Appl. Phys. Lett.*, 62(25):3241–3243, 1993.

[264] C. H. Lee, G. Yu, D. Moses, A. J. Heeger, and V. I. Srdanov. Nonlinear transient photovoltaic response in $Al/C_{60}/Au$ devices: Control of polarity with optical bias. *Appl. Phys. Lett.*, 65(6):664–666, 1994.

[265] CRC handbook of chemistry and physics (1992-1993).

[266] R. L. Hettich, R. N. Compton, and R. H. Ritchie. *Phys. Rev. Lett.*, 67:1242–1245, 1991.

[267] M. R. Pederson and A. A. Quong. Polarizabilities, charge states, and vibrational modes of isolated fullerene molecules. *Phys. Rev. B*, 46(20):13584–13591, 1992.

[268] N. Matsuzawa and D. A. Dixon. Local density functional calculations of the polarizability and second order hyperpolarizability of C_{60}. *Journal of Physical Chemistry*, 96(17):6872–6875, 1992.

[269] A. Fick. *Annln Phys.*, 170:59, 1855.

[270] J. Crank. *The Mathematics of Diffusion.* Oxford Univ. Press, Oxford, 2nd edition, 1975.

[271] B. S. Lim, A. S. Nowick, K.-W. Lee, and A. Viehbeck. Sorption of water and organic solutes in polyimide films and its effects on dielectric properties. *J. of Polym. Sci.*, 31:545–555, 1993.

[272] A. V. Hamza, J. Dykes, W. D. Mosley, L. Dinh, and M. Balooch. Reaction and passivation of aluminum with C_{60}. *Surface Science*, 318(3):368–378, 1994.

[273] A. F. Hebard, C. B. Eom, Y. Iwasa, K. B. Lyons, G. A. Thomas, D. H. Rapkine, R. M. Fleming, R. C. Haddon, J. M. Phillips, J. H. Marshall, and R. H. Eick. Charge transfer at aluminum-C_{60} interfaces in thin-film multilayer structures. *Phys. Rev. B*, 50(23):17740–17743, 1994.

[274] R. L. McNally, F. R. Brotzen, A. J. Griffin, Jr., P. J. Loos, and E. V. Barrera. Electronic application for fullerenes. In C. L. Renschler, D. M. Cox, J. J. Pouch, and Y. Achiba, editors, *Novel Forms of Carbon II*, volume 349 of *Mat. Res. Soc. Symp. Proc.*, pages 205–211, Pittsburgh, Pennsylvania, 1994. Materials Research Society.

[275] D. W. Owens, C. M. Aldao, D. M. Poirier, and J. H. Weaver. Charge transfer, doping, and interface morphologies for Al-C_{60}. *Phys. Rev. B*, 51(23):17068–72, 1995.

[276] T. Hashizume, K. Motai, X. D. Wang, H. Shinohara, Y. Saito, Y. Maruyama, K. Ohno, Y. Kawazoe, Y. Nishina, H. W. Pickering, Y. Kuk, and T. Sakura. Intramolecular structures of C_{60} molecules adsorbed on the Cu(111)-(1x1) surface. *Phys. Rev. Lett.*, 71(18):2959–2962, 1993.

[277] E. I. Altman and R. J. Colton. The interaction of C_{60} with noble metal surfaces. *Surface Science*, 295(1-2):13–33, 1993.

[278] E. I. Altman and R. J. Colton. Nucleation, growth, and structure of fullerene films on Au(111). *Surface Science*, 279(1-2):49–67, 1992.

[279] Y. Kuk, D. K. Kim, and Y. D. Suh et al. Stressed C_{60} layers on Au(001). *Phys. Rev. Lett.*, 70(13):1948–1951, 1993.

[280] S. J. Chase, W. S. Bacsa, M. G. Mitch, L. J. Pilione, and J. S. Lannin. Surface enhanced Raman scattering and photoemission of C_{60} on noble metal surfaces. *Phys. Rev. B*, 46(12):7873–7877, 1992.

[281] D. Sarkar and N. J. Halas. Diffusion of silver in C_{60} thin films. *Appl. Phys. Lett.*, 63(17):2438–2440, 1993.

[282] Z. H. Wang and M. S. Dresselhaus. Private communications (M.I.T. research group).

[283] Y. Wang, X. X. Bi, and P. C. Eklund. Private communications (University of Kentucky research group).

[284] S. R. Elliott. *Solid State Ionics*, 27:131, 1988.

[285] K. L. Ngai. *Comments Solid State Phys.*, 9:127, 1979.

[286] K. L. Ngai. *Comments Solid State Phys.*, 9:141, 1980.

[287] K. L. Ngai, R. W. Rendell, A. K. Rajagopal, and S. Teitler. *Ann. NY Acad. Sci.*, 484:150, 1986.

[288] K. L. Ngai, R. W. Rendell, A. K. Rajagopal, and S. Teitler. *J. Chem. Phys.*, 88:5086, 1988.

[289] K. Funke. *Z. Phys. Chem. NF*, 154:251, 1987.

[290] K. Funke. Ion dynamics and correlations: Translational and localized ionic hopping motion in solid electrolytes. *Philosophical Magazine, Part A, Defects and Mechanical Properties*, 68(4):711–724, 1993.

[291] K. Funke. *Prog. Solid State Chem.*, 22:111, 1993.

[292] H. Böttger and V. V. Bryksin. *Hopping Conduction in Solids.* VCH, Weinheim, Germany, 1985.

[293] A. L. Efros and B. I. Shklovskii. *Phys. Status Solidi (b)*, 76:475, 1976.

[294] B. Ya. Balagurov. *Sov. Phys. JETP*, 61:991, 1985.

[295] J. L. Barton. *Verres Refr.*, 20:320, 1966.

[296] T. Nakajima. In *1971 Annual Report, Conf. on Electrical Insulation and Dielectric Phenomena*, page 168. National Academy of Sciences, Washington, DC, 1972.

[297] H. Hamikawa. *J. Non-Cryst. Solids*, 18:173, 1975.

[298] A. Hunt. Frequency-dependent conductivity in glasses. *J. Phys.: Condens. Matter*, 2:9055–9063, 1990.

[299] A. Hunt. Transport in ionic conducting glasses. *J. Phys.: Condens. Matter*, 3:7831–7842, 1991.

[300] A. Hunt. The a.c. conductivity of variable range hopping systems such as amorphous semiconductors. *Philosophical Magazine B*, 64(5):579–589, 1991.

[301] A. Hunt. Dielectric and mechanical relaxation in liquids and glasses: Transition from effective medium to percolation treatments. *Solid State Communications*, 84(7):701–704, 1992.

[302] A. Hunt. Some universalities in the relaxation of glasses. *Journal of Non-Crystalline Solids*, 144(1):21–31, 1992.

[303] A. Hunt. Non-debye relaxation and the glass transition. *Journal of Non-Crystalline Solids*, 160(3):183–227, 1993.

[304] A. Hunt. Dielectric relaxation in dipole glasses, and thermal relaxation and the glass transition in systems with a maximum relaxation time. *Journal of Non-Crystalline Solids*, 160(1-2):42–51, 1993.

[305] A. Hunt. New developments in the theory of the hopping conductivity of spatially random systems. *Journal of Physics Condensed Matter*, 6(6):1239–1252, 1994.

[306] W. Schranz, A. Fuith, and P. Dolinar et al. Low frequency elastic properties of the structural and freezing transitions in single crystal C_{60}. *Phys. Rev. Lett.*, 71(10):1561–1564, 1993.

[307] F. Gugenberger, R. Heid, C. Meingast, P. Adelmann, M. Braun, H. Wühl, M. Haluska, and H. Kuzmany. Glass transition in single crystal C_{60} studied by high resolution dilatometry. *Phys. Rev. Lett.*, 69(26):3774–3777, 1992.

[308] G. Chern, H. Mathias, L. R. Testardi, L. Seger, and J. Schlenoff. Low-frequency dielectric permittivity of C_{60}. *J. of Superconductivity*, 8(2):207–210, 1995.

[309] D. G. Archer and P. Wang. The dielectric constant of water and Debye-Hückel limiting law slopes. *J. Phys. Chem. Ref. Data*, 19, 1990.

[310] N. Minami and M. Sato. Atmosphere sensitive photoconductivity of C_{60} thin films prepared in high vacuum. *Synthetic Metals*, 56(2-3):3092–3097, 1993.

[311] M. Fastow, Y. Kozirovski, M. Folman, and J. Heidberg. IR spectra of CO and NO adsorbed on C_{60}. *Journal of Physical Chemistry*, 96(15):6126–6128, 1992.

[312] Y. Nagano, T. Kiyobayashi, and T. Nitta. CO_2 absorption in C_{60} solid. *Chem. Phys. Lett.*, 217(3):186–190, 1994.

[313] A. F. Hebard. Private communications.

[314] National Instruments Corporation, Austin, TX. *LabVIEW User Manual*, 1992.